2014

An Investigation of Micro and Nanomanufactured Polymer Substrates to Direct Stem Cell Response for Biomedical Applications

John William Rodgers
Lehigh University

An Investigation of Micro and Nanomanufactured Polymer Substrates to Direct Stem Cell Response for Biomedical Applications

by

John W. Rodgers

Presented to the Graduate and Research Committee
of Lehigh University
in Candidacy for the Degree of
Doctor of Philosophy

in
Mechanical Engineering

Lehigh University

May 2014

Approved and recommended for acceptance as a dissertation in partial fulfillment of the requirements for the degree of Doctor of Philosophy.

_____
Date

_____
John P. Coulter

_____
Accepted Date

Committee Members:

_____
Sabrina S. Jedlicka

_____
Xiaohui Zhang

_____
Edmund B. Webb III

_____
Aleksandar K. Angelov

Acknowledgements

I would like to thank my parents for their continuous support and encouragement throughout this process, and my sister for always being willing to offer me positive words when I ran into difficulty in research. I would like to deeply thank my wife for persevering through a long distance relationship and being strong when the light at the end of the tunnel couldn't be seen. I would also like to thank my close friends for being there for me over the years, and for research ideas that led to surprising new discoveries.

I am greatly appreciative of Professor John Coulter for his advisory and friendship over my graduate career at Lehigh. He has taught me a great deal about meaningful research and cultivating a positive perspective when research may not go according to plan. I would also like to thank Professor Sabrina Jedlicka for her advisory and insight over the years. She has been a reliable, helpfully challenging, and supportive person throughout the whole process.

Thank you to Professor Frank Zhang, Professor Edmund Webb, and Aleksandar Angelov for all of your advice and guidance throughout my research. You collective expertise has served to further my research to greater levels. In addition, I would like to thank Eli Towne, Dick Towne, Professor David Angstadt, Professor Raymond Pearson, Ray Filosof, William Maroun, William Mushock, Robert Keyse, Joe Kendzulak, Kevin Conlon, Les Vescio, Ed Ibe, David Henry for providing the micromolding machine, and Bethan Baran for their technical support and help.

Thank you also to Meghan Casey (who did all of the cell culture associated with this dissertation) and Dr. Courtney Leblon for their contributions to this project. I would like to thank the members of the Manufacturing Science Laboratory past and present,

including Burak Bekisli (post-doc advisor), Tyler Skiba, Qi Li, Ryan Curry, Samarth Desai, Salah Alrihan, Majed Alsarheed, Chandresh Thakur, Jiheng Zhang, and Abdullah Alsaeeri.

“Whether you think you can or think you can’t, you’re right.”

-Henry Ford

Table of Contents

List of Figures

List of Tables

Abstract

The rapidly advancing field of micro and nano-manufacturing is continuously offering novel advantages to existing technologies. Micro-injection molding provides a unique opportunity to create substrates capable of controlling the mechanical environment in stem cell culture in a high throughput industrially relevant manner. The modification of such polymer surfaces to match the target surface stiffness of relatively more compliant biological tissues necessitates the movement towards higher aspect ratio smaller dimension features. The requirements provide a significant manufacturing challenge which is approaching a solution.

The development of high aspect ratio large feature density polymer microarrays requires the synergistic optimization of design, material, mold tooling, and processing. A conventional mold base with steel inserts and controllable resistance heating was assembled to incorporate interchangeable inserts with microfeatured silicon inlays. Ultraviolet (UV) lithography with dry etching was used to impart microfeatures into silicon wafers with a variety of different geometries containing aspect ratios ranging from 0.92 to 6. Multiple polymer resins, including polystyrene (PS), low density polyethylene (LDPE), cyclic olefin copolymer (COC), and thermoplastic polyurethane (TPU), were used to test replication and cellular response to materials with different bulk stiffness and topography-modified surface stiffness.

The maximum achieved microfeature aspect ratio was 9.3 (high impact polystyrene), owed to tensile stretching during part ejection. For non-stretched substrates, the maximum molded aspect ratio was 4.5 (LDPE) and highest replication quotient (RQ

= feature height / tooling feature depth) was 0.97 (COC). The maximum aspect ratio molded with consistent features across the entire surface was 2.1 (TPU).

Parameters shown to enhance replication were mold temperature ($T_{mold} = T_g$ was a critical replication transition point), injection velocity at higher mold temperatures, holding time, holding pressure, and nozzle temperature. The importance of certain parameters was material dependent, but mold temperature consistently had a relatively large impact.

A concern that was addressed for a high density array of microfeatures was the consistency of replication, which is vital for the intended application and seldom address in published literature. Increased consistency was attained through strategic placement of temperature control, modification of the main cavity design, and optimized silicon tooling with reduced microcavity nanoroughness.

Silicon tooling was fabricated with the initial objective being to achieve high aspect ratio negative features. However, with the realization of molding and demolding limitations, the tooling microfeature profiles were altered to include a taper and reduction of sidewall scalloping of the tooling. Sophisticated methods of dry etching were used, in which a novel etching technique known as “passivation compensation,” was utilized to manufacture microchannels containing low levels of roughness, a well-controlled tapered profile, and the prospect of high aspect ratios. With the new tooling, topography consistency was dramatically enhanced for both COC and TPU, with Taguchi orthogonal array optimization leading to RQs of 0.82 (aspect ratio = 2) and 0.85 (aspect ratio = 2.1), respectively.

Water contact angle (WCA) measurements for both COC and TPU generally increased with an increase in surface roughness (dictated by microfeature dimensions), reaching WCA measurements of 139.8 +/- 3.1^{o} and 141.1 +/- 2.0^{o}, respectively. WCA hysteresis appeared to increase with roughness up to a critical value for COC while continuing to increase for TPU with a transition, which is thought to be the result of material properties. Moreover, hydrophobic surfaces containing high levels of hysteresis were attributed to the "petal" effect associated with hierarchical surface structures. Hydrophobicity has been shown to be related to biological cell behavior, and thus is an effective characterization technique to measure interfacial properties.

Simulation of the injection molding process using conventional methods was used to describe general conditions present at microchannel inlets. The sprue gate and an increase in plate thickness gave the microfeatured region additional time to fill microfeatures prior to generation of a frozen layer. The delayed solidification is attributed to the low thermal conductivity associated with the polymer melt.

A cell sensing model was developed based on the mechanical interaction between cell and substrate. The model provides a useful design map by which nanofeatured polymer geometry and material choice can be made to achieve a particular apparent surface stiffness. Bending mechanics were simulated for a few specific examples, providing an indication of the limitations associated with using higher aspect ratio nanostructures. A bending example was applied to a manufactured tapered pillar to note the stiffness reduction achieved through use of the substrates molded during the current study.

Cell culture studies showed that the presence of topography had a dramatic effect on cellular morphology and on stress fiber thickness, causing an increase in thickness compared to flat controls. The cytoskeletal re-arrangements occurring may be indicative of a differentiation event, and future results will indicate whether that is the case. Unconventional morphology was observed in the presence of low aspect ratio COC microtopography, ranging from alignment with the micropattern to a circular conformation where adhesion is taking place exclusively in the middle of the cell.

Micromolding of tensile bars was conducted to better understand the processing effects on mechanical and thermal properties of microscale molded components. Such results could provide useful general trends for the consideration of mechanical properties of molded microfeatures being exposed to cellular mechanical traction forces, especially considering the extreme processing conditions necessary to fill increasingly small and high aspect ratio features.

Results revealed that the elastic modulus of COC is largely unaffected by a wide range processing conditions, but is reduced to approximately 41% of the value obtained from traditional tensile test results. TPU showed a dramatic dependence on molding properties, with higher injection velocities and lower mold temperatures resulting in reduced elastic modulus. Simulation was used to further elucidate the cause for varying properties. Microscale elastic modulus average values approximately 31% higher compared to traditional tensile test results. Trends in thermal properties were not apparent, and were difficult to detect from relatively weak melting peaks. The use of two different polymer lots elicited drastically different results, prompting the further

investigation of the differences. Crystallinity, viscosity, and chemical bond structure was found to be very different from one lot to the other.

The successful fabrication of uniform tapered microfeatures with middle range aspect ratios were manufactured, and the robust mold design and the tooling fabrication method provides a blueprint for achieving higher aspect ratios with a significant level of fidelity in the future. The enhanced macro and microscale mold design, combined with a deeper understanding of processing induced mechanical thermal microscale properties, can be used to tailor the substrate bio-interface properties to the desired mechanical structure for controllable hMSC behavior.

1 Introduction

1.1 Interdisciplinary Research

With the rapid advancement of technology, the remaining opportunities for scientific discovery are complex and unequivocally require unconventional solutions. To overcome such multifaceted challenges, multiple perspectives are necessary. Interdisciplinary research provides a greater arsenal for engineering a comprehensive solution, asking questions during the process which may have otherwise been overlooked.

Two fields which are fairly unrelated are combined in this project to provide a unique prospect not achieved through either field of study alone. Polymer processing provides a tool by which plastic parts are mass produced reliably, efficiently, and at low cost. The design and manufacturing of polymer parts requires an understanding of solid and fluid mechanics, materials science, and engineering principles. Bioengineering is a field which utilizes biology to solve problems currently facing the scientific community. By understanding the manner in which biological cells, tissues and organs function, devices, materials and processes can be developed to in some way enhance quality of life.

The capabilities recently achieved through polymer processing have tremendous potential for use in a bioengineering related manner. When designing a platform for a synthetic substrate to interface with a biological system in a reliable manner, a high level of precision is compulsory to ensure intentional and reproducible results. The advancements in specifically polymer injection molding has allowed for an extreme level of process control to precisely tune polymer part geometry,

morphology, and mechanical properties, and thus potentially offer a solution to a scientific bottleneck present in the biomedical field today.

1.2 Problem Description

Stem cells have the ability to self-renew and to differentiate into a variety of different cell types [**1**]. Consequently, they have been suggested for use in treating human diseases characterized by improperly functioning or damaged biological tissue where restoration of certain cell lineages would be ameliorable. Diseases which could stand to benefit from cellular therapy include: Parkinson's disease, Hurler's Syndrome, osteogenesis imperfecta, and cardiomyopathy [**2**,**3**]. In addition, a common issue with hMSCs *in vitro* ("in glass" or "in the laboratory") is spontaneous differentiation, in which other groups have previously sought to topographically induce cells to maintain their multipotent (i.e., undifferentiated) capacity [**4**].

When using stem cells to treat a particular ailment, it is ideal that a homogenous group of needed cells be cultured and implanted into the deficient region [**4**]. As a result, controlled cell fate modification *in vitro* is a crucial step in the transplant therapeutic process.

Multiple types of stem cells exist, with a majority of the clinical trials being performed using hematopoietic stem cells [**5**]. Human Mesenchymal Stem Cells (hMSCs) are multipotent cells found in bone marrow. They are capable of differentiating into primarily bone, cartilage, or fat cells. Additionally, they have been shown to trans-differentiate into muscle, heart muscle, and neural cells [**6**]. They are

relatively easy to isolate and are among the first stem cell types to be introduced to the clinic [**7**].

All cells are sensitive to the properties of their surrounding environment, responding to biochemical, molecular, and mechanical cues. *In vivo* (i.e., in the body), cells are surrounded by the extracellular matrix (ECM) which is a multi-phase environment composed of variant stiffness, feature size scales, and chemistry. Efforts have been made to mimic aspects of such an environment. However, the level of complexity associated with the ECM makes a comprehensive mimicry solution largely elusive.

Responses to particular stimuli include changes in adhesion, morphology motility, growth, proliferation, and in the case of stem cells, differentiation [**8**]. Moreover, cellular responses can be related to others. For instance, changes in morphology can be an indication differentiation.

Cells respond to mechanical stimuli is through a process known as "mechanotransduction," in which a cell is able to sense an extracellular mechanical signal, transfer the signal internally, and produce a specific biochemical modification in response. Anchorage-dependent cells (cells which require adherence to a surface to function) are physically connected to the ECM via transmembrane proteins known as integrins. Integrins are connected to intercellular structures called actin filaments, which provide mechanical support and shape to the cell. Nearly all actin-containing structures are dynamic and re-organize their structure in response to intracellular and extracellular signals [**9**].

The leading concept used to model the mechanical structure of a cell is the "tensegrity" theory. A tensegrity structure is one that is composed of continuous stretched elements and discontinuous compressed components. The network is able to balance and respond to external forces in a concerted manner. Within the context of cellular structure, the actin filaments represent the components in tension and microtubules (another cytoskeletal component) serve as the compressive domains (Figure **1-1**).

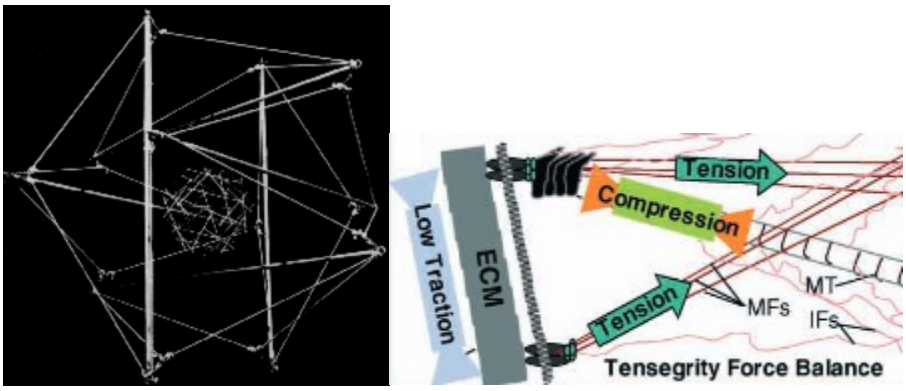

Figure 1-1: General representation of tensegrity model applied to a cell (left) and illustration showing actin filaments (MFs) and microtubules (MT) as part of the tensegrity network (right) **[**10**]**.

In an attempt to modify cellular properties through control of substrate stiffness, previous research has found that by fabricating a substrate with stiffness similar to a particular biological tissue, stem cells can be guided towards the differentiation pathway of the associated cell [**11**,**12**]. This has been accomplished through the use of gels whose bulk mechanical properties can be precisely controlled.

Cell tissues comprise a range of stiffness values which lie in the low kPa range (Figure 1-2). Thus, differentiation of stem cells into particular cell types can be

achieved simply through the tuning of substrate stiffness. Cellular manipulation in the absence of complex soluble chemistries would be ideal considering the issues associated with chemically induced cell function [**4**].

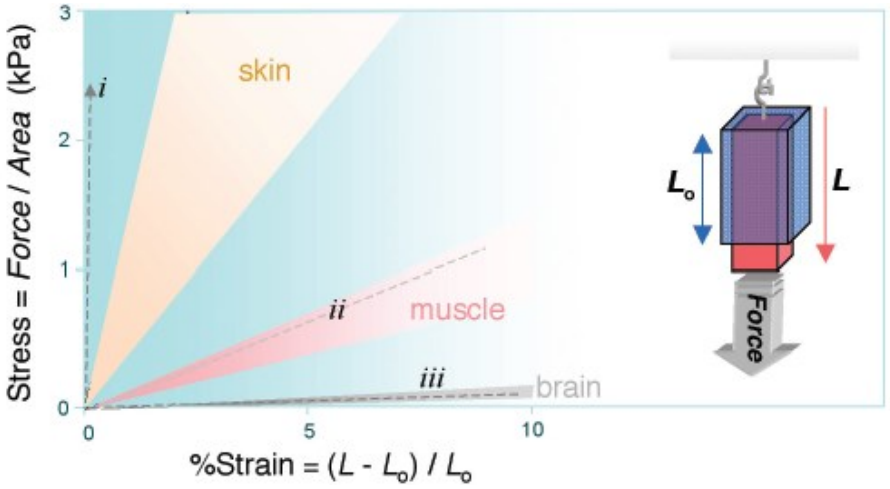

Figure 1-2: Stress strain plots for different biological tissues **[**13**]**.

Unfortunately, the processes utilized to manufacture substrates with highly controlled levels of stiffness are not amenable to commercially viable processing methods, requiring a significant amount of time for curing. Moreover, consistency of surfaces used is questionable and cannot be relied upon for constant mechanical properties.

1.3 Opportunity

Plastic cell cultureware is ubiquitous in biological laboratories, in which cells come into contact with the bottom of the cell culture well. The surface is pre-treated with oxygen plasma to reduce polymer hydrophobicity and subsequently enable better adhesion and growth [**14**]. Cell culture dishes, composed of polystyrene (PS), are

manufactured through the high rate process on injection molding, which enables the polymer parts to be mass produced.

Unfortunately, most injection moldable polymers have elastic moduli in the MPa to GPa range, with PS having a modulus of approximately 3 GPa. As a result, even the more compliant injection molded polymers are not able to match up with a majority of target tissues (Figure 1-4).

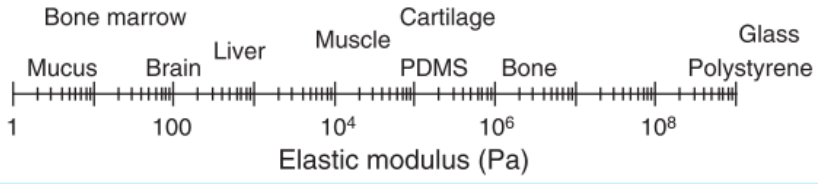

Figure 1-3: Comparison in elastic moduli between biological tissues and PS.

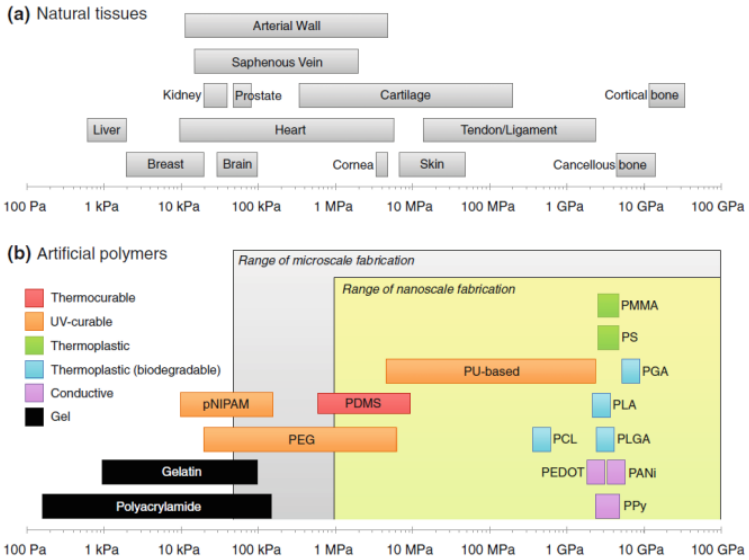

Figure 1-4: Elastic modulus comparison between biological tissues (a) and various polymers (b) [15].

The use of micro-injection molding can serve to attenuate the high stiffness associated with thermoplastic polymers. Multi-scale molded parts can be manufactured to create a micro or nanofeatured polymer surface containing bendable topography in a high

rate manner. The modified surface functions as a more compliant substrate to an anchoring cell, similar to what is typically experience by the cell when in contact with softer surfaces. By utilizing a precise high rate processing technique to intentionally control stem cell behavior, the potential large scale use of the substrates could provide far reaching assistance in stem cell development for cell-based treatments.

Two primary challenges lie in creating a topographic bio-interface capable of intentional stem cell control. First, an understanding of the perception a cell has to bendable topography is required. Although cells are exposed to both micro and nanotopography in vivo, there is still much to be understood regarding method and size scale of rigidity sensing. The most important challenge, however, is the ability to manufacture the desired substrate design with a significant level of fidelity. Limitations exist in terms of the feature aspect ratio (ratio of feature height to feature width) due to the difficulty filling and demolding such structures.

1.4 Dissertation Objectives

The goal of the conducted research was to move the technology of micro/nano topography induced stem cell behavior forward in terms of enhancing the manufacturability of topographic surfaces and simultaneously reach a deeper understanding of the features necessary to create the appropriate stiffness values to effectively control stem cell differentiation.

Replication, or the degree to which the feature matches with the tooling, and replication consistency across the part were the two primary manufacturing criteria to be optimized. Moreover, it was hoped that the most influential molding parameters would be

identified for each material used. A mold assembly capable of utilization in a mass production environment was also sought after.

In addition, a better understanding of processing-induced mechanical and thermal properties on microscale molded parts was desired. Both geometrical and material properties are responsible for mechanical response of polymer parts during function, which are directly related to processing conditions.

2 Related Scientific Development

2.1 Micro-Injection Molding Technology

Micro-injection molding is a high precision process that is capable of reliably manufacturing microscale polymer parts containing high quality surface features [**16**]. It is a rapidly advancing technology, as an increasing amount of assembly components are becoming miniaturized. Micro-injection molding has multiple definitions. It can apply to the molding of microscale parts, macroscale parts with microscale features, and macroscale parts with microscale tolerances [**17**].

2.2 Applications

Consumer trends involving the reduction in size of components have resulted in an increasing amount of potential applications for micromolded polymer parts, with a few examples shown in Figure 2-1. Typical parts made include: connectors, sensors, digital audio and optical storage (CD / DVD), gears, valves, microfluidic devices, and medical implants.

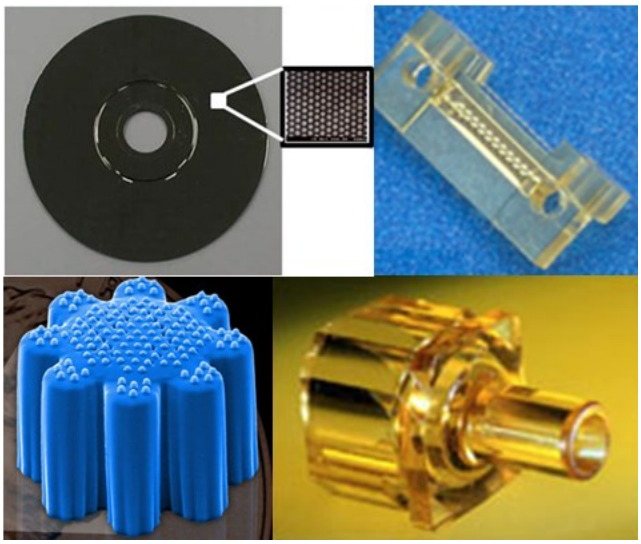

Figure 2-1: Examples of a few micromolded polymer parts (Sources: http://www.pepmicropep.com/, http://www.microengineeringsolutions.com/, http://www.accu-mold.com).

Molding of macroscale parts with micro or nanotopography is used for a variety of different applications specifically aimed at controlling surface interfacial effects in a useful way.

2.2.1 Nanotopographic Surfaces

The realization of the beneficial uses of micro and nanotopography was in large part due to examples found in nature. In fact, the given research is based upon the concept of biomimetics, or attempting to mimic structures made by nature to obtain specific properties for functionality of a certain product. A few potential applications for such properties are (windows for vehicles self-cleaning / anti-wetting surface), microelectromechanical systems (MEMS) surfaces (de-adhesion), and selectively adhesive gloves for vertical wall climbing (reversible adhesion). A few organisms, such as the lotus leaf and cicada *orni*, are equipped with nanotopography used for anti-wetting

purposes (Figure 2-2), and geckos are equipped with hierarchical topography which allows them to rapidly attach and detach their toes from substrates.

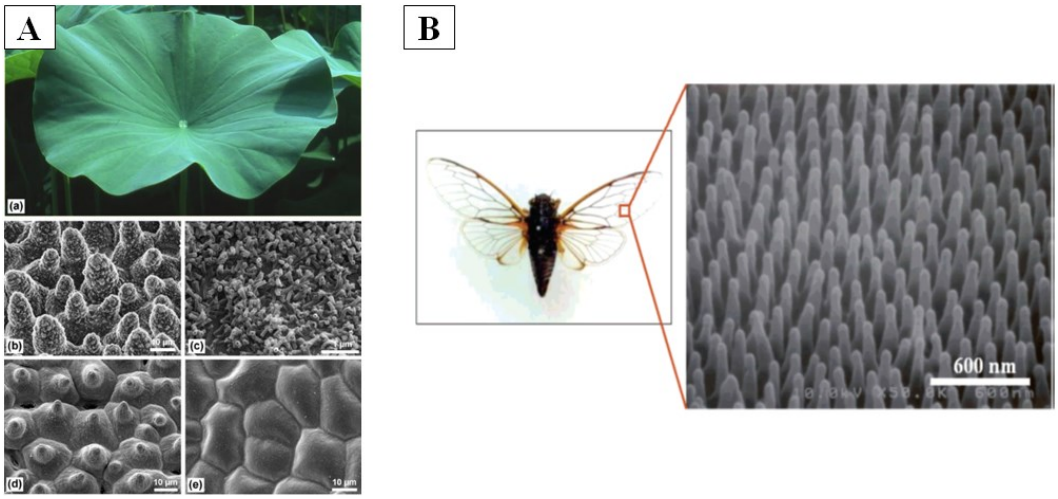

Figure 2-2: Image and micrographs of hierarchical super-hydrophobic lotus-leaf (A) and image of cicada orni (B) showing micrograph of wing nanotopography (inset) [18,19].

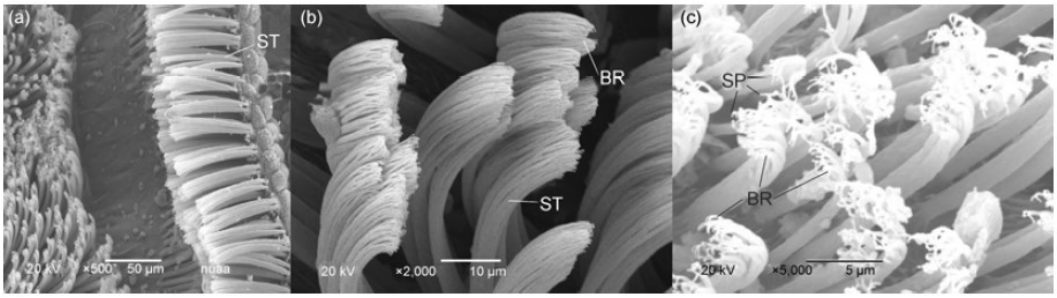

Figure 2-3: Hierarchical structure of gecko toe [20].

2.3 Machine Development

Microinjection molding requires the use of high precision molding equipment capable of producing repeatable shot sizes, velocity/pressure switchovers, and melt delivery. Although some components of micromolding machines are simply a scaled down version of a conventional molding machine (i.e., clamp force), some elements

require more significant alterations to provide adequate function. The typical single extrusion barrel used for both plastication and injection is separated into two separate compartments.

A screw uses mechanical and thermal energy to convert the solid resin into a homogenous viscous melt, which is subsequently introduced into the injection unit. The plunger, which is typically on the order of a few millimeters and offers a higher level of precision relative to a larger conically terminated screw, injects the molten polymer into the mold cavity. Figure **2-4** shows the geometrical differences between the two types of units.

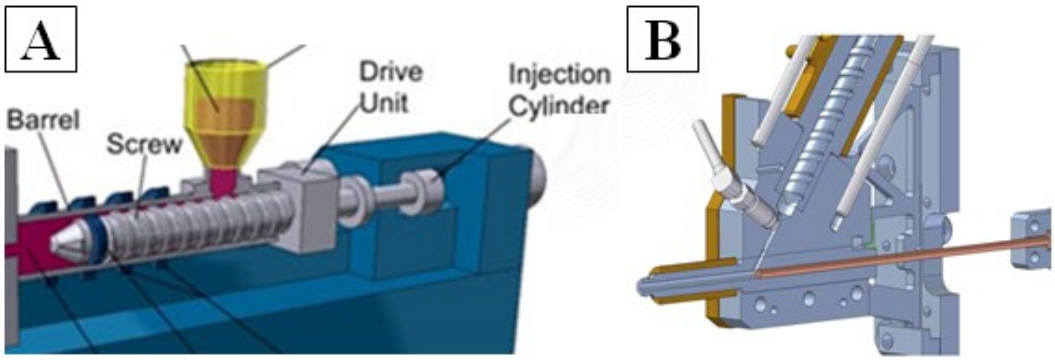

Figure 2-4: Traditional single-screw injection unit (A) and micro-injection molding plastication-injection separated melt delivery zones (B).

Another notable variation is the use of electrically controlled components to maintain a high level of precision. The micro-injection molding machine used over the course of molding trials is a Nissei AU3E, shown in Figure 2-5. It is an electrically controlled 3 ton 2-stage machine with an 8 mm plunger and separate plastication unit oriented at an angle relative to the injection unit.

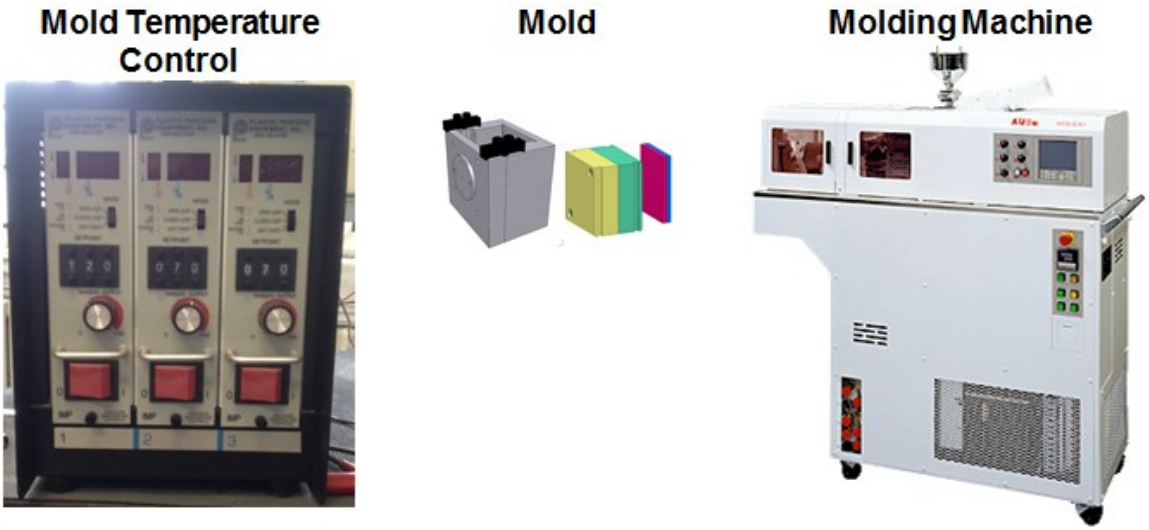

Figure 2-5: Nissei AU3E micro-injection molding machine with CAD model of mold and digital image of temperature control unit.

2.4 Tooling

Micromolding machines may have a significant level of precision, but also require highly precise tooling to take advantage of such machine enhancements. Micro and nanoscale tooling development is vastly different in terms of processing techniques from conventional mold making.

2.3.1 Ultraviolet Lithography

Tooling associated with conventional mold manufacturing can only reach dimensions of 50 m, below which fabrication techniques inherent to the microelectronics industry are required.

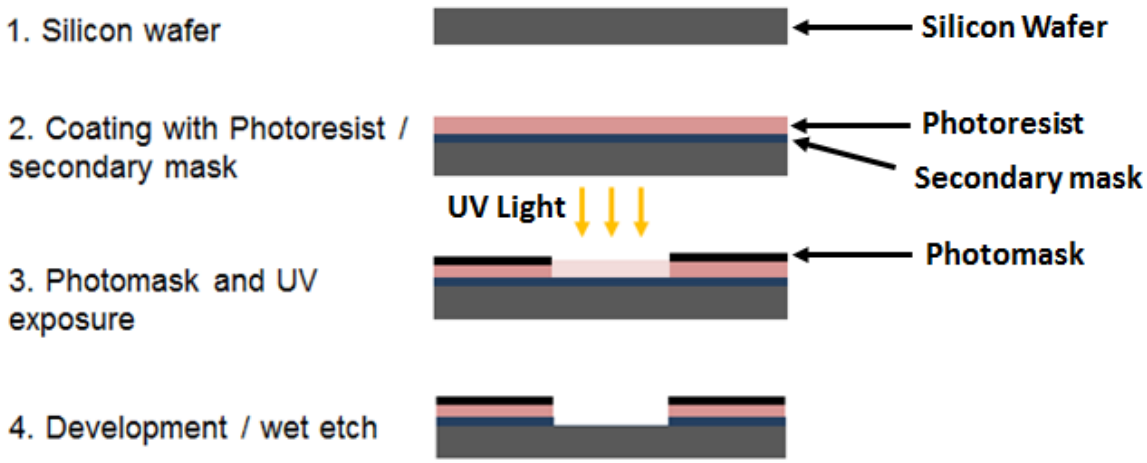

Figure 2-6: Schematic of the basic steps of the UV photolithography process.

2.4.2 Electron-Beam Lithography

To obtain mold features at the extreme nanoscale (i.e., < 100 nm), electron-beam lithography (EBL) can be used. However, the processing time can be significant for large pattern densities, as patterning takes place serially instead of in parallel. EBL, similarly to UVL, exposes regions of photoresist present on the surface of a silicon wafer, making the polymer soluble (in the case of positive photoresist) to developer used in a subsequent step. The exposure, however, is performed by an electron beam (inside an SEM chamber) which exposes distinct regions of the polymer dictated by code generated from patterning software. The code is used to control the movement of the SEM stage to specific positions. When transitioning from one feature to the next, a beam blanker is used to deflect the stream of electrons away from the substrate.

The amount of exposure is quantified as a specific dose, or total amount of charge applied to a particular location, given in μC. The necessary dose is dependent on the thickness of photoresist, size of pattern features, and beam energy [**21**].

2.4.3 Lithography Pattern Transfer

Once the features have been successfully created on a photo-sensitive substrate, the transfer to a material capable of withstanding extreme molding conditions inherent to the injection molding process is required.

2.4.3.1 Direct Transfer - Deep Reactive Ion Etching (DRIE)

To directly transfer a particular pattern, there are two methods: wet etching and dry etching. Wet etching has been confined to more cleaning and low precision processes, as it can only etch isotropically (with a few exceptions) [**22**]. Dry etching and more specifically Reactive Ion Etching (RIE) uses plasmas containing gaseous ions capable of reacting chemically with ions on the surface of a substrate. New volatile compounds are formed at the surface and evacuated. The process is repeated in a layer-by-layer removal process [**22**]. Although anisotropic etching can be achieved through RIE, it is somewhat limited at higher aspect ratios. Up until the end of 20^{th} century, there was no cost-effective viable solution to achieving such features [**21**]. With the dawn of high-density low pressure plasma sources and innovative etching techniques, silicon was able to be etched with higher aspect ratios without excessive photoresist etching and in a reasonable amount of time. High density and low pressure both contribute to a lower probability of ion collision and increase in the ion mean free path, which leads to increased ion directionality [**23**].

One of the most common plasmas used for etching is sulfur hexafluoride, or SF_6. SF_6 spontaneously etches into silicon, digging radially outward and creating a bulb-like

shape. SF_6 can be given brief directionality in the form of resist windows, but etches isotropically within such windows, as shown in Figure **2-7**.

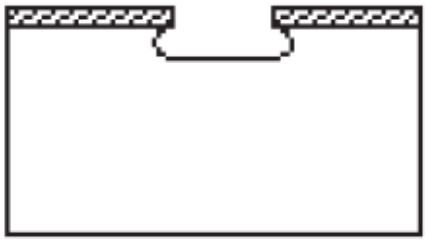

Figure 2-7: Schematic of SF6 etching of silicon through photoresist window **[**24**]**.

For high aspect ratios the "Bosch" process can be used [**25**]. The process utilizes cyclic alternation between SF_6 (etchant) and C_4F_8 (passivant), in which SF_6 etches isotropically and C_4F_8 protectively coats the surface. The following process repeats, with the coating on the horizontal surface being etched away due to physical bombardment of ions and vertical surface remaining protected. The net shape after multiple cycles looks like that in Figure 2-8. There are many factors involved with the etching process. They include: the flow and duration of plasmas, chamber temperature, substrate temperature, source power, and substrate bias. All such settings can be tuned to control the rate of etch, directionality, and surface quality of the exposed silicon regions.

Silicon has been used as a fairly robust tooling material previously, maintaining its fidelity at >3,000 cycles [**26**]. However, it has also been claimed that silicon is not a material adequately suited for high volume molding production, as it is relatively brittle and has limited longevity [**16**].

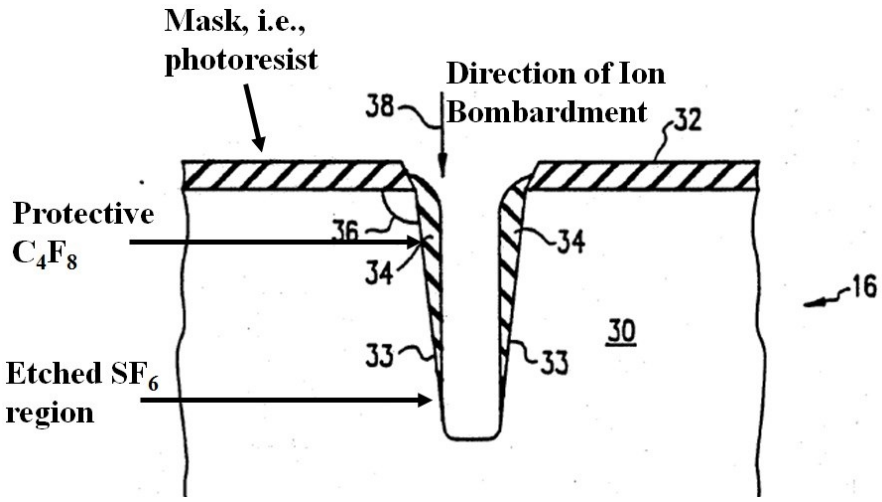

Figure 2-8: Deep reactive ion etching "Bosch process" schematic of etching with passivated sidewalls. Image adapted from [25].

2.4.3.2 Indirect Transfer - LIGA

When the objective of creating a mold is to manufacture parts in large quantities, robust tooling is required. To satisfy such requirements, tooling must be composed of a material capable of withstanding a significant number of cycles while maintaining geometrical and performance specifications. The process was developed in the 1990s with the purpose of transferring microstructured patterns from silicon wafers (which are thought to be more of a prototyping mold material) to relatively more resilient metal substrates for use as a mold inlay [**27**].

The process begins with the photoresist coating, exposure, and development of a base plate to create a pattern on the baseplate, ensuring that the pattern had the identical features desired for the final polymer part (unlike the use of a silicon wafer for direct molding, in which the features should be the inverse of the desired final pattern). The pattern is subsequently transferred to metal via electrodeposition, in which the baseplate serves as a conductive medium to attract metallic ions to the surface. The subsequent

metal part containing the deposited structures can then be used as an inlay for molding [**22**].

A few limitations in using the LIGA process is the difficulty in replicating draft angles (vital geometrical characteristic for proper microfeature demolding) and high aspect ratio features from the master [**28**,**29**].

2.4.4 Demolding Agents

A wide array of coatings have been suggested as demolding agents for micro and nanofeatured tooling, with the overall goal being to lower surface energy and promote de-adhesion at the time of ejection. Requirements of coating are that it be conformally applied across the microfeatured domain, it does not attach to the molded part, and it remains adhered to the tooling surface over the course the tooling lifetime.

In addition to its use as a sidewall protective layer during etching, OFCB can be utilized as an anti-stiction agent, serving to lower the surface energy of the silicon surface. OFCB has previously been successfully used in a process called pulsed plasma enhanced chemical vapor deposition (PECVD) to provide a Teflon^{TM} -like coating to implantable wires in medical applications. The pulsing of power (as opposed to continuous power) allows for a higher F/C ratios similar to that of Teflon [$(CF_2)_n$] [**30**]. Others have used OFCB for the purpose of enhanced demolding [**31**,**32**]. Other coatings, such as fluoroctatrichlorosilane (FOTS) [**33**], perfluorodecyltrichlorosilane (FDTS) [**34**], and n-dodecanethiol [**35**] have successfully enhanced replication previously compromised by demolding difficulties.

The two critical aspects of molding micro and nanofeatured polymer substrates are filling of the features and subsequent demolding. The former is predominantly dependent on processing parameters and the macroscale geometry of the mold cavity. The latter is dependent on both micro and nanocavity geometry and local surface chemistry. In traditional injection molding, a silicone-based aerosol agent is typically applied to the tooling surface to provide adequate release of the part in the case of part sticking. At the microscale and smaller, more sophisticated methods are necessary, because conventional mold release layers are not able to be applied conformally, and thus have been shown to alter feature geometry (as shown later in experimental details). A multitude of release agents, all designed with the intension of lowering interfacial surface energy between polymer and tooling, have been suggested for use in micro injection molding.

Mold release agents are especially critical for micro molding, as the required higher mold temperatures to fill small features also increases sticking of polymer to tooling features.

2.5 Process Development

2.5.1 Conventional Injection Molding

To understand the micro-injection molding process, a basic introduction to injection molding is necessary. The process of injection molding involves transforming polymer resin from one shape to another. To do so, polymer pellets are fed through a hopper and into a barrel, where they are heated up through a combination of conduction

(from resistance heater bands) and shear-induced heating (from rotating screw) to a temperature beyond the polymer melting point.

The screw (in the case of conventional molding) reciprocates backward, allowing polymer to fill the region in from of the screw tip. Once enough material has been transferred to the front of the barrel, the polymer can subsequently be injected into a mold cavity. As previously shown in Figure 2-4, the polymer in a micro-injection molding machine travels through an initial barrel with a screw followed by a secondary barrel containing a small injection piston. The mold consists of two halves that close during polymer injection and open as soon as the polymer has cooled to a low enough temperature. A cycle begins by polymer being injected at a specific velocity or pressure (though consistency from one part to the next is achieved by specifically using velocity control) until the cavity is almost full, at which point filling control is dictated by pressure for a specific period of time (i.e., the "holding phase"). The part cools for a certain period of time, the mold opens, and the part is ejected to end the cycle. Figure 2-9 shows the steps and approximate time distribution of the process.

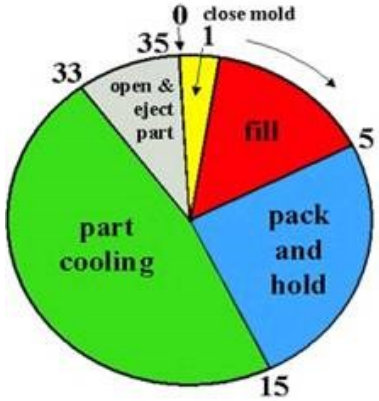

Figure 2-9: Steps of the injection molding process.

There are a wide range of parameters that can be controlled during molding, and all such settings contribute in some capacity. Table 2-1 shows a set of controllable parameters, some of which are varied to note the effects of replication over the course of the conducted research.

To fill microscale features with a significant level of replication, polymer viscosity must be tuned via molding parameters to facilitate adequate filling. Increasing settings typically results in a higher level of replication due to viscosity reduction in response to higher temperatures and applied forces. However, it is important to note that increasing parameters can have negative consequences, such as extended cycle times, reduced surface and feature edge quality, and reduced mechanical properties [**36**].

Table 2-1: Controllable injection molding parameters.

Parameter	Description
Mold Temperature (°C)	Known to effect surface finishing in conventional molding; very influential on micromolding
Barrel Temperatures (°C)	Temperature of the heater bands; contributes to overall "melt temperature"
Injection Velocity (mm/s)	Speed the screw / piston travels during injection
Injection Pressure (MPa)	Limit pressure imposed during filling
Injection Time (s)	Injection + Holding time
Holding Pressure (MPa)	Pressure applied after filling phase to complete fill and compensate for part shrinkage
V/P Switchover (mm)	Location of screw / plunger when injection switches from velocity to pressure control; should occur when part is approximately 90 -- 99 % full
Back Pressure (MPa)	Resistant pressure applied by screw during filling of a shot; has an effect on "melt temperature"
Screw Rotation Velocity (RPMs)	Angular velocity of the screw as a shot is filling up; has an effect on "melt temperature"
Cooling time (s)	Time between completion of injection / holding and ejection
Ejection Temperature (°C)	Temperature at which part is stable enough to be removed from the mold; often corresponds to Tg or Vicat softening temperature of polymer

2.5.2 Critical Parameters for Replication

Parameters deemed important to the overall replication of micromolded polymer parts are: mold temperature, melt temperature, injection velocity, injection pressure, and holding pressure [**36**,**37**,**38**]. Due to the wide variation in thermoplastic material properties, molding parameter effects and significance will vary. Aspect ratio also determines the degree of replication that can occur, as the general trend is a reduction in replication with increasing tooling aspect ratio [**39**].

2.5.3 Modeling of Microscale Flow

Micro and nanoscale flow have been successfully modeled without the use of special micro and nanoscale considerations [**40**,**41**,**42**]. However, other investigations have noted inconsistencies between traditional simulation and experimental results, and have addressed the differences through various model modifications [**43**,**44**,**45**]. Processing conditions with micro and nanoscale flow involve dramatically higher temperatures, pressures, and flow rate which impart increasingly extreme stress on the polymer molecules being transported through the molding cavities.

The material properties used in conventional simulation packages have been collected from standardized characterization tests, and are not unique to the cavity design or processing conditions being used. As a result, parameters critical to filling behavior have been altered to account for various microscale effects (mentioned later in Section 3.1). To test models, clever experimental schemes, such as weld line tracking [**43**], have been employed to change the model to more closely match results.

When simulating multi-scale flow, careful consideration must be made with regards to mesh size. Computationally, it is very expensive to mesh a macroscale model containing microscale features with both with the characteristic element dimension necessary for the microscale feature. Consequently, multi-scale meshing can be employed (Figure 2-10). An element size gradient must be used when transitioning from the macro to microscale feature to maintain a relatively constant size across a localized region and prevent a mesh-induced simulation inconsistency.

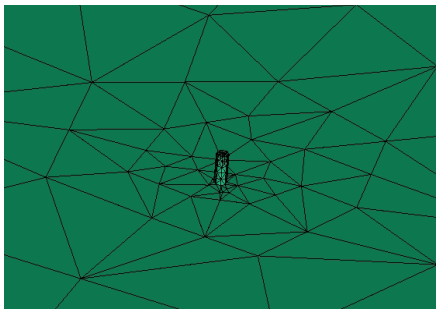

Figure 2-10: Multi-scale meshing used for simulation of molding macroscale parts with microscale features.

2.5.4 Mold Temperature Control Methods

For micro-injection molding, mold temperature is arguably the most influential parameter in determining replication quality. Therefore, the degree to which the mold temperature is controlled will dictate the precision with which parts can be molded. The microtooling surface temperature must be in some way monitored to ensure that the set temperature is the actual temperature at the tooling surface where the melt is approaching the micro-inlets. Non-local temperature sensing results in an incorrect assumption of real-time mold temperature, as heat is not uniformly distributed throughout the entirety of the tooling.

2.5.4.1Active Heating

As previously mentioned, mold temperature control is a critical micromolding parameter for successful replication. The two primary methods of mold temperature control are through the use of heat transfer fluids and electrical cartridge heaters, which create heat through electric resistance. Heat transfer fluids allow for both active heating and cooling of the mold, while cartridge heaters can only be actively heated [**46**]. Water can be used for instances where mold temperatures are maintained at less than 100 ^{o}C (i.e., above vaporization temperature of water), and heat transfer oils are used when mold temperatures must be higher than 100 ^{o}C. For applications, such as in the medical field, where sterility is required, cartridge heaters are commonly used in conjunction with thermocouples to provide a closed-loop temperature control of the measurement location. The disadvantage of electric heating is the inability to quickly remove heat from the system. A seemingly more effective and sterile heating and cooling method (but more costly solution) is the use of highly pressurized water, which can reach temperatures of up to 204 ^{o}C [**47**,**48**].

For micro-injection molding, it is recommended that the mold temperature be maintained at glass transition temperature or even melt temperature during filling and holding phases [**27**]. However, the part must be cooled below softening temperature to prevent geometrical distortion during ejection. To achieve such temperature values in a reasonable amount of time, a transient mold temperature system can be used. Known as the "variotherm process," the mold temperature can be increased prior to injection and cooled upon completion of the compensation phase, as shown in Figure 2-11. For cases where mold temperature is monitored near the cavity to allow for quick heater response

time, complications during polymer filling can occur. The heat from the polymer melt is transferred to the mold, causing a temporary spike in the reading, thereby signaling to the control system a temporary reduction in supplied heater current.

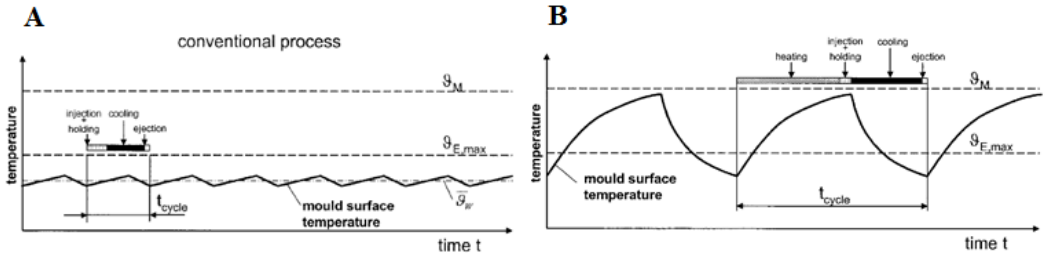

Figure 2-11: Conventional mold temperature (A) and variotherm (B) mold temperature control over the course of multiple cycles. The variotherm process between the ideal micromolding mold temperature and ejection temperature **[**49**].**

The reduction can result in a temporary temperature dip below the set mold temperature during the holding phase It is unclear as to whether such an activity will cause reduced replication, as the actual time of micro and nanofeature filling is a function of cavity layout and microfeature dimension size.

2.5.4.2 Passive Heating

An alternative to actively heating the mold is to retard heat transfer from polymer melt to tooling through the use of insulating materials. The reduction in heat transfer rate to provide an extended period of elevated heat is known as a "passive heating" system. The reduced rate allows the tooling to maintain a higher mold temperature for a longer period of time [**50**], thereby preventing premature polymer freezing at the microchannel inlets due to terminally high temperature dependent viscosity. Figure 2-12 shows the evolution of tooling temperature with and without an insulating layer.

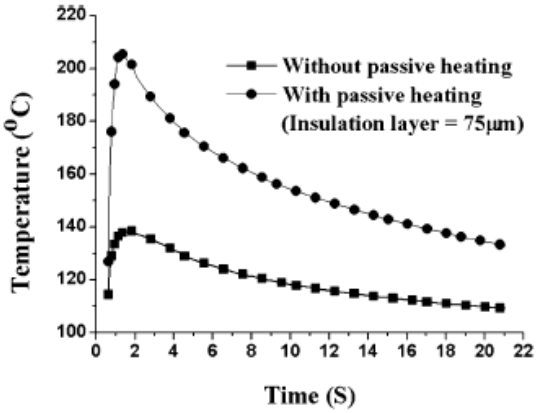

Figure 2-12: Passive heating resulting in an increased mold stamping surface temperature and duration of higher temperature (from [51]).

Although passive heating delays temperature loss, the heat eventually leaves the system and a convergence to a particular mold temperature occurs irrespective of insulation layer [**35**]. However, at the point of convergence, the filling and packing phases are complete, and elevated temperatures are unnecessary. An effective insulation layer will have a low thermal conductivity and resistance to degradation at all processing temperatures.

For the given study, materials used (silicon, aluminum, steel) contained fairly high levels of thermal conductivity. As a result active heating was employed throughout molding trials to counterbalance the effects of melt heat loss.

2.6 Material Development

A component of the micromolding field that has experienced minimal growth in comparison to tooling, process, and application development is in materials research. For microscale polymer parts, the entire volume of the substrate can be less than that of one polymer pellet. Polymers in pellet form contain a range of molecular weight values and

thus have a certain level of property variability. The polydispersity, or range of different molecular chain lengths present in a sample, can have a dramatic effect on mechanical and chemical properties. For macroscale parts, the sample properties are determined partially by the average molecular weight of the pellets initially used for molding. Ultimately, the combination of initial material properties and processing conditions dictate final part properties.

The lack of microscale specific materials is most likely directly caused by the lack of economic justification, as material providers are not willing to invest the resources into smaller batch sizes requested by buyers. Eventually, with the continuing increase in demand for micro and nanoscale polymer components, micro-specific resins are expected to emerge.

2.7 Micro/Nano Topographic Surface Characterization / Quality Control

Critical to the process of manufacturing parts containing surface features indistinguishable to the naked eye is the ability to characterize the surfaces. In micro-injection molding, the degree to which the polymer part surface geometry matches with the cavity surface geometry of the mold is known as "replication." Certain considerations, such as polymer shrinkage during cooling, need to be considered when assessing the level of replication. Criteria unique to the particular geometry must be developed and clearly defined to provide robust molding results.

Additionally, the mechanics of fluid flow inside of microscale domains has a profound impact on final part properties. For example, the filling of high aspect ratio microfeatures may cause extreme shearing of the polymer molecules during filling and

result in sub-optimal mechanical properties when used for a particular application. Thus, it is important to concurrently measure replication (surface-based quality control) with polymer part material properties (service-based quality control).

2.7.1 Scanning Electron Microscopy

A powerful imaging technique available for imaging micro and nanoscale surfaces is scanning electron microscopy (SEM). It is important to understand the way the microscope works due to the multiple ways an image can be collected. It is critical to control imaging conditions such that the appropriate information is obtained. During the process, electrons are accelerated towards and collide with the sample. The electron proceeds to either make contact with an electron from an atom within the material (which causes the material electron to be ejected and potentially exit the sample) or enters the sample and exits at another location. The first electron is termed a "secondary electron," and the latter is known as a "backscattered electron." Both types can get collected for subsequent image analysis, and both give the microscopist different information about the sample (Figure 2-13).

The primary parameters to be controlled are the working distance, strength of the condenser lens, accelerating voltage, and aperture. Different modes exist (though will not be discussed) to obtain desired results (i.e., range of field, surface sampling, etc.).

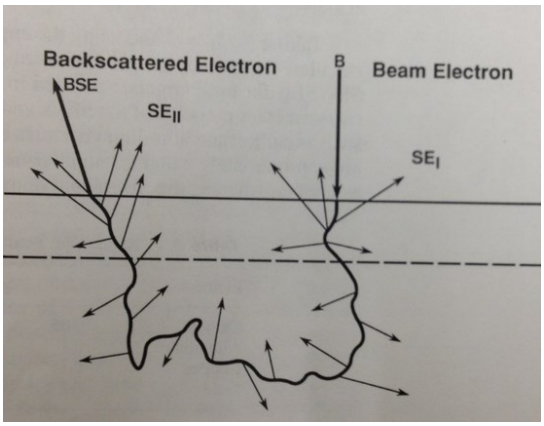

Figure 2-13: Schematic showing incident electron beam, generated secondary electrons (arrows protruding from main electron path), and a backscattered electron leaving the sample (BSE) **[**52**]**.

For imaging of polymers, it is imperative that accelerating voltages be kept relatively low to avoid damage to the sample, and that some type of conductive material be applied to the polymer to avoid the phenomenon of "charging." Charging of the sample occurs when an insulating material prevents the passage of the accelerating electrons from the beam to ground (i.e., stage on which the sample is sitting) [**52**]. Polymer samples were coated with a 5 nm thick layer of iridium to make the surface more conductive and further reduce the prospect of charging.

2.7.2 Interfacial Modification – Water Contact Angle Measurements

When engaging in surface engineering, quantitative methods of characterization are highly valuable to more deeply understand the potential effects of surface topography on the interfacing entity, such as biological cells. Water contact angle is a surface science measurement used to assess "wettability," or the degree to which water spreads over a given surface. Surfaces are characterized as either hydrophobic ("water fearing") or hydrophilic ("water loving"), in which a 90^{o} contact angle is the delineating value.

Water contact angle (WCA) analysis is a relatively facile but a very informative technique. The angle is a function of both surface energy (dictated by chemical composition) and surface structure [**53**]. A water droplet is composed of molecules which apply attractive forces to each other. The molecules at the surface are exposed to air molecules in addition to neighboring water molecules, and thus experience an asymmetric force distribution, and are pulled inward, creating an internal pressure that causes the droplet to alter its shape to achieve the lowest possible surface free energy. A schematic of the force imbalance is shown in Figure 2-14. The cumulative surface tension is the result of three specific interfaces: liquid/air, liquid/solid, and solid/air [**54**].

Figure 2-14: Attractive forces between water molecules in characteristic droplet **[**55**]**.

The incorporation of roughness to the surface alters the molecular force distribution at the droplet / substrate interface. Two primary models of the response of a water droplet to topography have been suggested, and the debate still exists as to which theory is correct. The two concepts are illustrated in Figure 2-15. Cassie believed that the water sinks in between the individual features, and the increased surface area present at the interface results in a modified water droplet surface tension that can cause either an increase or decrease in WCA. The equation involves the ratio of the total surface area and the apparent surface area.

$$\boldsymbol{cos(\theta_W) = rcos(\theta_o)}$$ Equation 2-1

θ_o is the contact angle on a flat surface and $\boldsymbol{r}$ is the ratio of unfolded surface area of the texture area and the area of a flat surface. In contrast, Cassie and Baxter postulated that the droplet remains above the roughness, allowing air pockets in between the micro/nano features to support the droplet. The presence of a heterogeneous substrate results in an increase in WCA, or a more hydrophobic surface, in all cases. The equation accounts for both the interaction between the droplet and air and solid fractions.

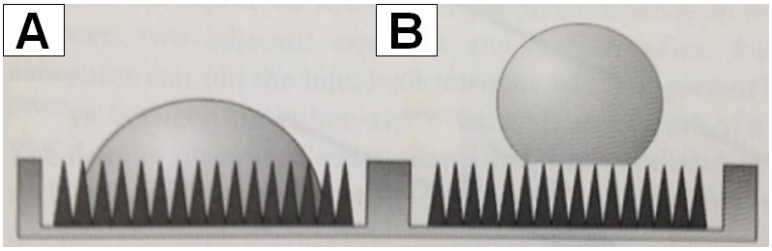

Figure 2-15: Schematic of water droplet / substrate interface for Wenzel effect (A) and Cassie-Baxter effect (B).

$$\boldsymbol{cos(\theta_C) = f_s(cos\theta_1) + f_a(cos\theta_2)}$$ Equation 2-2

The term $\boldsymbol{f_s}$ is the fraction of topography present beneath the droplet and f_a is the fraction of air beneath. Assuming the angle between water and air is π and knowing that $\boldsymbol{f_s}$+ $\boldsymbol{f_a}$= 1, the equation can be reduced to:

$$\boldsymbol{cos(\theta_C) = f_s(cos\theta_o + 1) - 1}$$ Equation 2-3

Reports indicate that at a certain roughness, a transition occurs from the Wenzel model (roughness based) to the Cassie model (based on the projected surface area covered by the topography) [**56**]. One of the great difficulties in solving the debate is the convolution of multiple properties on the effects of surface energy [**57**].

Two primary methods of measurement exist: static and dynamic analyses. Although static angles are considered the most common type [**58**], dynamic angles are more accurate due to the existence of contact angle hysteresis (CAH), or the difference between advancing and receding contact angles [**59**]. When initially placing a water droplet on a surface, the drop may be somewhere in between the two shapes shown in Figure 2-16. Dynamic angle analysis is a more accurate measurement of the contact angle, as it is able to avoid the use of an arbitrary angle generated from a static drop (which is in a metastable state). CAH is thought to be dependent on surface roughness and surface heterogeneity [**60**]. It is also suggested that the magnitude of CAH indicates which WCA state the droplet is in. A large value is thought to correspond to a Wenzel state [**61**].

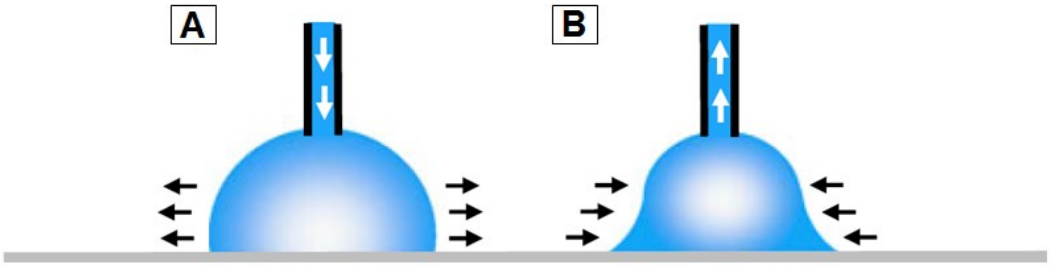

Figure 2-16: Schematic of advancing (A) and receding (B) contact angle **[**55**]**.

WCA is useful for the given project due its use in further characterizing surface properties to validate the presence and dimensions of microtopography, and provide an

indication of surface chemistry as well. Moreover, in terms of substrate use for stem cell culture, surface wettability has previously been found to be intimately related to initial protein adsorption, cellular adhesion, migration, proliferation, and differentiation [**62**,**63**,**57**].

2.8 Micro/Nano Patterned Polymer Substrates for Biomedical Applications

Cells are sensitive to topography and alter their behavior in response to specific geometrical cues. Moreover, it has been suggested that the synergistic use of specific stiffness and topography could be used to construct micro-environments for appropriate for intended cellular response [**15**].

Dalby et al was able to mimic bone tissue by culturing hMSCs on polymethylmethacrylate (PMMA) nanopits. Comparable levels of osteogenesis (bone formation) to culturing hMSCs treated with osteogenic media were found [**64**]. Kim et al was able to enhance proliferation of osteosarcoma cells with the use of nanofeatured polystyrene [**65**]. In both cases, the attempt to mimic topography is made, but with no apparent consideration of controlling substrate stiffness.

Microfluidic devices used for biomedical purposes can be reliably manufactured using polymeric substrates. Ahn et al was able to incorporate a micropatterned polymer "Lab-on-a-Chip" into a biosensor capable of multiparameter detection of blood components. Cyclic olefin copolymer (COC) was used to fabricate microfeatured polymer plates for use in the overall sensing assembly [**66**].

In addition to direct cell culturing on substrates, microfeatured biodegradable polymers have been patterned for use in drug delivery and for highly sensitive heart rate monitoring sensors [**67**,**68**].

2.8.1 High Aspect Ratio Topography Substrate Control for Cell Culture Plates

In terms of topographical control, a wide range of geometries have been used. For those that have explored higher aspect ratio features, the main emphasis on the research has been on measuring cellular traction forces and not analyzing the effects the topography-modified surface has on the cell [**69**,**70**]. In fact, it could be argued that measuring traction forces through the use of topography compromises the results, as cellular response is dependent on the shape and size of features [**71**,**72**].

A study by Fu et al explored the use of polymer microtopography as bendable features, interfacing with hMSCs at the surface. Polydimethylsiloxane (PDMS) microposts with different heights (resulting in different characteristic stiffness values) have been used to modify surface stiffness, in which taller pillars reduced cellular traction forces and induced adipogenic differentiation when hMSCs were cultured in bipotential media (osteogenic and adipogenic) [**73**].

2.9 Previous Lehigh Research

The micro/nano polymeric molding program at Lehigh University is the continued work of Alan Tom, Aleksandar Angelov, and Israd Jaafar, with the combined overall goal to further the understanding of the manufacturing of micro and nanofeatured surfaces through micro and nano-injection molding, while simultaneously discovering the

potential for additional applications. The previous researchers conducted studies using a 12-ton BOY micro-injection molding machine

Mr. Tom injection molded a micro gear with high density polyethylene (HDPE), poly oxy methylene (POM), and cyclic olefin copolymer (COC). The gear molding insert was 1,200 μm in diameter and was fabricated through the use of ultraviolet (UV) lithography. Taguchi arrays were used to analyze the effect of mold heating on the mechanical properties of the final part, which were measured through nano-indentation. It was determined that the highest mold temperatures and injection pressures did not yield optimum part properties, but greatest packing time did. Moreover, heated molding cycles were on the order of 5 times longer compared to the non-heated case. Mr. Tom also molded micro tensile bar specimens with POM and COC, and noted that elastic modulus increased with decreasing cross-sectional area [**74**].

Mr. Angelov used EBL with deep reactive ion etching (DRIE) to create nanofeatures on silicon wafers. Replicated nanofeatures with sizes as small as 25 nm were successfully injection molded using COC. Sub-micron diameter pillars with aspect ratios of 8 were achieved. Moreover, polymer optical diffraction gratings were successfully fabricated (Figure 2-17).

Mr. Jaafar fabricated a silicon mold insert containing 400 nm diameter nanochannels spaced 800 nm apart (center-to center distance) and 200 nm deep using E-beam lithography followed by DRIE. He molded with polystyrene, using a mold temperature slightly above the glass transition temperature (T_g) of the polymer. Molding was met with limited success, as the pegs were rounded at the top. When culturing

hMSC's on the nanotographic surface, the cells expressed increased amounts of filopodia (extensions of the cell body thought to be involved with cell sensing mechanisms in addition to lamellipodia) in comparison to a flat control (Figure 2-18). No differentiation analysis took place for the particular study.

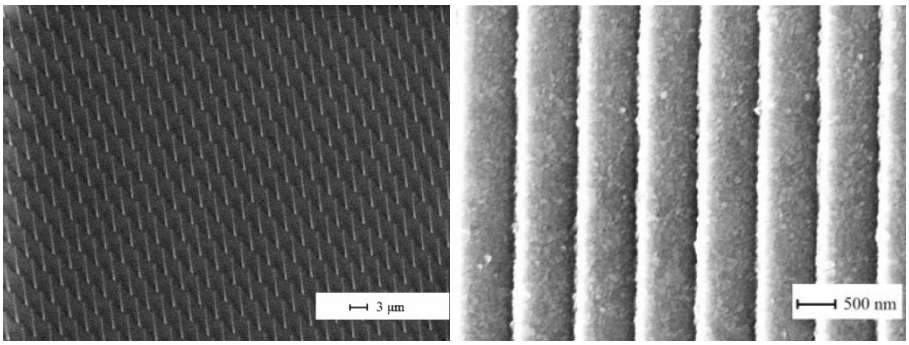

(a) (b)

Figure 2-17: 500 nm diameter 4 µm tall COC nanoposts (a) and COC optical diffraction grating structure covered with aluminum (b) [75] [76].

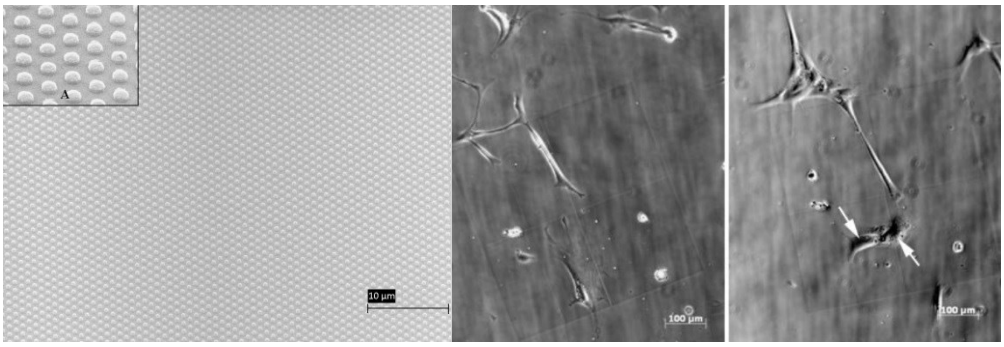

(a) (b)

Figure 2-18: Injection molded polystyrene 400 nm diameter 200 nm tall nanopegs (a) and hMSCs cultured on nanopegs (b) [77].

3 Modeling of Polymer Microfluidic Flow and Polymer Deflection Mechanics

Injection molding fluid mechanics has been well characterized and commercially available software, such as Autodesk Moldflow and Sigmasoft, offer simulation solutions to model the process. Fluid flow of thermoplastic polymers involves a complicated interaction between mass, momentum, and energy.

A few assumptions are made in macroscale fluid mechanics that are not necessarily true at the microscale. For instance, the "no slip" condition does not apply, as the shear stress built up along the walls would be too high to stay attached to the wall.

3.1 Traditional and Microscale Polymer Fluid Flow

Micro and nanoscale flow is governed by an altered set of parameters from that of conventional injection molding due to more extreme processing conditions and the effects of size scale which approach that of the macromolecular bond interactions. Table 3-1 shows a general comparison the size and molding condition differences between the two regimes. Actual values are cavity design, material, and process dependent. For multi-scale molding (invariably all micromolding to some extent is due to the macroscale nature of the melt delivery system), conditions may not be as extreme once the melt has reached the microfeature locations, which could occur near the end of macroscale part fill or beginning of the holding phase in the molding cycle [**40**].

Table 3-1: Comparison of molding conditions between conventional and micro/nanoscale molding.

Macro Molding Hele-Shaw assumption	Characteristic Property	Micro/Nano Molding Assumption
1000 μm	Cavity Thickness	0.05 – 10 μm
L=H/δ, where δ << 1	Cavity Length	L=H/δ where δ ≈ 1
10^7 N/m^2	Cavity Pressure	10^{15} N/m^2
10^4 Pa∗s	Cavity Viscosity	10^6 Pa∗s
-100K	$T_{mold} - T_{melt}$	+10K

The governing x-momentum equation for traditional molding can be modified through dimensional analysis to incorporate terms previously neglected due to insignificance.

$$\frac{\partial P}{\partial x} = \frac{\partial}{\partial z}\left[\eta \frac{\partial v_x}{\partial z}\right] + \frac{\partial}{\partial x}\left[2\eta \frac{\partial v_x}{\partial x}\right] + \frac{\partial}{\partial y}\left[\eta \frac{\partial v_x}{\partial y}\right] + \frac{\partial}{\partial y}\left[\eta \frac{\partial v_x}{\partial x}\right] + \frac{\partial}{\partial z}\left[\eta \frac{\partial v_x}{\partial x}\right] \quad \text{Equation 3-1}$$

In addition, thermoplastics are non-Newtonian materials, in which viscosity is a function of shear rate, temperature, and pressure. The Cross-WLF model is able to account for such effects.

$$\eta_b = \frac{\eta_0}{\left[1+\frac{\eta_0 \gamma}{\tau^*}\right]^{1-n}}, \text{ where } \eta_0 = D_1 \exp\left\{\frac{A_1[T-(D_2+D_3 p)]}{A_2+D_3 p+[T-(D_2+D_3 p)]}\right\} \quad \text{Equation 3-2}$$

This consideration is not novel to conventional injection molding. However, an adjustment of the bulk viscosity can be made through the incorporation of polymer chain

radius of gyration and experimental constant according to a non-local lubrication theory presented by Eringen and Okada [**78**].

$$\boldsymbol{\eta(\gamma, T, p)} = \boldsymbol{\phi(z)\eta_b(\gamma, T, p)} = \left[\mathbf{1} + \boldsymbol{\xi}\frac{\boldsymbol{g^2}}{\boldsymbol{z^2}}\right]\boldsymbol{\eta_b(\gamma, T, p)} \qquad \text{Equation 3-3}$$

ξ is a non-dimensional constant, g is the gyration radius of the fluid molecules, and z is the thickness of the channel. The model predicts a dramatic increase in viscosity when approaching the mold wall that cannot be neglected for features < 1 μm. An additional model which incorporates microfeature dimensions and empirically derived constants has also been used successfully in a limited capacity [**38**].

A few additional phenomena which occurs in micro and nanoscale flow is wall slip, which is neglected in modeling of macroscale flow. Shear stresses induced by higher pressures and flow rates, are too high to support a no-slip condition, and subsequently result in an altered flow front velocity profile, as a velocity component at the walls becomes significant.

$$\boldsymbol{u_s} = \frac{\boldsymbol{a}}{\mathbf{1}+\left[\frac{\sigma_c}{\sigma_w}\right]^k}\boldsymbol{\sigma_w}^{\boldsymbol{i}} \qquad \text{Equation 3-4}$$

The variable $\sigma_w$is wall shear stress, σ_c is critical wall stress for slip, i is the power-law index, and a is a scalar constant. When the wall shear stress is less than critical, the velocity term is reduced to "0." A more comprehensive expression for slip velocity which incorporates temperature, pressure, and polymer resin variability is:

$$u_s = \frac{\xi_o f_1(T)}{1+\left(\frac{\sigma_c}{\sigma_w}\right)^{100}}\left(1 - c_1 \tanh\frac{E+c_2\frac{\sigma_n}{\sigma_w}}{RT}\right)\left(\frac{\sigma_w}{\sigma_c I^{\frac{1}{4}}}\right)^m \qquad \text{Equation 3-5}$$

ξ_o, c_1, c_2, and m are coefficients, E is activation energy, σ_n is local normal stress, and I is resin polydispersity [**79**].

While the trends observed by the models were considered over the course of the conducted research, direct incorporation and modification of the models presented here were not directly addressed, as the given research focused more on empirically-driven results, with macroscale analytical computational fluid dynamic analysis being used to help further the understanding of replication results.

3.3 Micropillar bending mechanics

When using polymeric pillars for the purpose of resisting surface traction forces, a deeper understanding of pillar bending response is critical. The bending behavior of a beam is related to its material and geometrical properties. Bending mechanics can be modeled by the Euler-Bernoulli (E.-B.) beam bending approximation, which can be used to measure the amount of deflection of a beam in response to a particular force. A few assumptions are made when using the E.-B. equation. The beam cross-section is infinitely rigid (i.e., it maintains its shape), the cross-section remains plane following deformation, the cross-section plane remains normal to the axis of the beam, and the aspect ratio (height: width) must be >10 [**80**,**81**]. The general form of the equation is given below.

$$\frac{d^2}{dx^2}\left[EI(x)\frac{d^2v(x)}{dx^2}\right] = F(x) \qquad \text{Equation 3-6}$$

The direction along the axis of the beam is x, deflection perpendicular to x is v, E is elastic modulus, I is area moment of inertia, and F is the applied force. The area moment inertia predicts the resistance of a particular beam cross-section to bending. Assuming the term EI does not vary with x, the equation can be simplified to:

$$EI\frac{d^4(v(x))}{dx^4} = F(x) \qquad \text{Equation 3-7}$$

The equation can then be adapted based upon the location of the applied load and cross-sectional shape of the beam. For the special case where a force is applied at the tip perpendicular to the beam axis of a cantilever fixed at the opposite end (illustrated in Figure **3-1** , the equation reduces to:

$$\frac{\boldsymbol{F}}{\boldsymbol{\delta}} = \frac{\boldsymbol{3EI}}{\boldsymbol{L^3}} \qquad \text{Equation 3-8}$$

$\boldsymbol{\delta}$ is the deflection of the tip from an unperturbed state and $\boldsymbol{L}$ is the length of the beam. For the application of bendable topography interfacing with applied cellular traction forces, tip forces perpendicular to the beam axis is appropriate. In the case of a cylindrical beam (i.e., circular cross-section), the second or area moment of inertia is equal to:

$$\boldsymbol{I_{circle}} = \frac{\boldsymbol{\pi D^4}}{\boldsymbol{64}} \qquad \text{Equation 3-9}$$

The second moment of inertia is a measure of the resistance to bending of a beam, and is a function of its cross-sectional shape. I-beams are known for their high level of resistance to bending forces, and subsequently have a high second moment of inertia. The parameters associated with the degree of bending of a cylindrical beam are illustrated in Figure 3-1. The goal for the given study is to use the beams as stiffness reduction agents. Thus, a circular cross-section, which has the lowest second moment of inertia of all two dimensional shapes, was chosen. The subsequent equation incorporating the circular cross-section is shown in Equation 3-10.

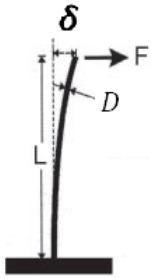

Figure 3-1: Schematic of beam deflection in response to bending force at tip.

$$\frac{F}{\delta} = \frac{3\pi E D^4}{64 L^3} \qquad \text{Equation 3-10}$$

The term $\frac{F}{\delta}$ is referred to as the stiffness of the pillar. When the beam does not satisfy the slenderness equation, i.e., an aspect ratio (L/D) of >10, a shear deformation term must be included in the deflection calculation, which is achieved through the use of a Timoshenko beam calculation [**82**]:

$$\boldsymbol{\delta = \frac{FL^3}{3EI} + \frac{\alpha FL}{GA}} \qquad \text{Equation 3-11}$$

α is the shear coefficient specific to a particular cross-section [**83**], G is the shear modulus, and A is the cross-sectional area. In the case of a circular cross-section, the value is a function of Poisson's ratio [**84**]:

$$\boldsymbol{\alpha = \frac{6(1+\nu)^2}{7+12\nu+4\nu^2}} \qquad \text{Equation 3-12}$$

Incorporating the shear term and the area moment of inertia for a cylindrical beam, the equation becomes:

$$\boldsymbol{\delta = \frac{64FL^3}{3\pi ED^4} + \frac{4\alpha FL}{G\pi D^2}} \qquad \text{Equation 3-13}$$

Pillar deflection is thus a function of $\boldsymbol{\nu}$, $\boldsymbol{G}$, and $\boldsymbol{E}$, with dimensional alterations leading to exponential alterations in deflection. The equation can be further reduced through the relationship between elastic and shear modulus ($\boldsymbol{G = \frac{E}{2(1+\nu)}}$).

$$\boldsymbol{\delta = \frac{8F}{\pi E}\left[\frac{8L^3}{3D^4} + \frac{\alpha L}{(1+\nu)D^2}\right]} \qquad \text{Equation 3-14}$$

The relation is specific to an individual bending beam. When considering the use of an array of micro or nanopillars, the surface stiffness control is achieved through not only altering pillar geometry and material properties, but also the spacing of such features.

Tapered beams are also considered here due to their enhanced manufacturability compared to straight pillars. Tapered beams of non-uniform cross-sections, in which bending mechanics become more complicated. Inertia becomes both a function of pillar diameter and height. Assuming a constant taper angle, the area moment of inertia becomes dependent on the base and tip diameter. A schematic of the geometrical parameters is shown in Figure 3-2.

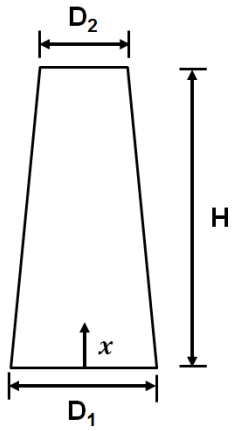

Figure 3-2: 2D Tapered beam geometry with variable beam cross-section.

It is expected that the stiffness of the beam will lie in between that of a pillar with a constant diameter of D_1 and a pillar with constant diameter of D_2.

$$\boldsymbol{D_x = D_1 - \frac{x[D_1 - D_2]}{H}} \qquad \text{Equation 3-15}$$

3.4 Cell Sensing Model

To guide any engineering design, geometrical, chemical, mechanical, and in the case of biomedical engineering, biological requirements of the device must be accounted

for. With regards to mechanical design for applications associated a cell-substrate bio-interface, cellular response to mechanical activity becomes critical.

In the same manner that materials are tested through measuring resistive force in response to applied strain or deflection, cells are equipped with their own mechanical sensory system, and are capable of measuring the degree of resistance of a substrate, i.e., stiffness. The cell sensing complexes are known as a "focal adhesions" (FAs). They are composed of a multitude of different proteins. Within the focal adhesion, transmembrane proteins known as "integrins," are the direct link between the ECM and the cytoskeletal actin filaments which are responsible for maintenance of cell shape and movement (Figure 3-3). Focal adhesions vary in size depending on the properties of the substrates to which they are attached. They are capable of applying stress to the substrate, and can use the amount of deflection as a measurement of surface compliance.

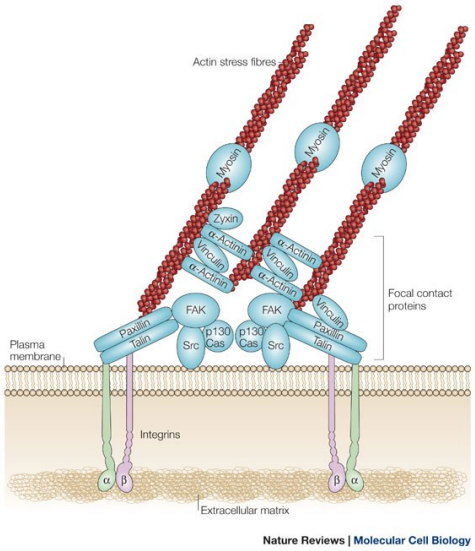

Figure 3-3: Schematic of cellular focal adhesion used for mechanical sensing [85].

In the case of a flat substrate, the stress applied by the FA to the part would be primarily shear stresses, as the force is applied perpendicular to the surface plane normal. However, with the incorporation of deflectable features, bending begins to factor into the force response computation in addition to shear. In applying such tangential forces with reference to the cell culture surface, focal adhesions of a particular size make contact with the surface [**86**].

The size and sensory precision associated with the FA contact point will dictate the manner in which the biological entity will interface and perceive the contacted substrate. FA size is dependent upon the interaction between the FA structure and the substrate, in which a cluster of integrins will first aggregate to a particular site, and a more developed adhesion will form [**87**]. FA area has been reported to be in the range of 0.78 to 1.14 μm^2 for fibroblast cells [**88**]. To simplify the cellular sensing model, a constant contact area between FA and substrate of 1 μm^2 was used.

To provide the cell with an "apparent" stiffness different from that of the bulk modulus, the model requires that at least one pillar be underneath the FA. In the case of orthogonally arrayed features, the relationship between pitch and number of pillars per unit area is:

$$\boldsymbol{\rho_{pillars}} = \frac{\boldsymbol{Pillars}}{\boldsymbol{\mu m^2}} = \frac{\mathbf{1}}{\boldsymbol{\chi^2}} \qquad \text{Equation 3-16}$$

$\boldsymbol{\chi}$ is the pitch, or spacing between pillars. The deflection imposed by the FA would be the cumulative bending and shearing of pillars within the area. However, under

the assumption that cellular force transduction occurs at a precision no greater than that of a focal adhesion, the interaction would be perceived as an interaction similar to that shown in Figure 3-4, in which solely shear forces are occurring. In designing pillar geometries to match the stiffness of biological tissues, the deflection of a network of polymer pillars would have to match the deflection allowed by flat target biological tissue.

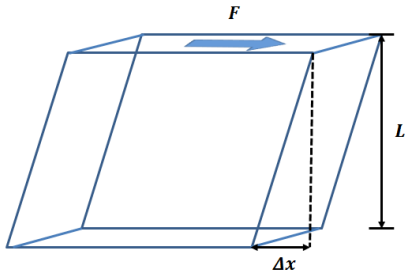

Figure 3-4: Shear force imposed on a unit block.

$$G = \frac{\tau}{\gamma} = \frac{\frac{F}{A}}{\frac{\Delta x}{L}} = \frac{FL}{A\Delta x}\ ,\ \Delta x = \frac{FL}{AG} \qquad \text{Equation 3-17}$$

Assuming that all pillars are subjected to equal forces for the topographic surface under an individual FA, the Δx associated with the tissue to be mimicked needs to match the δ of all pillars being subjected to deflection. The concept is illustrated in Figure 3-5.

It is important to note that the traction force applied to each pillar will be a fraction of the total FA applied force. To relate single bending beam mechanics with the shear interaction occurring with a flat surface, the two equations can be set equal to each other, with the force on each pillar being a function of pillar spacing.

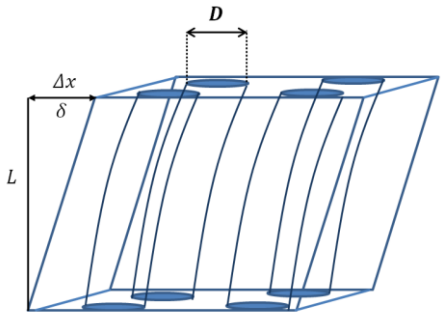

Figure 3-5: Schematic of FA deflection of pillars and perceived deflection of a flat substrate.

$$\Delta x = \delta \qquad \text{Equation 3-18}$$

$$\frac{F_{FA}L}{A_{FA}G_{target\ cell}} = \frac{8F_{pillar}}{\pi E_{substrate}}\left[\frac{8L^3}{3E_{substrate}D^4} + \frac{\alpha L}{(1+\nu_{substrate})D^2}\right] \qquad \text{Equation 3-19}$$

$$F_{pillar} = \frac{F_{FA}}{\rho_{pillar}} = \chi^2 * F_{FA} \qquad \text{Equation 3-20}$$

$$G_{target\ cell} = \frac{E_{target\ cell}}{2(1+\upsilon_{target\ cell})} \qquad \text{Equation 3-21}$$

(A_{FA} assumed to be = 1 μm^2, $\upsilon_{target\ cell}$ = **0.5** [**89**])

$$\frac{3F_{FA}L}{E_{target\ cell}} = \frac{8\chi^2 * F_{FA}}{\pi E_{substrate}}\left[\frac{8L^3}{3D^4} + \frac{\alpha(1+\nu_{substrate})L}{D^2}\right] \qquad \text{Equation 3-22}$$

$$E_{target\ cell} = \frac{3\pi E_{substrate}}{8\chi^2\left[\frac{8L^2}{3D^4} + \frac{\alpha(1+\nu_{substrate})}{D^2}\right]} \qquad \text{Equation 3-23}$$

The final equation relates the intended elastic modulus to be mimicked with the material and geometrical properties of the polymer topography. Certain factors have a more dramatic effect than others, and constraints exist for geometrical parameters. Pillar spacing (χ) must be ≤ 1 μm, as the FA would otherwise not be able to interact with more than one pillar at a time. Moreover, pillar diameter and height must correlate such that adjacent pillars will not bend and make contact with each other, altering the summed pillar deflection experienced by FA during sensing.

In attempting to mimic certain stiffness values, the objective is to create an apparent stiffness equal to that of target biological tissues. Consequently, substrate deflection must correspond to a stiffness related to particular tissue types. Cell stiffness has previously been mechanically characterized for multiple properties, including elastic modulus. Although a wide variety of obtained values have been obtained, bio-related topography maps necessitate the use of particular values as an initial assumption. Engler et. al. came up with elastic modulus values of 0.1-1 kPa for neurons, 8-17 kPa for myoblasts (muscle cells), and 25-40 kPa for osteoblasts (bone cells) [**11**].

3.4.1 Cell Sensing Model with Straight Pillars

The derived equation from the previous section can be used to tailor the geometry of topography to achieve desired apparent stiffness values that match target cell moduli. The presence of shear provides additional pillar deflection resulting in a lower apparent modulus for a given pillar geometry and spacing at lower aspect ratios. However, the difference is fairly small, and becomes negligible at aspect ratios > 2 (Figure 3-6).

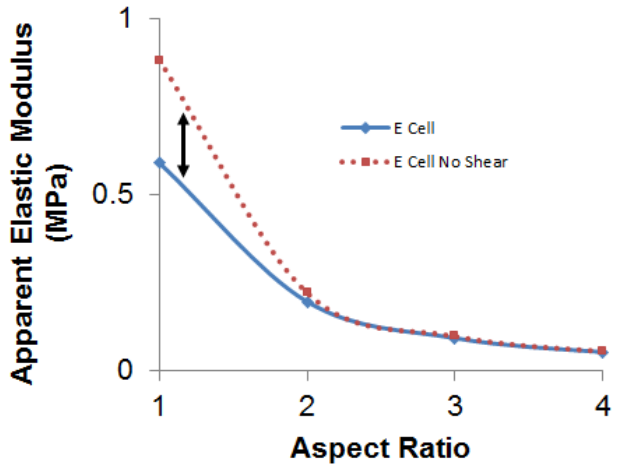

Figure 3-6: Effect of shear on apparent elastic modulus of 200 nm diameter 500 nm spaced pillars with elastic modulus = 12.5 MPa.

To reach apparent elastic moduli that match biological tissue such as neural, muscle, or bone, the increase in aspect ratio (L/D) and pitch is required. Figure 3-7 illustrates the comparison between interfaces containing pillars with different pitches using a pillar diameter of 200 nm. Even at an aspect ratio of >10, the pillars spaced farthest apart are unable to reach the elastic modulus of neural tissue. Muscle tissue, however, can be mimicked using a 0.8 µm pitch and aspect ratio ca. 4.5.

When decreasing pillar radius to 100 nm, lower aspect ratios can be used to achieve a particular apparent elastic modulus. For example, muscle tissue stiffness can be mimicked using a 0.8 µm pitch with an aspect ratio between 2 and 3. Neuronal tissue stiffness can be reached using a 0.8 µm pitch and aspect ratio of 9.

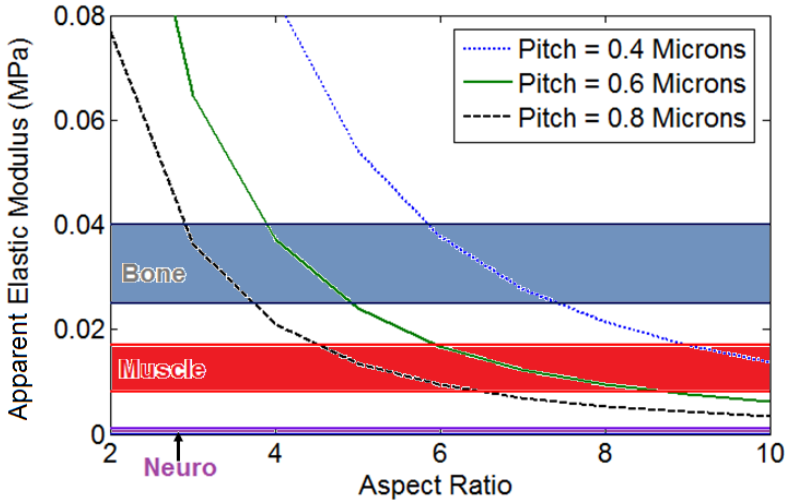

Figure 3-7: Biomechanical interface design map (BMIM) using a constant pillar diameter of 200 nm (0.2 µm) and TPU (E = 12.5 MPa) as the polymer.

A further reduction of pillar diameter to 50 nm allows for significant stiffness reduction, as shown in Figure 3-9. For the 0.6 µm pitch, an aspect ratio of only 6 is necessary to mimic neural tissue stiffness. At the same pitch, muscle tissue stiffness occurs using an aspect ratio < 2.

Although the design maps indicate that certain stiffness values can be attained, the pillars must be able to maintain stability in their unperturbed form.

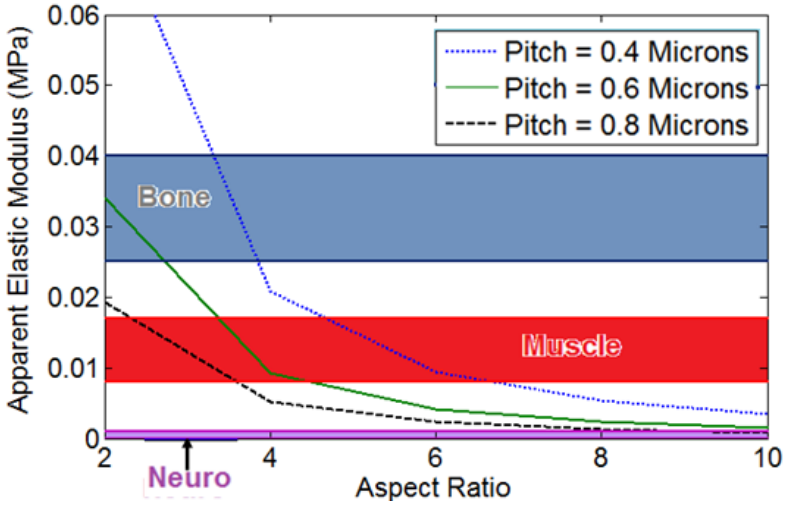

Figure 3-8: BMIM using constant pillar diameter of 100 nm (0.1 μm) and TPU as the polymer.

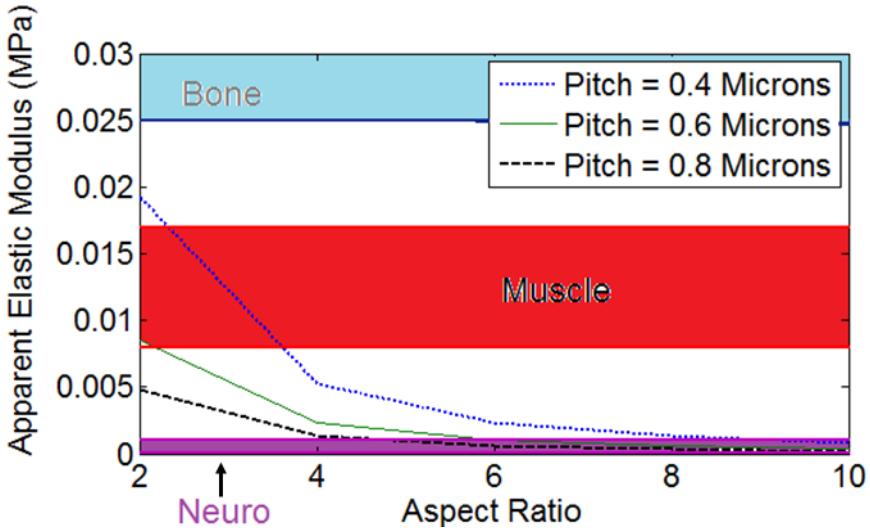

Figure 3-9: BMIM using constant pillar diameter of 50 nm (0.05 μm) TPU pillars.

3.4.2 Micro / Nanopillar Bending Simulation

Nanopillar beam bending simulations were run to compare to the BMIM results with those predicted by numerical methods.

3.4.2.1 Methods

Simulation was conducted using the commercial finite element analysis package Autodesk Simulation Mechanical. Deflections of TPU nano and microposts were simulated by fixing one end and applying a traction force to the other end. The material properties used for TPU are shown in Table 3-2.

Table 3-2: Properties of TPU used for pillar bending study.

Property	Value
Mass Density	71.1
Modulus of Elasticity (MPa)	12.5
Poisson's Ratio	0.395
Thermal Coefficient of Expansion (1/°C)	0.0000965

Forces were chosen based on the assumed cell sensing area (1 μm for nanoscale and 10 μm for microscale), the forces typically applied by hMSCs, and the pillar density chosen. Displacement values of the pillar tips and von Mises stresses were recorded and reported.

3.4.2.2 Nano and Micropillar Bending Results

The issue that arises from cell sensing is not necessarily the ability of the pillar to bending, but the amount of deflection that must occur in order to achieve a certain apparent stiffness. For example, assuming an hMSC applied traction stress of 3 nN/μm^2 (previously observed [**73**]) and substrate thickness of 1.6 μm (corresponding to actual pillar length), the tips of the pillars 0.2 μm in diameter and 1.6 μm long (which would correspond to the muscle region in Figure 3-7) would need to deflect approximately 1.04 μm, or 65% of its length to achieve the appropriate stiffness mimicry of muscle tissue. For a case where the 3 nN is shared by 4 pillars over a 1 μm^2 region (i.e., a pitch of 0.5 μm), the following stress and deflection results were obtained in Figure 3-10. Maximum stresses (concentrated near the pillar base) of > 1500 kPa are predicted. For pillars spaced 0.5 apart, the deflection would result in contact between pillars. In addition, pillar fracture may occur or cease to follow predictable bending behavior at higher deflections.

To simulate osteoblast stiffness (~40 kPa) using the same dimensions, the deflection can be reduced through a decrease in spacing. For a pillar density of 12 / FA (i.e., 12 pillars / μm^2), the resultant deflection is predicted to be 0.362 µm. The consideration must be made as to what traction force a cell will apply, as the geometrical surface design should account for a range of force values.

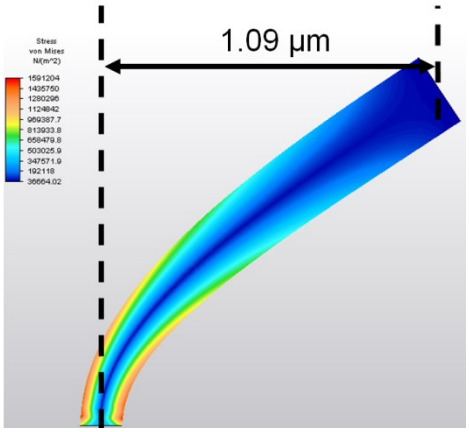

Figure 3-10: von Mises stress and deflection for 0.2 µm diameter 1.6 µm long TPU pillar.

For the same mimicry of bone tissue, Figure 3-11 shows the range of stresses a focal adhesion can apply and the resultant pillar deflection. Both properties show a linear trend, with deflection increasing 4.9 nm / kPa traction force and maximum pillar stress increasing at a rate of 5.8 kPa / kPa traction force.

Over the course of the given research, due to the challenges associated with consistent replication of large arrays of microfeatures, microscale features were targeted over nanoscale. Shown later in the paper, tapered microscale TPU pillars were replicated. To assess their bending mechanics due to applied traction forces, a static stress analysis was performed on the molded geometry. The molded pillars and simulation representation are shown in Figure 3-12.

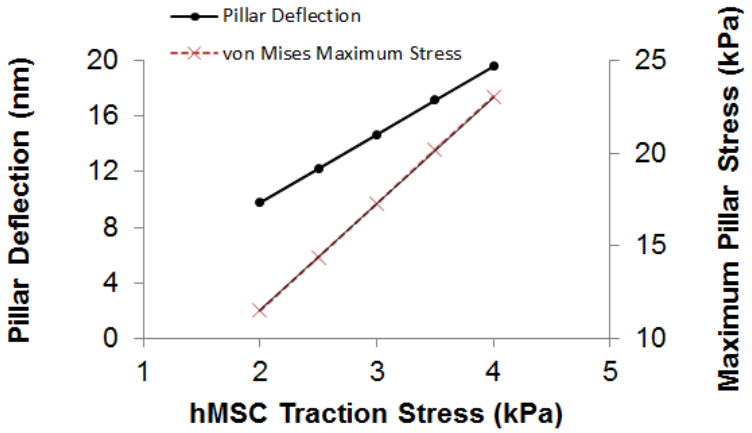

Figure 3-11: TPU pillar deflection and stress at different cellular traction stresses for 0.2 µm diameter 1.6 µm long with 12 pillar / µm density to mimic bone tissue.

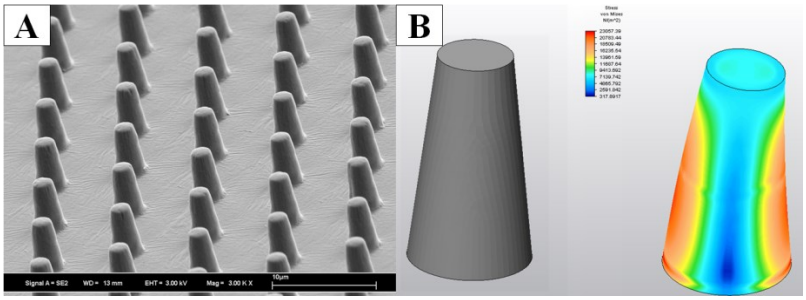

Figure 3-12: Micrograph of micro-injection molding tapered TPU pillars (A) and FEM representation of individual pillar (B).

Results reveal a very small amount of deflection in response to the applied forces for expected focal adhesion stress ranges. Although the deflection is minimal, the presence of topography does offer a surface reduction in comparison to the bulk substrate (which deflects approximately 0.9 nm in response to 3 nN traction force for substrate with same thickness as pillar height).

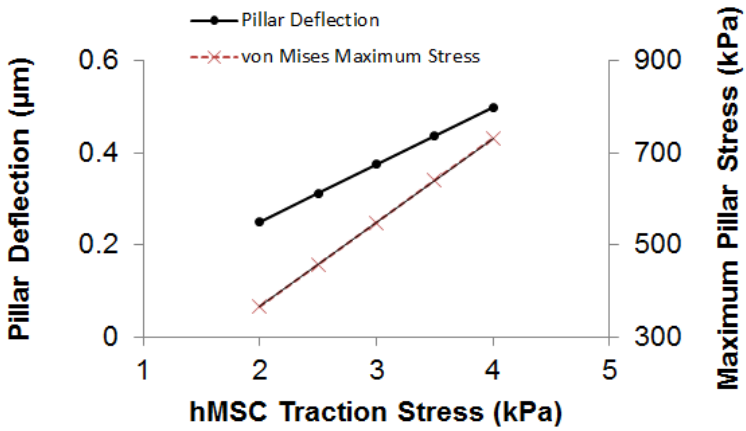

Figure 3-13: Tapered pillar deflection and pillar stress at different traction forces.

3.5 Pillar Stability

Beyond the ability to successfully replicate high aspect ratio micro and nanostructures, they must be able to maintain their structure with high fidelity to perform their intended function. A few criteria must be addressed when assessing whether certain geometries will perform well. The main issues to be addressed are pillar collapse, pillar condensation, and pillar fracture.

Two primary models of polymer pillar collapse have previously been proposed. Gravity is considered to be the driving force for a model by Hui et al [**90**]. The critical (minimum) elastic modulus that dictates pillar collapse is:

$$\boldsymbol{E_{crit}} = \frac{\boldsymbol{qh^3}}{\boldsymbol{7.837I}} \qquad \text{Equation 3-24}$$

The value q is gravitational force per unit length, h is the height of the pillar, and I is the moment of inertia of a pillar. $q = \rho g \pi d^2/4$ and for a cylindrical pillar (ρ is material density and d is pillar diameter) and $I = \pi d^4/64$. However, when experimentally applied, pillars failed at heights far below the critical height predicted by the gravitational force

model [**91**]. Roca-Cusachs addressed the discrepancy by proposing that at the nanoscale, gravity does not make a significant contribution to pillar collapse. Rather, as the scale of a feature is reduced, molecular adhesion force dominates, and thus is responsible for polymer pillar collapse [**92**]. The critical aspect ratio ($\frac{h}{b}$) for lateral collapse (L) is given in Equation 3-25:

$$\left(\frac{h}{b}\right)_L = \left[\frac{\pi^4 3^3}{2^{11}(1-\upsilon^2)}\right]^{\frac{1}{12}} k^{\frac{1}{2}} \left(\frac{E}{W}\right)^{\frac{1}{3}} b^{\frac{1}{3}} \qquad \text{Equation 3-25}$$

The parameter h is the height of the bent portion of the collapsed pillar, k is s/b (s is interpost spacing and b is pillar diameter), W is the work of adhesion of the material to itself, and $\boldsymbol{\upsilon}$ is Poisson's ratio. Thus, the maximum allowable aspect ratio is dependent upon the particular material and geometry of the pillar. The equation predicts that a low work of adhesion, greater interpost spacing, larger diameter, and greater elastic modulus leads to a higher maximum aspect ratio. Figure 3-14 shows a schematic of a failed pillar, with labeled variables.

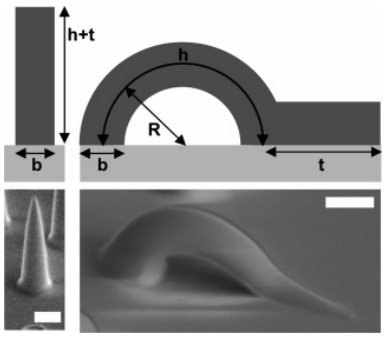

Figure 3-14:Schematic and SEM image of Collapse Polymer Pillar **[**92**]**.

When fabricating pillars and other structures with relatively high aspect ratios, the prospect of structure collapse needs to be considered. In addition, fibers that are able to avoid collapse also may be susceptible to fiber condensation, which is dependent upon geometry and spacing. Condensation is a function of fiber radius (R), aspect ratio (λ), fiber spacing (area fraction of fibers, *f*), elastic modulus (E), and work of adhesion between adjacent tips (γ') [**93**].

$$\boldsymbol{R \geq \frac{8\gamma'\sqrt{h(f)}}{E}\lambda^3,\ \frac{1}{h(f)} = \left(\sqrt{\frac{\pi}{4f}} - 1\right)^2} \qquad \text{Equation 3-26}$$

Equation 3-26 is based on the fibers having spherical tips. Another concern that needs to be taken into account is the size dependence of the elastic modulus of a material. As features decrease to the lower nanometer range, the localized molecular structure begins to factor into the mechanical properties of the polymer. In electrospun nanofibers, for example, the elastic modulus exponentially increases for diameters < 100 nm due to the molecular orientation imparted to the fibers during processing. Polystyrene, for example, has a radius of gyration ¼ the diameter of a 100 nm fiber [**45**]. The mechanical properties of the individual molecular strands become increasingly significant with decreasing feature sizes.

4 Microfeatured Tooling and Mold Assembly for Stem Cell Culture Substrates

To manufacture a macroscale part containing microtopography orders of magnitude smaller than the bulk part in a high rate manner, micro-injection molding can be utilized. Fabrication of such a mold requires the use of multiple fabrication methods. Over the course of the given research, traditional computer numerical control (CNC)

milling was utilized to create the ancillary assembly and macroscale cavities necessary to interface with microfeatured silicon inlays containing microscale networks. In addition, at a slightly larger microscale, micro mills were employed to create a microscale cavity for the investigation of mechanical and thermal properties on process condition variation.

For the extreme microscale (i.e., 1-5 μm), Ultraviolet (UV) lithography combined with dry etching was used to manufacture microfeatures.

4.1 Microscale Tooling Process

The procedure of converting flat tooling into a micropatterned substrate involves a series of steps, with overall purpose being to obtain optimum properties of the photoresist, the masking agent used to define the geometry of the pattern being created in the silicon tooling.

4.1.1 Ultraviolet Lithography Process

Techniques used for the electronics industry, such as UV lithography, are used when the desired dimensions are below the abilities offered through traditional machining methods, which is ca. 50 μm [**94**]. Due to the desire to manufacture tooling containing features with dimensions on the order of a few microns and smaller, UV lithography was employed. The same basic process was employed for all microfeatured tooling trials, and will be presented as a general standard operating procedure used.

The entire process is outlined in Table 4-1. The key discrepancy between studies was the use of synergistic protective coatings underlying the photoresist used to provide additional protection from subsequent plasma etching. Fuji-film OCG825 positive

photoresist (PR) was used due to its high thermal stability and outstanding coating uniformity [**95**]. OCG825 is a highly thermally stable PR which uses ethyl-3-ethoxypropionate as a solvent [**96**]. The thickness is determined by the duration and speed of spinning. OCG825 was used in all lithography studies.

Table 4-1: Ultraviolet Lithography standard operating procedure; steps leading up to feature transfer via etching.

Step	Conditions	Purpose
1. Immerse in 5:1:1 H_20:NH_3OH:H_2O_2	75 ºC / 5 min.	Removes organic contaminants
2. Rinse with deionized H_20	5X	Removal of first step solution
3. Spin-dry	2300 RPMs / 3 min.	Dry wafer
4. Dehydrate Bake	130 ºC / 30 min.	Ensure complete moisture removal
5. Vapor Prime 1:1 HMDS:xylene	10 minutes	Vapor prime for better photoresist adhesion
6. Positive Photoresist Spin-coat (OCG 825)	5,000 RPMs / 40 s	PR coating to subsequent exposure, development, and mask for etching.
7. Critical Bake in box oven	100 ºC / 40 min.	Remove PR solvents
8. PR Exposure	25 mW / 1.3 – 2 s	Expose PR regions where photomask is transparent, allowing exposed PR to be removed with developer
9. Developer Immersion (OCG 809)	45 s	Removal of exposed photoresist
10. Rinse with deionized H_20	5X	Remove residual PR / developer
11. Spin-dry wafers	2300 RPMs / 3 min.	Remove residual water
12. Hard Bake	130 ºC / 30 min.	Increase adhesion between PR/silicon; remove remaining solvents

Exposure was performed with a Karl Suss MJB3 mask aligner, which is equipped with a microscope, stage with wafer vacuum fixation, and a 25 mW mercury lamp to supply the light. The exposure took place in contact mode (i.e. the photomask physically contacted the PR). Throughout the course of study, a specific photolithography mask was used that contains 2 μm diameter orthogonally arrayed circular windows, as shown in Figure 4-1.

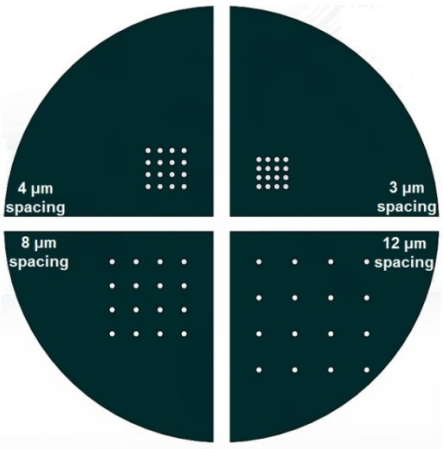

Figure 4-1: Schematic of photolithography mask used for micropatterning photoresist. Windows are 2 µm in diameter. Note: windows not draw to scale, and cover the entirety of each quarter.

4.1.2 Deep Reactive Ion Etching

The requirement for high aspect ratio features necessitated the use of sophisticated electronic fabrication methods. DRIE, a technique capable of imparting high aspect ratio features into silicon, was employed to fabricate microfeatured tooling. DRIE employs the use of a high density low pressure system to reduce the probability of ion collision during plasma dispensing into the chamber [**97**].

Parameters such as plasma flow rate, plasma flow time, activation: passivation ratio, process time, chamber temperature, source power, and wafer chuck power, were altered with the intention of controlling height, depth, and overall profile shape of the microfeatures. Ion etching is a complex process involving control of many different processing parameters which all impact the overall microfeature quality and characteristics to some extent. The main plasmas used in all studies were sulfur hexafluoride (SF_6) and octafluorocyclobutane (C_4F_8), with oxygen plasma being used for

a few of the later tooling fabrication trials. All etching consisted of some form of cyclic activation and passivation recipe to impart the final negative silicon features.

4.1.2.1 Photoresist Etch Rate

SF_6 etches the entire cross-section of the silicon, both exposed silicon and photoresist alike. The ratio of substrate etching to photoresist etching is known as "etching selectivity," in which a larger value corresponds to an increased resistance of the mask during the etching process. Higher etching selectivity facilitates deeper features in the silicon [**22**]. To ensure that photoresist protects unexposed silicon regions throughout the process, a study to determine the etch rate of SF_6 into OCG 825 photoresist was conducted for the conditions shown in Figure 4-2. The photoresist thickness was measured using an Alpha-step 200 profilometer (Tencor Instruments).

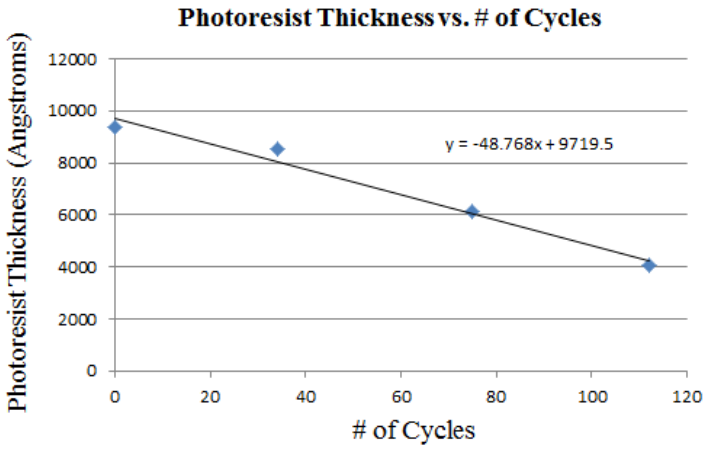

Figure 4-2 Photoresist thickness reduction as a function of Bosch cycles with one Bosch cycle being a 3 s: 2 s 125 sccm: 100 sccm ratio of SF_6:C_4F_8, respectively. Chamber temperature was maintained at 10 ^{o}C.

A relatively linear relationship is apparent, in which approximately 49 angstroms of photoresist is removed per cycle. The trend of etch rate was used as a benchmark for

etching studies when determining the thickness of photoresist necessary to protect initially coated regions until the end of etching.

4.1.3 Vertical Channel High Aspect Ratio Tooling

Due to the desire to manufacture high aspect ratio cylindrical polymer pillars, UV lithography, combined with a specialized dry etching technique known as the Bosch process (previously explained in section 2.4.3.1) was used to create deep vertical channels.

4.1.3.1 Trial 1 – Photolithography and Etching

The Bosch process was used to achieve relatively high aspect ratio vertical negative microstructures on silicon wafers. Photoresist was used to mask specific portions of the wafer for subsequent permanent pattern transfer via dry etching.

4.1.3.1.1 Experimental

The lithography and etching process was conducted using benchmark parameters gathered from previous work [**77**,**75**]. A PR exposure time of 2 s was chosen. The main parameters are shown in Table 4-2.

Table 4-2: DRIE conditions for first trial. C4F8 step was applied at end of process as anti-stiction layer.

Gas	Gas Flow (sccm)	Duration (s)	Source Generator (W)	Total Duration (s)
SF_6	200	2	1500	80
C_4F_8	150	1	1500	40
C_4F_8	150	8	1500	8

4.1.3.1.2 Results

Etched microchannels with 3 µm and 4 µm spacing are shown in Figure 2-2. It is clear that the window dimensions significantly exceed that of the photolithography mask, as precise transfer would result in a 1 µm gap between the edges of the 3 µm spaced channels. Instead, the channels have actually connected, creating a network of positive star-shaped pillars. The channel widening could be the result of the mask not fully contacting the PR, leading to proximity effects [**21**]. It could also be the result of excessive exposure time, allowing for additional PR chemical alterations.

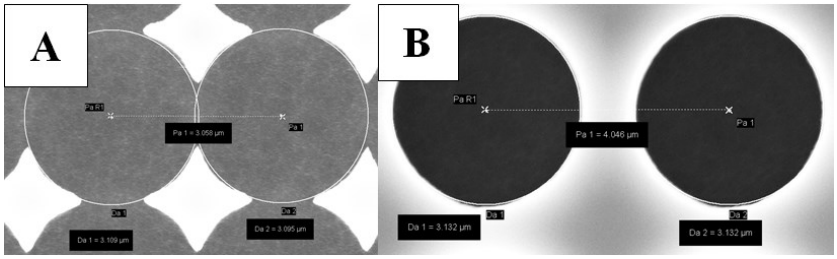

Figure 4-3: Micrographs of microchannels resulting from UV lithography trial 1.

The dimensions of both tooling features are shown in Figure 4-4. The corresponding etch rate was > 2 µm / min and was feature density dependent (Table 4-3). The increase in channel depth can be attributed to the microloading effect, in which etch rate is dependent on pattern density and is increased for lower pattern densities [**98**].

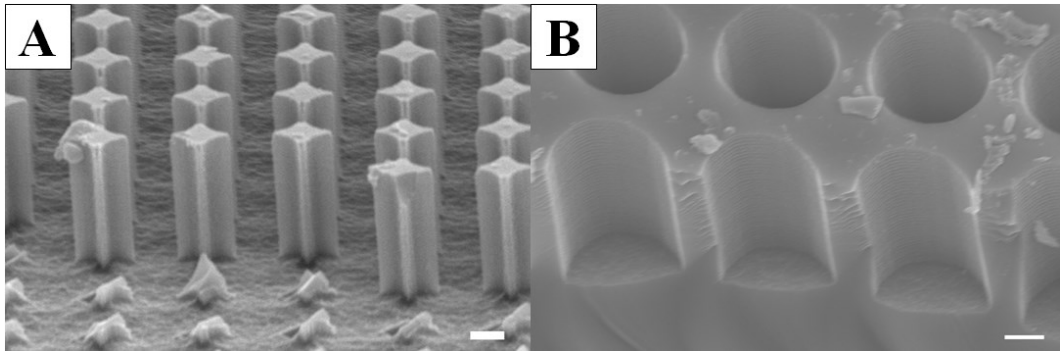

Figure 4-4: Micrographs of 3 µm spaced silicon micropillars (A) and 4 µm spaced microchannels (B). Bars indicate 1 µm.

The parameters used were identical to previous work, in which a mask containing 0.5 µm diameter 2.5 µm spaced orthogonally arrayed windows was used [**75**]. The etch rate previously was approximately 2.25 µm / min, but feature density was lower (3.14 % vs. 48.7 %). It appears that in comparing the two trials, the microloading effect and aspect ratio dependent etch rate effect balanced each other.

Table 4-3: Micropillar / microchannel dimensions and etch rate.

	3 µm	4 µm
Channel Depth (µm)	4.46 ± .01	5.14 ± .11
Aspect Ratio	N/A	1.63
Etch Rate (µm/min)	2.23	2.57

Critical to the quality of mold tooling in addition to the appropriate main feature dimensions is a smooth surface with features that are at least somewhat positively tapered [**99**]. Unfortunately, the Bosch process imparts scalloped sidewalls to anisotropically etched silicon (Figure 4-5) which could potentially function as nano-capable of causing increased friction between polymer and silicon during demolding.

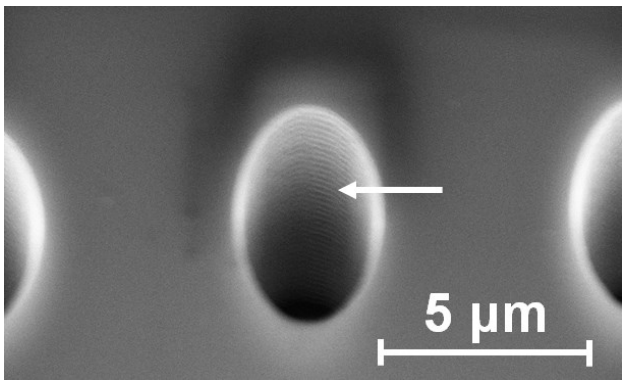

Figure 4-5: Micrograph illustrating the presence of scallops imparted to channel (as indicated by the arrow).

Despite the presence of scallops, both negative and positive features were successfully imparted into the silicon tooling. The tooling was used in the first molding trial as described later in Section 5.3. Aspect ratios were kept fairly low to establish general processing conditions prior to high aspect ratio tooling fabrication trials.

4.1.3.2 Trial 2 – High Aspect Ratio Microchannel Tooling

A more aggressive etching scheme was employed for the second trial to achieve higher aspect ratio cylindrical microchannels. The Bosch process is capable of achieving high aspect ratio negative features in silicon, a characteristic necessary to make the sought after high aspect ratio positive features during polymer replication. From the results obtained from trial 1, etching parameters were tuned for the purpose of greater etching depth and lower vertical wall roughness.

4.1.3.2.1Experimental

A 900 nm layer of photoresist was deposited onto the wafer surface, and the photolithography process was executed, yielding PR windows containing exposed silicon (Figure 4-6).

The results obtained from the first etching study were used to alter the etching recipe. The flow rate ratio was changed to reduce scalloping, which is an inevitable processing result derived from the inherent isotropic etching nature of SF_6 into silicon. A few notable changes are the reduction in flow rate for both plasmas, reduction in source power, and change in ratio of activation time to passivation time. It was expected that reducing the etchant (SF_6) and lowering the source power would limit lateral etching. A

3:1 activation to passivation time ratio was used to allow for reasonable etch rate, considering the lowering of other etch-dependent parameters. Table 4-4 shows the settings used for etching.

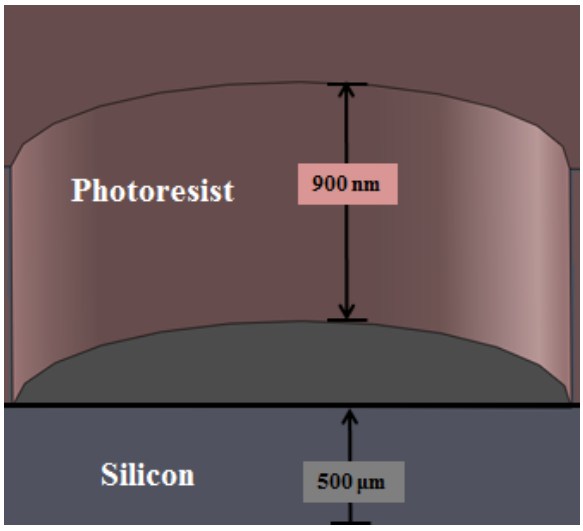

Figure 4-6: Schematic of photoresist window in preparation for etching.

Table 4-4: Etching conditions for high aspect ratio microchannels.

Conditions	Plasma Type	flow (SCCM)	time /cycle (s)	Source Power (W)	Number of Cycles	Total Processing time
Bosch	SF6	125	3	1200	135	10m 20s
	C4F8	100	1	1200		
Anti-stiction Coat	C4F8 (final coat)	150	8	1200	1	8s

4.1.3.2.2 Results

High aspect ratio microchannels were etched into silicon. The 3 µm spaced microchannels, though unattached at the surface, connect directly below the surface, as shown in Figure 4-7A. The connection could be due to an excess of lateral etching occurring near the top of the channel. Especially as the etching gets deeper, the probability of fluorine radicals making contact with regions near the surface increases.

For both pillar spacing arrays, the channels appear to be straight with a minimal amount of scalloping on the sidewalls.

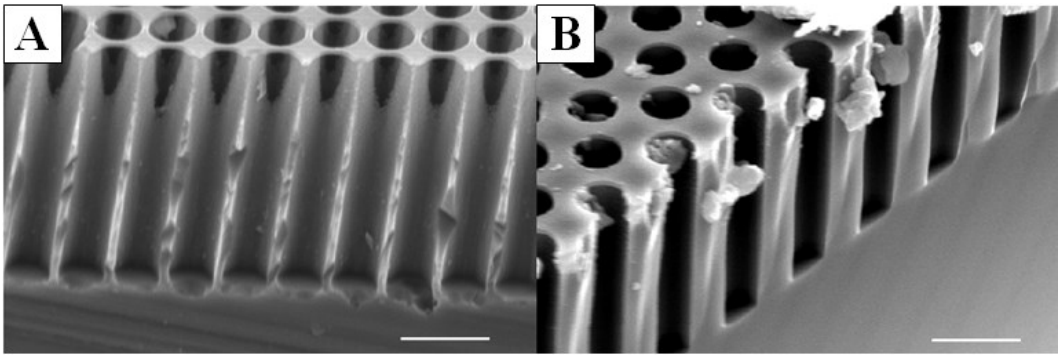

Figure 4-7: Micrographs of 3 μm spaced (A) and 4 μm spaced high aspect ratio microchannels (B). White bar indicates 5 μm.

There appeared to be a slightly dependency of etch rate on spacing, as Table 4-5 shows the difference in channel depth and etch rate. The difference could be due to the connection of channels of the 3 μm spaced channels providing additional opportunities for the plasma radicals to infiltrate the microchannels and etch deeper. The results were not consistent with the microloading effect, as closer spacing facilitated a higher etch rate. The cause is unclear, as a similar scenario occurred in the first etching trial, and the features followed the expected microloading trend.

As expected based on the parameters chosen, the etch rates were dramatically reduced from the first trial (from ca. 2.4 μm / min to ca. 1.35 μm / min). The reduction in etch rate is an inevitable tradeoff when attempting to limit sidewall scalloping [**100**].

It is important to consider that the parameters chosen for the first trial were referenced from previous research that focused on etching nanoscale features [**75**]. Etching schemes should be specific to the specific feature size to be manufactured, and

the goal for the given etching process was to begin to develop a library of etching recipes specific to the lower microscale.

Table 4-5: Channel properties and spacing-dependent etch rate for trial 2 high aspect ratio vertical tooling.

	3 µm	4 µm
Channel Depth (µm)	14.75 ±0.14	13.14 ±0.18
Aspect Ratio	5.65	4.91
Etch Rate (µm/min)	1.43	1.27

4.1.3.3 Trial 3 –High Aspect Ratio Low Roughness Microchannels

Based upon the prevalence of inconsistency of replication due to feature rupture at certain surface locations, tooling with a lower level of sidewall scallop roughness was sought after. An additional objective was to etch 3 µm spaced microchannels without features connecting to each other.

4.1.3.3.1 Experimental

To provide additional protection beyond that of the typical PR coating, an additional layer of silicon dioxide (SiO_2) was applied onto the silicon surface as a secondary mask. The photolithography process took place as previously. However, at the time PR windows were created, the SiO_2 was removed from the windows through an HF etch, leaving bare silicon. A schematic of the window can be seen in Figure 4-8.

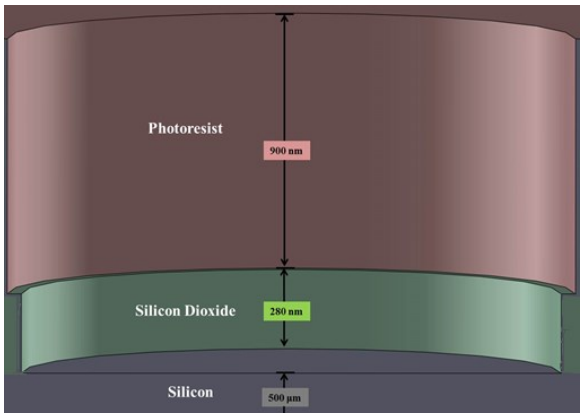

Figure 4-8: Illustration of PR and SiO2 coated silicon wafer with characteristic window.

Etching parameters were kept the same as the previous trial, however, the ratio of activation to passivation time was changed from 3:1 to 3:2 to increase the amount of sidewall protection and thereby limit lateral etching. Lateral etching not only causes more scalloping, but could cause the features to connect, as was the case with the previous trial. The number of cycles was increased to counterbalance the increased total time of passivation to achieve a similar etch depth.

Table 4-6: Etching conditions for high aspect ratio low roughness microchannels.

Conditions	Plasma Type	flow (SCCM)	time /cycle (s)	Source Power (W)	Number of Cycles	Total Processing time
Bosch	SF6 C4F8	125 100	3 2	1200 1200	155	12m 55s
Anti-stiction Coat	C4F8 (final coat)	150	8	1200	1	8s

4.1.3.3.2 Results

High aspect ratio microchannels with relatively low sidewall roughness were successfully fabricated (Figure 4-9). The 3 µm spaced channels do not connect as they

did in the previous trial. Depth measurements reveal that the depth of the 4 µm spaced microchannels was greater than that of the 3 µm spaced channels (Table 4-7). The increase in channel depth for a lower pattern density can once again be attributed to the microloading effect. The previous trial did not follow the same trend due to the channels connecting with one another. For the given trial, the etch rate is further reduced from the previous trial due to the increased passivation time per cycle.

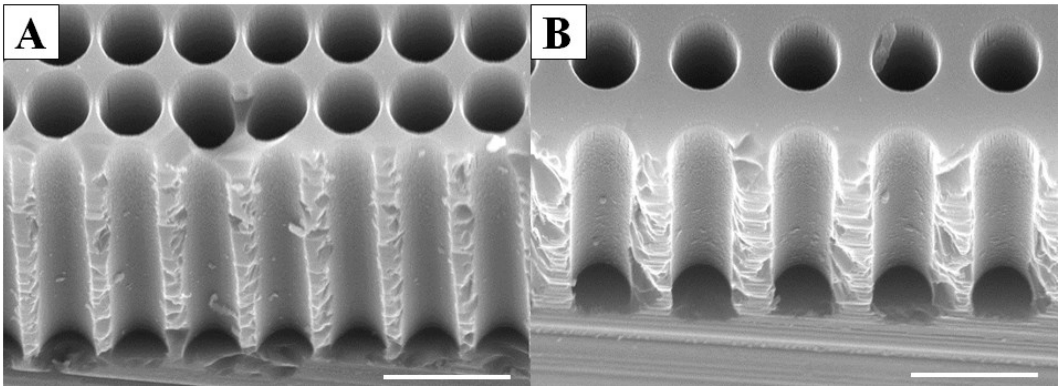

Figure 4-9: Micrographs of 3 µm spaced (A) and 4 µm spaced (B) microchannels.

Table 4-7: Channel properties of trial 3 vertical high aspect ratio channels.

	3 µm	4 µm
Channel Depth (µm)	13.17 ± 0.14	14.02 ± 0.03
Aspect Ratio	5.14	5.46
Etch Rate (µm/min)	1.02	1.09

4.1.3.4 Trial 4 – High Aspect Ratio Microchannels with Aluminum Mask

A higher aspect ratio was desired. Etching conditions were varied slightly from the previous trial to achieve deeper channels while maintaining sidewall integrity.

4.1.3.4.1 Experimental

Parameters were kept the same except for the amount of flow of SF_6, which was increased by a value of 10. An aluminum mask was used as a secondary mask, and a similar procedure to that of the SiO_2 mask was performed. Instead of an HF etch, a PAN etch was used to remove aluminum present in the channels. A PAN etch consists of the use of phosphoric, acetic, and nitric acid to wet etch aluminum. A 170 nm thick aluminum layer was present beneath a 900 nm layer of PR (Figure 4-10).

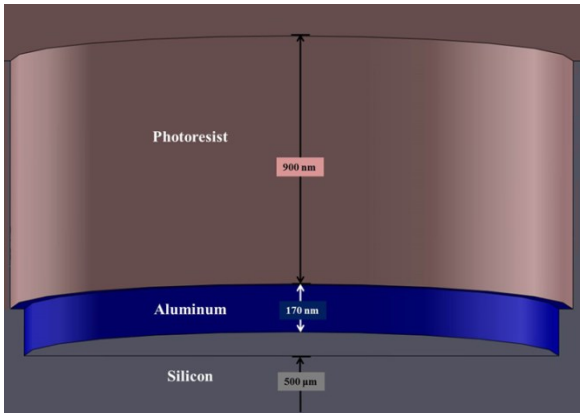

Figure 4-10: Illustration of UV lithography PR window with secondary aluminum mask.

Table 4-8: Etching conditions for trial 4 higher aspect ratio microchannels.

Conditions	Plasma Type	flow (SCCM)	time /cycle (s)	Source Power (W)	Number of Cycles	Total Processing time
Bosch	SF6	135	3	1200	155	12m 55s
	C4F8	100	2	1200		
Anti-stiction Coat	C4F8 (final coat)	150	8	1200	1	8s

4.1.3.4.2 Results

High aspect ratio microchannels were etched. However, the quality of the sidewalls appears to be compromised, as vertical streaks are present along the walls,

especially closer to the top surface (Figure 4-11). The surface irregularities could be the result of a phenomenon known as "micromasking" in which small contaminants at the surface shield plasma radicals from the silicon surface [**21**]. Possibly, the aluminum used to provide additional masking was not cleanly etched. It appears that the streaks did not continue the entire way down the channel, indicating that at some depth, the micromasking effects became negligible or the contaminant was etched away.

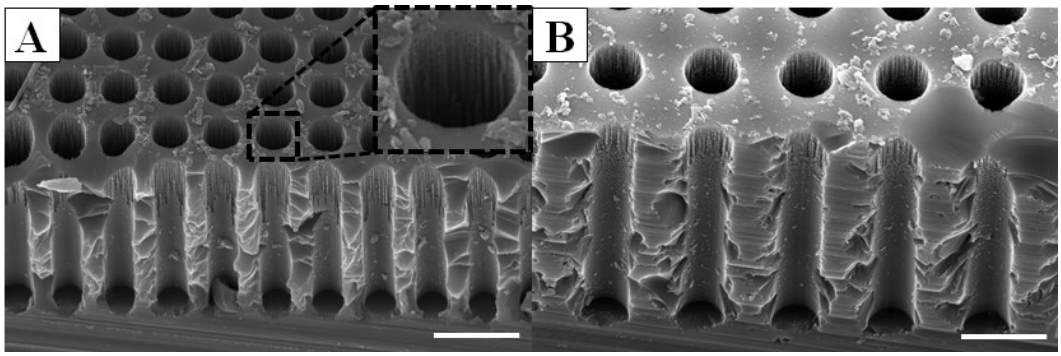

Figure 4-11: Micrographs of high aspect ratio microchannels with 3 µm (A) and 4 µm (B) spacing. The inset highlights the streaking present near the top of the channels.

Unlike the other previous trials, the statistical difference etch depth was insignificant. Aspect ratios of ca. 6 were attained. The etch rate remained around 1 µm/min, indicating that a 10 sccm increase in SF_6 flow rate does not have a significant effect on etch rate.

Table 4-9: Microchannel dimensions and etch rates for trial 4.

	3 µm	4 µm
Channel Depth (µm)	13.7 ±0.06	13.59 ±0.07
Aspect Ratio	6	5.96
Etch Rate (µm/min)	1.06	1.05

Although the microchannels appear straight, the surface texture imparted to the sidewalls could potentially have deleterious effects on the surface quality and replication potential of molded parts.

4.1.2.5 Vertical Channels for 10 x 10 mm² wafers

An alteration in the microfeatured tooling surface area was made to increase the distance between the silicon and ejector pins (since the mold assembly contains very discrete ejector pin locations). The wafers were reduced in size from 11 x 11 mm^2 to 10 x 10 mm^2. Moreover, lower aspect ratio microfeatures were sought after to allow for more feasible replication given previous results. For the given application, consistent topography is the primary concern over localized high aspect ratio features. Lithography involved identical steps for two separate wafers, and two different etching schemes were employed: a short channel and a deep channel etching process.

4.1.2.5.1 Experimental

The same process as previously mentioned was performed to achieve a silicon wafer coated with a uniform layer of photoresist with orthogonal circular windows. A silicon oxide layer below the photoresist served as additional protection in case of excessive etching into the polymer.

Table 4-10: Etching conditions for short and long vertical channels.

Conditions	Plasma Type	Gas Flow (SCCM)	time /cycle (s)	RF Source (W)	Cycles	Proccessing Time (s)	Substrate Low Frequency Power (W)	LF Power Duration (ms)
Bosch	SF_6	125	3	1200	34 (short) 75 (long)	170 (short) 375 (long)	80	10
	C_4F_8	100	2	1200				
Anti-stiction Coat	C_4F_8	150	20	1500	1	20s	0	90

4.1.4.5.2 Results

Microscopy revealed that vertical microchannels were successfully imparted to the silicon (Figure 4-12 and Figure 4-13). As expected, an increase in the number of Bosch cycles resulted in a larger depth and higher aspect ratio. Etch rate was dependent on aspect ratio, in which the etch rate was reduced with increasing aspect ratio. This phenomenon has previously been observed and is thought to be the result of an ion angular velocity component created from collisions between the plasma species and gas molecules [**101**]. As the ions travel through the etched channel, the probability increases that they will hit the sidewalls. The increased number of sidewall-ion interaction can also cause an increase in sidewall erosion nearer to the top of the channel. There appears to be a cone-shaped feature at the surface of the deep etched channels, which could be the result of PR deterioration (Figure 4-13A). Considering the same feature is not present in the short channel case, it is assumed that the feature did not begin to occur until at least 34 cycles into the process.

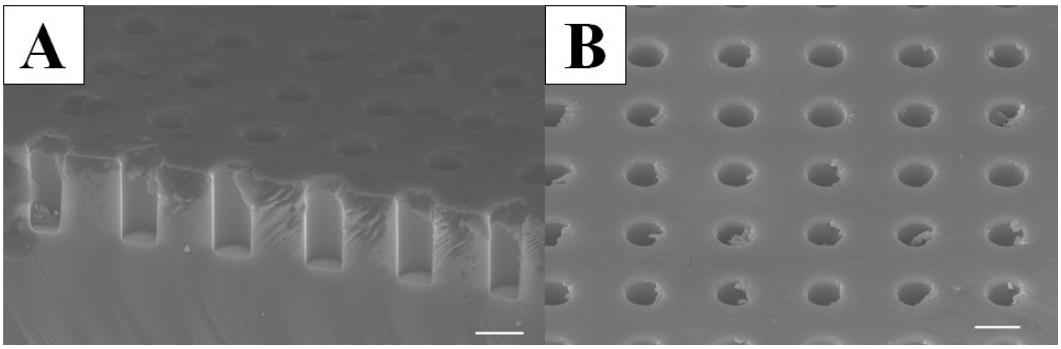

Figure 4-12: Micrographs of short channel profile (A) and overhead view (B) of 4 µm spaced microchannels. Bar indicates 2 µm.

Measurements show a slight dependence on spacing, as the 4 µm spaced microchannels have a slightly larger diameter while maintaining a similar etch depth. The

increase in cycle number does not follow a linear trend in etch depth. As a result, when attempting to reach a certain depth, the number of cycles should be matched up to a curve generated from previous experimental results to predict the final etch depth (Table 4-11). The etch rate is dramatically higher compared to deep channel etching. The increase is consistent with the well-known aspect ratio dependent etch rate.

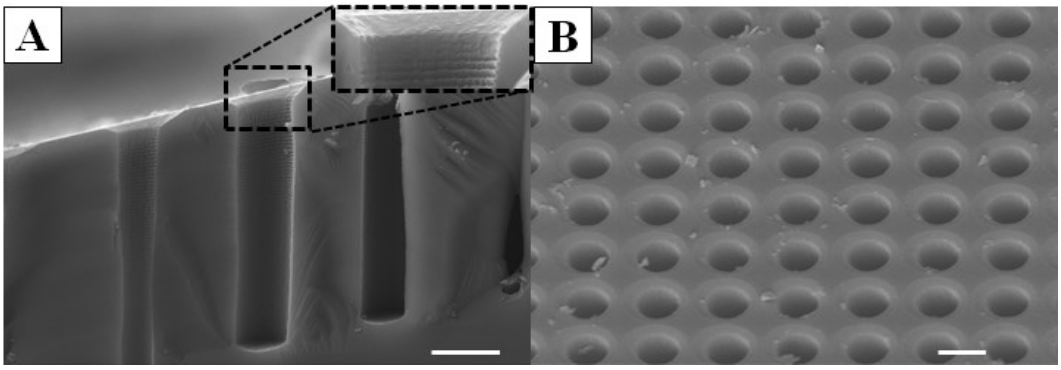

Figure 4-13: Micrographs of deep channel side profile (A) illustrating flared feature at surface (inset) and tilted view (B) of 4 µm spaced microchannels. Bar indicates 2 µm.

The increase in cycle number does not follow a linear trend in etch depth. As a result, when attempting to reach a certain depth, the number of cycles should be matched up to a curve generated from previous experimental results to predict the final etch depth.

Table 4-11: Short and deep channel dimensions.

	Short		Deep
Spacing (µm)	3	4	4
Channel Depth	4.75 ± 0.04	4.77 ± 0.03	7.09± .01
Aspect Ratio	2.95	2.77	3.9
Etch Rate	1.68		1.13

4.1.5 Tapered Tooling Trial 1: Isotropic/Anisotropic Cycling

To address the difficulty in molding vertical high aspect ratio features, etching schemes focused on drafted features were executed. Unsuccessful replication is more often caused by inadequate demolding more so than inability to fill microcavities, with draft angles as low as 2^{o} resulting in a significant reduction in demolding forces [**102**]. It has been suggested that draft angles up to 5^{o} should be applied to allow for good release of the polymer from the tooling. Improper demolding can thus result in both part and tooling damage [**103**,**104**]. For specifically silicon microfeatured tooling, it has been suggested that the critical geometrical factors to achieve proper demolding are the angle and smoothness of the sidewalls [**105**].

The first recipe selected followed a concept introduced by Roxhed et al. [**106**], in which isotropic and anisotropic (Bosch) etching was employed to create a net tapered vertical profile. As far as the author is aware, the Roxhed method had not been used at the extreme microscale regime (< 5 μm) to date. The premise of the process is that a vertical channel is etched with the Bosch process, expanded laterally with an isotropic etch, and the process repeats, creating a net tapered profile, as shown in Figure 4-14.

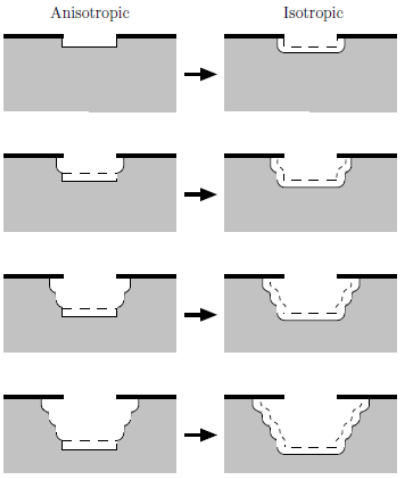

Table 1. Process parameters for the anisotropic and isotropic etch steps.

	Anisotropic etch step	Anisotropic passivation step	Isotropic etch
Time	9 s	7 s	t_i
Step overlap	1 s	0.5 s	N/A
Gas flow	150 sccm SF_6	100 sccm C_4F_8	100 sccm SF_6
Pressure	APC[a] fixed: 60°	APC fixed: 60°	15 mTorr
Coil power	600 W	600 W	600 W
Platen power	12 W	0 W	0 W

[a] Automatic pressure control (APC) is deactivated and the exhaust valve is set at a fixed angle.

Figure 4-14: Schematic of tapered etching, with alternate anisotropic and isotropic features with subsequent etching parameters for Roxhed study [106].

4.1.5.1 Experimental Details

The recipe used followed the same concept of vertical etching followed by isotropic etching to widen the channel closer to the top. Table 4-12 shows the settings used for the study. It was anticipating that a tapered profile would results from the cyclical use of the Bosch process and SF_6 isotropic etching.

Table 4-12: Etching conditions for Isotropic/Anisotropic cycling recipe.

Conditions	Plasma Type	flow (SCCM)	time /cycle (s)	RF Source (W)	Cycles	Processing time	Substrate Low Freq. Power (W)	LF Power Duration (ms)
Bosch (Anisotropic)	SF6	125	3	1000	34	2m 50s	80	10
	C4F8	100	2	1000				
Isotropic	SF6	125	15	1000	1	10s	0	90

4.1.5.2 Results

Contrary to expectations, the sidewall polymer layer appeared to completely impede widening of the vertical walls, and the etchant concentrated at the bottom of the channels. The recipe was executed once and twice, as shown in Figure 4-15. For the two cycle process, the profile created by one cycle essentially repeated itself at a lower depth

in the channel. The discrepancy between the results obtained by Roxhed and the given one are thought to be due to a difference in SF_6/C_4F_8 plasma ratios (3/2 vs. 9/7), source generator power (1000 W vs. 600 W), and the feature size (2 μm vs.100 μm). The more consistent deposition of passivation at a higher power may have enhanced the polymer integrity. A very important observation to make is that the etching width of the channel below the first blown out region was consistent with the diameter of the photoresist windows. This characteristic is attributed to the vertical directionality of the SF_6 plasma entering the channel. The results obtained provide valuable insight into etchant behavior, and are used in the subsequent study as a reference for a new etching scheme.

It was determined that a 15 s isotropic etch resulted in a 20% lateral expansion of etched silicon in relation to the photoresist window, as shown in Figure 4-15A.

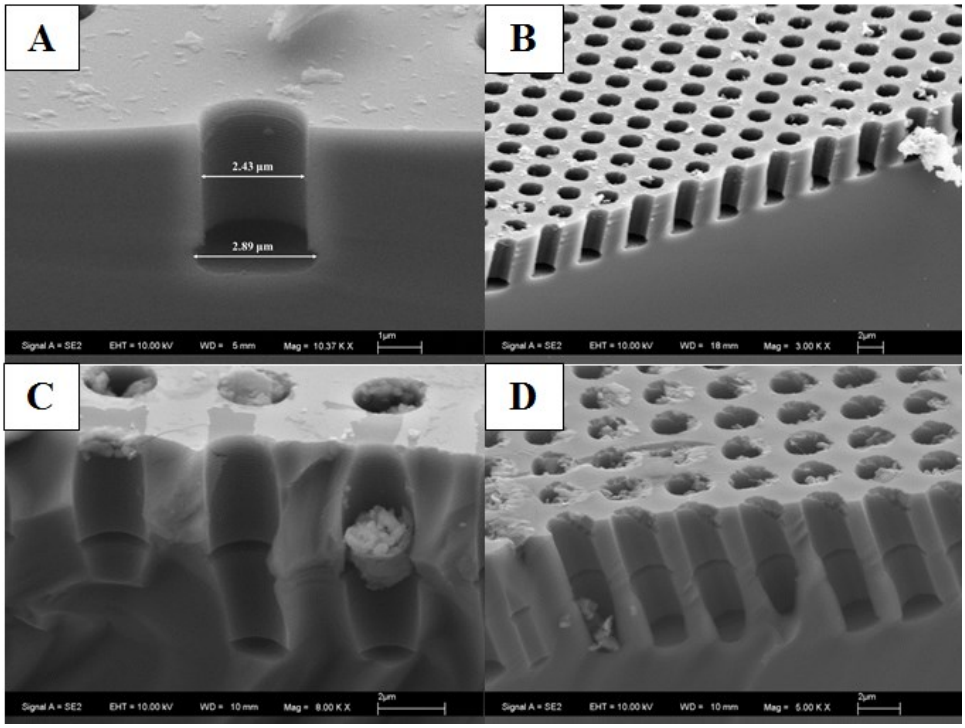

Figure 4-15: Micrographs of etched channels using isotropic/anisotropic cycling. Etched channels from one cycle (A, B) and two cycles (C, D).

4.1.6 Tapered Tooling Trial 2: Gradient Bosch and Variable Isotropy

Two primary methods were subsequently attempted. The "gradient Bosch" process, a novel processing scheme developed based upon results in the first taper trial, uses a primarily isotropic etch that gradually transitions into a Bosch etch. The second method, known as "Variable Isotropy," is derived from a study by Vasilache et al. In the process, a series of Bosch cycles are run, followed by an O_2 ash, and concluded with an isotropic etch. The three steps are run cyclically in series. The Bosch etch yields a vertical channel, the O_2 plasma removes the sidewall passivation layer, and the isotropic etch widens the entire channel in all directions. The final etch also is thought to have a polishing effect on the vertical channel faces [**107**]. Such a method allows SF_6 to etch silicon in all directions, though it will still etch more vertically than laterally due to ion bombardment directionality. Figure 4-16 shows the steps involved with variable isotropy. Both schemes were executed with the intent to manufacture high aspect ratio tapered microchannels.

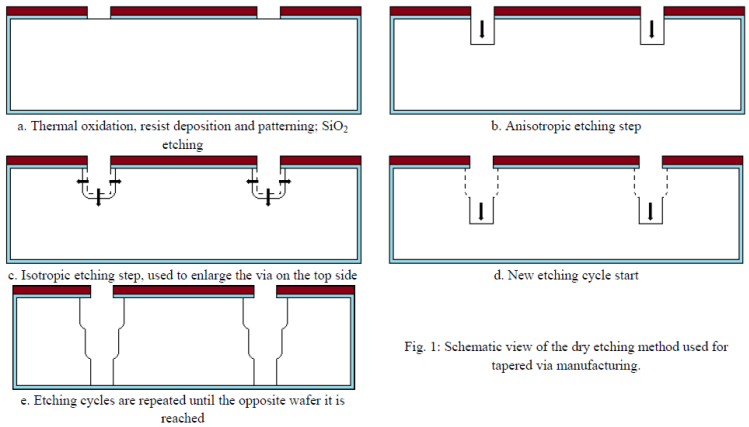

Figure 4-16: Variable isotropy process suggested by Vasilache et. al. **[**107**]**

4.1.6.1 Experimental Details

The Gradient Bosch process began with a 15 s etch period, followed by 2 s of passivation. The etching period was subsequently reduced by 2 s each cycle until reaching a 3:2 etch: passivation ratio, respectively (Table 4-13). At a ratio of 3:2, 34 Bosch cycles were run. The process took place at 10 ^{o}C, with a pulsed low frequency substrate holder power of 80 W for 10 ms and 0 W for 90 ms to promote formation of the protective passivation layer.

The variable isotropy process was run as shown in Table 4-14. To provide a widening of the channel opening immediately, the etching process began with an isotropic etch with SF_6. A three step process ensued, which was comprised of a Bosch etch to create a vertical channel, O_2 ash to remove the passivation layer, and SF_6 isotropic etch to widen the vertical channel and provide a polishing effect to the scalloped sidewalls.

Table 4-13: Etch recipe for trial 2 using a "Gradient Bosch" method

Conditions	Plasma Type	flow (SCCM)	time /cycle (s)	Source Power (W)	Number of Cycles	Total Processing time
Bosch 15	SF6	125	15		1	17 s
	C4F8	100	2			
Bosch 13	SF6	125	13		1	15 s
	C4F8	100	2			
Bosch 11	SF6	125	11		1	13 s
	C4F8	100	2			
Bosch 9	SF6	125	9		1	11 s
	C4F8	100	2	1000		
Bosch 7	SF6	125	7		1	9 s
	C4F8	100	2			
Bosch 5	SF6	125	5		1	7 s
	C4F8	100	2			
Bosch (3)	SF6	125	3		34	2 m 50 s
	C4F8	100	2			
			Resist Strip			
Anti-stiction	C4F8	150	20	1500	1	20 s

Table 4-14: Etch recipe for trial 2 using "Variable Isotropy" method

Conditions	Plasma Type	flow (SCCM)	time /cycle (s)	Source Power (W)	Number of Cycles	Total Processing time	Number of Cycles
Bosch	SF6	125	3	1000	34	2m 50s	3
	C4F8	100	2	1000			
O2 Ash	O2	100	20	1000	1	20s	
Isotropic	SF6	125	10	1000	1	10s	

4.1.6.2 Results

For the gradient Bosch process, it was determined that the vertical etch rate into silicon followed an approximately linear relationship for all duty cycles of around 51 nm/s (Figure 4-17). Vertical etching rate appears to remain relatively constant when transitioning from a primarily isotropic etch process to anisotropic etching. The truncated etching that occurs during the Bosch process (a "stop-and-go" type of etching) was expected to lower the rate of etch compared to the more isotropic portion of the process. However, it is possible that the concentration of radicals contributing to lateral etching for the more isotropic duty cycles may have offset the otherwise lower vertical etch rate during the Bosch process.

The effective taper angle generated from the Gradient Bosch process is 5.4^{o}, with a majority of the taper being near the top of the channel. The aspect ratio of the channel is ca. 2.25 (based on average diameter of channel; image shown in Figure 4-18. The top of the channel was found to be ca. 51% wider compared to the bottom. The widening occurred due to both the initial 15 s isotropic etch and the subsequent etches which served to further widen the top region of the channel.

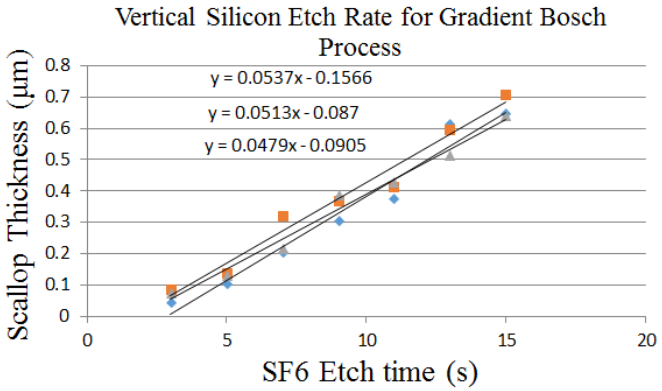

Figure 4-17: Etching rate for Bosch etching utilizing different duty cycles of activation and passivation.

Although a taper was successfully imparted into the microfeatures, the scalloping effect was quite prominent, and detrimentally so near the top of the channel. Scallops with excessively extended projections away from the major axis of the channel become undercuts during molding, preventing removal of the molded feature from the channel, or causing a severe amount of stretch during demolding.

The Bosch process is essentially a series of small isotropic etches. Consequently, the longer SF_6 is permitted to etch uninterrupted, the more isotropic the features will be due to the fact that SF_6 spontaneously etches silicon. The relatively small amount of C_4F_8 compared to SF_6 (which protects the sidewalls) allows the etchant to expand the channel in all directions, therefore allowing chemical reactions to dominate over physical (bombardment) ones.

The second process attempted of trial 2 of variable isotropy also resulting in tapered features, but with a profile much different than that of the gradient Bosch process (Figure 4-19). The effective taper angle of the channels was 3.4^{o}, and a step is visible at approximately half of the channel depth. A streak appearance is visible closer to the top

of the channel, while scallops are still visible near the bottom. The streaks are due to the isotropic etching that followed the O_2 removal of the sidewall passivation layer combined with the complete removal of the photoresist prior to process termination.

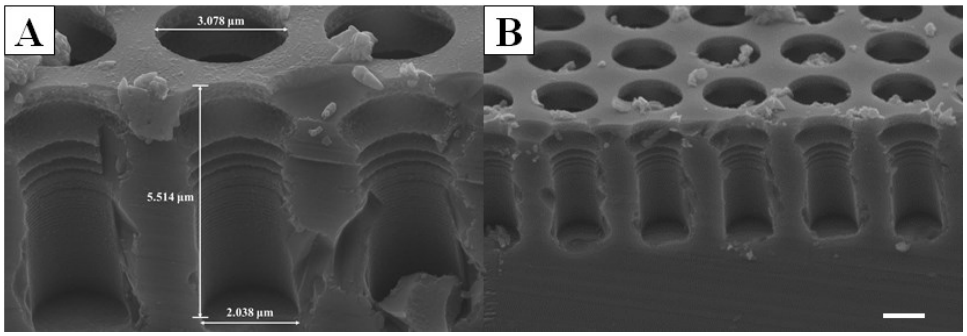

Figure 4-18: Micrographs of channels etched using the "Gradient Bosch" process dimensioned (A) and at lower magnification (B). Bar indicates 2 µm.

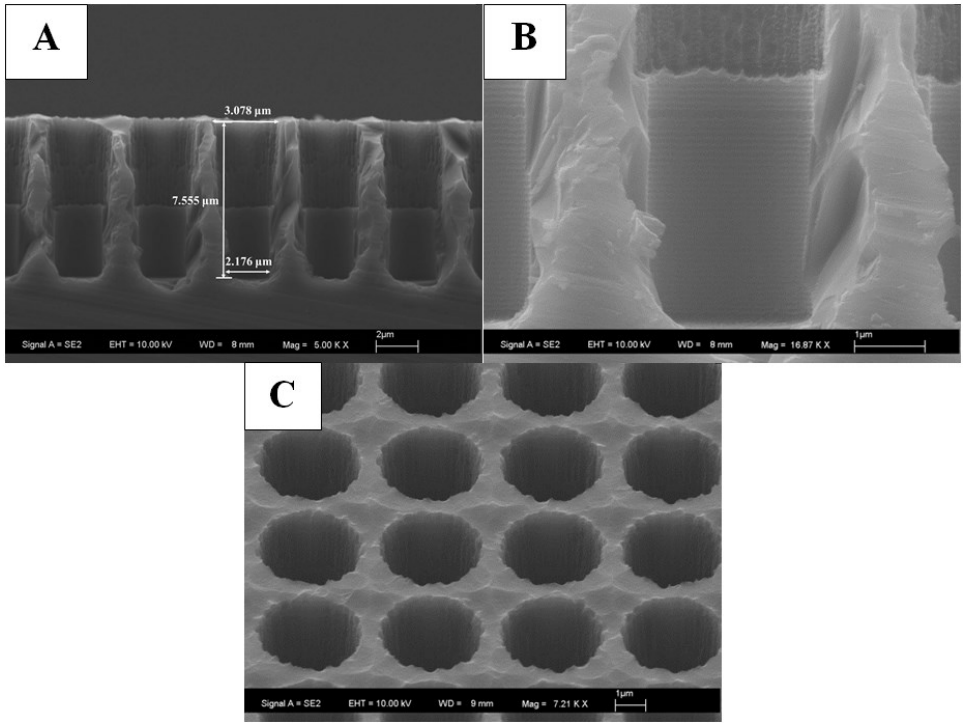

Figure 4-19: Micrographs of "Variable Isotropy" process. Dimensions are shown (A) as well as the “streak/scallop” transition (B), and top surface illustrating the cause of streaks at the top of the channel (C).

4.1.7 Tapered Tooling Trial 3: Variable Isotropy

The third trial followed the variable isotropy process once more, but with a less aggressive etching scheme to prevent exhaustive etching of the photoresist. It is important to note that both the etchant and oxygen plasma remove photoresist. Consequently, for lower photoresist thickness values, oxygen and SF_6 density and duration must be carefully tuned.

4.1.7.1 Experimental Details

An initial isotropic etch was performed to create a widened profile at the top of the microchannels. It was expected that the etching would occur mainly in the regions not protected by photoresist and adjacent silicon regions directly underneath the photoresist.

Table 4-15: Etching recipe used for taper trial 3 silicon tooling.

Conditions	Plasma Type	flow (SCCM)	time /cycle (s)	Source Power (W)	Number of Cycles	Total Processing time	Number of Cycles
Isotropic Etch	SF6	125	8	1000	1	8s	1
Bosch	SF6	125	3	1000	23	1m 55s	2
	C4F8	100	2	1000			
O2 Ash	O2	100	10	1000	1	10s	
Isotropic Etch	SF6	125	8	1000	1	8s	

4.7.1.2 Results

A taper was once again successfully imparted into the microchannels. However, a scalloping effect did persist, as displayed in Figure 4-20D, with a bulge of ca. 26 nm. It appear that closer to the top of the channel, the scalloping has been reduced, though more disordered nanoscale roughness appears to persist in place of more ordered scallops.

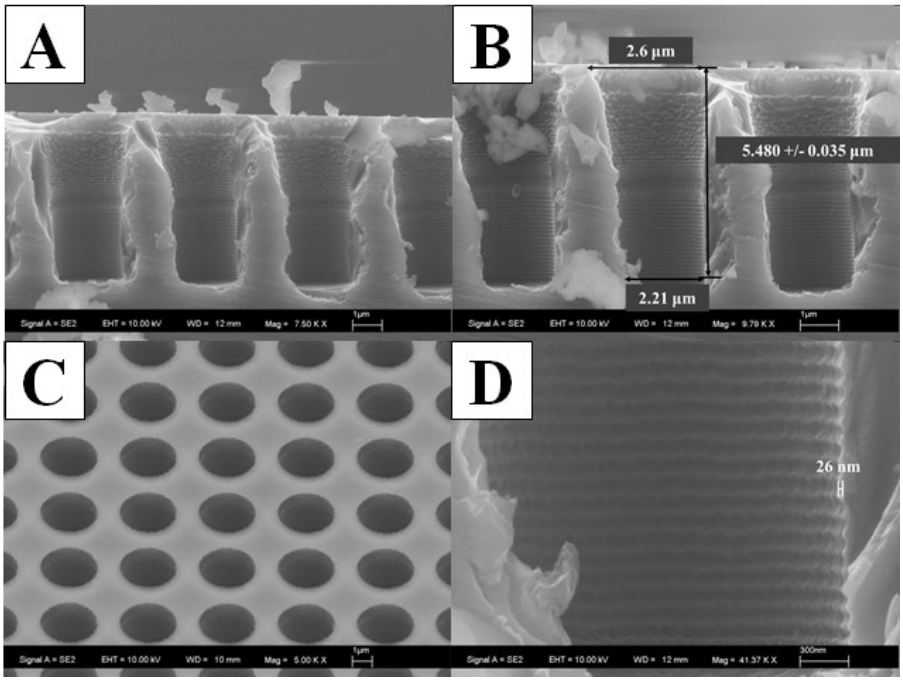

Figure 4-20: Micrographs of the variable isotropy process. (A) shows the entire profile, (B) shows the dimensions of the tapered channel of a wafer containing a final 20 s deposition anti-stiction coating (used later for molding in Section 5.7.2), (C) is a top down view of the silicon wafer surface, and (D) displays a high magnification view of scallops from the Bosch process.

4.1.8 Taper Trial 4 – Passivation Compensation

In response to sub-optimal replication results attributed to tooling feature roughness, a novel etching process was executed, known as the "passivation compensation" technique, to controllably impart a draft onto the vertical faces of the microfeatures.

4.1.8.1 Experimental Details

The novel processing method takes advantage of altering the flow of passivation over the course of the etching process, in which protection of the sidewalls is increased as the etching process proceeds. A few other process modifications were made, including an

increase in process temperature (thought to contribute to channel tapering [**108**]), increased coil power, very short cycle times for the Bosch process (to reduce scallop roughness [**109**]), and constant power supply to the substrate holder instead of pulsing. The settings are displayed below in Table 4-16. The same process was repeated, except for an increase of each Bosch step from 1 minute to 3 minutes to create a deeper profile.

Table **4-17** shows the alteration in parameters.

Table 4-16: Passivation Compensation Settings (Short Channels)

Conditions	Plasma Type	flow (SCCM)	time /cycle (s)	Source Power (W)	Chuck Power (W)	Number of Cycles	Total Processing time	T_{chuck} (°C)
Bosch Low Passivation	SF_6	125	1	1200	25	30	1m	20
	C_4F_8	50	1	1200				20
Bosch Middle Passivation	SF_6	125	1	1200	25	30	1m	20
	C_4F_8	75	1	1200				20
Bosch High Passivation	SF_6	125	1	1200	25	30	1m	20
	C_4F_8	100	1	1200				20
O_2 depassivation	O_2	100	15	1200	25	1	15s	20
SF_6 Polish	SF_6	75	15	500	25	1	15s	20

Table 4-17 : Passivation Compensation (Deep Channels)

Conditions	Plasma Type	flow (SCCM)	time /cycle (s)	Source Power (W)	Chuck Power (W)	Number of Cycles	Total Processing time	T_{chuck} (°C)
Bosch Low Passivation	SF_6	125	1	1200	25	30	3 m	20
	C_4F_8	50	1	1200				20
Bosch Middle Passivation	SF_6	125	1	1200	25	30	3 m	20
	C_4F_8	75	1	1200				20
Bosch High Passivation	SF_6	125	1	1200	25	30	3 m	20
	C_4F_8	100	1	1200				20
O_2 depassivation	O_2	100	15	1200	25	1	15s	20
SF_6 Polish	SF_6	75	15	500	25	1	15s	20

4.1.7.2 Results

Short channels with a taper of 3.6° were successfully etched into the photoresist-coated silicon wafers (Figure 4-21). The typical scallop pattern associated with the Bosch process was not visible on the sidewalls. The most probable causes of the absent scallops

are the short cycle times (2 s / cycle) and the polishing step at the end of the process. The use of an increasing flow of passivant appears to have imparted a taper to the vertical profile of each microchannel. As previously mentioned, sulfur radicals etch silicon spontaneously (i.e., isotropically). However, if the radical comes into contact with C_4F_8, a fluorocarbon compound is formed and the sulfur is no longer active [**22**].

If less passivation polymer is present to prevent the etching, the sulfur radicals are afforded the opportunity to etch to a farther vertically and laterally. In the case of the passivation compensation technique, the ability of the radicals to react with silicon is increasingly reduced. For the "Bosch Low Passivation Step," the C_4F_8 flow rate is less than half of that of SF_6. The ratio of activation: passivation starts at 5:2 and finishes at 5:4. As a result, the sidewalls become increasingly protected and lateral etching is reduced as the channel gets deeper. The higher processing temperature may have also made a contribution to the taper.

The deep channel etching parameters also created tapered channels with no scallops on the vertical surface of the microchannels, as shown in Figure 4-22. A draft angle of 4.9^o was imparted to the deeper channels. A few additional characteristics are highlighted in Table 4-18.

The deeper channels contain a greater taper angle despite the use of similar etching conditions. The increase is thought to be due to the increased inability of the etchant to penetrate the channels and the build-up of the passivation layer. In addition, the etch rate decreases with increasing aspect ratio. Aspect ratio – dependent etch rate is a common phenomenon of Bosch etching resulting from the depletion of fluorine radicals with increasing depth [**110**]. It should be noted that etch rate is not as much a concern as

microchannel profile and surface quality. In fact, minimizing surface roughness is achieved through rapid cycling of activation and passivation, which creates a relatively slow etch rate (compared to typical etch rates of 1.5 – 4 µm [**111**]). Lowering the scalloping effect is usually achieved at the cost of lower throughput [**112**].

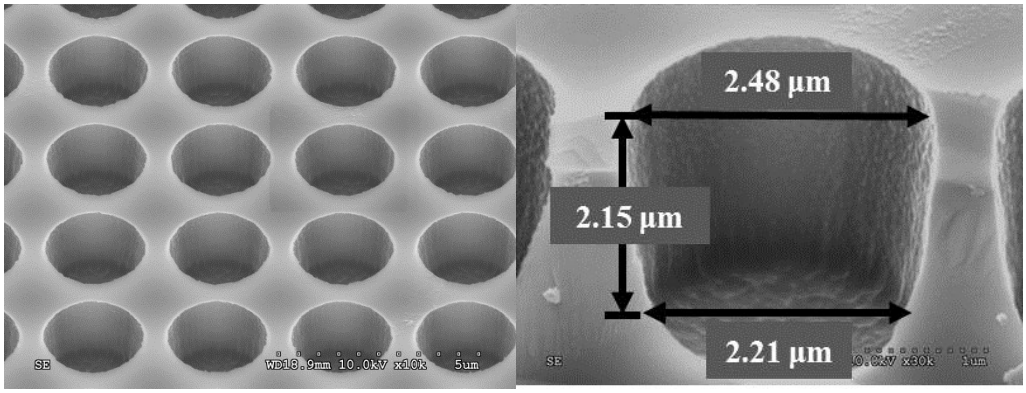

Figure 4-21: Micrographs of taper trial 4 short channels.

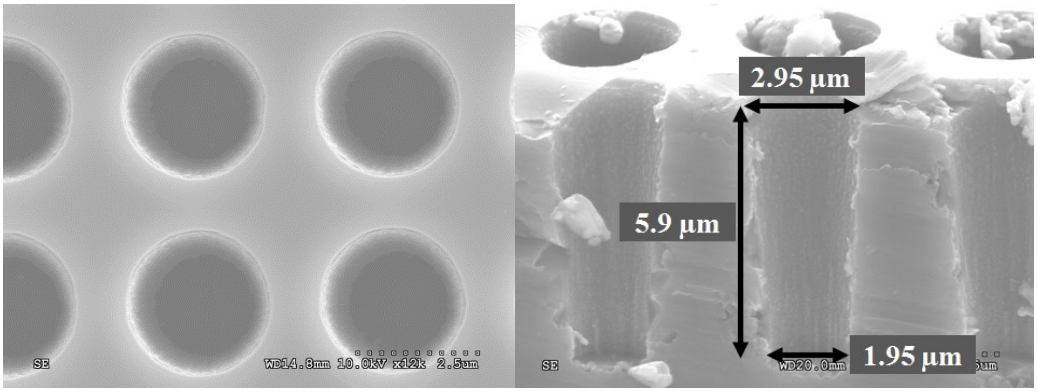

Figure 4-22: Micrographs of taper trial 4 deep channels.

Table 4-18: Metrics for microchannels. *Average channel diameter is used for calculation.

	Short	Deep
Aspect Ratio*	0.92	2.4
Draft Angle (degrees)	3.6	4.9
Etch Rate (µm/min)	0.717	0.652

4.2 Mold Assembly Fabrication

Success in micro-injection molding is contingent upon a robust tooling assembly, as well-controlled melt delivery and appropriate part handling is dictated by the molding assembly used.

4.2.1 Mold Base, Inserts, and Temperature Control System

A challenge in using non-conventional tooling in an injection molding assembly is the manner in which the tooling is incorporated into the mold. In an effort to standardize the assembly, a commercially-available Master Unit Die (MUD) mold base with matching steel inserts was purchased from DME (Figure 4-23). The steel inserts are composed of pre-hardened 4130 steel.

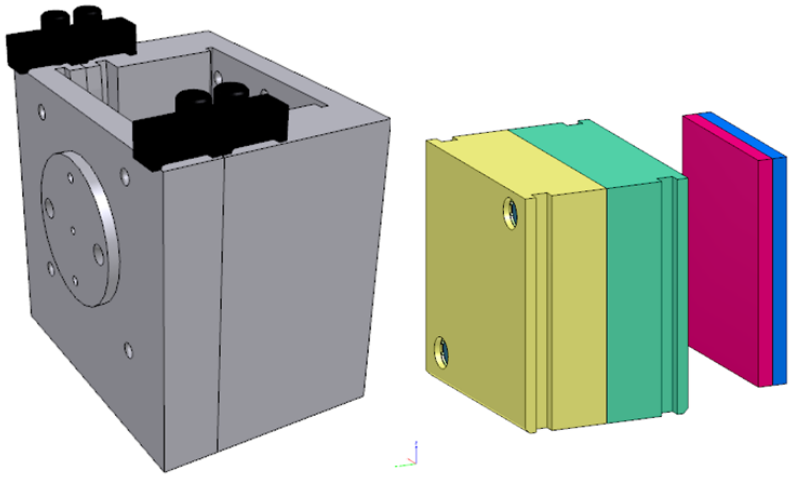

Figure 4-23: DME MUD Quick-Change System 05/05 UF 321 with quick change companion inserts.

To adapt the mold to contain the silicon tooling, a series of alterations were executed. To provide for adequate mold opening distance, the moving plate was machined and a pocket was milled to create a cavity for a smaller mold insert, as shown

in Figure 4-24. In addition, holes for ejector pin holes and cartridge heaters were drilled into the moving half of the mold.

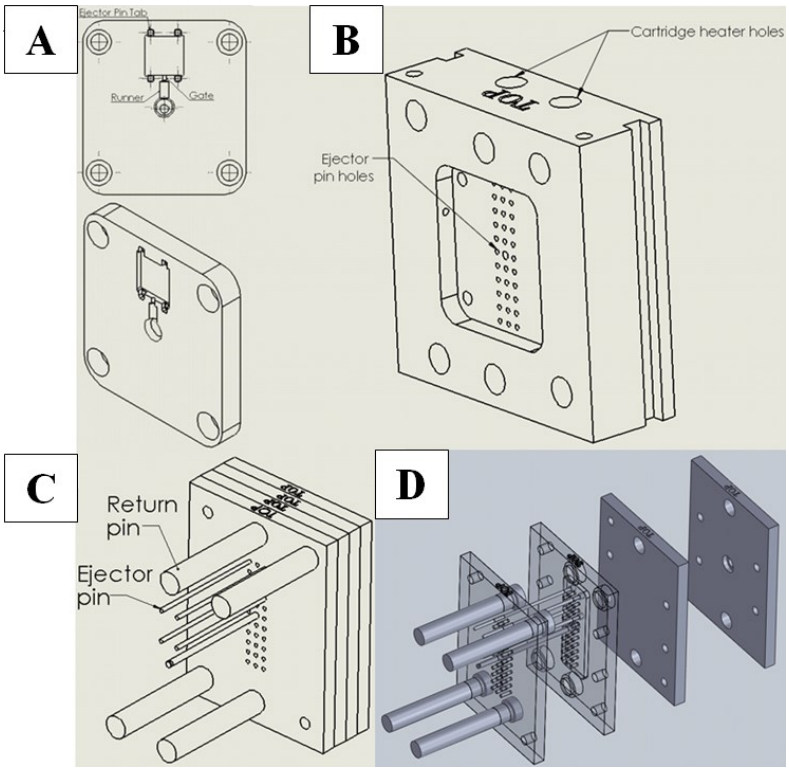

Figure 4-24: Aluminum insert (A), machined back half mold to incorporate cartridge heaters, ejector pins, and separate insert (B), and ejector system assembled (C) and exploded (D).

4.2.2 Aluminum inserts

Aluminum inserts were manufactured to facilitate convenient interchangeability of multiple microfeature designs. 6061 aluminum was machined with a taper on the outside and fixed to the back half steel insert via 8-32 socket head cap screws.

4.2.3 Epoxy Assembly

Considering the microfeatured tooling was imparted to a silicon substrate, the silicon needed to in some way be fixed to the aluminum insert. Fixation required the following characteristics:

1. Firm adherence to aluminum piece.
2. Complete seal between edge of silicon and aluminum.
3. Controlled thermal behavior for microfeatured interface temperature control.
4. Integrity of fixing agent for adequate number of cycles.
5. Provide fixation of inlay parallel to surface.

The requirements listed led to selection of a high temperature relatively thermally insulating epoxy, T-515, from Zymet, Inc. It is a 2-component silica-filled thixotropic thermally curable epoxy with a glass transition temperature of 110 ^{o}C and bondline temperature of 150 ^{o}C. It has a relatively low thermal conductivity (~ 1 W/mK), and is typically used for the bonding of transformers. The epoxy was used to fix the silicon tooling to the aluminum insert, as shown in Figure 4-25. Many variations of the given aluminum insert were manufactured over the course of given research, in which the main cavity geometry was altered for different reasons (Figure 4-26).

For inserts utilizing epoxy, the assembly shown in Figure 4-27 was used. Thermocouples embedded into both mold halves allowed for mold temperature control and monitoring throughout the molding process.

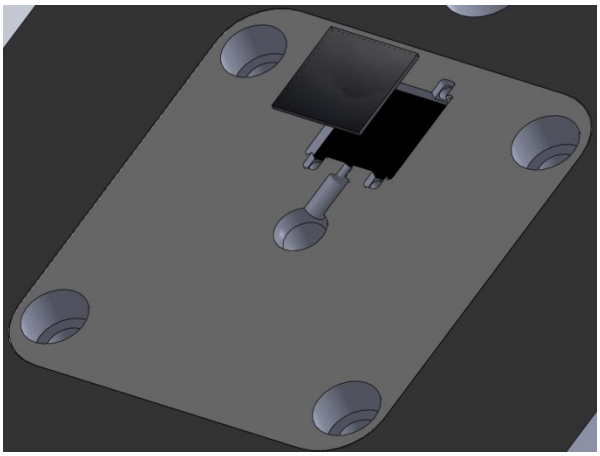

Figure 4-25: Illustration of silicon being fixed to aluminum insert.

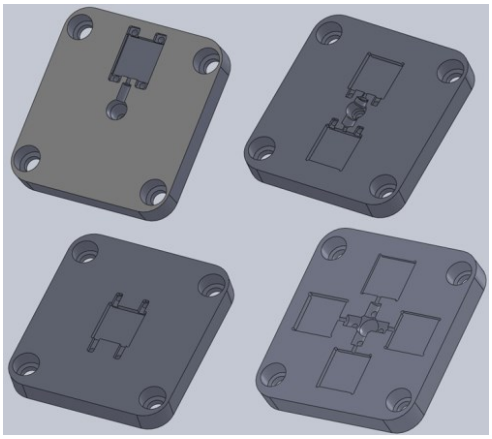

Figure 4-26: Insert designs used / modeled for use in micromolding assembly.

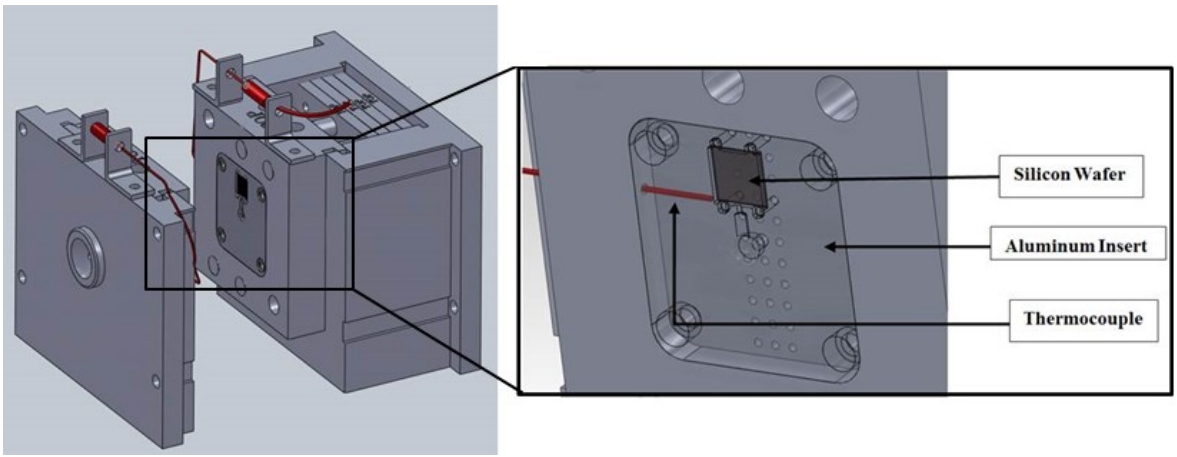

Figure 4-27: Full micromold assembly with wire thermocouples. Aluminum insert is transparent to show alignment of ejector pin holes.

4.2.4 Silicon Clamp Assembly

Efforts were made to engineer an insert that would allow for interchangeable silicon tooling and thus eliminate the need for machining new aluminum inserts when tooling fracture or excessive polymer clogging of the microchannels occurred. The difficulty arises in the balance between applying enough clamping force to create a seal at the silicon – aluminum interface and avoiding excessive force capable of damaging the tooling during assembly.

The incorporation of a relatively brittle material that must be firmly fixed into place can be a challenge, and indeed was during the process of designing and implementing a silicon-clamping assembly.

4.2.4.1 Silicon Clamp Design

To non-destructively fix the silicon wafer with the aluminum tooling, a custom polytetrafluoroethylene (PTFE) gasket was utilized. Figure 4-28 shows the components and their relative orientation within the assembly. The silicon insert contacts PTFE near the edges. The front gasket provides a seal inside the molding cavity to prevent polymer from filling beyond the cavity surface, and the back gasket provides impact resistance inherent to the molding process. A similar concept has been used by Chandekar et al. [**113**]. However, the design presented here is able to attain a higher percentage of microfeatured area over the surface of the entire part. Figure 4-29 provides a profile view to better understand how the clamp assembly functions as a cavity in addition to a silicon fixture device. Another feature of the new design is the use of a fan gate, which is commonly used to provide a more uniform melt profile across a cavity during filling.

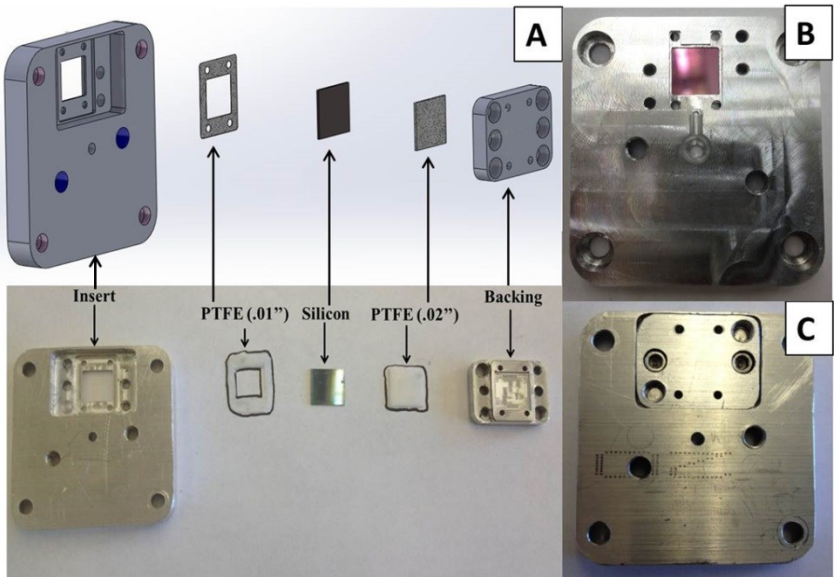

Figure 4-28: Modified aluminum assembly to include silicon clamp design. CAD representation and digital image of exploded assembly (A) and digital images of the front (B) and back (C) of the assembled insert are shown.

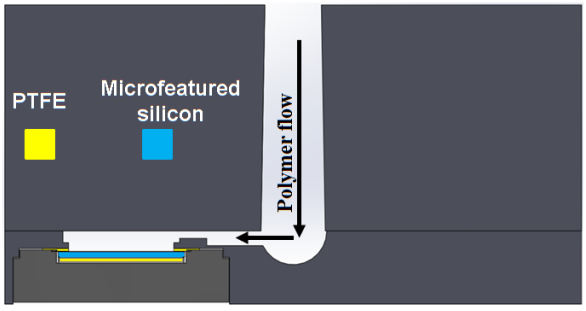

Figure 4-29: Two dimensional representation of polymer flow using clamp assembly.

4.2.5 Steel insert clamp assembly

Due to deformation of ejector pin holes occurring in aluminum inserts, a new insert design utilizing a steel (1018) insert was employed. Unfortunately, a small region of the cavity surface between the microfeatured domain and ejector pin raised thickness region was thin and unsupported, and bowed inward, thereby permanently deforming the cavity. The clamp design was abandoned following the steel clamp trial.

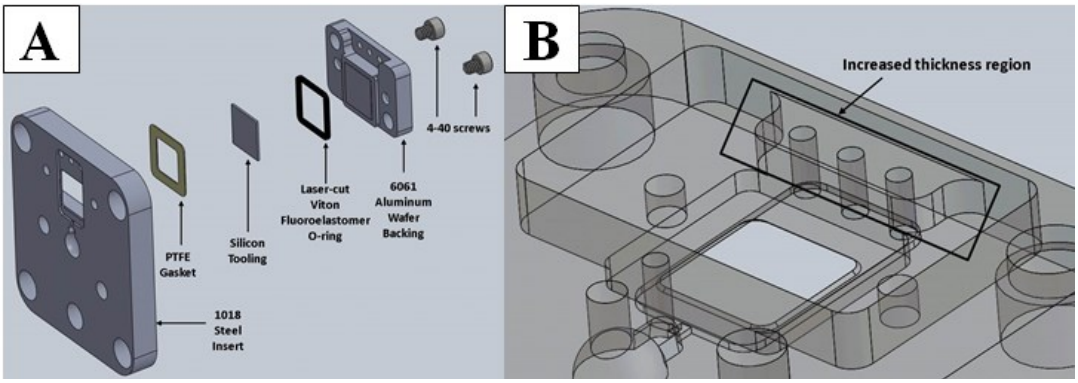

Figure 4-30: Revised clamp design incorporating steel into insert and custom laser cut Viton O-ring (A) and increased thickness region to ensure ejector pin hole does not deform.

4.2.6 Sprue Gate Insert

To address concerns with inconsistent replication and difficulty in reliably fixing silicon tooling within the clamp design, the mold cavity design was altered once more. A sprue gate cavity design was engineered, and silicon fixing was once again accomplished using epoxy. Figure 4-31 shows the sprue gate design. A part thickness of 0.03'' was used to match the typical thickness of a cell culture plate.

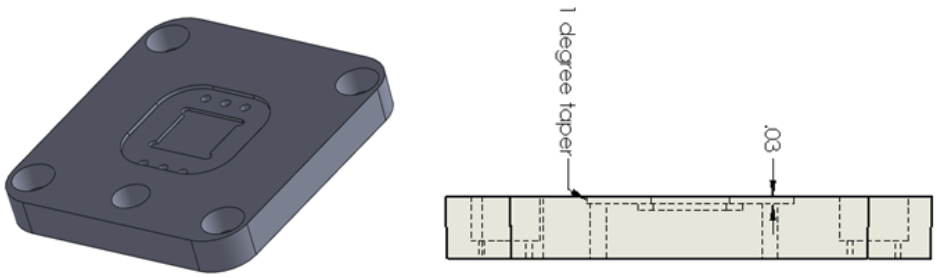

Figure 4-31: CAD model of sprue gate aluminum insert design with drawing showing key dimensional components (units are in inches).

4.2.7 Embedded cartridge heater assembly

Given previous difficulty in attaining consistent replication, an alternate assembly was manufactured which incorporated more localized heating to avoid the potential of uneven heating. In addition to enhancing condition uniformity across the cavity surface,

the use of localized heating is a much more economical compared to heating the entire mold in terms of energy cost and cycle time [**35**].

It is imperative that to precisely and quickly control mold temperature at the tooling cavity surface, the heating element and temperature sensor be in close proximity to the cavity surface. To address the issue, a cartridge heater was embedded in the aluminum insert containing the microfeatured tooling approximately 0.08'' from the cavity surface (Figure 4-32).

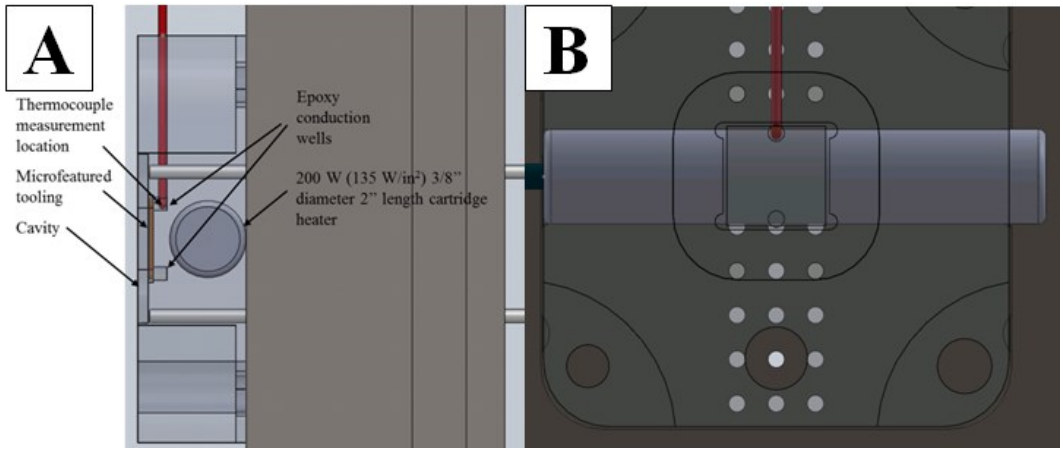

Figure 4-32: Side (A) and front (B) view of back half mold assembly containing aluminum insert with embedded cartridge heater.

The temperature of the insert was maintained by drilling a thermocouple hole that contacted the epoxy used to fix the silicon wafer into place. The new assembly successfully positioned the heating element and heating sensor in close proximity to the silicon inlay. Figure 4-33 shows the filling of epoxy into machined aluminum pockets followed by the fixing of the microfeatured silicon into the previously milled aluminum pocket. Therefore, a direct thermal connection between the thermocouple and the tooling is made, and rapid heat response can take place as a result.

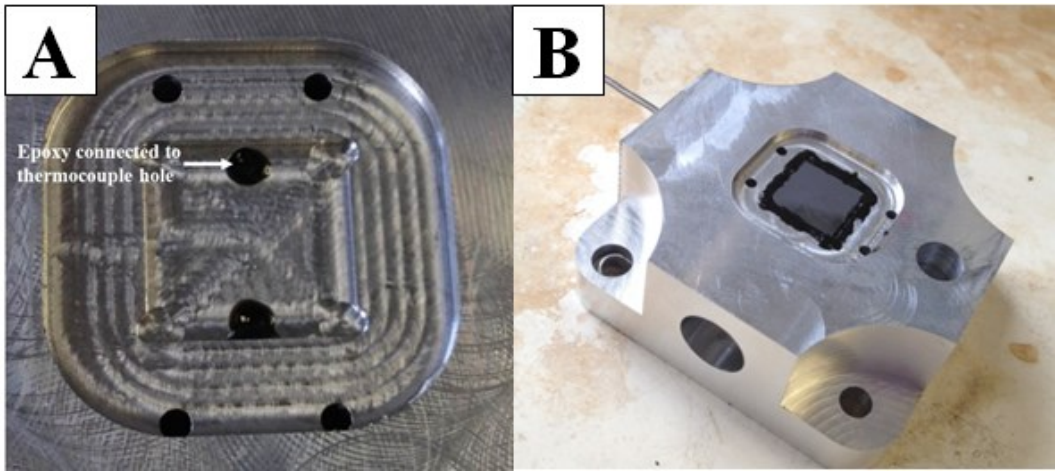

Figure 4-33: Image of epoxy-filled well to thermally connect silicon tooling with temperature sensing (A), and machined insert with epoxy-fixed silicon tooling (B).

4.2.7.1 Temperature Response Time Comparison

To quantify the response of temperature to time, the following equation can be used [**27**]:

$$P = \frac{M_v * \lambda * V[T_f - T_i]}{t} \qquad \text{Equation 4-1}$$

P is power, which is equal to the watt density of the cartridge heater multiplied by the effective heating surface area contact between the cartridge heater and mold. $M_v$is mold density, $V$is the volume of the mold element being heated, and $T_f$and $T_i$are the desired final temperature and starting mold temperature, respectively. In variotherm systems where rapid mold temperature fluctuations are necessary to achieve proper mold temperatures while maintaining reasonable cycle times, careful consideration of all parameters associated with Equation 4-1 must be considered. The difference in heating systems and material properties are outlined in Table 4-19.

When comparing the initial mold assembly (2 cartridge heaters embedded in the steel back half mold) with the revised assembly (cartridge heater embedded in the aluminum insert) a dramatic difference in response time can be realized, as shown in Figure 4-34. The localized heating and reduced volume results in less than half the amount of time to reach a desire temperature.

Table 4-19: Properties of Two Back Half Mold Heating Systems

Property	Back Half Mold (4130 Steel)	Aluminum Insert (6061)
Density (g/cm^3)	7.85	2.7
Specific Heat Capacity (J/g*K)	0.477	0.902
Volume (cm^3)	228.7	33.81
Cumulative Power Density of Cartridge Heaters used (W/cm^2)	63.6	21
Effective Heating Surface Area (cm^2)	17.95	5.99

The lower density and volume of the aluminum insert serves to offset the high power density and low specific heat of the steel-embedded cartridge heaters and thereby allow for a more rapid temperature change. In addition, the revised heating scheme lowers the temperature response time of the temperature control system due to the reduced distance from the heating element to the thermocouple sensor tip, as previously displayed in Figure 4-32. It should be noted that the steel-embedded cartridge heaters are involved with heating of the aluminum insert in the first assembly. However, to reach a desired mold temperature, the steel mold half must transfer heat to the aluminum part, and must be heated to provide such heat to the cavity surface.

The newer scheme avoids the necessity of heating the steel mold half and requires significantly less power to achieve the desired mold temperature change, a power usage of only 22% of the power used prior to the new design. An added benefit is the uniformity with which heating unit can provide heat, as the cartridge heater spans a majority of the microfeatured surface (shown previously in Figure 4-32B).

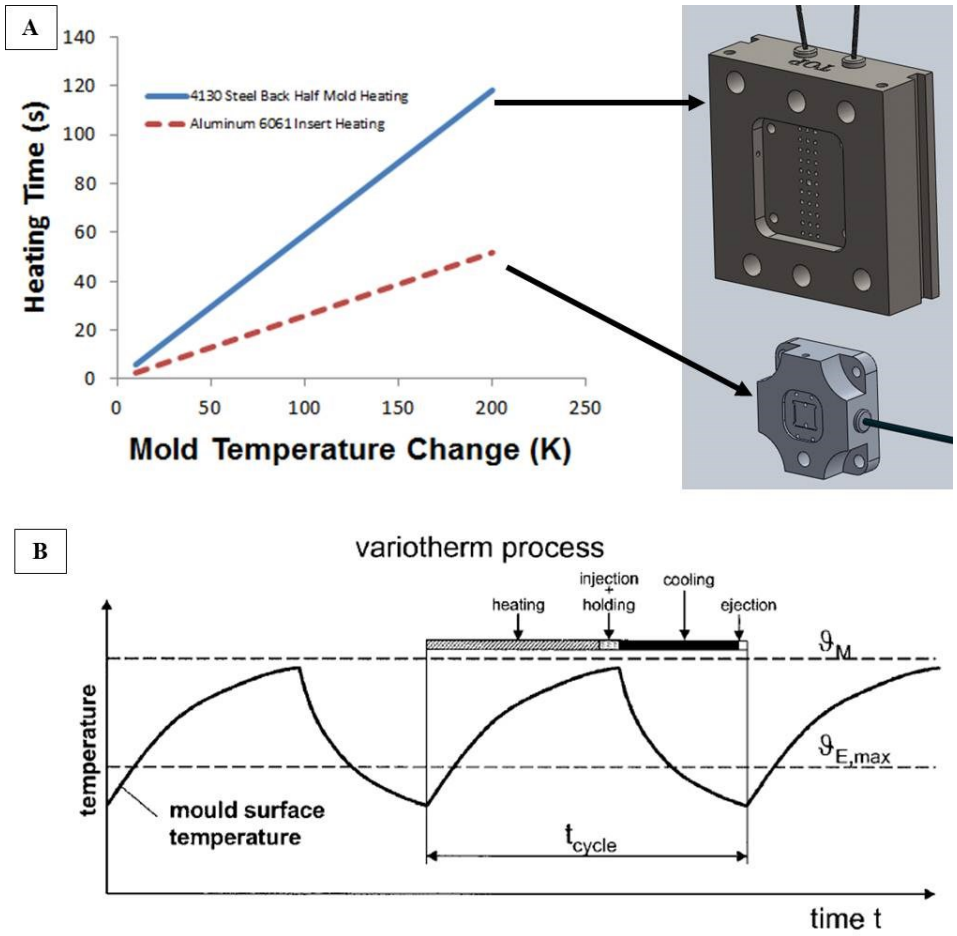

Figure 4-34: Comparison of temperature response time of old and new back half mold heating systems as a function of required mold temperature change (A) and variotherm process illustrating the heating portion of the variotherm cycle (B).

5 Micro-Injection Molding of Stem Cell Culture Substrates

The manufacturing of microfeatured substrates was executed with the intention of guiding stem cell development through the use of finely tuned microtopography. A detailed examination of the material, tooling, and processing was conducted to move closer to intentional stem cell fate control.

5.1 Polymers

All substrates used to interface with biological cells were composed of thermoplastic polymers due to use of the high-rate manufacturing technique of micro-injection molding. A vast array of polymers containing dramatic variations in material properties is commercially available. The ideal polymer will be biocompatible, allow for a high level of replication at the micro and nanoscale, be stiff enough for microfeatures to remain stable and compliant enough to avoid pillar rupture during ejection, and match the appropriate stiffness to mimic the compliance of the desired tissue type. A range of biocompatible polymers with a range of mechanical properties were explored to decipher both the appropriate material and manufacturable geometries.

5.1.1 Polystyrene

Polystyrene is an amorphous thermoplastic which is highly transparent, relatively brittle, and is fairly inexpensive. Its molecular structure is a carbon backbone with phenyl rings as pendent groups, as shown in Figure 5-1. Polystyrene can be atactic (no order to the phenyl groups), syndiotactic (diagonally orientated phenyl groups), or isotactic (phenyl groups all on the same side). It is most typical that PS is atactic.

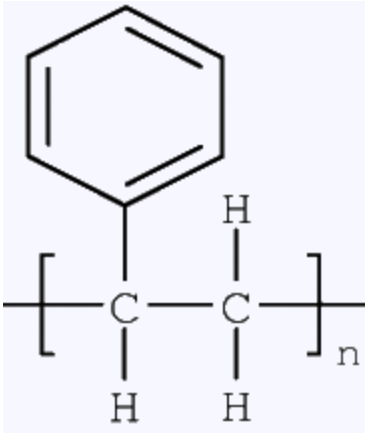

Figure 5-1: Polystyrene monomer.

5.1.1.1 High Heat Crystal Polystyrene (666D)

High heat crystal polystyrene (HHCP) is a heat resistant medium flow grade of polystyrene used in medical and packaging applications [**114**]. It is amorphous despite the name implying otherwise, as the phenyl pendent groups create steric hindrances between adjacent molecular chains. Its properties are given in Table 5-1.

Table 5-1: Properties of HHCPS (666D) **[**114**]**.

Property	Standard	Value
Melt Flow Index (200 °C / 5kg; g/10 min.)	ASTM D-1238	8
Heat Deflection Temperature (°C)	ASTM D-648	89
Specific Gravity	ASTM D-792	1.04
Shrinkage (%)	ASTM D-955	0.4-0.7
CTE (cm/cm/°C)	ASTM D-696	$9x10^{-5}$
Elastic Modulus (MPa)	ASTM D-638	3172
Poisson's Ratio	ASTM E-132	0.35

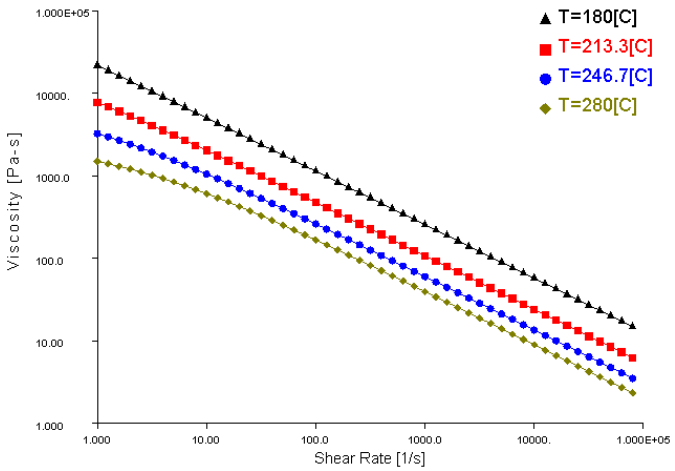

Figure 5-2: Viscosity as a function of shear rate for different melt temperatures for HHCPS. Values are based on the Cross-WLF model [115].

5.1.1.2 High Impact Polystyrene

Modifications can be made to polymers to tailor their properties to a given application. Monomers can be grafted into the existing polymer chains to create a copolymer. In the case of PS, which is normally brittle, polybutadiene can be grafted in to form a polymer with an added level of ductility. Polybutadiene, used most commonly for synthetic rubber in tires, is a flexible molecule characterized by its cis double bond structure, shown in Figure **5-3**.

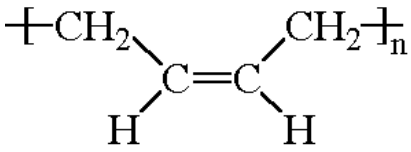

Figure 5-3: Butadiene structure grafted into polystyrene backbone for HIPS.

Some of the properties of HIPS is shown in Table 5-2. The difference in ductility between HIPS and HHCPS is most clearly seen when comparing their elongation values, which are 3 % and 50 % for HHCPS and HIPS, respectively. Other key differences are the melt flow indices and elastic moduli.

Table 5-2: Properties of HIPS (EC3600) [116].

Property	Standard	Value
Melt Flow Index (200 °C / 5kg; g/10 min.)	ASTM D-1238	2
Heat Deflection Temperature (°C)	ASTM D-648	88
Specific Gravity	ASTM D-792	1.04
Shrinkage (%)	ASTM D-955	0.4-0.8
CTE (cm/cm/°C)	ASTM D-696	$9x10^{-5}$
Elastic Modulus (MPa)	ASTM D-638	1200

5.1.2 Cyclic Olefin Copolymer

Cyclic olefin copolymer (COC) is an amorphous polymer synthesized from norbornene and ethylene through the use of a metallocene catalyst. The bulky norbornene side groups cause steric hindrance, thereby preventing any crystallization. It is used for a multitude of applications such as optics, electronics, and the medical device field. COC is highly transparent, has high heat resistance, and has a low level of water absorption.

Figure 5-4: COC Monomer containing ethylene and norbornene polymer segments

Important to the intended application is the ability of the polymer to withstand autoclaving, a heat intensive process that biological polymer parts used in biological laboratories is routinely exposed to prior to packaging. COC is used in many industries in the form of microplates (diagnostics), syringes (healthcare), and display screens (optics), among others. It has been used extensively in micro and nano-injection molding due to its high flow capacity. It also has low levels of birefringence, and is resistant to water absorption. Some properties of COC are shown in Table 5-3.

Table 5-3: Properties of TOPAS 5013-S4.

Property	Standard	Value
Melt Volume Flow Rate (cm^3/10 min. at 260 °C / 2.16; kg)	ISO 1133	48
Heat Deflection Temperature (°C)	ISO 75	130
Density (g/cm^3)	ISO 1183	1.02
Shrinkage (%)	-	0.4-0.7
Elastic Modulus (MPa; 1 mm/min)	ISO 527	3200
Poisson's Ratio	-	0.405
Glass Transition Temperature (°C)	ISO 11357	134

The flow behavior of COC is significantly higher compared to PS as evidenced by the dramatically lower viscosity at all processing temperatures and shear rates (Figure 5-5). While sensitive to shear rate, COC does not appear to be dramatically affected by changes in melt temperature.

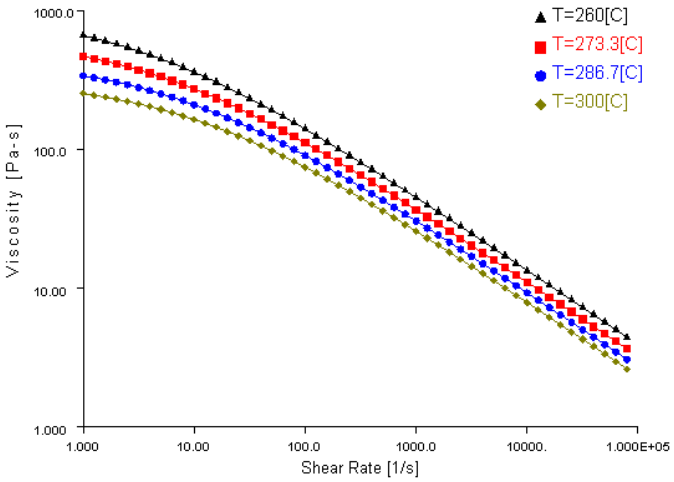

Figure 5-5: Viscosity as a function of shear rate for different melt temperatures for COC. Values are based on the Cross-WLF model **[**115**]**.

5.1.3 Low Density Polyethylene

Low density polyethylene (LDPE) is a semi-crystalline thermoplastic characterized by its long side chains [**117**]. Its rheological properties are considered

relatively difficult to model and characterize due to the irregularity of long branched chains [**118**]. The basic structure is shown in Figure 5-6.

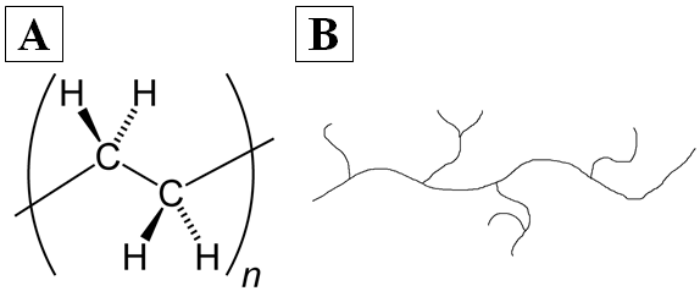

Figure 5-6: Chemical structure of polyethylene monomer (A) and typical branched morphology associate with LDPE.

Table 5-4 shows the properties of the specific resin used. LDPE has an intermediate stiffness compared to the high modulus PS and COC and low modulus thermoplastic polyurethane. As the name implies, the polymer has a low density, and its level of flow is greater than that of PS.

Table 5-4: Properties of LDPE (CP-851)

Property	Standard	Value
Melt Flow Rate (g/10 minutes, 2.16 kg at 190 °C)	ASTM D-1238(E)	20
Vicat Softening Temperature (°C)	-	92
Density (g/cm3)	ASTM D-792	0.923
Elastic Modulus (MPa)	ASTM D-638	100.7

5.1.4 Thermoplastic Polyurethane

Thermoplastic polyurethanes (TPUs) are linear block copolymers that are members of the group of thermoplastic elastomers (TPEs). They have been used as coatings, in footwear, and for flexible tubing [**119**]. TPEs are unique in that they contain

the mechanical properties of vulcanized rubber while still allowing for thermoplastic-based processing [**120**]. They contain soft and hard segments, in which the soft segment is actually above its glass transition temperature at the serve temperature [**117**]. More specifically, the hard regions are composed of short chain diols and diisocynates, while the flexible regions are composed of long chain diols (Figure 5-7). Hard segments are able to form two main types of crystalline structures which can result in multiple melting peaks when the material is heated [**121**]. The two structures are type I, which is related to a higher degree of phase mixing, and type II, which is involved with stronger phase separation. TPU soft and hard segments form distinct phases, in which phase separation is dependent on cooling rate and annealing conditions [**121**].

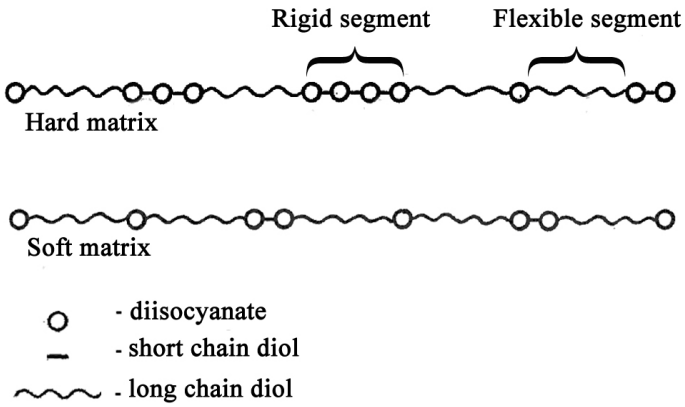

Figure 5-7: General structure of thermoplastic polyurethanes **[**122**]**.

The specific TPU used, Texin 985, is based on poly(tetramethylene glycol) (PTMG), butanediol (BDO), and 4,4'-methylenebis(phenyl isocyanate) (MDI) with a shore hardness of approximately 85A [**123**]. The chemical structure of all three molecules is shown in Figure 5-8. The hard segments of the polymer are comprised of BDO and

MDI, with PTMG representing soft segments [**124**]. The monomers are shown in Figure 5-8, and the synthesized TPU monomer is shown in Figure 5-9.

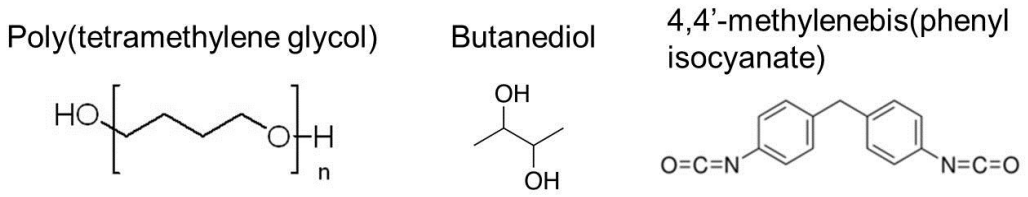

Figure 5-8: Monomers used to synthesize Texin 985.

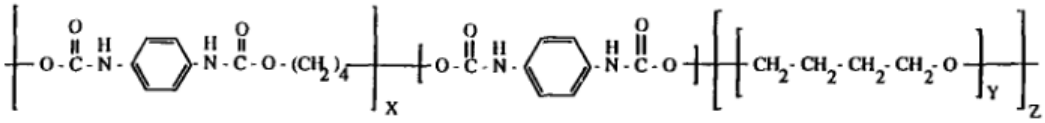

Figure 5-9: TPU polymerized structure **[**125**]**.

TPU is able to achieve both processability and compliance through a nanoscale multiphase molecular makeup. The combination of soft and rigid segments is linked together through the reaction of diisocyanates and difunctional polyols [**122**]. Polyurethane is typically a thermoset material, i.e., a cross-linked polymer processed by irreversible curing. However, the hard segments present in the thermoplastic polyurethane structure provide physical crosslinks (as opposed to chemical) [**120**]. Soft segments allow the material to be compliant, while hard segments serve as mechanical re-enforcement. The properties of the resin are shown in Table 5-5. TPU viscosity is much less than that of PS, but comparable to COC.

TPU viscosity appears to have be highly dependent on temperature at low shear rates, and less so for shear rates in excess of 10,000 s^{-1} (Figure 5-10). TPU viscosity is much less than that of PS but comparable to COC.

Table 5-5: Properties of TPU (Texin 985).

Property	Standard	Value
Vicat Softening Temperature (°C)	ASTM D-1525	80
Specific Gravity (°C)	ASTM D-792	1.12
Shrinkage (mm/mm)	ASTM D-955	0.008
Elastic Modulus (MPa)	ASTM D-638	12.5
Glass Transition Temperature (°C)	DMA	-46

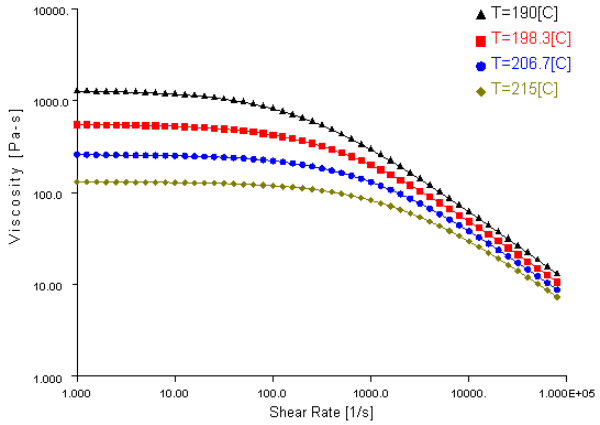

Figure 5-10: Cross-WLF plot of TPU (Texin 985) viscosity dependence on shear rate at different melt temperatures.

TPU properties can be tuned through the alteration of polymer chemistry and through processing induced changes. However, it should be noted that even optical processing conditions results in domains of very diverse shape and size [**126**].

5.2 Trial 1 – Polystyrene Study

Two types of polystyrene (PS) were used to mold polymer plates containing micropillars on the surface. PS is the industry standard for polymer cell cultureware due to its high transparency, acceptable mechanical properties, and low cost. Mold

temperature was the only varied parameter. Mold temperature is considered the most influential parameter associated with replication fidelity [**35**].

5.2.1 Experimental

The tooling used for the study was a single cavity mold containing a microfeatured silicon inlay fixed to the main cavity wall on the moving half of the mold (Figure 5-11). Tabs were added to the edges for part ejection, the part thickness was 0.04'', and a short runner and gate connecting the sprue to the part was used (Figure 5-12). The design resulted in an impingement flow into the microfeatures. Impingement flow is the movement of the main melt flow perpendicular to the major dimension of the microfeatures.

In comparing this particular flow type with parallel flow, conflicting conclusions have been made as to which filling mode results in better replication [**42**,**94**]. The potential drawback of a parallel flow design is the presence of gate vestige in the middle of the part as opposed to the gate remnants occurring on the edge of the part. The advantage of the parallel flow design is the melt velocity is traveling in the direction of the inlet and does not need to turn to fill the microfeatures.

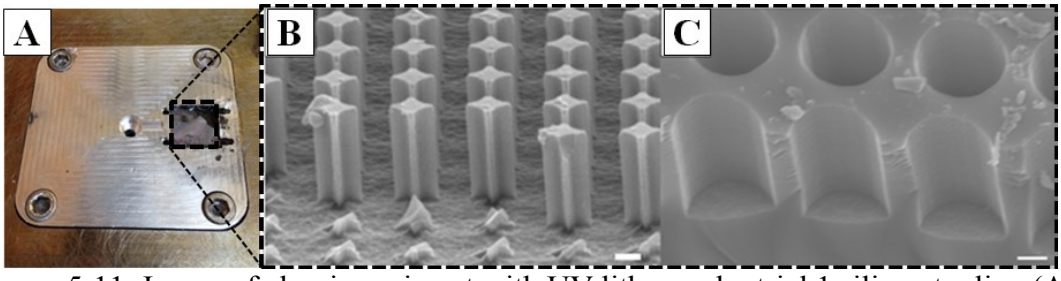

Figure 5-11: Image of aluminum insert with UV lithography trial 1 silicon tooling (A), micrograph of Si 3 μm spaced orthogonal array of micropillars (positive tooling; B) and 4 μm spaced orthogonal array of microchannels (negative tooling; C).

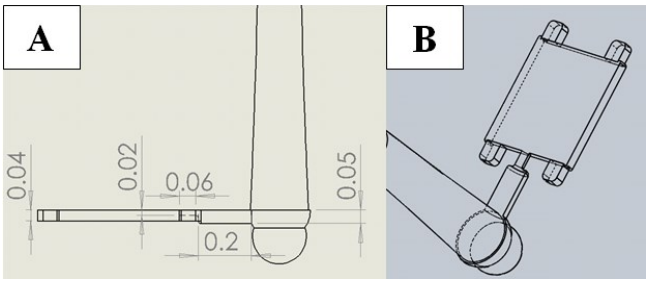

Figure 5-12: Schematic of molded part dimensioned (A) and with an isometric view (B). Units are given in inches.

Table 5-6: Injection molding settings used for trial 1.

Property	Value
Mold Temperature (°C)	104.4, 126.7, 148.9
Injection Velocity (mm/s)	80
Ejection Temperature (°C)	93.3
Barrel Temperature (°C)	143.3 (throat) – 237.8 (nozzle)

The molding conditions were chosen in accordance with recommended values [**114**,**116**], except for mold temperature, which was increased beyond the recommended range to facilitate microchannel filling. HHCPS was molded onto both positive and negative tooling. HIPS was only molded onto negative tooling, thereby creating positive features. Molding was executed through the use of a Nissei AU3E 3-ton 2 stage micro-injection molding machine. This particular machine was used for the duration of the molding trials conducted.

5.2.2 Results

The change in mold temperature imparted dramatic replication differences for both polymers and tooling used. Figure 5-13 shows a reduction in replication with an increase in mold temperature, as the diamond-shaped cavities appear to be filled in at

mold temperatures of 126.7 ^{o}C and 148.9 ^{o}C. The result is surprising, as it is usually the case that an increased mold temperature enhances replication. The additional heat provided by higher mold temperatures may have allowed polymer molecules to remain mobile and fill the concave regions upon part ejection from the mold. Another possibility is that the silicon pillar tips may have partially bonded with the polymer, thereby stretching the regions in contact with the pillars during part ejection.

At a mold temperature of 148.9 ^{o}C, there is a distinct development of "seashell" multi-layer structures, as shown in Figure 5-13C. The findings suggest that for positive tooling features, higher mold temperatures may be unnecessary and even deleterious to the replication process.

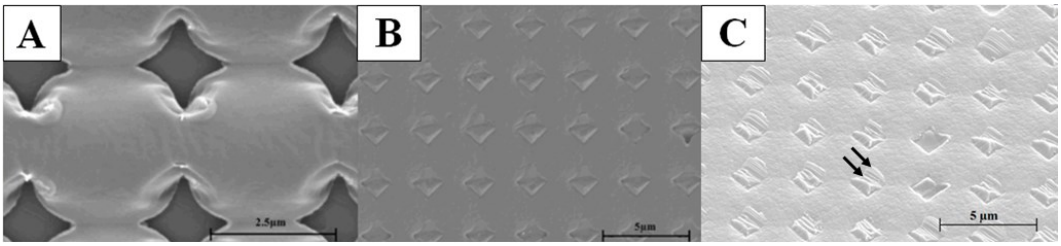

Figure 5-13: Micrograph of HHCPS using positive tooling and mold temperature of 104.4 ^{o}C (A), 126.7 ^{o}C (B), and 148.9 ^{o}C (C). Arrows indicate the presence of a "seashell" pattern on a diamond shape.

Negative microscale tooling, which includes the flow of polymer into microscale inlets and through channels, requires higher mold temperatures to maintain a low enough viscosity for the polymer to penetrate the relatively small region prior to solidification. Figure 5-14 shows replication of both types of PS polymers, in which neither show significant replication. Evidence of micropillar formation is minimal for HHCPS, in which witness circles are present at the surface.

There appears to be tensile fracture occurring for the HIPS pillars. It is unexpected that HIPS appears to have filled better than HHCPS considering that it has an MFI of only ¼ that of HHCPS (MFI; higher value indicates a high flow material). It is important to note, however, that the test to determine MFI is performed at one specific temperature and under one particular load. Thus, different loading and temperature conditions, such as those used to mold the given parts, could very well result in different viscosity values.

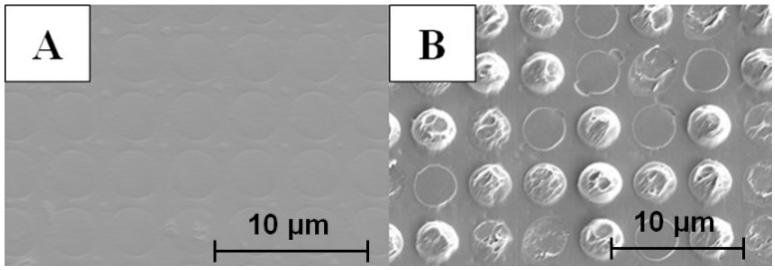

Figure 5-14: Micrographs of HHCPS (A) and HIPS (B) surfaces molded using a mold temperature of 104.4 ^{o}C. HIP appears to have regions of damaged pillars.

A mold temperature increase to a value beyond the glass transition temperature of both polymers resulted in enhanced replication, as shown in Figure 5-15. For both materials, the pillars appear to be stretched, with some being stretched to the point of failure. The height of pillars for both materials significantly exceeds the microchannel depth, indicating that all pillars were in some manner distorted during ejection.

Although consistency was compromised due to excessive pillar tensile stresses, there were regions of consistent pillars present on the surface (Figure 5-16). The inconsistency across the surface is attributed to the variant pressure and temperature conditions across the surface of the tooling. One of the concerns associated with the inherent uni-directional flow associated with injection molding (polymer always initially

exits injection unit in one direction) is the ability to approach uniform conditions across the intended region to be filled. Inconsistencies become immediately apparent in the case of micro-arrays, as the features function as micro-scale filling sensors during molding. Despite the lack of a completely uniform network of pillars for the given study, it is still valuable to observe the general effect of processing conditions on feature replication.

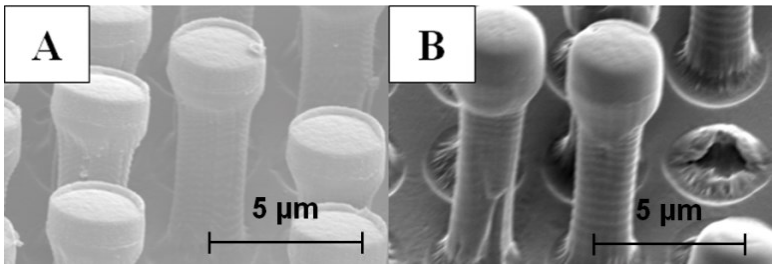

Figure 5-15: Micrographs of HHCPS (A) and HIPS (B) surfaces molded using a mold temperature of 126.7 ^{o}C. Pillars appear to have mushroom shape with tensile stress applied.

Mold temperatures of 148.9 ^{o}C resulted in greater heights but reduced consistency, as shown in Figure 5-17. In the case of HHCPS, all molded pillars were collapsed. HIPS pillars that weren't fractured and removed remained standing, and withstood significant elongation. Pillar diameters are dramatically reduced with the increase in height, which is the expected result of the Poisson effect. Figure 5-18 quantifies the dramatic effect of mold temperature on pillar height. HIPS is able to elongate to a greater extent due to its relatively flexible molecular composition in comparison to the more brittle polystyrene. The same resistance to brittle failure allows the material to also avoid collapse.

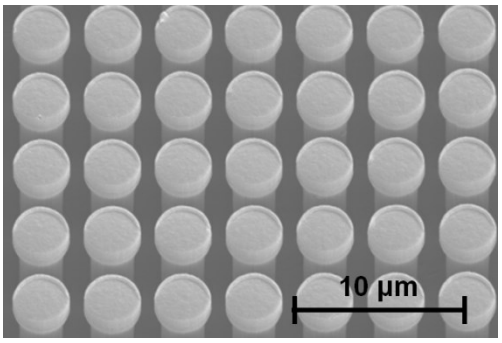

Figure 5-16: Micrograph of microfeatured surface. Part was molded using a mold temperature of 126.7 ^{o}C

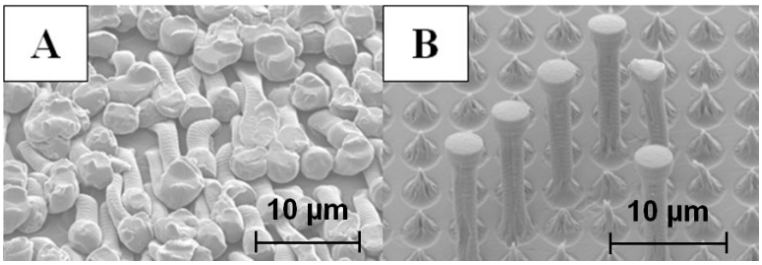

Figure 5-17: Micrographs of HHCPS (A) and HIPS (B) surfaces molded using a mold temperature of 148.9 ^{o}C. HHCPS pillars have all collapsed, while HIPS pillars remain standing. A majority of HIPS pillars have been fractured due to excessive tensile stress.

HIPS is able to withstand additional strain at higher mold temperatures due to the temperature effect on strain, as shown in Figure 5-19. Although significant heights were obtained, it would be difficult to control replication across the entire surface, especially with an increased strain of the pillars whose cylindrical geometry offers very low resistance to bending forces. Nevertheless, a strain of ca. 366% was observed, assuming that complete fill occurred prior to ejection. Such strain is dramatically higher than reported values of 50 % [**114**]. It should also be noted that a HHCPS pillar elongation of ca. 230 % occurred at the middle mold temperature. It is believed that either some microscale enhancement of plasticity is occurring.

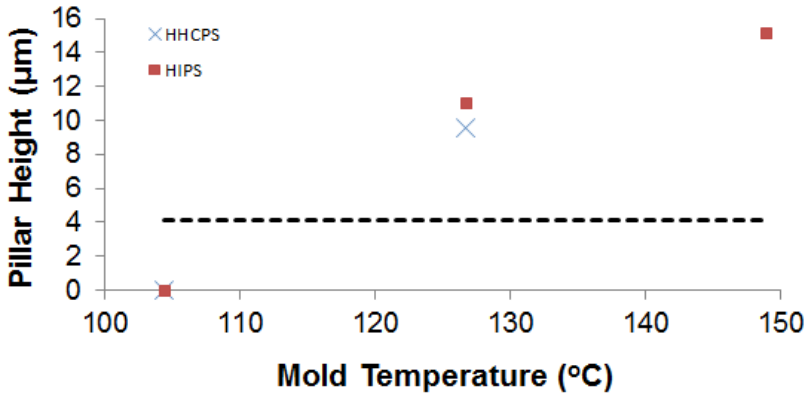

Figure 5-18: Pillar height of HHCPS and HIPS as a function of mold temperature. Dotted line indicates polymer with perfect replication.

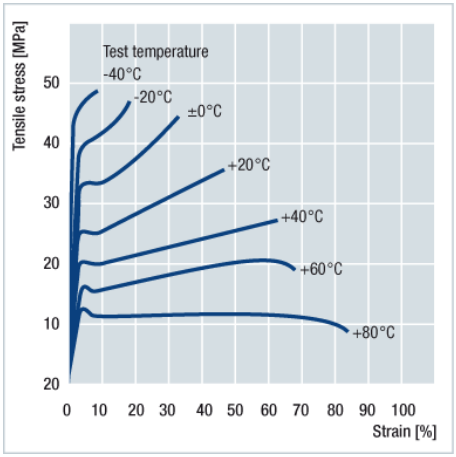

Figure 5-19: Effect of temperature on amount of strain [127].

In using an actively heated but passively cooled molding system, the cycle time increased to a great extent with the use of higher mold temperatures, as shown in Figure 5-20. The balance between the use of higher mold temperatures for increased replication quality and maintenance of reasonable cycle times for low cost production is always a concern for molding, and heating and cooling mold control plays a vital role in determining such a balance [**36**]. Due the relatively low thermal inertia of the tooling used (i.e., slow response to set temperature changes), the cycle time became quite long at higher mold temperatures.

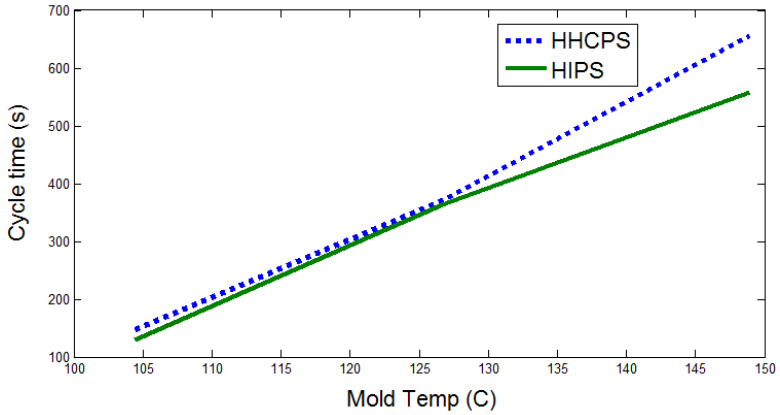

Figure 5-20: Cycle time as a function of mold temperature during filling. Use of the variotherm process with passive cooling results in longer cooling times.

5.2.2.1 Focused Ion Beam (FIB) Investigation of Microchannel Profile

The presence of a mushroom-shaped profile led to further questioning of the microchannel profile, as it was expected that the general pillar shape would be a straight constant diameter channel. Focused ion beam (FIB) was used to remove a specific region of silicon to reveal the interior of the microchannels. FIB is a technology which employs an ion source capable of physically bombarding a sample in a similar fashion to a scanning electron microscope. The key distinction is the use of ions (charged atoms) instead of electrons.

For the given study, a FEI Strata Dual Beam 235 FIB was used. The system allows for the simultaneous use of both beams. Gallium (Ga^{2+}) ions were used to dig a trench into the sample, while the electron beam was used for imaging. A trench was created such that propagation of the hole commenced perpendicular to the channel vertical cross-section (i.e., circle). Figure 5-21 shows an apparent etching through at the bottom of the channel, indicating the presence of a widened bottom.

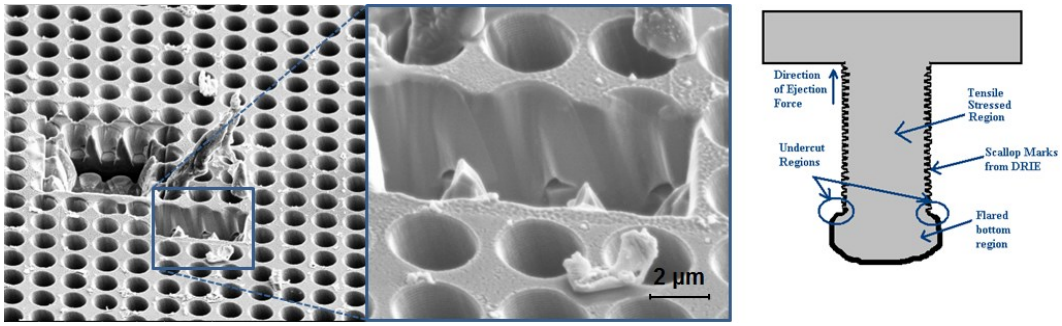

Figure 5-21: Micrographs of region exposed to gallium ions to reveal widening of profile at bottom of microchannels (inset) and schematic of microchannel geometry highlighting mechanical interaction between silicon and polymer (right).

5.3 Polystyrene Injection Velocity / Mold Temperature Study

A study on polystyrene replication in response to various molding parameters was conducted to gain a deeper perspective of processing effects on replication of individual microfeatures and microfeature consistency across the surface of the substrate. Previous research involving the replication of an array of micro/nanostructured surfaces has encountered inhomogeneous replication [**40**,**34**,**36**]. Injection molding is a process that inherently imparts variant conditions across the cavity surface, as polymer part filling is a highly anisotropic process. The objective in optimizing part design and processing is to obtain uniform conditions across the molding cavity. When microfeatures are present at the main cavity walls, the variation in physical conditions across the surface can become apparent in the form of inconsistent replication.

The objective of the study was to further observe the effects of molding conditions on replication and to achieve higher replication as a result of using lower aspect ratio microfeatures.

5.3.1 Experimental

5.3.1.1 Mold Assembly

A clamp gate aluminum insert design was used to fix silicon tooling in place for use in molding. Microfeatured silicon tooling fabricated in section 4.1.2.5 was used. Ejector pins were positioned symmetrically in the lateral direction to uniformly eject the part.

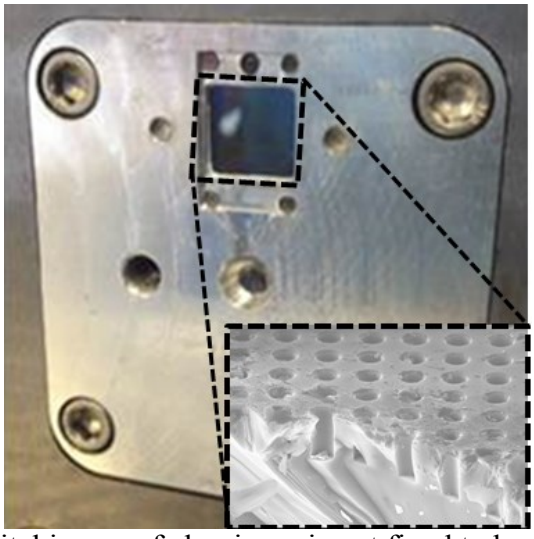

Figure 5-22: Digital image of aluminum insert fixed to back half mold with microfeatured tooling used (inset).

5.3.1.2 Molding

To obtain a better understanding of the effects of processing on polymer replication, mold temperature and injection flow rate (i.e., velocity) were altered. The two main characteristics observed were degree of replication and replication consistency. When attempting to fabricate a part with a microfeature surface density of > 1 million features / cm^2, the difficulty lies in filling all such structures evenly and prior to premature solidification. To observe solidification activity, parts were molded with a

mold temperature below and above the polymer T_g. Polystyrene (666D) was the polymer used for the given study. Molding parameters are shown in Table 5-7.

Table 5-7: Molding conditions for trials 1 & 2. T_{barrel} are $T_{nozzle}/T_{plunger}/T_{joint}/T_{screw,\ front}/T_{screw,\ rear}$.

Trial #	T_{mold} (°C)	T_{barrel} (°C)	Flow Rate (cm^3/s)	P_{hold} (MPa)	P_{back} (MPa)
1	65.6	232.2 / 226.7 / 226.7 / 221.1 / 201.7	7.54	19.3	4.1
	76.7		2.51		
	76.7		5.03		
	76.7		7.54		
2	104.4	248.9 / 243.3 / 232.2 / 221.1 / 201.7	2.01		
	104.4		4.02		
	104.4		6.03		

The injection time (filling time + holding time) was maintained at 8 s to ensure the part was packed to the point of gate freeze, cooling time was held constant at 20 s to ensure full part solidification prior to ejection, holding pressure was maintained at a relatively low value of 19.3 MPa to compensate for shrinkage without unnecessary applied force, and a low back pressure of 4.1 MPa was used to limit excessive polymer shear during the filling of a shot. Barrel temperatures were maintained in the middle of the recommended range for the particular material being used [**114**].

For trial 2, the mold temperature was held constant above T_g during filling and packing, and flow rate was varied. Only three different conditions were used for trial 2 due to mold temperature being the only parameter being varied. To further facilitate microfeature filling, the barrel temperatures were increased. The cooling time was dictated by the time necessary for the mold to cool to a temperature of 82.2 °C.

Surfaces were characterized via microscopic analysis, in which replication and microfeature consistency were assessed. Specific regions of the microfeatured surface, specified in Figure 5-23, were analyzed to provide a comprehensive understanding of the effects of molding parameters and macroscopic geometric location within the main cavity.

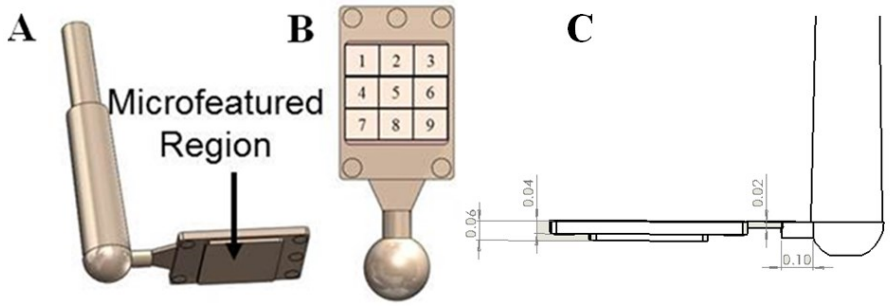

Figure 5-23: CAD model of part illustrating location of the microfeatured region (A) the 9 distinct imaging locations (B), and dimensioned polymer part with attached sprue (C).

Replication as a function of proximity to the gate was analyzed, in which region 8 corresponded to "gate," region 5 corresponded to "middle," and region 2 corresponded to "end."

5.3.2 Results

The degree of replication and consistency was highly dependent on processing parameters. As expected, mold temperature, especially when increased to values above PS T_g (for 100 ^oC), significantly impacted results.

5.3.2.1 Trial 1: $T_{mold} < T_{g, PS}$

For lower mold temperatures (trial 1), replication was more sensitive to mold temperature changes than flow rate variation. Figure 5-24 show the dramatic difference in replication with an increase in flow rate. However, replication is not affected by flow rate when $T_{mold} < T_{g, PS}$ (Figure 5-25).

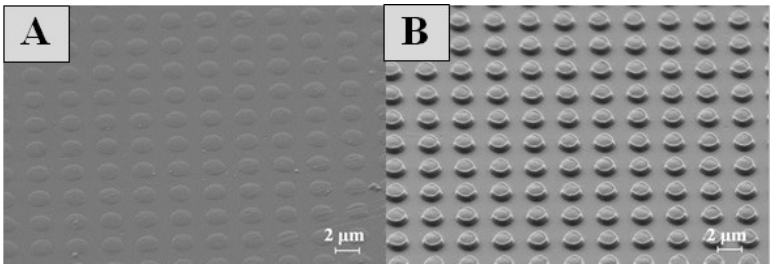

Figure 5-24: Trial 1 micrographs of topography near gate of T_{mold} = 65.6 ^{o}C (A) vs. T_{mold} = 76.7 ^{o}C at identical flow rate of 7.54 cm^3/s.

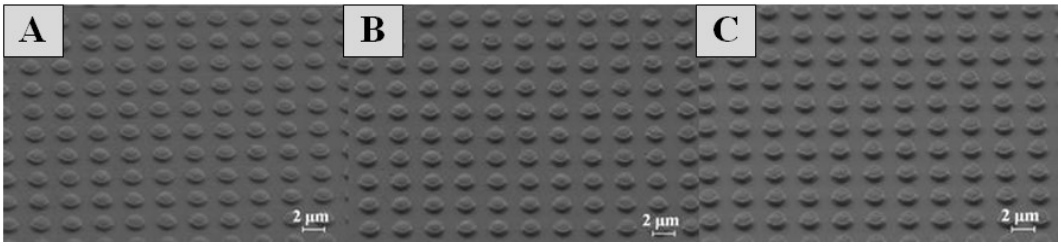

Figure 5-25: Trial 1 micrographs of topography near gate showing the effect of flow rate on replication at T_{mold} = 76.7 ^{o}C. Substrates were molded with: Q_{inj} = 2.51 cm^3/s (A), 5.03 cm^3/s (B), and 7.54 cm^3/s (C).

Replication for all trial 1 conditions was relatively low even for the tallest pillars (ca. 17% replication). The increase in replication mold temperature is approximately 0.015/^{o}C (replication quotient: ΔT), which is comparable to trends observed for nanofeatured DVDs (0.02/^{o}C [**128**]). For trial 2, a larger range of topography variation was observed.

5.3.2.2 Trial 2: $T_{mold} > T_{g,\,PS}$

At mold temperatures above the glass transition temperature of a molded polymer, the heat transfer from polymer to mold wall is reduced and polymer solidification is delayed, thereby enabling a greater degree of fill. In trial 1, the mold temperature used may have resulted in a specific solidification time that prevented the melt from penetrating beyond a certain distance within the microchannels regardless of melt flow velocity. In trial 2, the delay in solidification appears to provide the opportunity to fill the microchannels to a greater extent. Moreover, replication exhibits sensitivity to changes in flow rate at the elevated mold temperature. At a relatively low velocity, replication is dramatically enhanced, but at the expense of feature height consistency (Figure 5-26).

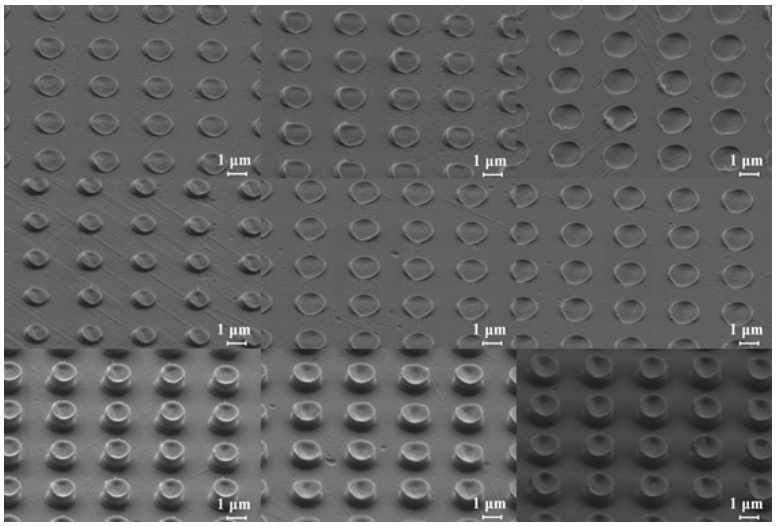

Figure 5-26: Trial 2 micrographs of 9 regions previously shown in Figure 5-23B molded at low flow rate.

Replication is further enhanced with increasing flow rate, reaching replication quotients of 0.267 and 0.609 for the intermediate and high flow rates, respectively. However, the increase in flow rate also imparts higher degrees of replication anisotropy

across the surface, as pillar heights are dramatically different at the highest flow rate (Figure 5-29). The intermediate flow rate appears to create the most consistent network of pillar heights. Thus, there appears to be an optimum flow rate at which the degree of replication and the level of consistency can be balanced.

In terms of replication beyond simple height measurements, the pillars exhibit a diverse array of shapes, especially at their tips. The tip region is a useful indication of the polymer flow history, as it directly relates to the microfluidic flow front at the point of solidification.

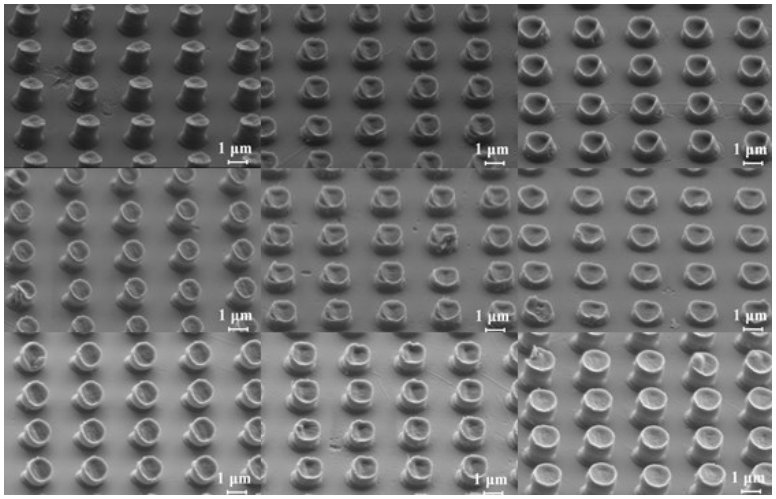

Figure 5-27: Trial 2 micrographs of 9 regions of PS previously shown in Figure 5-23B molded at intermediate flow rate.

Typically, the shorter pillars have relatively concave tips, while the concavity appears to be reduced with increasing replication. The tip surface could be the result of polymer slip along the microchannel surface. Yao et al previously determined that at a size scale of a few microns or less, wall stress is too high to allow for the "no-slip" condition for polystyrene, and wall slippage should occur [**45**]. Potentially, the enhanced

flow permitted through wall slip could allow the polymer near the wall to a greater extent in relation to the center of the channel.

The uneven tip surface could also be due to the presence of trapped air inside of the cavity. Traditional injection molding involves venting of air from the tooling cavity through either shallow channels which run along the tooling surface at the parting plane or through the clearance between the ejector pins and ejector pin holes. However, designs which include microcavities with relatively high aspect ratios present a challenge, as the air can get trapped inside the microchannels as the melt flows across the main cavity surface.Another potential cause for the pillar tip shape is the presence of a micro sink mark, in which the core of the pillar is insulated from the relatively cooler walls of the microcavity. When the hotter internal polymer cools, it shrinks and can pull the solidified polymer towards the center of the feature.

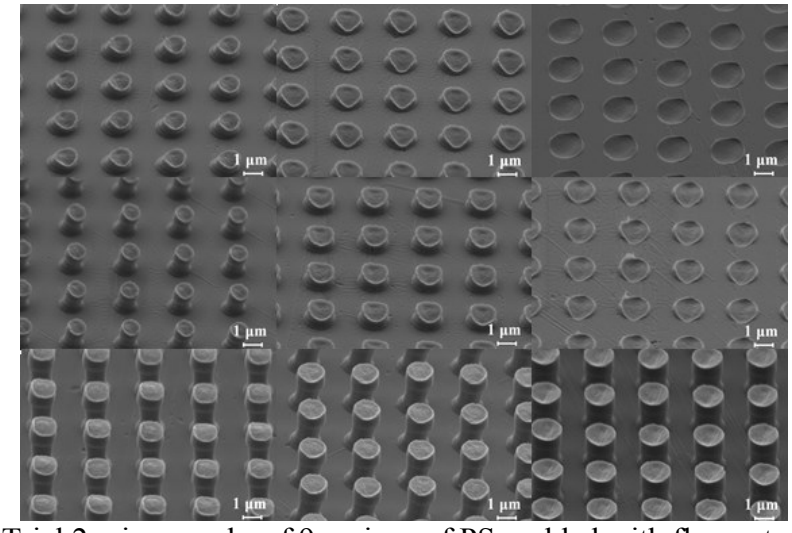

Figure 5-28: Trial 2 micrographs of 9 regions of PS molded with flow rate of 6.03 cm^3/s.

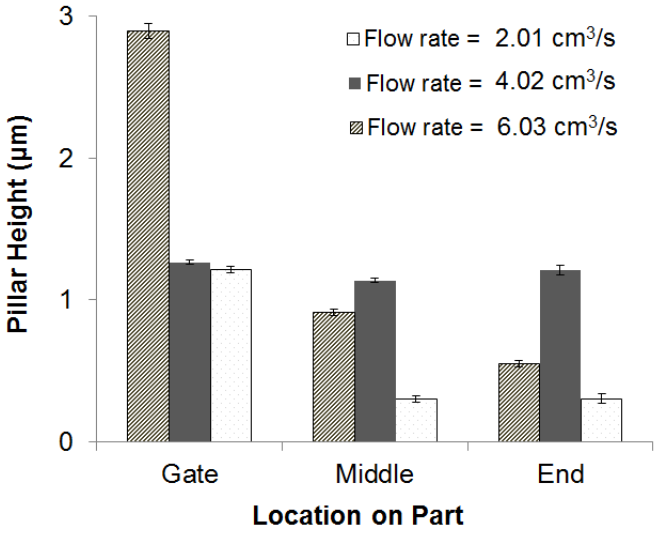

Figure 5-29: PS Pillar height as a function of flow rate at different locations on microfeatured surface.

Within specific regions, microfeatures display uniform geometrical properties, which indicates the presence of uniform molding conditions in localized areas (Figure 5-30). Due to the lack of a taper angle of the tooling and the nano-undercuts present from scalloped microchannels, the pillars become slightly stretched due to the friction between pillar and microchannel during demolding. However, the microfeature deformation seen here is dramatically reduced from pillar extension observed during the study reported in section 5.2.

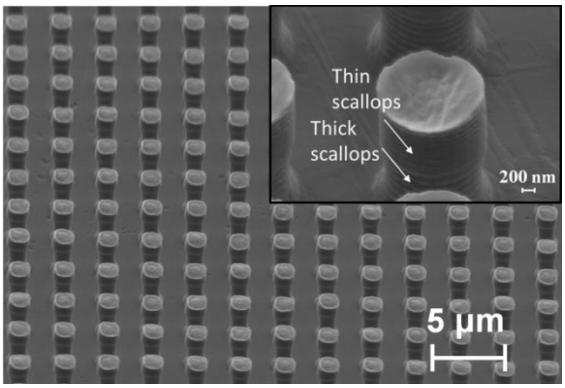

Figure 5-30: Micrograph of uniform replication near gate. Differences in pillar scallop thickness along the vertical surfaces indicate tensile deformation of the microfeatures.

If the amount of stretching could be reliably controlled, as has been achieved previously [**129**], stretching could be a benefit to the realization of higher aspect ratios. However, caution must be taken to ensure the stretching deformation does not impart deleterious microfeature properties for its given function.

5.3.2.3 Conclusion

Mold temperature and injection velocity were both shown to alter replication of the microfeatures. Injection velocity does not significantly affect replication at mold temperatures below polymer T_g. Filling is enhanced by flow rate at mold temperatures above T_g, giving rise to viscosity low enough to support enhanced microcavity flow. Certain microscale effects, such as trapped air, locally higher viscosity, or wall slip are thought to be responsible for the characteristics of the pillar tips. With regards to the microcavity walls, scallops present from etching imparted a certain level of tensile stress on micropillars. Maximum replication was 0.61, which occurred at the highest mold temperature and injection velocity.

5.4 Low Density Polyethylene L9 Taguchi Array

To create a polymer surface with a high degree of compliance, the use of high aspect ratio topography alone may not be sufficient enough to reach values analogous to biological tissue. Thus, a polymer in a higher inherent level of compliance (i.e., lower elastic modulus) was used. Low density polyethylene (LDPE) was molded, and robust experimentation was used to determine processing effects on replication.

5.4.1 Experimental

The assembly used was the same as that in section 5.3, with the differences being silicon tooling and the presence of tabs on the part that interface with the ejector pins (instead of the cavity being a rectangular plate, Figure 5-31). Silicon tooling with relatively high aspect ratio negative microfeatures was used to allow for a large range of pillar heights to assess the effects of molding parameters on replication. An L9 Taguchi orthogonal array was used to determine the effects and magnitude of molding parameter changes on replication.

Experimental efficiency is becoming increasingly valuable in a fast-paced industrial manufacturing environment. To maximize experimental results, a specific method of testing can reduce the number of experiments run. Taguchi orthogonal arrays take into account the interactions between variables and determine which controllable parameters most affect the measured metric and which level of the parameter yields the best result. The use of Taguchi arrays prevents the need for additional costly instrumentation which would otherwise be necessary to more closely monitor the given manufacturing process and bring it into control [**130**]. Over the course of the given research, multiple arrays are used to provide informative and expansive understanding of the effects of various molding parameters on micromolding replication.

Parameters previously mentioned to impact micromolding fidelity were used: mold temperature, nozzle temperature, injection velocity, and holding pressure (Table 5-8) [**34**].

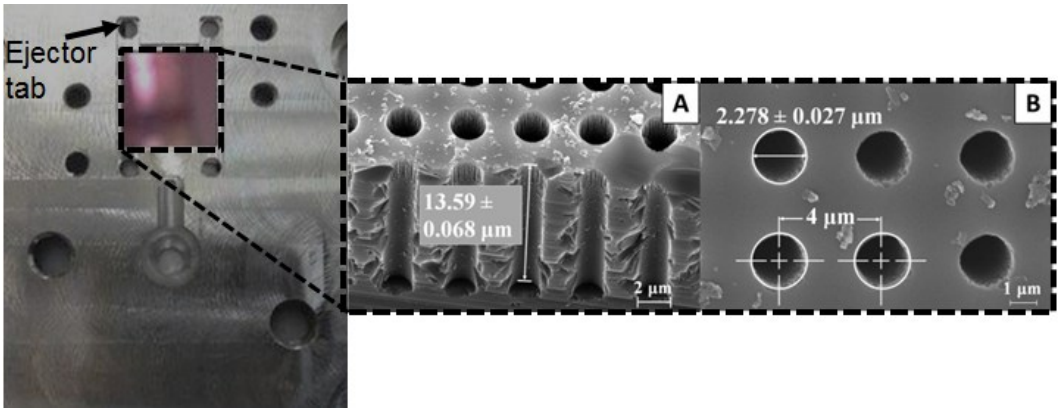

Figure 5-31: Aluminum insert and tooling (inset) used for LDPE orthogonal array study.

Relatively low injection velocities were used to avoid excessive impact forces to the silicon tooling, holding time was maintained for a long enough time to ensure gate solidification, and mold temperatures just below the softening point were used to facilitate a higher degree of replication while attempting to avoid pillar fracture.

Table 5-8: Experimental molding parameters used for L9 Taguchi Array.

Process Parameter	Value
Nozzle Temperature (°C)	135/140.6/146.1
Mold Temperature (°C)	71.1/76.7/82.2
Injection Velocity (mm/s)	15/25/35
Holding Pressure (MPa)	36.54/39.3/42.06
Holding Time (s)	10
Cooling Time (s)	30

Maximum replication was assessed through pillar height measurements near the gate, in which five measurements were taken. Replication as a function of proximity from the gate was also assessed by imaging the gate, middle, and end regions of the sample containing the highest degree of replication (Figure 5-32).

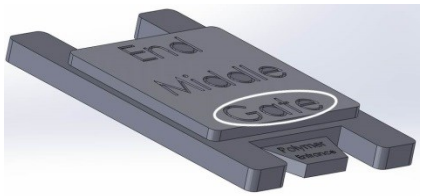

Figure 5-32: CAD model of measurement regions. L9 measurements were taken near gate.

To qualitatively analyze cellular response to the presence of LDPE topography, cell culture immunocytochemistry (ICC) was used to observe hMSC morphology. hMSCs on LDPE topography were compared to tissue culture treated glass controls.

LDPE samples were embedded in 1.5% agarose and sterilized with 0.3% hydrogen peroxide. Following sterilization, samples were washed with 1X phosphate buffered solution (PBS), incubated for 24 h in Mesenchymal Stem Cell Basal Medium (Lonza) at 37°C and 5% CO_2. The hMSCs were formalin fixed and analyzed for actin/vinculin expression. Rhodamine phalloidin was used to visualize actin and Anti-vinculin was used to visualize focal adhesions. Nuclei were stained with Hoechst 33258.

5.4.2 Results

5.4.2.1 Replication

Average recorded pillar heights ranged from 0.88 ± 0.03 μm to 8.724 μm ± 0.15 (RQs of 0.065 and 0.642, respectively), with the highest individual measurement being 9.13 μm (RQ = 0.672).

Mold temperature had the most dramatic impact on replication, showing a general trend of higher levels of replication with an increase in temperature. Nozzle temperature, which affects polymer melt temperature, had a substantial, albeit lesser, impact on replication. No substantial trend was observed with regards to nozzle temperature

variation. Higher injection velocities had a positive influence on pillar height, while holding pressure changes resulted in insignificant differences. Holding pressure differences used for the current study do not span a relatively smaller range, which may be the cause for the insignificance.

Table 5-9: Pillar height measurements for 9 Taguchi conditions.

Condition	Mold Temperature (°C)	Nozzle Temperature (°C)	Injection Velocity (mm/s)	Holding Pressure (MPa)	R1	R2	R3	R4	R5	Ave.
1	71.1	135	15	36.54	1.84	1.84	1.91	1.91	1.91	1.882
2	71.1	140.6	25	39.3	0.82	0.94	0.88	0.82	0.94	0.88
3	71.1	146.1	35	42.06	2.01	1.94	2.14	1.84	2.83	2.152
4	76.7	135	25	42.06	2	2.59	2.59	2.59	2.77	2.508
5	76.7	140.6	35	36.54	3.02	3.12	3.12	3.04	2.38	2.936
6	76.7	146.1	15	39.3	1.9	2.25	1.87	1.98	2.16	2.032
7	82.2	135	35	39.3	8.52	9.13	8.86	8.86	8.25	8.724
8	82.2	140.6	15	42.06	2.91	2.09	2.79	2.2	2.39	2.476
9	82.2	146.1	25	36.54	5.07	6.19	3.15	3.04	5.87	4.664

Polymer replication, in addition to being processing and mold cavity design dependent, is also material dependent. Depending on the material chemistry, molded polymers can be more sensitive to certain parameters over others. In the case of semi-crystalline materials, such as LDPE, processing conditions dictate the crystallization behavior, which will subsequently alter surface properties (in addition to the geometrical surface modifications made through micro-injection molding) [**131**].

Figure 5-34 shows the variation in replication for the 9 molding trials. Microfeatures with greater heights exhibit a certain degree of curving, which could be due to the relatively low stiffness of LDPE.

Replication was found to be dependent on proximity from the gate, with a similar trend to the previous study with polystyrene (section 5.3). Figure 5-35 shows the discrepancy in pillar height across the part. It is assumed that at the moment the main cavity fills, a higher level of pressure is available near the gate, allowing for a deeper infiltration of polymer into the microchannels in comparison to regions farther away.

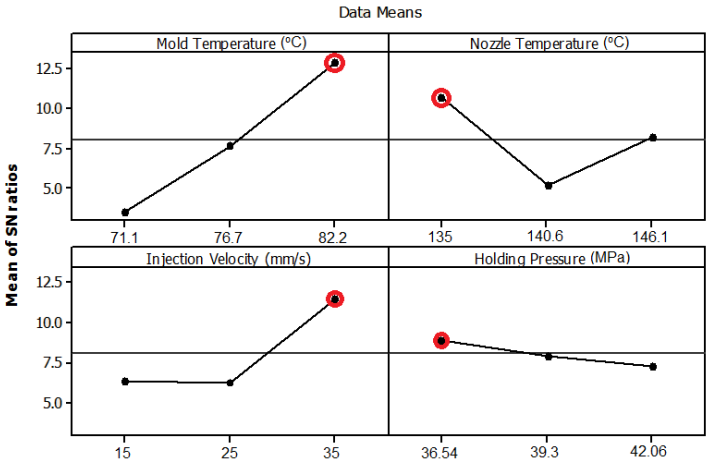

Level	Mold Temperature (°C)	Nozzle Temperature (°C)	Injection Velocity (mm/s)	Holding Pressure (MPa)
1	3.568	10.699	6.413	8.957
2	7.704	5.236	6.276	7.910
3	12.877	8.214	11.461	7.282
Delta	9.309	5.463	5.185	1.675
Rank	1	2	3	4

Figure 5-33: Signal-noise ratio plots and resultant response table for LDPE L9 Taguchi array. Optimization settings are circled on graphs.

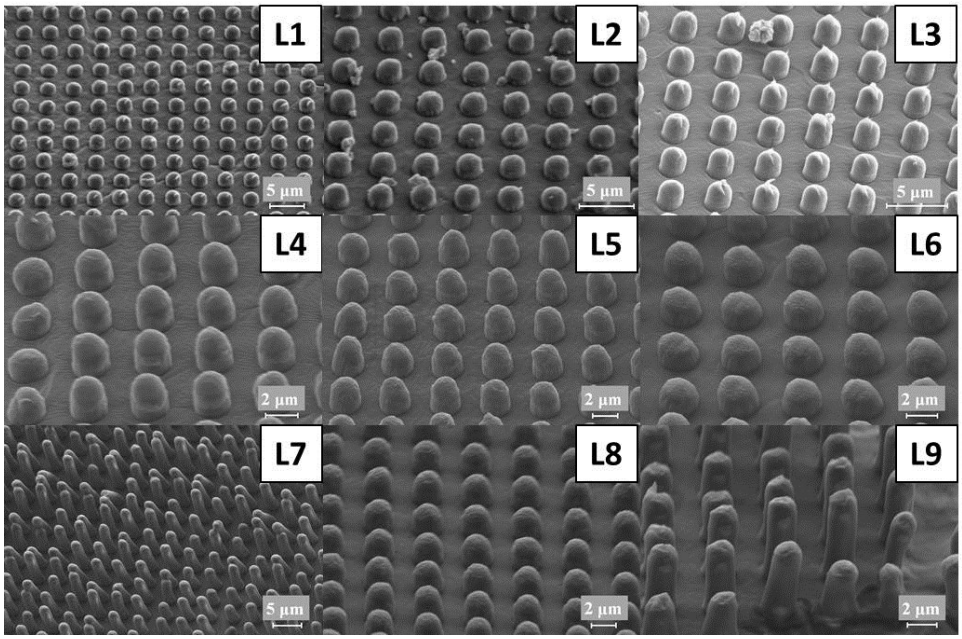

Figure 5-34: Micrographs of replication for L9 Taguchi array trials.

A verification study is usually conducted using optimized parameters. However, condition 7 settings contain all of the optimized parameters except for holding pressure, which has a negligible effect on replication. Thus, it was assumed that the optimum RQ for the given set of testing parameters, mold cavity geometry, and material was 0.642.

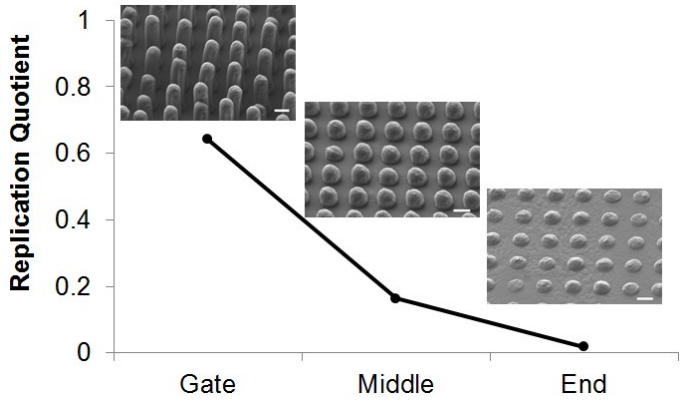

Figure 5-35: Gate proximity dependent replication of part molded with highest level of replication with micrographs of associated regions. The bar indicates 2 µm.

One key difference noted between polystyrene and low density polyethylene is the difference in nanotopography along the vertical faces of the pillars. While PS appears to transfer the scalloping pattern very reliably, LDPE does not display distinct ridges. The increased compliance associate with LDPE may be responsible for the variance. During ejection, the sides of the pillars are subjected to shear forces due to the scallops present in the tooling. While PS appears to remain in the microcavities until the pillars are stretched enough to cause a reduction in diameter, LDPE is able to deform easier and release from the tooling. During its exit from the mold, the scallops shear the surface of the pillar, largely removing the scallop texture initially imparted during molding.

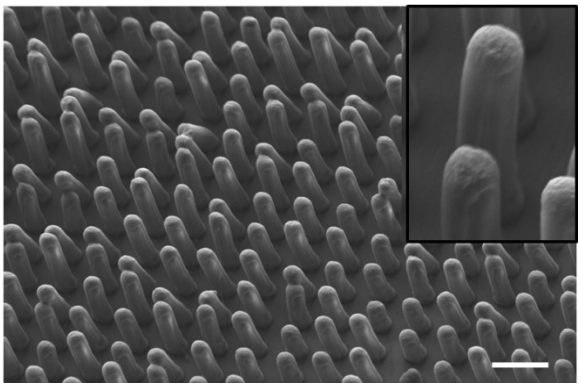

Figure 5-36: Micrograph of larger region of topography illustrating relatively smooth pillar vertical walls (inset). Bar indicates 5 µm.

5.4.2.2 Cell Culture ICC

ICC revealed a substantial alteration in cellular morphology with the presence of LDPE topography. Cell shape displayed patterns that involved high levels of well-ordered curved cytoskeleton structures (Figure 5-37A) to angular narrow conformations (Figure 5-37C).

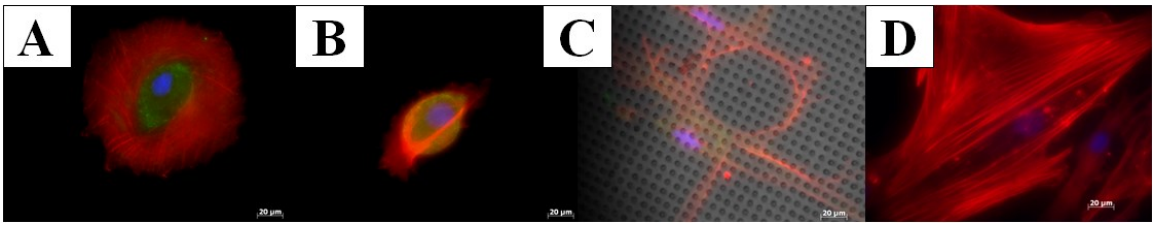

Figure 5-37: ICC images of hMSCs exposed to LDPE topography (A, B, C) compared to tissue culture treated glass controls (D). Cells are stained for actin (red), vinculin (green), and nuclei (blue).

5.4.2.3 Conclusion

The silicon clamp aluminum insert was successfully used in the mold assembly. The Taguchi array revealed that for LDPE and the given tooling, mold temperature had the greatest impact on replication, with the highest mold temperature being beneficial for replication. The low-level nozzle temperature and high injection velocity also enhanced

replication, but not as significantly. A maximum replication of 0.64 was achieved using tooling with an aspect ratio of 5.96. Dramatic differences in replication were seen across the part due to variant conditions across the main cavity.

5.5 Cyclic Olefin Copolymer Sprue Gate Study

In addition to having ideal optical and chemical properties, COC has been used extensively as the polymer of choice for micro and nano injection molding studies [**132**,**34**,**133**,**134**]. COC was molded using a mold assembly containing a sprue gate. The sprue gate allows for a more uniform distribution of conditions across the microfeatured surface, as the flow is distributed radially outward from the center axis of the sprue instead of the sprue being offset from the main cavity, which is the case for mold designs containing a runner system. The new melt delivery design was expected to reduce variance in replication across the microfeatured surface experienced in the previous studies.

5.5.1 Experimental

5.5.1.1Molding

Molding studies involved the use of microfeatured tooling manufactured in Section 4.1.4.5 with a sprue gate main cavity design (Figure 5-38). 3 and 4 μm spaced short channel tooling (3 not shown) and 4 μm spaced deep channel tooling was used. Most molding parameters were chosen based on recommended values with the exception of mold temperature (maintained at ca. $T_{g,\,COC}$), injection pressure (lower to limit initial impact force), and lower holding pressure (to prevent overpacking).

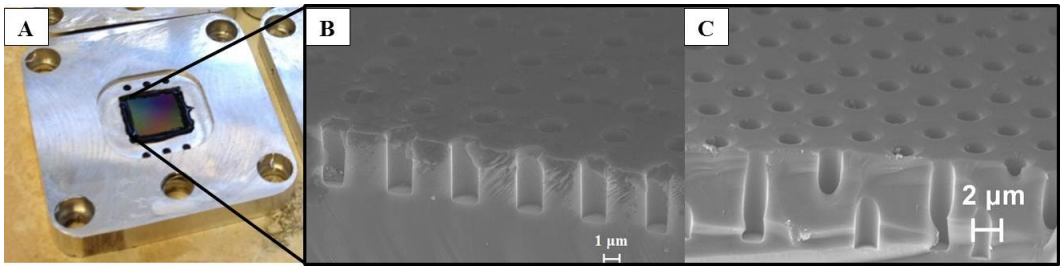

Figure 5-38: Aluminum insert for sprue gate assembly (A) with microfeatured tooling with both short (B) and deep (C) channels.

Temperatures and pressures were increased when molding into deep channel tooling to facilitate a higher degree of fill. An extensive parameter study was not performed, as it was expected that COC, given its extensive use in micromolding and high flow characteristics, would allow for high replication when attempting relatively low aspect ratios.

Table 5-10: Molding parameters for short and deep channel tooling.

Process Parameter	Short Channel	Deep Channel
Nozzle Temperature (°C)	287.8	293.3
Mold Temperature (°C)	135.6	135.6
Injection Velocity (mm/s)	70	130
Injection Limit Pressure (MPa)	20	63
Holding Pressure (MPa)	20	35
Holding Time (s)	11	16
Cooling time (s)	80	80
Ejection Temperature (°C)	115.6	115.6

5.5.1.2 Simulation

Macroscale simulation of the molding process was executed using Autodesk Moldflow Insight to derive a better understanding of polymer flow behavior up to the location of microfeature filling. The process settings were those from the short channel molding in Table 5-10.

5.5.1.3 Water Contact Angle

Water contact angle of samples was measured using a light source and CCD camera equipped with a 5X objective lens directly connected to image collection software. A light filter was place in front of the light source to remove extraneous wavelengths. A microsyringe was held in place above a leveled sample, and a 2 μl water droplet was discharged from the syringe with the needle remaining submerged in the droplet. Immediately following formation of the droplet, the system was permitted to reach steady state conditions, and an image was collected. The droplet was then slowly aspirated until the receding state was achieved, and system was again allowed to reach steady state prior to image collection.

Three images were taken for each condition (advancing, receding, and sessile). Two measurements were taken for each image (one for each side). The use of advancing and receding contact angles were used to avoid the prospect of a metastable water droplet, which has an arbitrary contact angle value between advancing and receding, and can subsequently lead to inconsistent results [**135**]. Values were reported as mean ± standard error. The advancing contact angle (maximum possible water angle) was compared to predicted values.

Wettability of surfaces in nature is defined by the unique surface micro and nanotopography of an organism, in which increased roughness can result in increased hydrophobicity and enhanced self-cleaning properties [**60**]. Synthetically, the creation of microstructures can create the same wettability alterations, thereby creating a biomimetic interface which is thought to be related to the same surface tension effects associated with bioadhesion modification [**136**].

5.5.1.4 Cell Culture Fiber Thickness Measurements

Previous cell culture results revealed an alteration in morphology due to the presence of LDPE micropillars. However, no quantitative results were able to be collected due to the inhomogeneity of the surface. Considering the consistent topography molded here, microfeature-induced morphology changes and stress fiber thickness alterations were studied. Identical ICC protocol as that used in Section 5.4.1was employed to assess cellular morphology and actin filament thickness with the except of using flat COC as a control instead of tissue culture treated glass. ImageJ software was used to measure fibers. A line profile of fluorescence intensity was able to be plotted as a function of distance across the cell. Figure 5-39 shows the method of thickness measurement. Measurements were taken perpendicular to the main stress fiber direction.

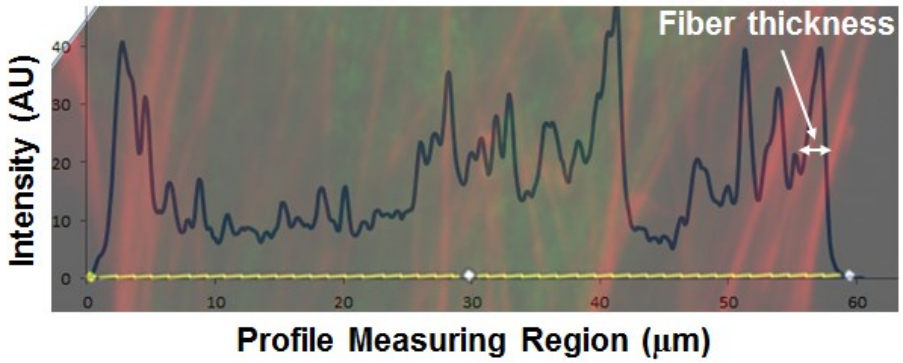

Figure 5-39: Characteristic fluorescence intensity line profile with matching stress fibers in background.

5.5.2 Results

Molding was monitored and assessed through the use of pressure and velocity profiles. Microfeatured surfaces were characterized through microscopy and water contact angle to observe the changes in surface energy as a function of microtopography.

In addition, cell culture and immunocytochemistry was performed to assess the effect of microtopography on cellular morphology.

5.5.2.1 Molding and Replication

The molded part is shown in Figure 5-40. The microfeatured region is optically apparent due to the reduction in transparency caused by the microfeatures.

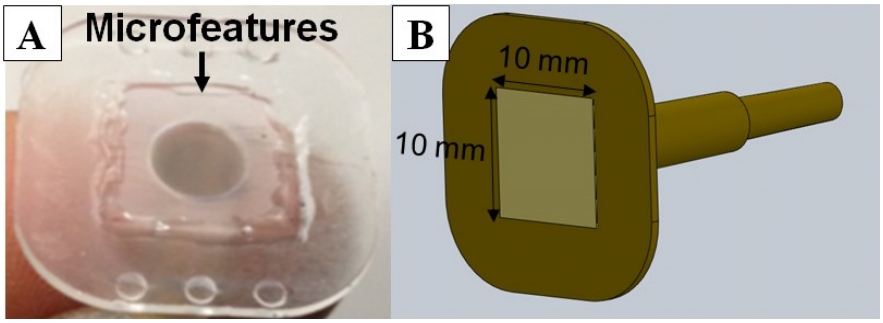

Figure 5-40: Image of molded part (A) and CAD representation of microfeatured region (B).

Velocity and pressure profiles reveal that for short channel molding, the filling phase was largely pressure limited, as can be seen in Figure 5-41. A slight spike in pressure is observed during the holding phase, which might be the result of additional pressure necessary to fill the microfeatures. A rapid acceleration of the plunger occurs from 0.1 to 0.2 s of filling, followed by a parabolic decline in velocity up to the location of the pressure spike.

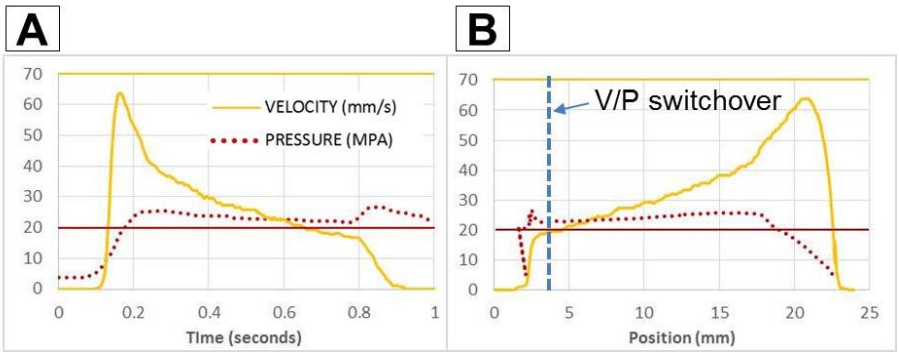

Figure 5-41: Velocity and pressure profiles vs. time (A) and plunger position (B).

Pressure controlled filling, although prone to process inconsistency, is an effective means to avoid fracture of relatively brittle tooling. It is also important to note that although the velocity was set to 70 mm/s, the plunger does not reach the value at any point during filling, as the limit pressure limits velocity after the initial acceleration. The feature replication was consistent across the part surface for both 3 and 4 µm spaced pillars, as shown in Figure 5-42.

There was a distinct discrepancy in pillar height, in which a lower pillar height was present for the pillars spaced closer together (Table 5-11).

Table 5-11: Insert channel depth and resultant pillar height for COC molded in Figure 5-42.

	Microchannel	3 µm spacing	4 µm spacing
Depth/Height (µm)	4.75 ± .03	1.04 ± .03	2.37 ± 0.12
Diameter (µm)	1.61 ± .03	1.63 ± .03	1.61 ± .01
Aspect Ratio	2.95	0.64	1.47

For the 4 µm spaced pillars, there appears to be a slight mushroom shape, indicative of a slight stretching of the pillars during demolding (Figure 5-42). The replication quotient for the 3 and 4 µm center-to-center spacing was 0.219 and 0.499,

respectively. Although relatively low levels of replication occurred, the consistency achieved is significantly higher compared to previous molding trials.

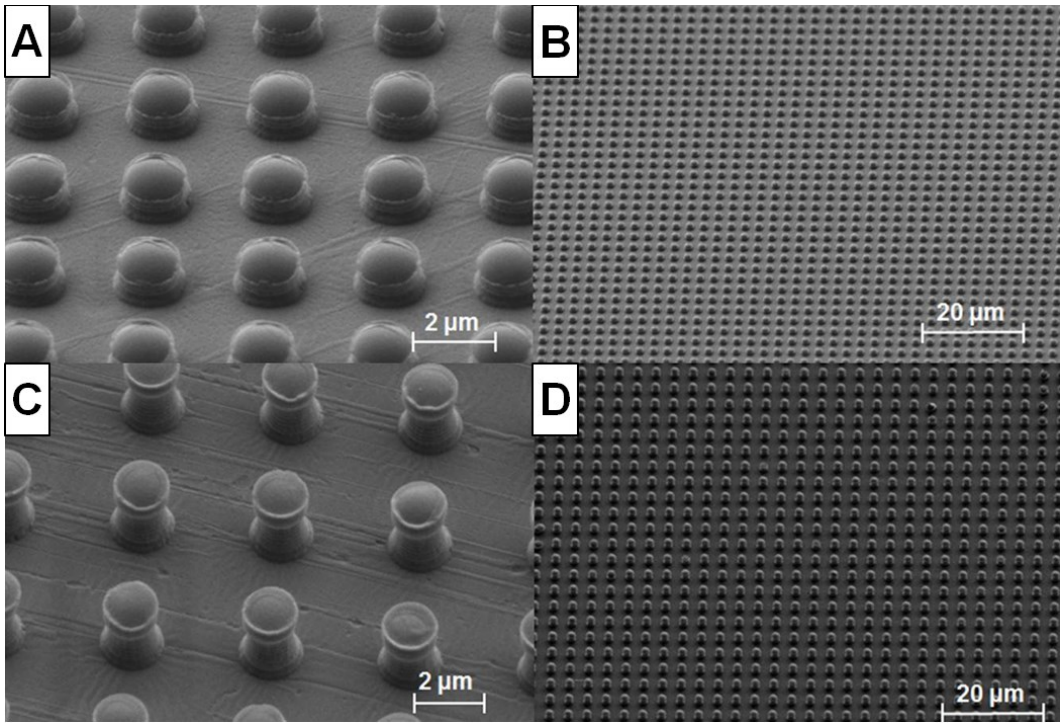

Figure 5-42: Micrographs of pillars molded using short microchannel silicon insert shown in Figure 5-38B. 3 µm spaced pillars at high (A) and low (B) magnification, and 4 µm spaced pillars at high (C) and low (D) magnification.

High aspect ratio positive features were difficult to create in a reliable and consistent manner when molding into the deep channel inlay, as variations were seen across the part (Figure 5-43). Moreover, pillars with higher replication, which were located near the sprue, appear to be stretched and bent.

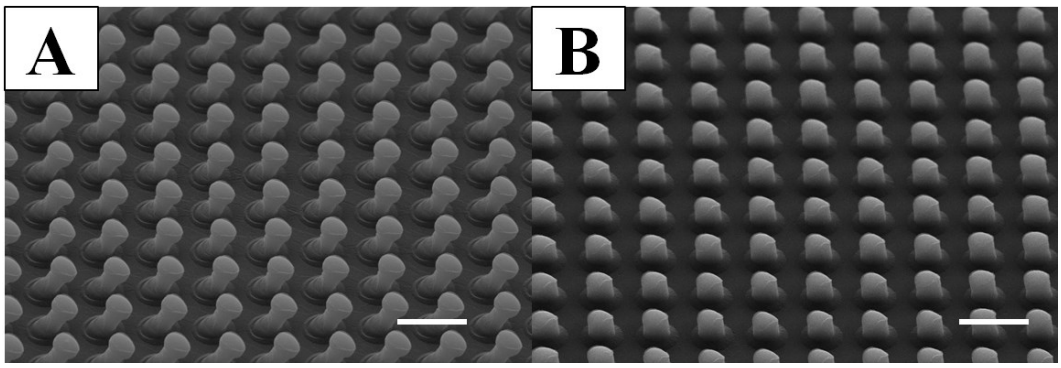

Figure 5-43: Micrographs of COC molded using deep 4 µm spaced microchannel insert. Images were taken near the sprue (A) and the edge of the microfeatured region. Bars indicate 5 µm.

5.5.2.2 Macroscale Simulation to Understand Microscale Replication

Molding simulation results provide useful insight into the melt behavior at the micro-cavity region. For mold tooling that is fairly thermally conducted, a concern that can arise is rapid heat transfer out of the melt and into the tooling prior to adequate replication. A useful aspect of the given mold geometry is the relatively thick sprue being in close proximity with the microfeatured region. The thick polymer domain is able to maintain a low viscosity due to the inherent insulating properties of the polymer. The concept of increasing thickness to delay microcavity solidification has previously been suggested [**38**]. Thus, the region directly below the sprue, i.e., the microfeatured region, remains at a low viscosity for an extended period of time.

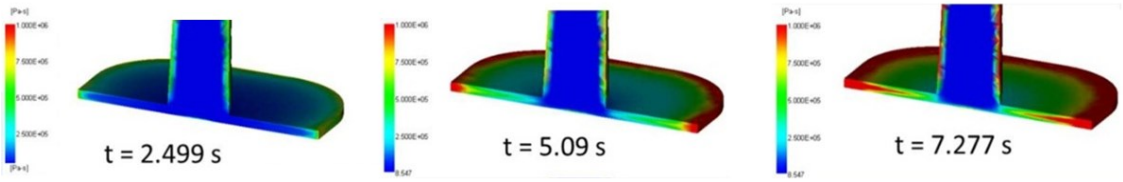

Figure 5-44: Viscosity evolution during the holding phase of the molding cycle.

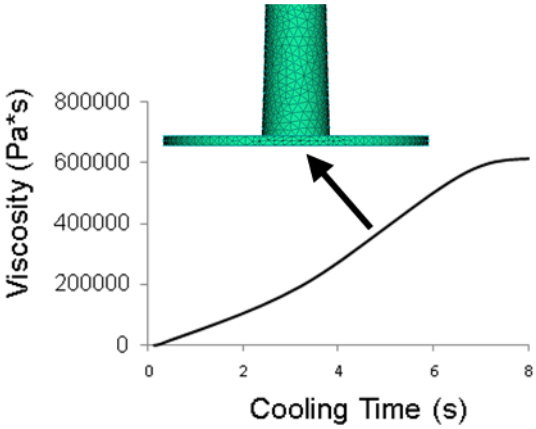

Figure 5-45: Delayed viscosity increase at polymer-silicon interface due to insulating sprue.

5.5.2.3 Effect of Autoclaving on Topography

Autoclaving of the microfeatured samples revealed no significant changes in microfeature geometry resulting from the process. A concern with autoclaving is that the process could impart unintended micro and/or nanofeatures on the surface, thereby providing an uncontrolled topographic environment different from that of the originally molded part.

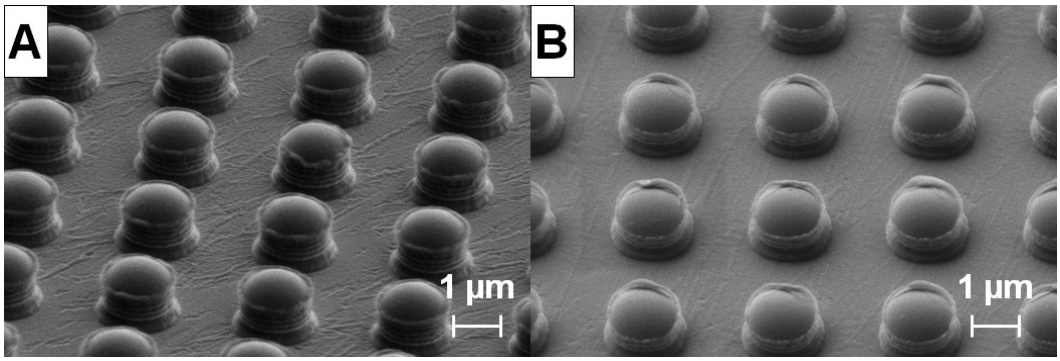

Figure 5-46: Micrographs of 3 spaced pillars before (A) and after (B) autoclaving.

5.5.2.4 Surface Characterization of COC – Water Contact Angle

Substrates molded into the short channels were used for the subsequent studies, and those molded onto the deeper channels were omitted due to the lack of replication consistency.

Microtopography dramatically affected water contact angle, in which microfeatured surfaces induced a higher level of hydrophobicity, as shown in Figure 5-47. Hysteresis, defined as the difference between the advancing and receding contact angle, was shown to increase slightly with an increase in pillar density (define here as number of pillars per unit of projected surface area). The hysteresis values of the flat, 4 μm spaced pillars, and 3 μm spaced pillars were 11 ± 2.8°, 78 ± 3.7°, and 82 ± 3.3°, respectively. Higher hysteresis values are associated with a Wenzel state (i.e., water penetrates in between features), in which the water has difficulty detaching from the surface during water recession [**53**].

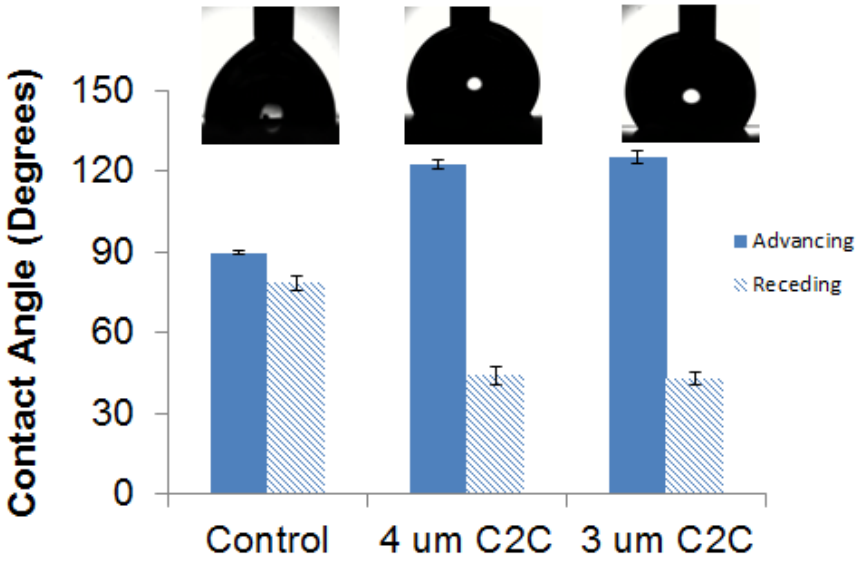

Figure 5-47: Advancing and receding contact angle as a function of surface microtopography. Characteristic images of advancing angle water droplets are shown above associated values.

The experimental values were compared to Wenzel and Cassie models to further assess what state the water droplets were in. The Wenzel roughness values are a function of the vertical surface area of the pillars, as the remaining surface area is perpendicular to the surface normal. Figure 5-48 illustrates the relevant components of a microtopographic surface for both models.

Equation 5-1 shows the relationship between cylindrical pillar diameter, height, pitch (a function of pillar area density), and subsequent roughness factor.

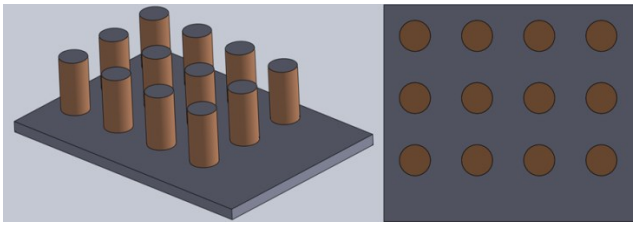

Figure 5-48: CAD representation of parameters critical to Wenzel and Cassie states. Wenzel roughness is dependent on vertical surface components (left) and Cassie solid-liquid fraction dependends on feature area density (right).

$$\mathbf{r_{Wenzel}} = \frac{\boldsymbol{\pi}\mathbf{DH+Pitch^2}}{\mathbf{Pitch^2}} = \frac{A_{actual}}{A_{projected}} \qquad \text{Equation 5-1}$$

The generalized equation for the Cassie solid fraction due to constant diameter orthogonally arrayed pillars is shown in Equation 5-2.

$$\mathbf{f_{s,Cassie-Baxter}} = \frac{\boldsymbol{\pi}\mathbf{D^2}}{\mathbf{4*Pitch^2}} \qquad \text{Equation 5-2}$$

The roughness and solid area fraction values for the topographic surfaces, as well as predicted Wenzel and Cassie contact angles, are shown in Table 5-12. It is important

to note that due to the greater pillar height, the 4 μm spaced pillars have a slightly greater roughness value despite having a lower pillar area density compared to the 3 μm spaced pillars. The Wenzel model appears to predict an increase in hydrophilicity with the presence of microtopography for the given substrate.

Table 5-12: WCA theory variables and predicted values.

	4 μm C2C	3 μm C2C
r	1.75	1.59
f_s	0.127	0.232
Wenzel	89.3	89.4
Cassie	150.7	140
Actual (advancing)	122.7 ± 1.8	125.4 ± 2.4

Figure 5-49 shows that for flat materials that are hydrophilic, Wenzel predicts that the 3 μm spacing will have a greater contact angle compared to the 4 μm spacing, but both surfaces will induce increased hydrophilicity compared to a flat surface. For flat material WCAs > 90^o, the trend switches. Wenzel generally predicts that increased roughness will make a hydrophilic surface more hydrophilic and a hydrophobic surface more hydrophobic. Neither measured angle appears to have a value near the predicted value.

The Cassie-Baxter model predicts a dramatic increase in WCA as a function of topography (Figure 5-50). Although WCA does increase with the presence of topography, it does not do so to the extent of Cassie predictions. Moreover, Cassie predicts that surface with lower feature area density will create a higher WCA. However, the opposite is true experimentally. The nanoscale features present on each micropillar (i.e., side scallops) may contribute to the discrepancy in the trend.

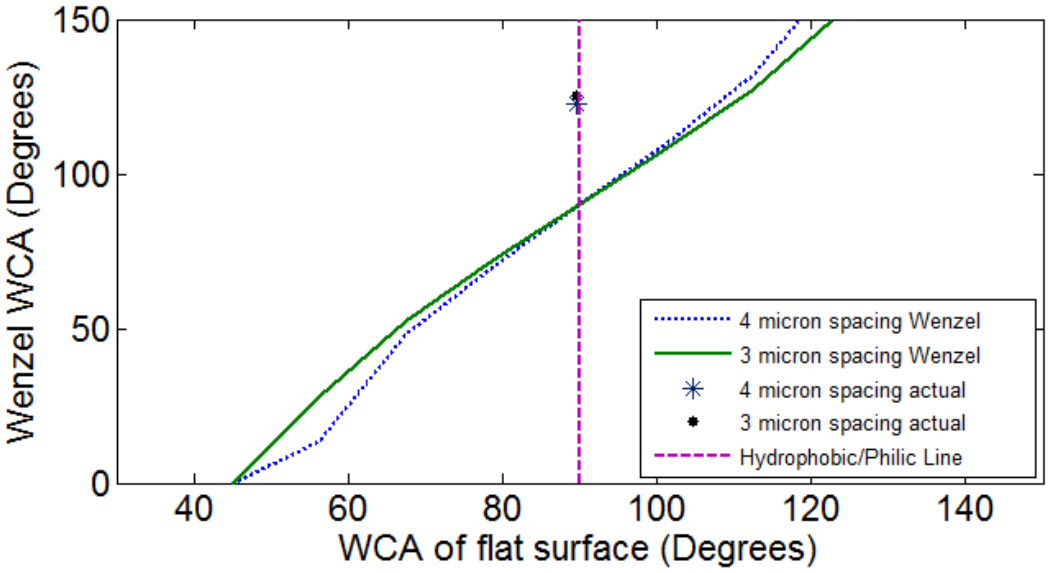

Figure 5-49: Comparison of Wenzel model of wettability with experimental results for advancing contact angle.

It has previously been suggested that at a certain roughness, a transition between Wenzel and Cassie occurs [**61**]. At roughness values between 1 and 1.35, a Wenzel state is expected, in which contact angle increases with an increase in roughness. At values greater than 1.35, the system is expected to be in a Cassie state, such that the water is unable to infiltrate regions in between microfeatures and the advancing and receding contact angles remain constant independent of roughness (since the water is sitting on top of the features and is unaware of feature height). Consequently, it was expected that both topographic surfaces would fall into a Cassie state given their roughness values being > 1.35.

To further understand the wettability on the surface due to topography, hysteresis was shown as a function of roughness. Hysteresis increased dramatically when comparing the flat substrate with microfeatured substrate. However, values were not significantly different between the two microtopographic surfaces.

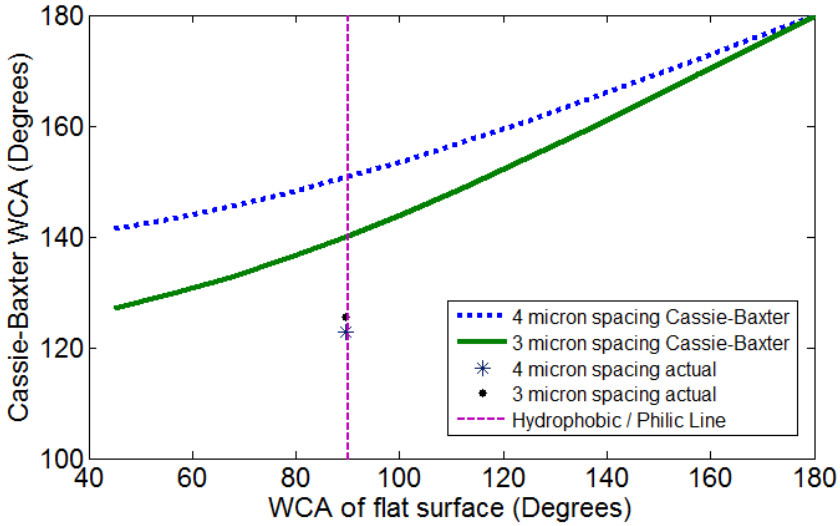

Figure 5-50: Comparison of Cassie-Baxter model of wettability with experimental results for advancing contact angle.

High values of hysteresis are typically associated with a Wenzel state, in which higher values of roughness correspond to a higher level of hysteresis, as shown in Figure 5-51. However, cases do exist where hydrophobic Cassie surfaces can exhibit significant levels of hysteresis. Rose petals, which are highly hydrophobic, also show high levels of water adhesion.

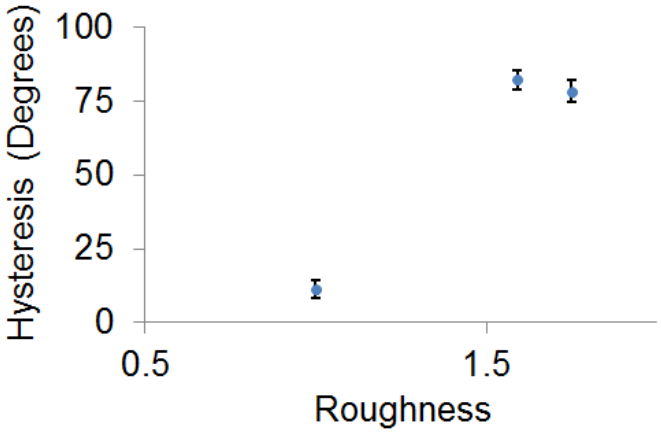

Figure 5-51: Hysteresis as a function of Wenzel roughness. Both topographic surfaces exhibit values with experimental error of each other.

The unique combination is derived from a hierarchical structure of micropapillae and nanofolds, in which the water infiltrates the regions between microfeatures but does not penetrate regions between nanofeatures [**137**]. It is believed that the same phenomenon is occurring, as micropillars with nanoridges are present on the surfaces used for the current study.

5.5.2.5 Cell Culture – Effect of COC Microtopography on Morphology and Stress fiber thickness

Topography alters the geometrical properties of the surface, which subsequently creates a unique interfacial environment of specific wettability, mechanics, and chemical structure. All such properties have the potential to affect stem cell activity [**57**,**13**]. Dramatic cytoskeletal organization was clearly visible when comparing the flat COC (control) to the microfeatured substrate. Figure 5-52 shows a high level of cellular branching across the microfeatured surface, with specific filopodia aligning along particular microfeature rows (Figure 5-52B). Moreover, it appears that in certain areas, stress fibers are adjacently orienting along the micropillar rows in a highly organized and cooperative manner (Figure 5-53).

Beyond qualitative morphological differences, microstructured COC surface also affected hMSC stress fiber thickness in a substantial way (Figure 5-54). The thickness and organization of stress fibers is directly related to substrate rigidity, and play a critical role in directing stem cell fate [**138**].

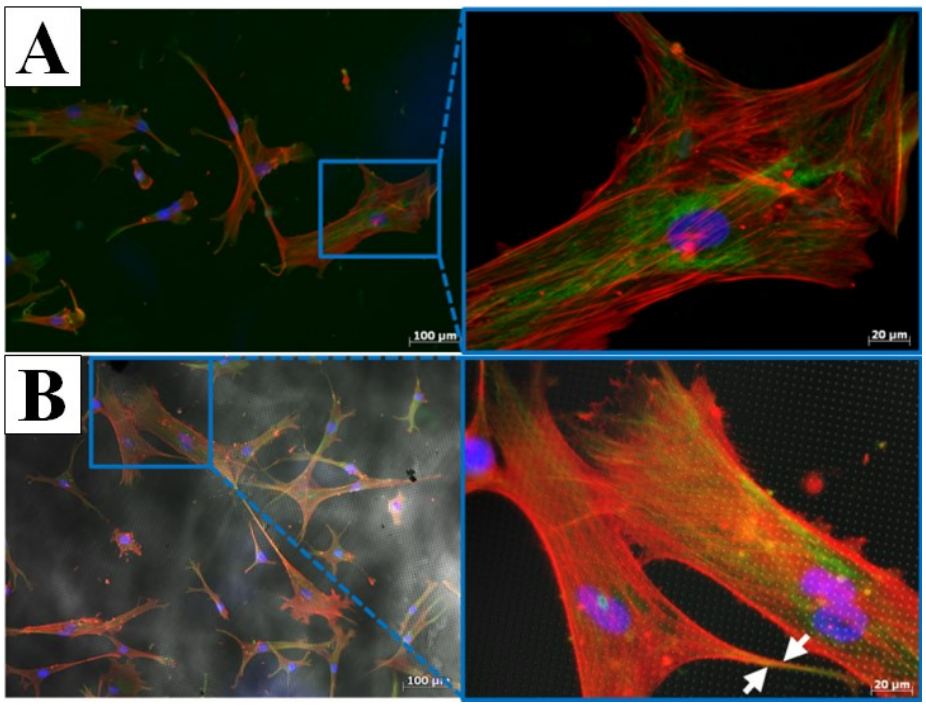

Figure 5-52: ICC micrographs comparing hMSCs cultured on flat (A) and 4 µm spaced (B) COC. Cells are stained for actin (red), vinculin (green), and nuclei (blue). The inset shows two cells and their topography – dependent morphology. Arrows indicate a cellular extension aligning with a row of micropillars.

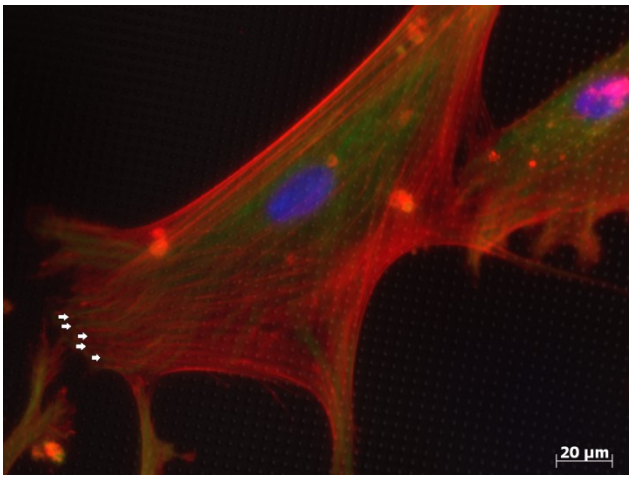

Figure 5-53: ICC micrograph illustrating the dramatic stress fiber alignment to COC microtopography. Cells are stained for actin (red), vinculin (green), and nuclei (blue). Vinculin structures, indicative of focal adhesions, appear along micropillars, and are observable near the lower left edge of the cell (arrows).

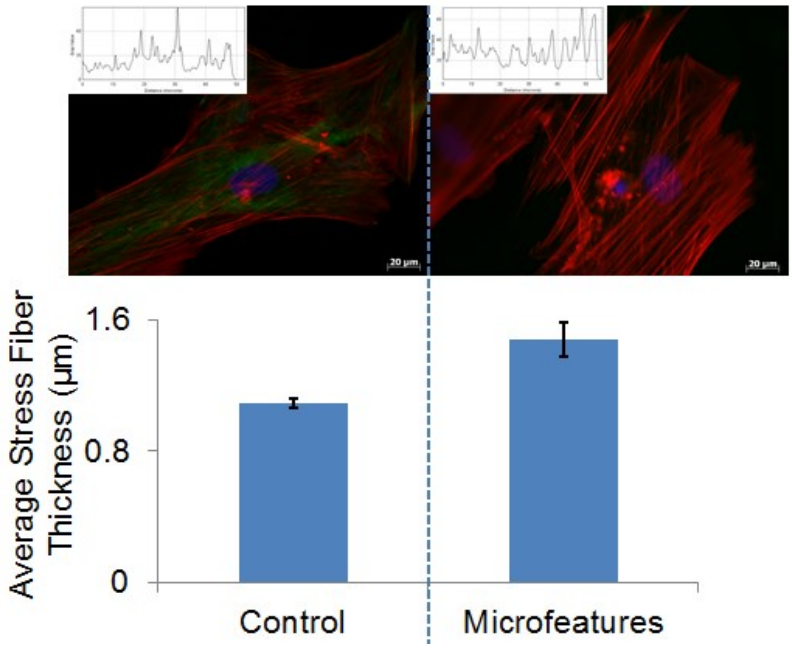

Figure 5-54: Average stress fiber thickness for hMSCs on control and microfeatured COC with corresponding ICC micrographs and intensity line plots (inset). A 2 tailed paired Student t-test yields a $p < 0.05$.

Both surfaces appear to allow cells to develop well-ordered cytoskeletal networks. However, the enhanced degree to which the microfeatured polymer substrate is able to assemble a substantially more robust actin fiber network indicates that intracellular signaling has occurred and potentially other cellular alterations have taken place as well.

5.5.3 Conclusion

Microtopographic surfaces enhanced hydrophobicity, with a higher solid area fraction of features causing slightly higher contact angles. Both topographies induced angles above that predicted by the Wenzel model and below that of the Cassie model, indicating that the microfeatures induced an intermediate state of wettability. The results followed the Cassie model in that the WCA increased with the presence of microfeatures.

However, results did not follow the general trend of increasing contact angle with decreasing feature area density predicted by the Cassie model. The combination of high contact angle and significant CAH is described by a phenomenon found on the surfaces of rose petals, in which water is in a Wenzel state at the microscale but a Cassie state at the nanoscale. Microtography also modified cellular morphology and significantly increased stress fiber thickness. Although the distinct change in cytoskeletal structure could very well be associated with other more substantial alterations (i.e. differentiation), the effects in such a regards remain unclear.

5.6 Cyclic Olefin Copolymer Sprue Gate with no Ejector Pins

To fill microchannels, a sufficient amount of pressure must be present to push the polymer melt into the cavities. As mold temperature is increased to higher values, thermal expansion of the mold occurs. The mold assembly is composed of different materials containing a range of thermal properties. Consequently, the system dimensions change as a function of temperature, but must still perform its intended function at the elevated values. Considering that injection molding involves many moving parts that seal and slide across one another, uneven changes in dimensions across the assembly can be a concern.

One key mechanical interaction is between the ejector pins and ejector pin holes. S-7 tool steel (ejector pin material) and 6061 aluminum (insert) have coefficients of linear thermal expansion of $1.258 \times 10^{-5}\ K^{-1}$ and $2.36 \times 10^{-5}\ K^{-1}$, respectively. The mold is designed such that the diameter of the ejector pin very closely matches the diameter of the ejector pin hole at room temperature (i.e., when it is assembled). When the mold

temperature is increased to a value near glass transition temperature of COC, the aluminum will expand to a larger degree than the ejector pin (schematic shown in Figure 5-55).

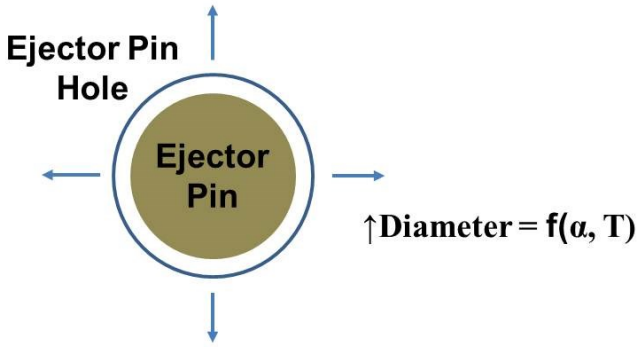

Figure 5-55: Schematic of thermally-induced expansion at the ejector pin / ejector pin hole interface.

The expansion discrepancy can be quantified through the equation:

$$\frac{\Delta L}{L_o} = \alpha * \Delta T \qquad \text{Equation 5-3}$$

If the mold temperature is increased from room temperature (21 ^{o}C) to $T_{g,COC}$ (135 ^{o}C), a gap of approximately 1μm results. Although seemingly insignificant, the thermally-induced gap is on the same order of magnitude as the features being filled. Moreover, in the case of the previous study, the gaps occupy a surface area of 3.11 x10^{-4} cm^2, which is approximately 12,000 times the surface area of one microchannel. Essentially, a large area of fill can be generated from thermal expansion which could potentially detract from pressure which could otherwise be used to fill microchannel inlets.

Ejector pin holes were omitted for the mold design to avoid the thermally-induced gaps present at higher mold temperatures, with the goal of increasing available pressure to fill microchannels.

5.6.1 Experimental

A steel (1018) sprue gate insert was used with silicon tooling from Section 4.1.3.3 (Figure 5-56). A basic mold temperature and injection velocity parameter study was conducted to quickly assess the use of the new insert. Constant and varied parameters are shown in Table 5-13. Ejection of the part was achieved through manual removal using the sprue as a grip.

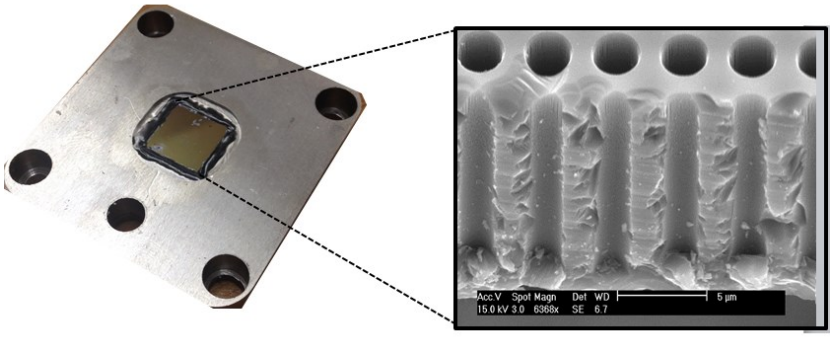

Figure 5-56: Sprue gate steel insert with no ejector pins. Tooling used had 12 µm spacing, but was etched using the same recipe as the microchannels shown.

Table 5-13: Molding parameters used for COC with sprue gate insert with no ejector pins.

Parameters	Value
Injection Velocity (mm/s)	100,200
Mold Temperature (^{o}C)	95, 125, 135
Barrel Temperatures (^{o}C)	293.3/287.8/276.7/248.9/182.2
Holding Pressure (MPa)	4
Holding Time (s)	30
Ejection Temperature (^{o}C)	95

5.6.2 Results

Injection velocity did not appear to have an effect on replication using mold temperatures below or at T_g of COC. Moreover, values of replication were very low even using a mold temperature at polymer T_g. In fact, replication was comparable to what was achieved using the short channel tooling from Section 5.5. The low values could be due to the complete inability for the air in the cavity to escape, as the lack of ejector pins provides no escape. Potentially, the air trapping thought to occur in microchannels is amplified with the lack of any air vents.

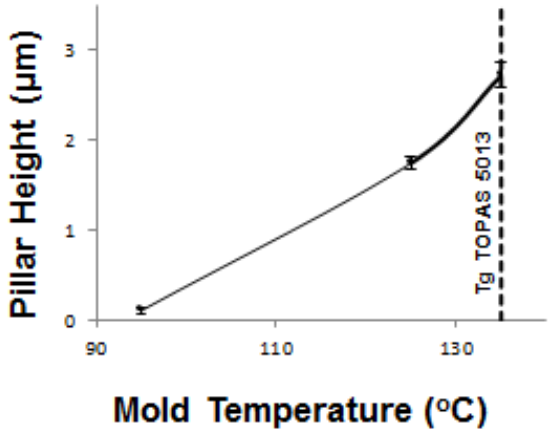

Figure 5-57: Pillar height as a function of mold temperature of COC using sprue gate insert with no ejector pin holes.

The shape of the pillars appeared very inconsistent with the tooling used, indicating that the demolding process may have imparted a certain level of deformation to the features.

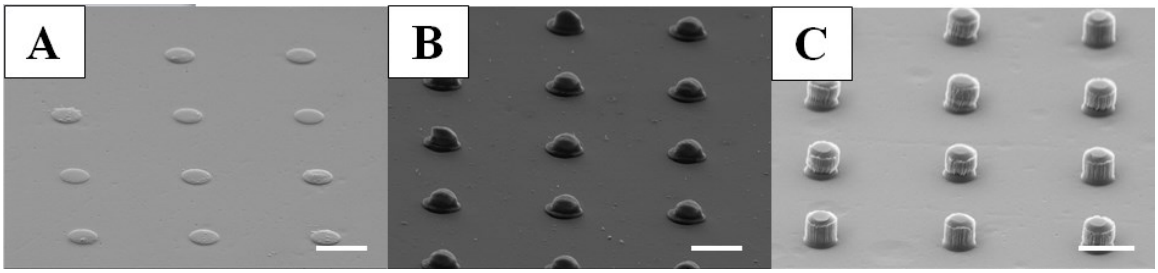

Figure 5-58: Micrographs of pillars molded at a mold temperature 95 (A), 125 (B), and 135 (C) ^{o}C. Bar indicates 3 µm.

The low values of replication prompted a drastic design alteration of both the macroscale insert (6061 aluminum or 1018 steel) and the silicon inlay, as multiple issues existed with both components that limited replication and consistency potential.

5.7 Embedded Cartridge Heater Assembly

5.7.1 In-Mold Rheology of Tooling

When using new mold tooling and a particular material, valuable data to obtain is the response of the polymer to varying shear rate. Polymer viscosity, which is a critical property dictating filling capacity of the tooling, is shear rate dependent. When increasing shear rate, the material transitions from a polymer whose viscosity is dependent on shear to a more Newtonian behavior (non-shear rate dependent viscosity). Since shear rate is directly proportional to injection velocity, the transition can be observed through a basic study of varying the velocity and noting the changes in fill time and pressure necessary to maintain the specific velocity being tested. It is paramount to then process above the transition zone such that small variations in shear rate do not result in large fluctuations in viscosity (and subsequently filling behavior).

The polymer filling behavior is unique to the particular cavity being used. Consequently, it is useful to measure the rheological behavior of the melt for each tooling and polymer used. *In situ* rheology can be utilized to identify what filling velocity is necessary to maintain constant polymer viscosity from one cycle to the next. A viscosity curve can be generated by measuring the fill time and maximum pressure necessary to move the injection plunger forward at a specific velocity. The equation used to calculate such apparent viscosity values at different filling velocities is:

$$\boldsymbol{\eta_{apparent} = t_{fill} * P_{max}} \qquad \text{Equation 5-4}$$

The calculation is based on the well-known Hagen Poiseuille equation, which is given to be:

$$\boldsymbol{Q = \frac{\pi R^4 \Delta P}{8 \eta L}} \qquad \text{Equation 5-5}$$

Flow rate ($\boldsymbol{Q}$) through a channel is a function of the channel radius (**R**)**,** channel distance ($\boldsymbol{L}$), polymer viscosity ($\boldsymbol{\eta}$), and pressure drop across the distance of the channel ($\boldsymbol{\Delta P}$). In generating a viscosity curve, the objective is to determine the velocity at which viscosity no longer changes. Viscosity of thermoplastic polymers decreases with increasing velocity (i.e., shear rate), but ceases to decrease at a certain value. Once the transition is obtained, one can assume that by staying at an injection velocity greater than the transition, variation in viscosity from one cycle to the next can be minimized. For velocities below that of the critical value, the slightest change in velocity from one

molding cycle to the next can lead to changes in viscosity and subsequently changes in replication quality.

5.7.1.1 Viscosity Curve for COC with Embedded Cartridge Heater Tooling

For cyclic olefin copolymer, it was determined through in-mold rheology that injection velocity should be maintained at or above 15 cm/s (flow rate = 0.0754 cm^3/ s) to avoid variation in viscosity from one shot to the next. Figure 5-59 shows the effect of increased injection velocity (which is directly related to shear rate) on viscosity, in which only slight variations in viscosity are seen at higher flow rates. Although higher fill rates more effectively attenuate process inconsistencies, careful consideration must be made to ensure shear rates capable of inducing polymer degradation are avoided [**139**]. The viscosity curves also show a dependence of mold temperature on viscosity. The viscosity appears to be consistently lower at injection velocities > 120 mm/s, and is dramatically lower at slower injection velocities. The reduced viscosity can be attributed to a reduction in frozen layer at the wall. The values shown are higher than those previously shown in Figure 5-5. The difference can be attributed to the use of a different geometry from that used by the Autodesk company.

The results of the *in situ* rheology (in which viscosity has a low level of variance at velocities >150 mm/s) were used to determine the proper velocity for use in with microfeatured tooling (with the assumption that the effect of the microfeatures on macroscale polymer viscosity was negligible).

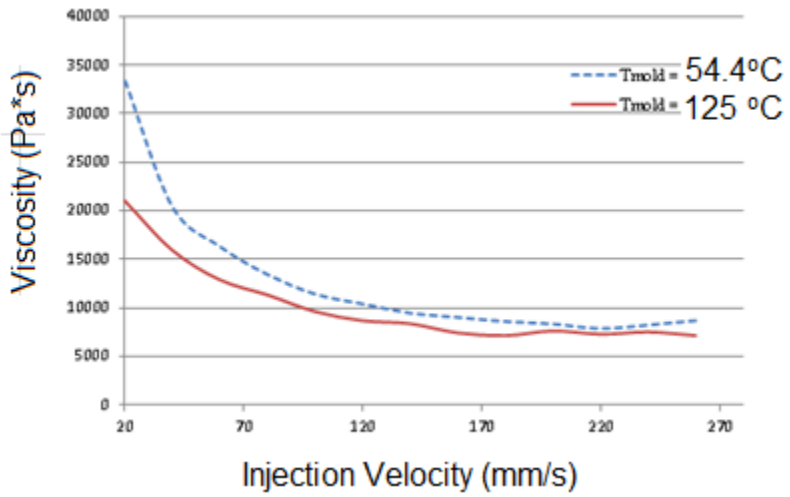

Figure 5-59: Viscosity curve for sprue gate cartridge heater embedded insert at mold temperatures of 54.4 °C and 125 °C with COC.

5.7.1.2 Viscosity Curve for TPU with Embedded Cartridge Heater Tooling

It was determined that the critical injection velocity for TPU was ca. 100 mm/s (Figure 5-60). One of the concerns with injecting at higher flow rates is the increased shear rate associated with such a change. It is imperative to understand the impact the cavity geometry can have on final part properties.

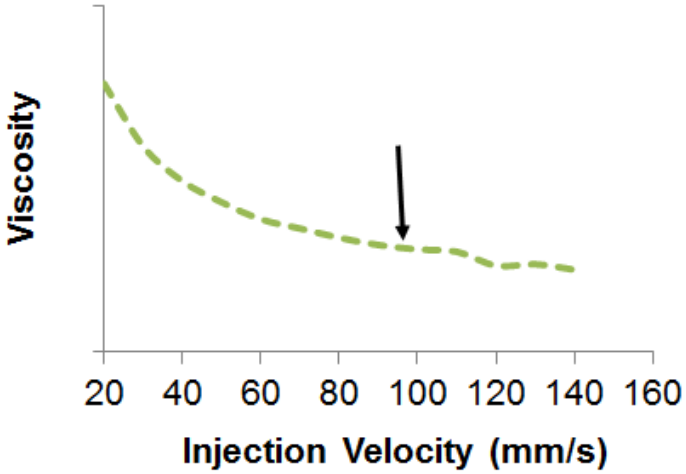

Figure 5-60: Viscosity curve for TPU (Texin 985). Mold temperature was maintained at 43.3 °C.

5.7.2 COC with Taper Trial 3 Tooling

After determining appropriate parameters for creating tapered microchannels in the silicon tooling, molding trials were conducted. High quality tooling is vital for adequate replication. The presence of a positive taper is an improvement on the vertical sidewalls, which are prone to demolding concerns.

5.7.2.1 Experimental

Molding studies were executed using the new aluminum insert and tooling from tapered tooling trial 3 (from Section 4.1.7). Temperatures and pressures were chosen in accordance with recommended processing parameters. Injection velocity was chosen based upon the viscosity curve generated in the previous section. The mold temperature was increased to above recommended conventional injection molding processing values to facilitate microfeature filling. The molding parameters are shown in Table 5-14. An aluminum insert containing an embedded cartridge heater was used with the variable isotropy silicon inlay manufactured from section 4.1.6 (Figure 5-61).

Table 5-14: Molding parameters for trial 1

Process Parameter	Value
Nozzle Temperature (°C)	293.3
Mold Temperature (°C)	104.4, 115.6,126.7,137.8
Injection Velocity (mm/s)	160
Holding Pressure (MPa)	30
Holding Time (s)	10
Cooling time (s)	80
Ejection Temperature (°C)	104.4

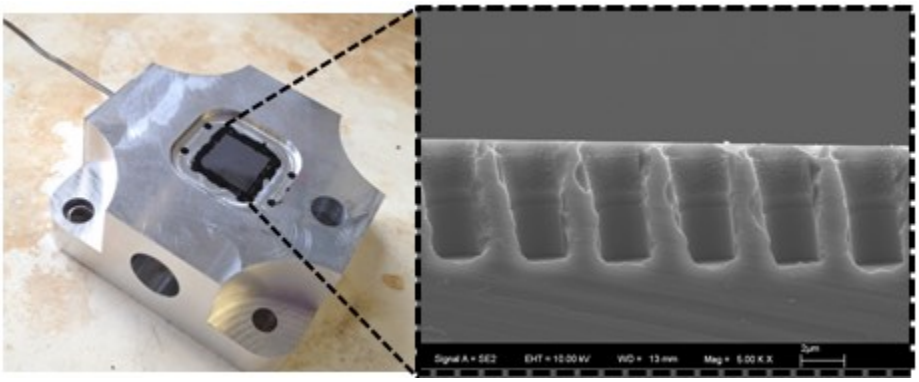

Figure 5-61: Insert used for COC mold temperature study.

Replication was quantified through normalization of pillar heights with the tooling channel depth. Consistency of replication was measured through imaging nine distinct regions on the polymer plate surface, as shown in Figure 5-62.

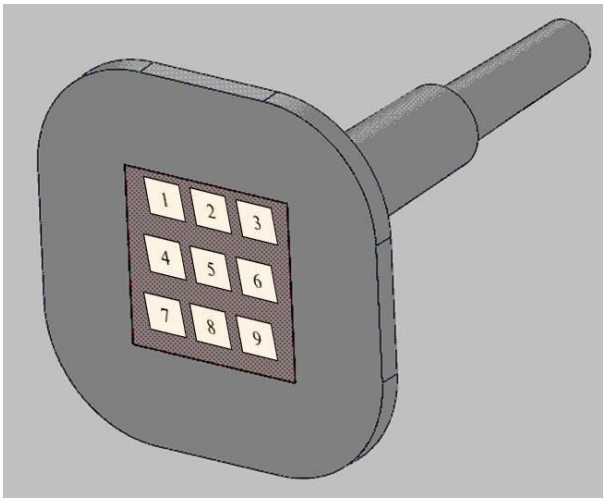

Figure 5-62: Schematic illustrating the 9 regions where images were collected.

5.7.2.2 Results

As expected, mold temperature had a dramatic impact on replication (), with mold temperatures above $T_{g,COC,\ 5013}$ (= 135 ^{o}C) yielding the highest values. At a mold temperature of 137.8 ^{o}C, the replication quotient (RQ) was 0.97, or 97% filling depth

(which is the highest value achieved throughout the study). Micrographs showing the degree of replication are shown in Figure 5-64.

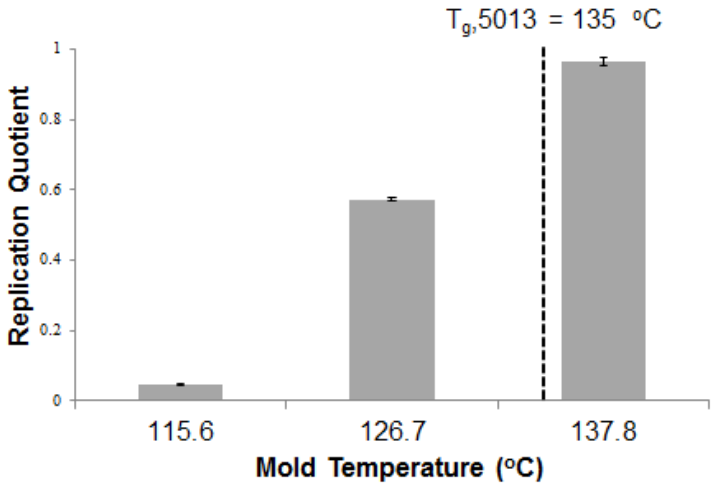

Figure 5-63: Replication as a function of mold temperature. Significant replication was achieved when using a mold temperature >T_g.

Unlike the study in Section 5.2 where pillar stretching facilitated RQ values of over 3, it appears that a low amount of tensile stress has been imparted to the microfeatures. The stability of the features can be attributed to the relatively large base of the feature.

There appears to be some type of sheath structure closer to the bottom of the pillars, especially for pillars molded with the highest mold temperature, which does not follow the features of the microchannel. Closer to the top of the pillars, the scalloping pattern present from microchannel manufacturing can be seen.

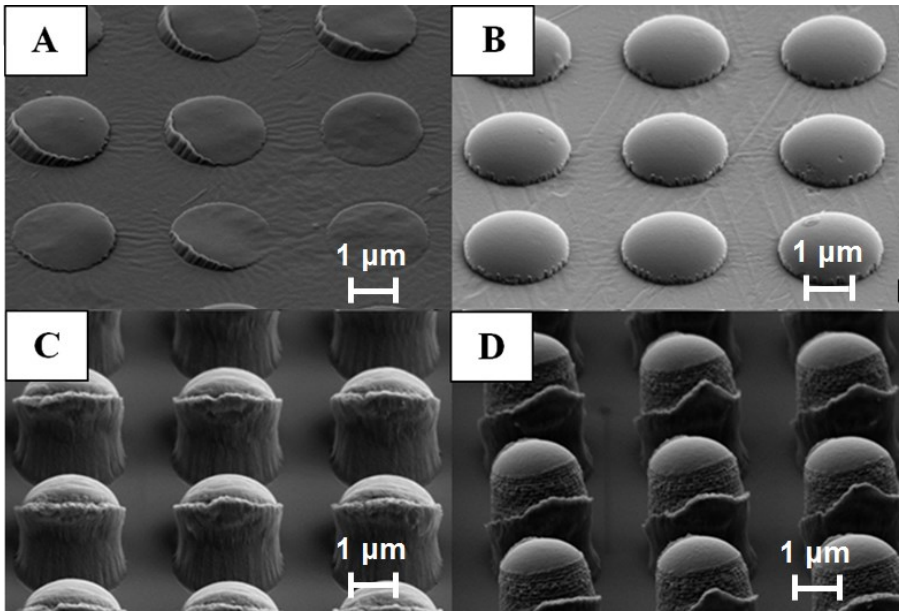

Figure 5-64: Micrographs of 4 µm spaced pillars molded at different mold temperatures. (A) T_{mold} = 104.4 ^{o}C, (B) 115.6 ^{o}C, (C) 126.7 ^{o}C, and (D) 137.8 ^{o}C.

A concern always present with a large array of microfeatures is consistency of the features. Various issues can arise that have the ability to compromise consistency. Pillar height was consistent across the micropatterned region at mold temperatures below glass transition (Figure 5-65 and Figure 5-66). However, at the highest mold temperature, pillars across the middle of the part appear to be ruptured, as shown in Figure 5-66. The replication quality deterioration is thought to be a result of insufficient draft of the macroscopic part. During ejection, the ejector pins can deform the polymer plate if the part sticks to the cavity, causing the part to bow and push the middle into the tooling, as shown in Figure 5-68C.

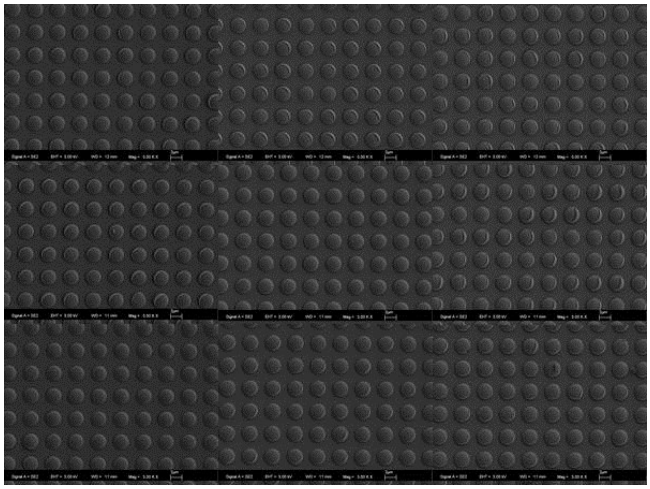

Figure 5-65: Micrograph of surface of part molded with T_{mold} = 115.6 ^{o}C.

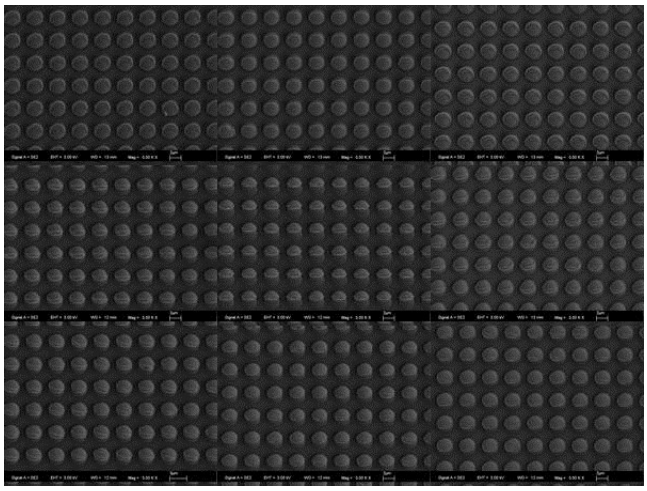

Figure 5-66: Micrograph of surface of part molded with T_{mold} = 126.7 ^{o}C.

The concentration of compressive force on micropillars in a localized area can thus lead to detrimental effects on the final part. The lowest mold temperature is not included due to the negligible replication.

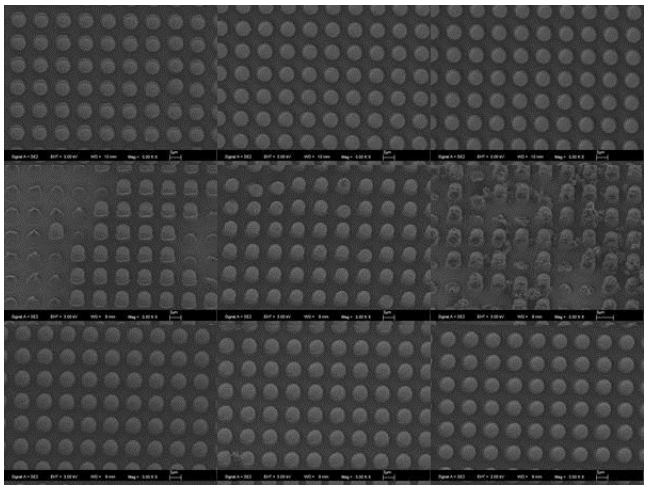

Figure 5-67: Micrograph of surface of part molded with T_{mold} = 137.8 ^{o}F.

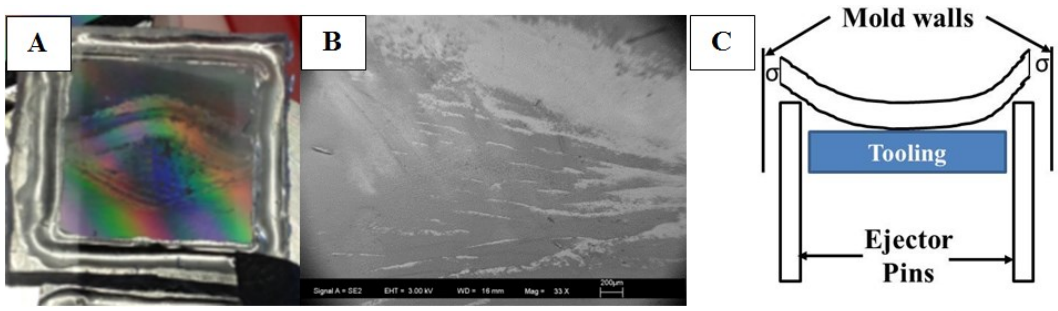

Figure 5-68: Photograph of part molded using a mold temperature of 137.8 ^{o}C with microfeatured and non-microfeatured regions clearly visible (A), micrograph of part displaying the same inhomogeneity (B), and schematic illustrating deflection of part responsible for inconsistent replication (C).

5.7.3 COC Molding with Taper Trial 4 Short Channels

Multiple revisions were made following inconsistent replication across the part surface. To ameliorate the excessive stress applied to the vertical surfaces of the part causing deflection, a 5^{o} draft (initially 2^{o}) was applied to such surfaces. In addition, silicon tooling containing a more gradual draft angle and void of scallops (which functioned as nano-undercuts) was used. The improved tooling is shown in section 4.1.7 and the insert assembly is shown in Figure 5-69.

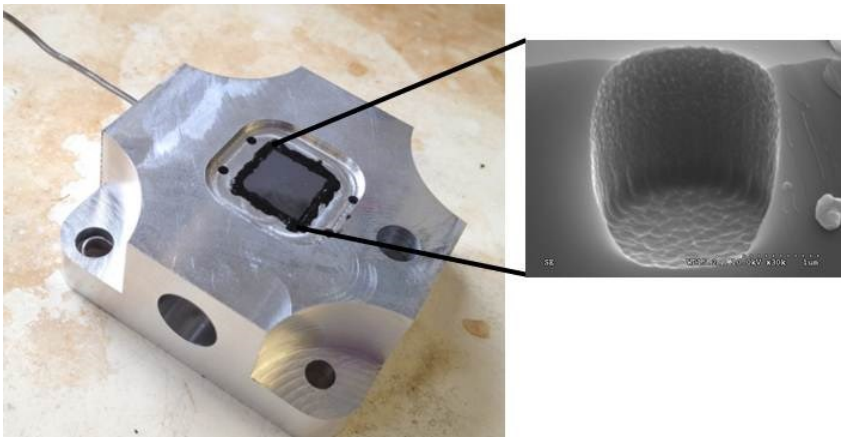

Figure 5-69: Aluminum and silicon (inset) tooling used for molding.

5.7.3.1 Experimental

Nearly identical processing parameters from the previous trial were used (using taper trial 3 tooling) due to the high RQ previously attained (except for cooling time) The mold temperature was increased slightly to ensure that the mold temperature did not get lower than T_g of the polymer for any cycle.

Table 5-15: Processing parameters for COC short taper trial molding study.

Process Parameter	Value
Nozzle Temperature (°C)	293
Mold Temperature (°C)	137.8
Injection Velocity (mm/s)	70
Injection Limit Pressure (MPa)	20
Holding Pressure (MPa)	30
Holding Time (s)	10
Cooling time (s)	45
Ejection Temperature (°C)	104.4

5.7.3.2 Results

Uniform pillars were seen across the entirety of the microfeatured surface as shown in Figure 5-70. The average pillar height was 1.71 ± 0.02 μm, which corresponds to a replication quotient of 0.76. Although the microfeature achieved contained a

relatively low aspect ratio, it was vital to qualify the use of the tooling etched with the passivation compensation technique. In addition to relatively high replication, the reduction of surface texture of the microfeature vertical faces indicates that the novel tooling fabrication scheme resulted in increased tooling quality through the reduction of scallops.

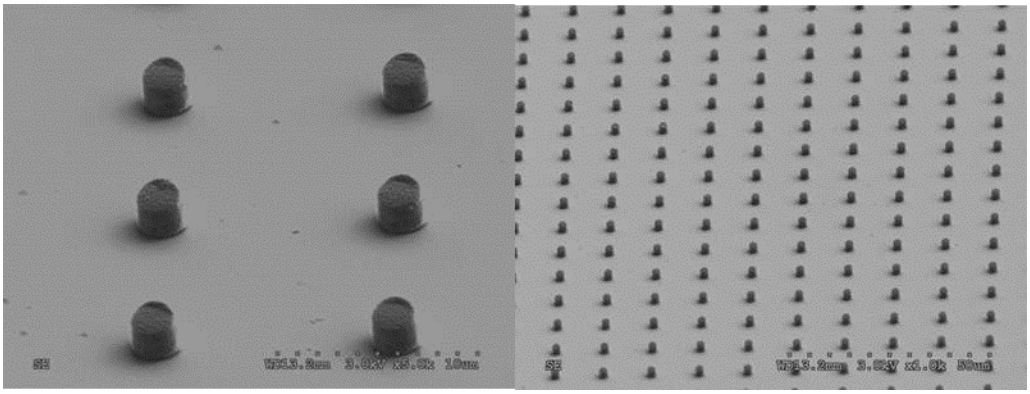

Figure 5-70: Micrographs of COC micropillars molded with short channels.

To further test the limits of replication using passivation compensation tooling, COC was also molded into deeper channels and replication was optimized using a Taguchi orthogonal array.

5.7.4 COC Molding with Taper Trial 4 Deep Channels – L9 Taguchi Array

Upon replicating the short channels with a significant level of replication relative to the total channel depth with a high level of consistency, deeper channel inlays were used to create higher aspect ratio pillars. Significant challenges are associated with molding topography with high aspect ratio features, as replication of individual microchannels can prove difficult, as well as consistent replication across a surface

containing millions of features. It has previously been mentioned that maximum achievable aspect ratios are reduced with decreasing feature size [**140**].

5.7.4.1Experimental

As previously mentioned, the use of a direct sprue gate was employed to facilitate a high level of processing uniformity across the part surface. The tooling design is shown in Figure 5-71, which contains microchannels with a depth of 5.9 μm.

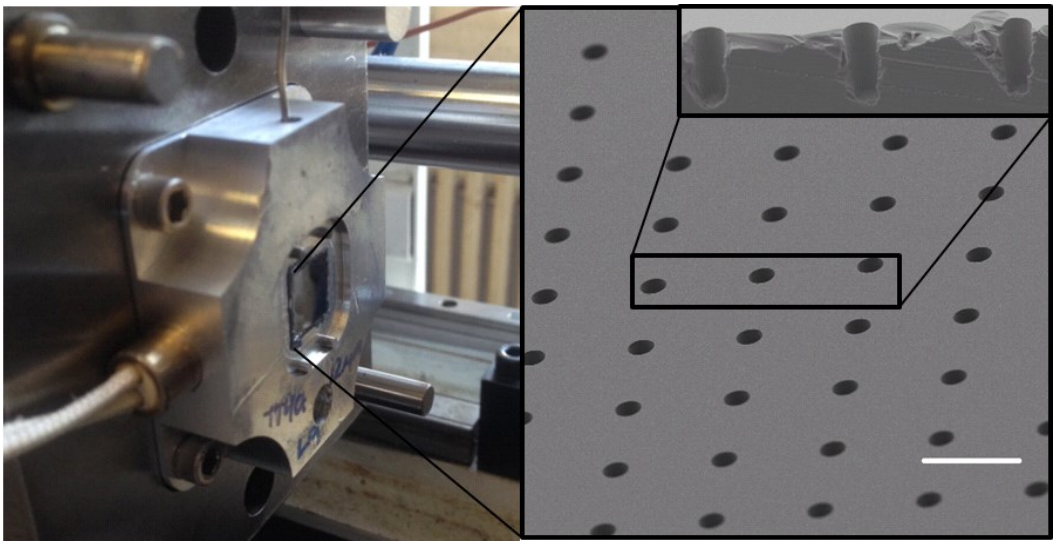

Figure 5-71: Tooling used for L9 Taguchi Arrays showing 12 spaced microchannels with tapered profile. Bar indicates 10 μm.

A robust Taguchi orthogonal array was used to identify the optimum molding parameters, and to determine which mold settings were more significant compared to others. The chosen parameters are shown in Table 5-16. For analysis of results, a Taguchi signal/noise ratio analysis using the "Larger-is-better" criterion to assess which parameters most dramatically altered replication.

Table 5-16: Processing parameters for L9 study with long tapered channels trial 4 molding study

Parameters	Value
Nozzle Temperature	293.3
Mold Temperature (°C)	132.2, 137.8, 143.3
Injection Velocity (mm/s)	100,150,200
Holding Pressure (MPa)	30,40,50
Holding Time (s)	4,7,10
Cooling Time (s)	40
Ejection Temperature (°C)	95

5.7.4.2 Results

Pillar heights ranged from 2 to 4.3 µm, corresponding to replication quotients of 0.34 and 0.73, respectively. Measurements of each trial are shown in

Table **5-17**. Figure **5-72** shows the signal/noise plots for all processing parameters used. Mold temperature was the most influential parameter affecting replication. Moreover, the middle level mold temperature facilitated replication more than the highest value. Holding time also significantly affected replication, with higher values being more advantageous. Injection velocity and holding pressure both had a small effect comparatively.

The subsequent optimized parameters were the middle mold temperature (280 °F), high level hold time (10 s), high injection velocity (200 mm/s), and middle holding/packing pressure (40 MPa). Not all optimized values corresponded to high levels (mold temperature, holding pressure) and some parameters had no definite trend of increasing replication with increasing value (i.e., injection velocity and holding pressure).

Table 5-17: L9 Replication for Taper Trial 4 deep channels with COC. Units of height are μm.

Condition	Mold Temperature °C	Injection Velocity (mm/s)	Holding Pressure (MPa)	Holding Time (s)	R1	R2	R3	R4	R5	R6	Ave.
1	132.2	100	20	4	2.06	1.92	2.22	2.16	2.06	1.84	2.04
2	132.2	150	30	7	2.73	2.73	2.55	2.64	2.57	2.61	2.64
3	132.2	200	40	10	2.91	2.74	2.70	2.51	2.71	2.90	2.75
4	137.8	100	30	10	4.56	4.50	4.69	4.60	4.61	4.55	4.59
5	137.8	150	40	4	3.03	2.78	2.96	3.04	3.00	3.04	2.98
6	137.8	200	20	7	4.30	4.40	4.55	4.47	4.08	4.28	4.35
7	143.3	100	40	7	3.98	4.10	4.03	4.07	4.01	4.16	4.06
8	143.3	150	20	10	4.05	4.16	3.87	4.13	4.12	4.07	4.07
9	143.3	200	30	4	3.14	3.35	3.61	3.34	3.37	3.23	3.34

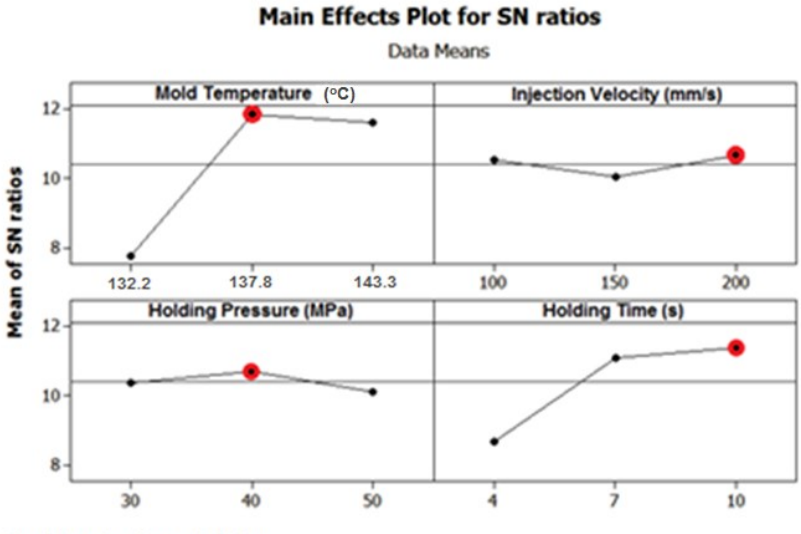

Signal-to-noise: Larger is better

Response Table for Signal to Noise Ratios
Larger is better

Level	Mold Temperature (Deg C)	Injection Velocity (mm/s)	Holding Pressure (MPa)	Holding Time (s)
1	7.769	10.514	10.359	8.687
2	11.809	10.017	10.698	11.109
3	11.598	10.645	10.120	11.380
Delta	4.040	0.628	0.578	2.693
Rank	1	3	4	2

Figure 5-72: Signal/Noise ratio main effects plots with significance rankings for COC replication. Optimized parameters are circled in red.

Aside from height, pillar shape appeared to match the same tapered structure present on the microchannels. Overall shape profile quality appears to be best for

conditions 4 and 7, in which the common parameter between the two is a low injection velocity (100 mm/s). Perhaps the lower velocity imparted a lower shear rate during microchannel filling, resulting in less built up residual stress. Frozen stress can result in polymer warpage if unevenly distributed through the feature, which could be the cause of pillar bending for conditions 3, 6, and 8.

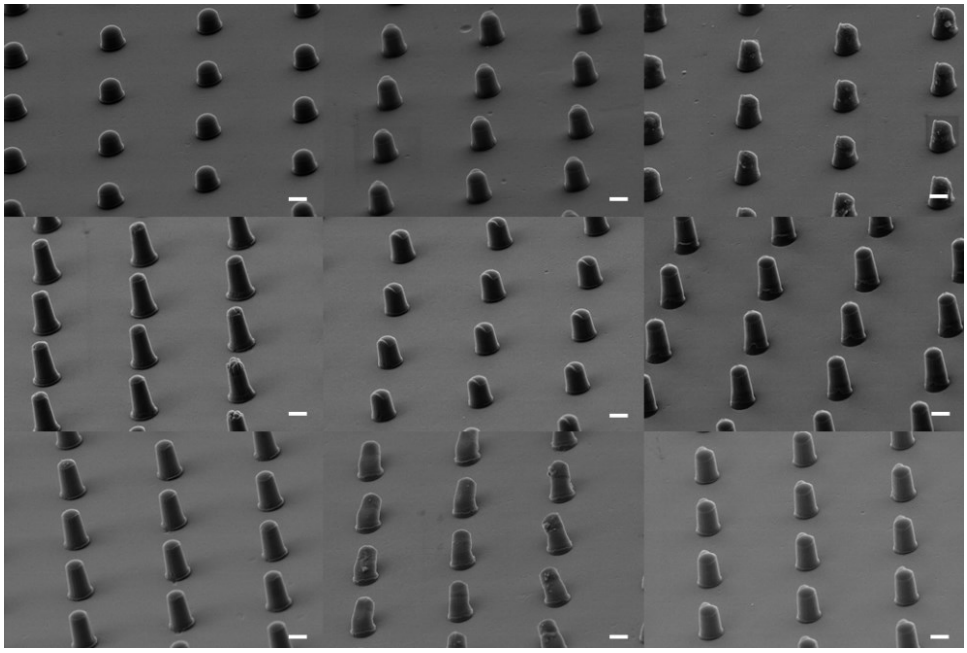

Figure 5-73: Micrographs of molded 12 μm spaced COC micropillars for Taguchi orthogonal array. Condition one is the top left image, and the conditions progress from left to right and top to bottom. White bar indicates 2 μm in length.

5.7.5 Optimization Verification – COC

The optimized parameters were used to verify the results of the conducted experiment and achieve the highest possible level of replication. Based on prediction calculations, the expected subsequent pillar height was 4.5 μm.

5.7.5.1Experimental

Table 5-16 processing parameters were used with the optimized parameters previously determined. 12 μm spaced microchannel tooling used to verify that optimized parameters resulted in optimized values 3, 4, and 8 μm spaced micropillars were also molded to observe if values were altered by microfeatured spacing. It has been claimed that spacing between microfeatures does not alter replication [**36**] and that surface roughness does not impact cavity filling [**141**]. However, the microfeature geometry and surface area coverage may be significant enough to alter fluid mechanics at the inlay-polymer interface.

5.7.5.2 Results

The use of closely spaced tapered features in molding was detrimental to the tooling at the optimized injection velocity, as shown in Figure 5-74. The distance between features for the 3 μm spaced tooling was ca. 0.175 μm. The impulse force associated with injection created excessive stress at the inlay surface, thereby fracturing the top tooling layer and permanently damaging the silicon. For an interaction where the polymer is making direct contact with a surface perpendicular to the flow vector, a dramatic change in momentum is inevitable, making relatively delicate features susceptible to damage. The same type of fracture occurred for microchannels spaced 4 μm apart.

Fracture also occurred for the inlay with 4 μm spaced channels. To allow for replication without tooling damage, an injection velocity of 100 mm/s was used instead of 200 mm/s for only the 4 μm spacing inlay. The alteration was made to avoid fracture

of the inlay during molding. It was expected that the change would not impart significant variation in replication, as the previously executed Taguchi analysis indicates minimal change in replication when comparing 100 mm/s with 200 mm/s.

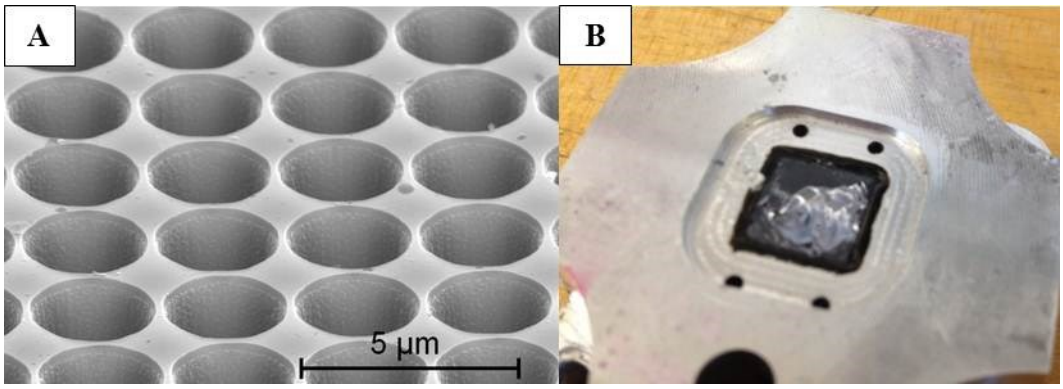

Figure 5-74: Taper trial 4 long channels with 3 µm C2C spacing (A) and fracture of silicon surface due to impact force applied during molding (B).

Molded pillars appear to have a tapered profile from the base for approximately half of their heights. However, a distinct head region is present at the top of the pillars (Figure 5-75), which may contribute to tensile stress and elongation of pillars.

For the 8 µm and 4 µm spaced inlays, highly uniform microtopographic regions were successfully molded, as shown in Figure 5-76 and Figure 5-77. There appears to be somewhat of a correlation between feature replication and feature spacing. Figure 5-78 shows the trend of spacing effects on replication. Studies that have noted no difference in replication based on feature spacing have utilized only localized regions of microfeatures, while the current study involves the use of a relatively large surface area of microfeatures. Replication was lower than expected for 4 µm and 8 µm spaced features, and higher than expected for 12 µm spaced features (if assuming similar replication to the 12 µm spaced pillars). The height enhancement may be the result of tensile pillar stretching during demolding.

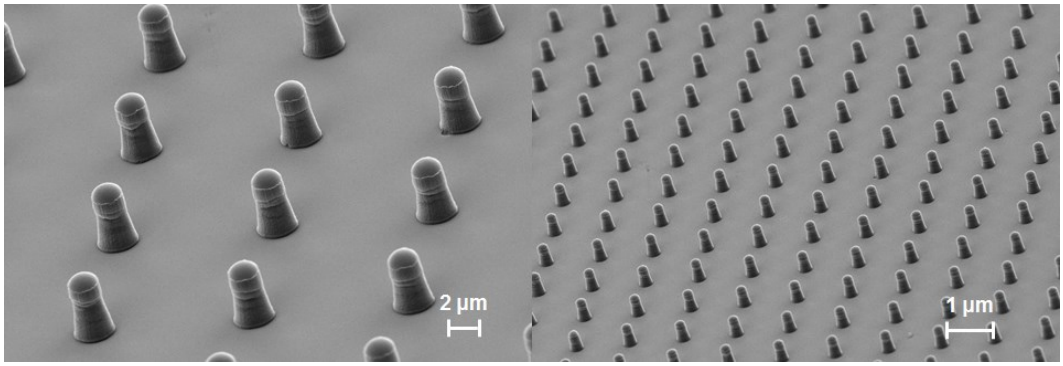

Figure 5-75: Micrographs of 12 µm spaced COC pillars verifying replication of optimized parameters. Pillar height was 4.84 ± 0.04 µm. The base and tip diameters were 2.91 ± 0.01 µm and 2.15 ± 0.01 µm, respectively.

The argument could be made that the lower injection velocity used for the 4 µm spacing could have caused the lower pillar heights. However, the 8 µm spaced micropillars are also significantly below that of the 12 µm spaced pillars.

The variation in spacing directly affects the number of micro-inlets to be filled, and thus may alter the available pressure. Moreover, the increased surface area associated with additional microfeatures may result in enhanced heat transfer away from the polymer melt to the relatively cooling inlay, thereby preventing further flow into the microfeatures. For regions where the melt front is traveling perpendicular to the axis of the microchannels, a "rippling" effect could occur, especially in the case of the 4 µm spaced microchannels, where the channels consume more surface area than flat silicon.

The potential could exist for the flow to be subjected to roughness effects, which for macroscale molding is only critical in terms of appearance and surface finish. At the microscale, the roughness could alter polymer flow and heat transfer [**142**]. Zhang et al has previously noted the reduction of overall part filling with an increase in surface

roughness due to an increased resistance to flow [**141**]. Thus, the extent to which the microfeatures were effecting replication should be carefully considered.

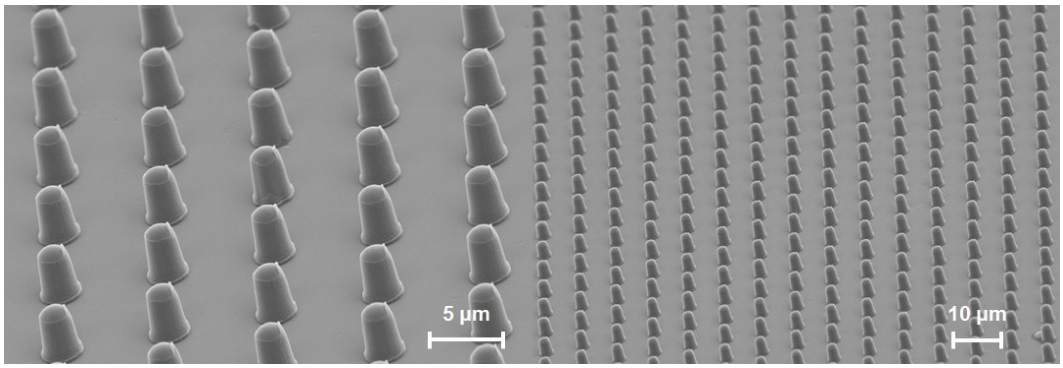

Figure 5-76: Micrographs of 8 µm spaced COC micropillars using optimized molding parameters.

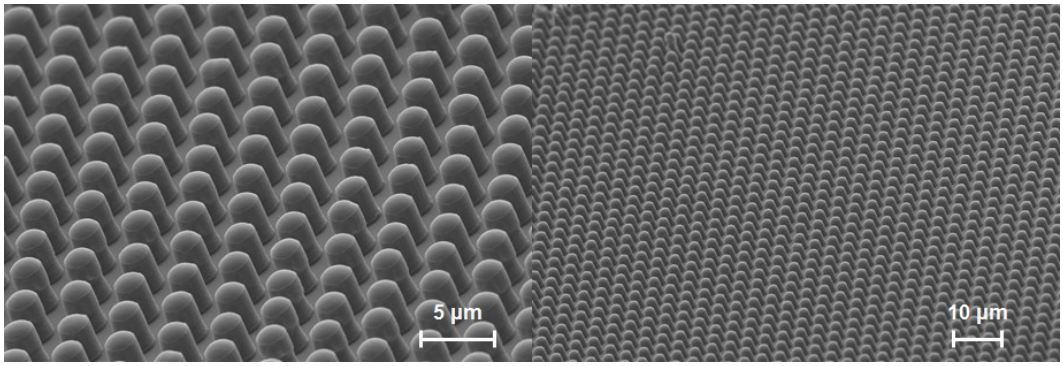

Figure 5-77: Micrographs of 4 µm spaced COC micropillars using optimized molding parameters.

There was a directionally dependent lip at the tip of pillars filled outside of the main gate area for all three spaced topographies, as shown in Figure 5-79. The lip is found closer to the middle of the part, indicating that the feature is due to some type of gate proximity effect. One potential cause of the tip protrusion is the effect of shrinkage that can occur towards the center of the macroscale plate during cooling. While shrinkage amounts are fairly small for the macroscale plate, the change in dimension may be large relative to the micropillars in relation to the silicon channels they occupy prior to

ejection. Thus, during demolding, even with the use of tapered tooling, a certain amount of friction can build up preferentially along one side of the micropillar wall. This issue has previously been observed by Guo et al during the process of hot embossing [**143**].

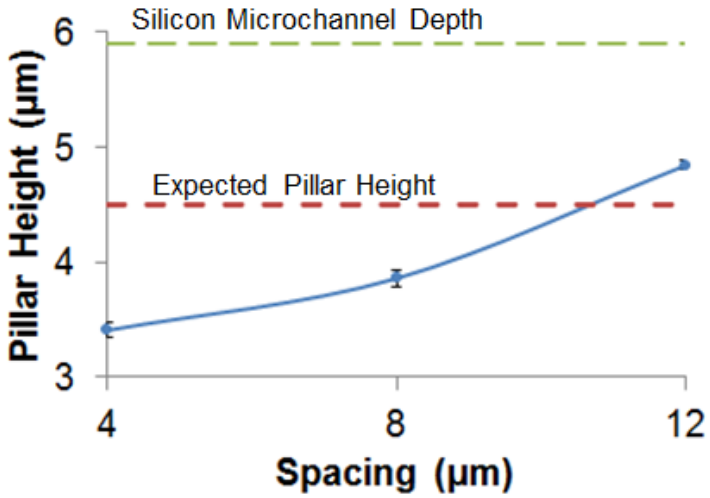

Figure 5-78: COC Pillar height as a function of spacing using optimized values. Values compared to expected and maximum replication.

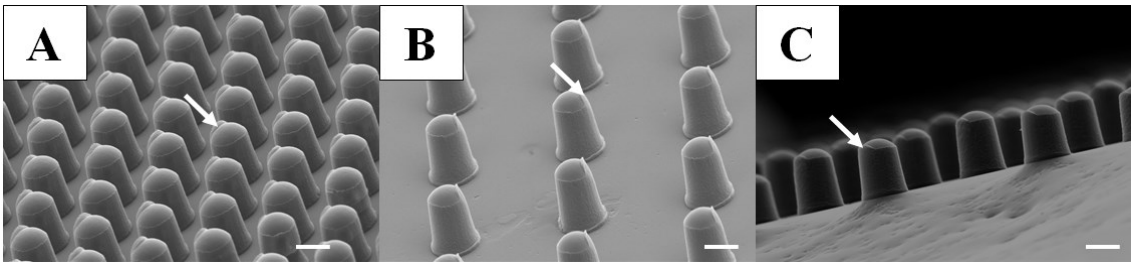

Figure 5-79: Presence of lip at tips of pillars. The lip is positioned closer to the gate of the part. Arrows point to individual lips, and bars indicate a 2 µm length.

5.7.6 COC Water Contact Angle Analysis of L9 Optimized Tapered Beams

It was expected that topography would induced dramatic changes in hydrophobicity. Unlike the previous WCA experimentation, the pillars used for the given study are tapered, thereby complicating the roughness and solid area fraction comparison.

5.7.6.1 Experimental

Highly consistent pillar networks with three different pitches (shown previously in Section 5.7.5.2) were characterized via water contact angle analysis using the same protocol as Section 5.5.1.3. To measure Wenzel roughness and Cassie solid surface fraction, the average diameter of the pillar was used. Advancing, receding, and static angle measurements were taken and recorded. Results were reported as average ± standard error.

5.7.6.2 Results

Contact angle increased with increasing pillar density and increasing roughness, which is the opposite of what is predicted with regards to Wenzel and Cassie states (Figure 5-80). Measured values for the 12 and 8 μm spacing fall between Wenzel and Cassie predictions, while the 4 μm spaced pillars slightly exceeds that of the Cassie prediction (Table 5-18).

The COC surface transitioned from slightly hydrophilic to relatively hydrophobic with a reduction in pillar spacing (i.e., increase in pillar density). Moreover, hysteresis varied across conditions.

The discrepancy between experimental and predicted values could be a transition from a Wenzel to a Cassie state. As roughness increases, the surface becomes increasingly hydrophobic and approaches (and surpasses) predicted Cassie contact angles.

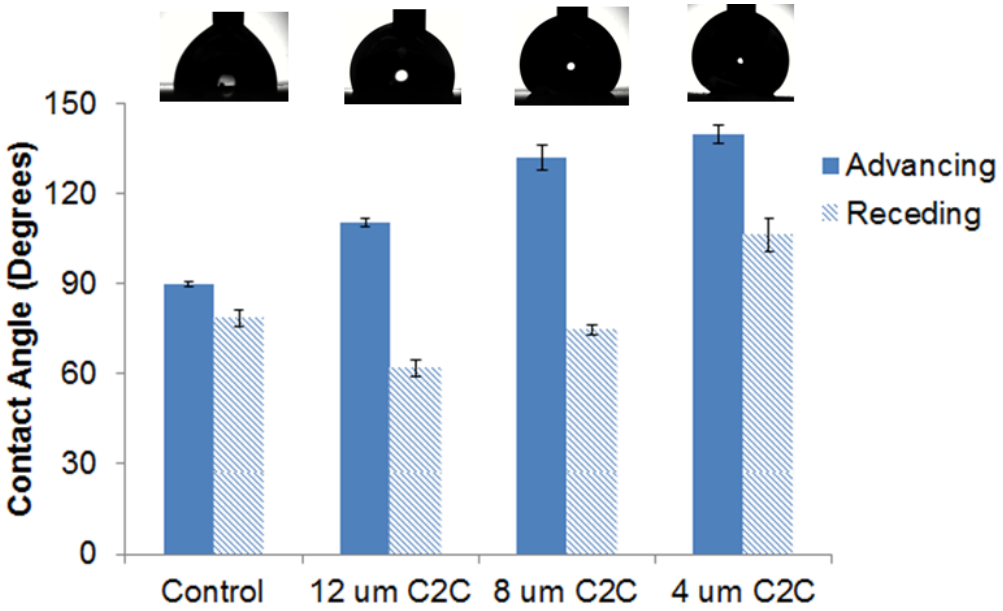

Figure 5-80: Advancing and receding water contact angles for control and microfeatured COC substrates with characteristic advancing contact angle digital images.

Table 5-18: Wenzel and Cassie values for microtopographic surfaces, predicted values, and actual values.

	12 µm C2C	8 µm C2C	4 µm C2C
r	1.27	1.49	2.7
f_s	0.0349	0.0830	0.3167
Wenzel	89.56	89.48	89.06
Cassie	164.77	156.42	132.95
Actual (advancing)	110.33 ± 1.51	131.73 ± 4.30	139.78 ± 3.08

To further explore the potential of such a transition, hysteresis values were calculated as a function of surface roughness. It appears that hysteresis initially increases with increasing roughness and then is reduced at higher roughness values, as shown in Figure 5-81. A possible explanation is the transition from a Wenzel to Cassie state due to a higher roughness. As previously mentioned, roughness values > 1.35 typically follow a Cassie regime, in which solid surface fraction dictates hysteresis instead of Wenzel

roughness. In the previous WCA study, hysteresis was large for both topographies and not dependent on roughness or solid area fraction. The rose petal effect seen previously may have been attenuated in the given study via smoother vertical microfeature surfaces. The easier release of the droplet from the microtopography may be the result of reduced nanotopography on the micropillar surfaces.

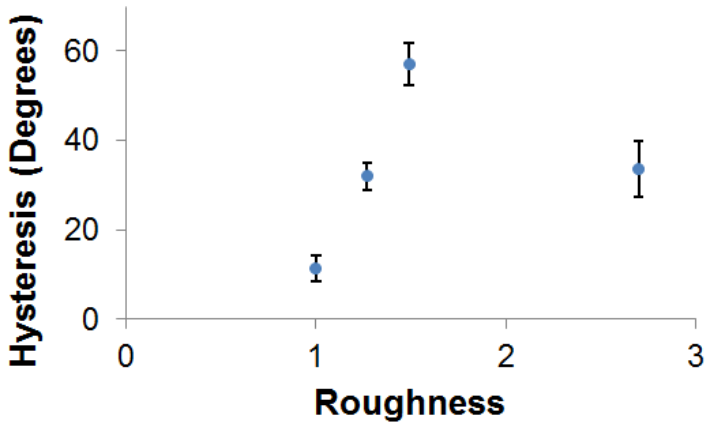

Figure 5-81: Hysteresis as a function of roughness of water droplets on flat (r=1) and microfeatured COC substrates.

5.7.7 Conclusion – COC

A consistent array of micropillars was molded through robust experimentation, in which mold temperature was identified as the most influential parameter (mid-level being optimum). Holding time was also a somewhat important factor. Optimization verification resulted in a maximum replication of 0.82, in which spacing slightly effected replication.

Tapered microtopography induced variations in wettability. Specifically, a reduction in pillar spacing enhanced hydrophobicity. The increase is thought to be the result of a transition from a Wenzel to a Cassie state. Hysteresis, which provides an

indication of the "stickiness" of a surface, increased initially with increasing pillar area density, but was reduced at the highest density.

The wettability of a substrate has significant implication for interfacial interactions between substrates and biological cells, as cells are profoundly impacted simultaneously by surface chemistry, topography, and wettability [**144**]. Thus, the detailed analysis of the surface characteristics of a substrate allows for a more intentional robust control when engineering the appropriate surface for stem cell development.

5.7.8 TPU Molding with Taper Trial 4 Deep Channels – L9 Taguchi Array

Processing parameter effects are material and geometry dependent. To assess the importance of different parameters while molding TPU, another orthogonal array was used. The tooling was identical to that of the COC L9 study. Barry et al. has previously reported that for Texin 990 (similar properties to Texin 985) replication of nanofeatures was enhanced significantly by higher mold temperatures and, to a lesser extent, by higher injection velocities [**33**]. Although TPU flexibility helps to prevent brittle fracture of microfeatures, replication may not be as precise due to the rounding of corners experienced by more compliant materials [**90**].

5.7.8.1 Experimental

TPU micromolding was conducted using a design of experiments approach, in which mold temperature, nozzle temperature, injection velocity, and holding pressure were varied, and pillar height was used as the experimental metric. Values for all parameters were chosen based on recommended values and levels that could potentially

enhance microscale replication (i.e., higher mold temperature, nozzle temperature, etc.). The process parameters are shown in Table 5-19. Injection velocities were kept fairly low due to an inconsistent velocity profile at values > 80 mm/s. The tooling previously used in Figure 5-71 was once again utilized for molding.

Table 5-19: Experimental molding parameters used for TPU L9 orthogonal array.

Process Parameter	Value
Injection Velocity (mm/s)	30, 55, 80
Holding Pressure (MPa)	25, 35, 45
Nozzle Temperature (°C)	200, 213, 226
Mold Temperature (°C)	40, 55, 70
Barrel Temperatures (°C)	T_{nozzle}/193.3/187.8/ 187.8/182.2
Holding Time (s)	7
Cooling Time (s)	20

Six pillar height measurements were recorded for each condition. For the Taguchi analysis, the "Larger-is-Better" signal-to-noise ratio calculation was chosen, as the objective with molding was to achieve as close to 100% pillar replication (i.e., pillar height = 5.9 μm) as possible.

5.7.8.2 Results

Pillar height ranged from a value of 1.9 μm to 5.54 μm, corresponding to replication quotients of 0.32 and 0.94, respectively. Measured pillar heights are shown in Table 5-20. Maximum replication was significantly greater than that of COC. The wide variation in replication indicates that the parameter ranges chosen were sufficient to observe dramatic effects on molding. Taguchi analysis reveals that holding pressure had

the most significant impact on replication compared to all other varied parameters (Figure 5-82). Nozzle temperature variations had the least amount of impact.

Table 5-20: TPU Pillar heights for each condition and average. Values used for Taguchi replication results.

Condition	R1	R2	R3	R4	R5	R6	Ave.
1	1.94	2.08	1.81	1.70	2.04	1.81	1.90
2	4.22	4.25	4.33	4.50	4.81	4.35	4.41
3	4.98	5.09	4.92	4.80	4.84	4.77	4.90
4	4.36	4.44	4.26	4.33	4.48	4.39	4.38
5	5.60	5.47	5.65	4.92	5.29	5.32	5.38
6	6.03	5.82	6.09	5.18	4.84	5.27	5.54
7	4.69	5.05	4.63	4.98	4.61	4.96	4.82
8	4.75	4.86	4.79	5.01	5.08	4.79	4.88
9	3.12	2.37	2.37	2.49	2.72	2.45	2.59

The optimized parameters were the mid-level mold temperature (55 ^{o}C), mid-level nozzle temperature (213 ^{o}C), high level injection velocity (80 mm/s), and mid-level holding pressure (35 MPa). As was the case with the COC L9 trial, the highest settings in all varied parameters did not necessarily translate to higher replication. The optimal conditions are higher than recommended processing conditions for mold and nozzle temperature, and on the lower range of recommended holding pressure. Unlike the COC trial, holding pressure had the largest impact on replication, while mold temperature was the second most influential parameter. Nozzle temperature was found to have the least significant impact compared to the other parameters. Overall melt temperature is determined by a the combination of many different parameters used to control the physical transfer and heat transfer of the resin as it moves from the hopper to the mold.

Consequently, a change in nozzle temperature may have not altered the melt temperature to a great extent to bring about changes in replication.

Replicated structures varied in quality for the different molding conditions (Figure 5-83). There were slightly raised linear structures present between features, especially for lower mold temperature conditions. The marks could be caused by roughness-induced flow pattern alterations amplified by increased shear rate resulting from lower mold temperatures. In general, the pillars with the most consistent shape were those molded at the mid-level mold temperature.

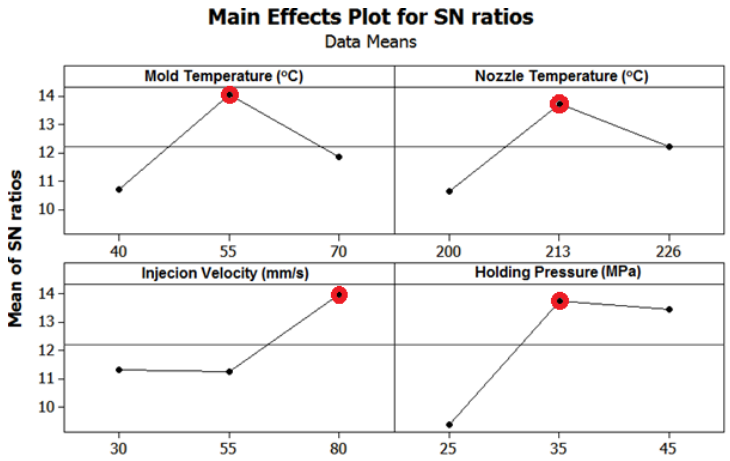

Level	Mold Temperature	Nozzle Temperature	Injection Velocity	Holding Pressure
1	10.718	10.652	11.343	9.403
2	14.057	13.735	11.272	13.759
3	11.845	12.232	14.006	13.458
Delta	3.339	3.083	2.734	4.356
Rank	2	4	3	1

Figure 5-82: Signal-to-Noise ratio plots and relative parameter importance rankings of controlled molding parameters for TPU Taguchi array.

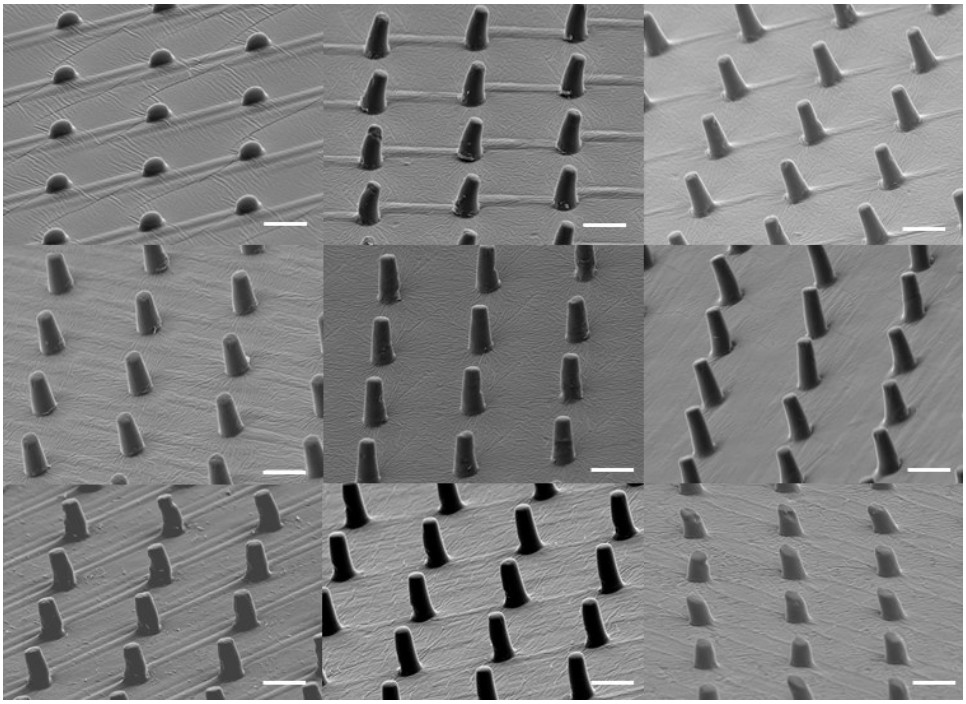

Figure 5-83: Micrographs of TPU L9 Taguchi array micropillars. Conditions are ordered from top left (condition 1) to bottom right (condition 9).

Based on the results, it was expected that a pillar height of 5.02 μm could be achieved using the optimized molding parameters. In addition, considering the middle mold temperature was the optimum setting, the shape quality of the pillar was expected to have a high level of surface quality.

5.7.9 Optimization Verification – TPU

To verify Taguchi results and to address potential spacing effects associated with replication (which occurred for COC), TPU was molded using the optimized set of parameter values. Unlike COC, TPU was not significantly affected by spacing, with both measured pillar heights being similar and near the expected result (Figure 5-84).

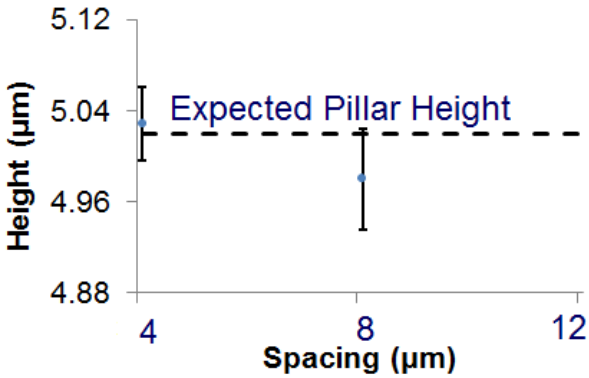

Figure 5-84: TPU pillar height as a function of spacing. 12 µm spacing not shown due to excessive polymer clogging skewed results.

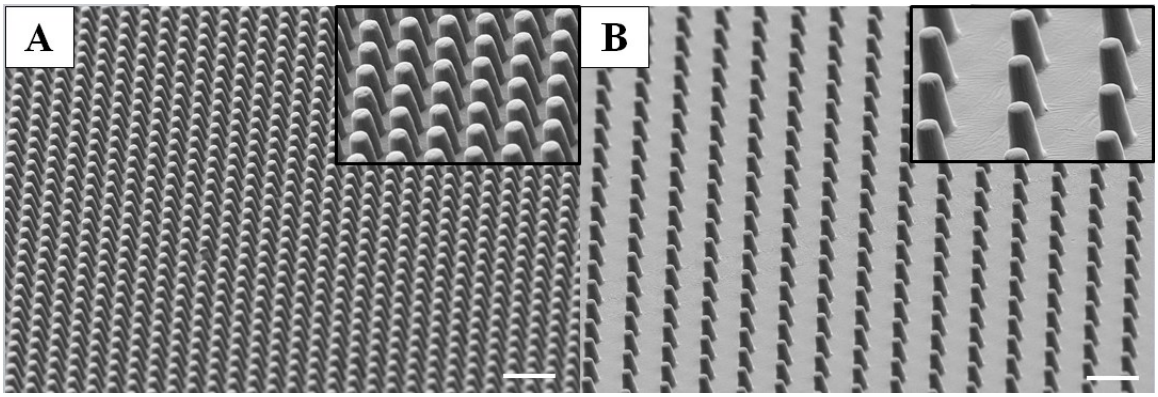

Figure 5-85: Micrographs of TPU microfeatured surfaces molded with optimized parameters. 4 µm (A) and 8 µm spaced micropillars are shown with high magnification inset for both. Bar indicates 10 µm.

5.7.10 TPU Water Contact Angle Analysis of L9 Optimized Tapered Beams

Wenzel roughness values exceed the Wenzel / Cassie transition for both tested microfeature samples (Table 5-21), and the Cassie solid surface fraction was approximately four times greater for the 4 µm spaced samples over the 8 m spaced, as was expected considering the relation between pitch and pillar density of orthogonally arrays (pillar density = $1/\text{pitch}^2$).

Wettability of flat TPU substrates were slightly hydrophobic ($\theta_{adv} = 97.2 \pm 1.0^{o}$), which was unexpected considering that hygroscopic materials typically have lower

advancing contacting angles [**145**]. The curious results maybe the effect of modified macromolecular structure at the surface imparted during processing.

Microfeatures dramatically modified the wettability of TPU substrates to nearly superhydrophobic values in terms of contact angle, as shown in Figure 5-86. Values exceeded Wenzel predicted angles, while Cassie predictions were above actual measurements for the 8 µm spacing and slightly below for the 4 µm spacing. Results followed the general trend offered by the Wenzel model of increasing hydrophobicity with increasing topographic density.

Table 5-21: Wenzel and Cassie values for TPU microtopographic surfaces, predicted values, and actual values.

	8 µm C2C	4 µm C2C
r	1.59	3.4
fs	0.071	0.289
Wenzel	101.495	115.222
Cassie	159.7	138.35
Actual (advancing)	120.6 ± 5.4	141.1 ± 2.0

Hysteresis appears to increase with an increase in WCA (Figure 5-87). It was expected that the rose petal effect, mentioned in section 5.5.2.4, would be attenuated by the reduction of scalloped features on the sides of the pillars (as was the case in section 5.7.6.2 with tapered COC pillars). However, a significant level of hysteresis still occurs even in the absence of nanotopography. The enhancement may be the result of the difference in bulk material properties between COC and TPU, and possibly due to the hygroscopic nature of TPU. The increase of hysteresis with increasing solid surface

fraction has previously been observed (on patterned silicon wafers), but also with a simultaneous reduction of both advancing and receding angles [**61**].

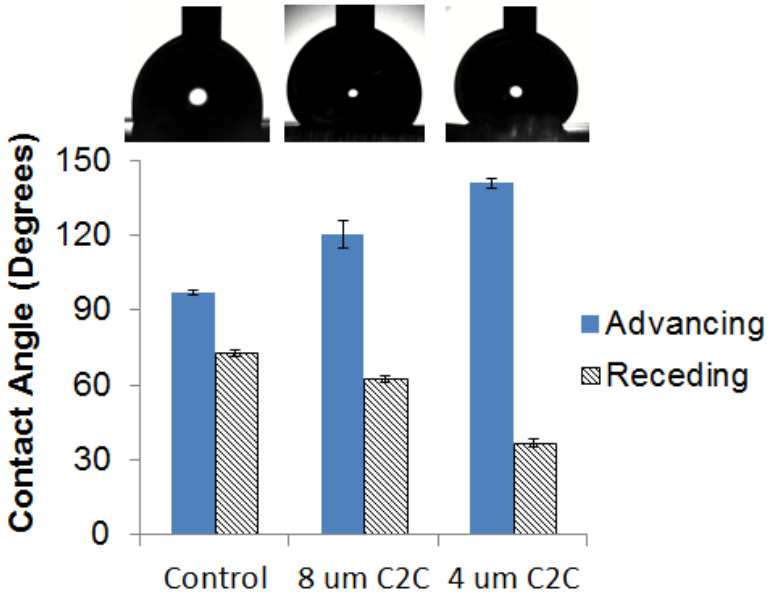

Figure 5-86: Advancing and receding contact angles as a function of topography. Characteristic digital images of advancing angle water droplet is shown above associated data.

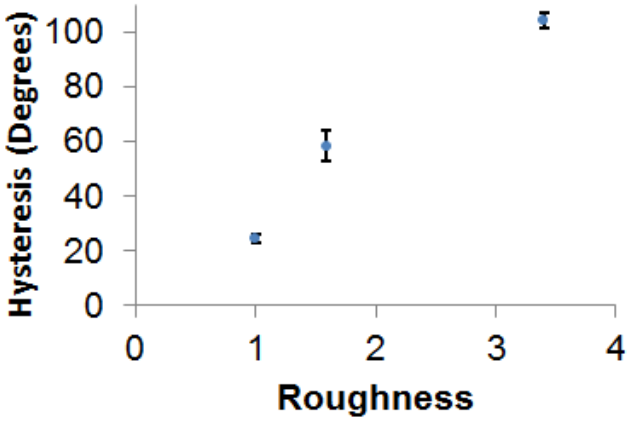

Figure 5-87: Hysteresis as a function of roughness of water droplets on flat (r=1) and microfeatured TPU substrates.

5.7.11 Conclusion –TPU

TPU replication was highly uniform and reached a replication of 0.85 with the optimization verification. Molding parameters shown to most dramatically effect molding quality were holding pressure and mold temperature. There was no space dependence on replication.

Water contact angles showed that TPU was slightly hydrophobic, and hydrophobicity increased with surface roughness. Contact angle hysteresis continued to increase with roughness in contrast to COC. The difference may be due to material properties.

5.7.12 Conclusion

The embedded cartridge heater assembly, combined with tapered tooling, dramatically enhanced micro-injection molding replication capabilities. The localized heating and temperature control combined with microscale features designed with the consideration of traditional injection molding principles led to replication degree, quality, and consistency previously unachievable. COC and TPU with aspect ratios of >2 were obtained in a highly reliable and high rate manner. Replication values of

Wettability was measured as a function of topography and compared to well-established contact angle theories. Considering that the hydrophobicity of a substrate has previously been proven to influence cytoskeletal organization, which can be linked to cell fate, an ideal bio-interfacial design will incorporate tuned wettability in addition to specific mechanical and biochemical properties.

6 Mechanical and Thermal Properties of Microscale Polymer Parts

Vital to engineering design is the characterization of the mechanical properties of a molded part, as part function is dictated by geometrical and material characteristics. Microscale phenomena has been known to alter mechanical properties, as multiple studies have observed changes in elastic modulus, weld line strength, and yield stress when transitioning from macro to microscale dimensions [**146**,**147**,**148**]. However, not much research has been conducted on the impact that different processing parameters have on one specific microscale geometry.

For a processing technique such as injection molding, which involves high levels of pressure, temperature, and shear, the resultant part properties can be dramatically different from parts fabricated under less extreme manufacturing conditions (i.e., drop casting, hot embossing, etc.). Moreover, parameters used to mold microscale features are often outside of processing ranges recommended for traditional injection molding (due to the added temperature and pressure necessary to fill the part), which can alter part properties to an even greater extent.

With respect to semi-crystalline polymers, processing conditions will undoubtedly affect crystallization behavior and subsequently the mechanical properties [**149**]. Amorphous polymers will also be affected, as polymer chain orientation (which plays a large role in material resistance to deformation) is dependent on molding parameters. Moreover, both amorphous and semi-crystalline polymers experience a reduction in molecular weight during the molding process, which will also affect part performance.

Parts containing microscale domains designed specifically to allow for characterization were molded using a variety of different processing conditions, and

tested mechanically and thermally to cultivate a deeper perspective on processing dependent properties.

6.1 Microscale Tensile Specimen Trial 1 – Cyclic Olefin Copolymer

Micro tensile bars were manufactured, in which the gage region (i.e., region to be mechanically tested) was a microscale feature. Elastic modulus is a critical parameter associated with pillar bending mechanics and the overall cell sensing model for a cell interacting with a microfeatured substrate. Although elastic modulus is considered a bulk property (i.e., the value does not change with shape or size), multiple reports have concluded that at smaller dimensions, mechanical properties can vary from macroscale values [**147**,**150**,**151**,**148**].

In the same manner that a micro-injection molding machine is not simply a reduced-scale version of a conventional molding machine, a micro tensile bar design needs to account for the difficulties associated with handling and characterizing micro and nanoscale components. A wide range of small-scale tensile testing approaches has been investigated, in which both manual and automated systems have been explored [**150**].

6.1.1 Micro Tensile Bar Design

One useful property inherent to the injection molding process is the connectivity between sprue and part, which results in a mount for easier specimen handling (Figure 6-1B). The molded tensile bar includes an additional tab region used to aid in ejection the

part out of the cavity, as the ejector pins used in the existing assembly are too large to fit inside of the shoulder domains.

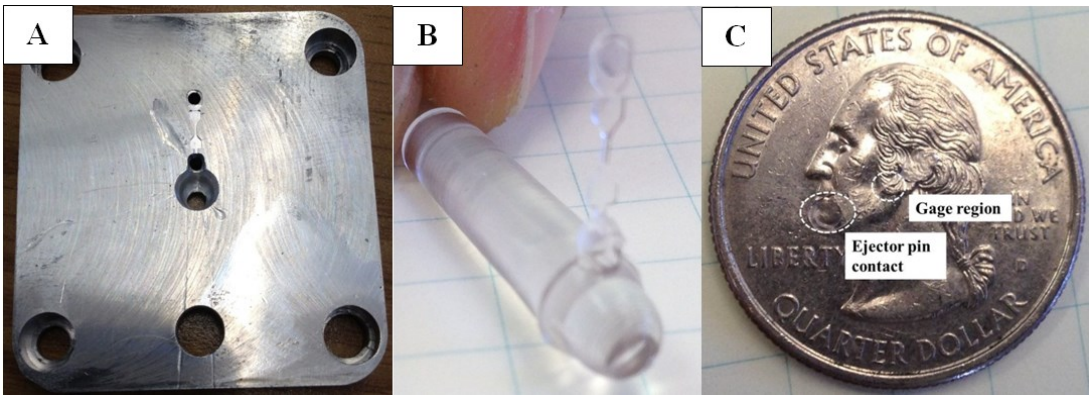

Figure 6-1: Tensile testing mold insert (A), molded micro tensile bar (B), and tensile bar on quarter for reference (C).

The key disparities between the macro and microscale geometries are larger shoulder regions and a thicker gage region (relative to gage width). The altered geometry, shown in Figure 6-2, is used to allow for easier handling and gripping, and prevention of fracture prior to testing. After molding, a few post-processing operations were required to prepare the sample for subsequent characterization. The part was de-gated and the additional tab was removed so that the tensile bar could fit securely into the micro tensile testing fixture, as shown in Figure **6-3**.

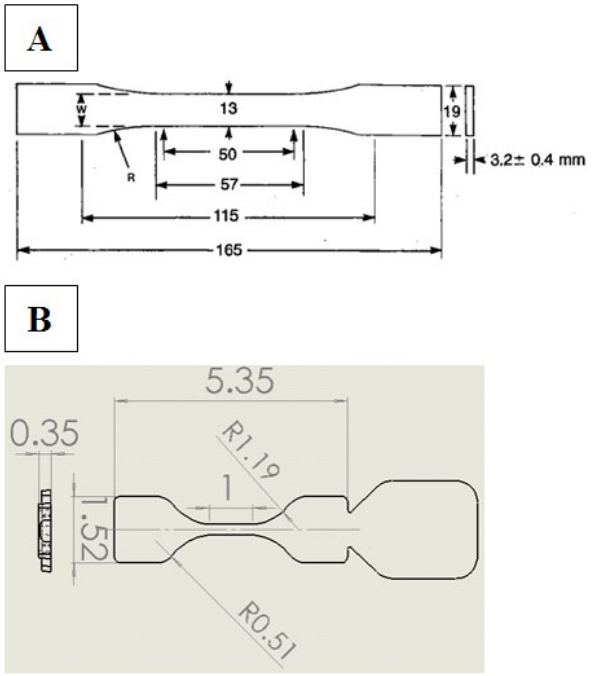

Figure 6-2: Comparison of ASTM D638 standard type I tensile bar (A) and designed micro tensile bar (B). All units are given in mm.

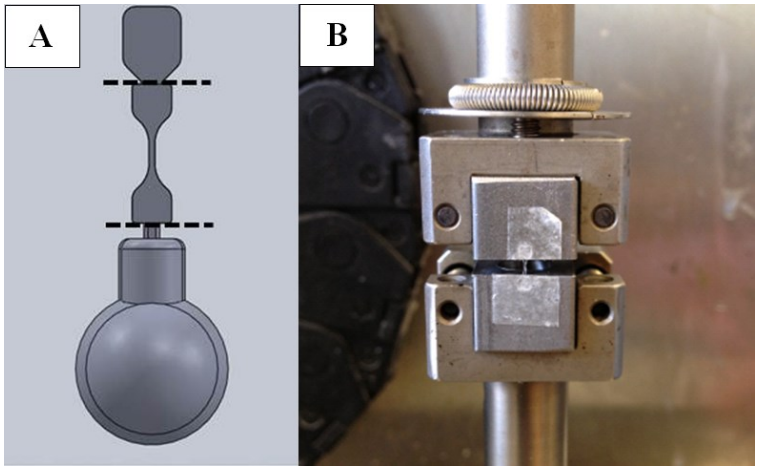

Figure 6-3: Schematic of molded tensile bar showing location of preparation cuts (A), and photograph of experimental tensile testing set-up (B).

6.1.2 Experimental

Process dependent micromechanical and thermal properties were assessed through the micro-injection molding and testing of polymer tensile specimens approximately 1/6 the mass of a single resin pellet, containing microscale gage region.

6.1.2.1Molding

Tensile bar specimens were molded using the constant parameters shown in Table 6-1 and the varied settings shown in Table 6-2. For the mold temperature of 126.7 ^{o}C, the assembly was permitted to cool to an ejection temperature of 104.4 ^{o}C prior to ejection. The micro tensile cavity and molded part dimensions were verified through the use of scanning electron microscopy.

Table 6-1: Constant conditions for COC molded tensile bars.

Parameters	Value
Holding Pressure (MPa)	20
Holding Time (s)	10
Barrel Temperature (^{o}C)	293.3/287.8/276.7/248.9/182.2
V/P Switchover (mm)	4
Cooling Time (s)	30

Table 6-2: Tested parameter settings for COC micro tensile bar molding.

Condition	Mold Temperature (^{o}C)	Injection Velocity (mm/s)
1	60	100
2	60	180
3	60	260
4	82.2	100
5	82.2	180
6	82.2	260
7	104.4	100
8	104.4	180
9	104.4	260
10	126.7	100
11	126.7	180
12	126.7	260

6.1.2.2 Mechanical Characterization

The samples were tested mechanically using a tensile testing procedure commonly used for thin plastic sheeting in the form of ASTM standard D882-12. This method was chosen since it allows for calculation of elastic modulus. Although the

molded dimensions are not classified as a film (according to ASTM D883), the part is thinner than the minimal thickness required for commonly used ASTM D638 standard procedure. The device used was a Rheometrics ARES system, which has a precision of 0.1 mg and can measure forces up to 2 kg.

For each condition, eight samples were tested, in which the highest and lowest values were discarded. Samples were stretched uniaxially at a constant crosshead speed of .0777 mm/min, which corresponds to a strain rate of 0.035/min. The strain was chosen to be lower than that of the macroscale study (0.1/min) to more deliberately observe mechanical deformation activity. Strain was measured through displacement values of the upper grip as a function of time. The following calculations were used to generate stress and strain values to determine elastic modulus.

$$\boldsymbol{\sigma} = \frac{\boldsymbol{F}}{\boldsymbol{A_{gage,CS}}}, \ \boldsymbol{\varepsilon} = \frac{\boldsymbol{dx_{cross-head}}}{\boldsymbol{L_{gage}}} \qquad \text{Equation 6-1}$$

A two-tailed paired student t-test was conducted, and results were considered significant if $p < 0.05$. Results were reported as mean ± standard error.

6.1.2.3 Thermal Characterization – Differential Scanning Calorimetry

Differential scanning calorimetry (DSC) was used to characterize the effects of mold temperature and shear rate on the thermal properties of the COC tensile test specimens. More specifically, glass transition temperature (T_g) changes were measured as a function of processing parameters. The thermal and mechanical properties of the polymer have been shown to be controlled by the COC norbornene content, in which a

higher % of norbornene corresponds to a higher glass transition temperature, greater stiffness, and more strength [**152**]. With regards to the effects of process-induced changes, microscale processing has been shown to result in modified part mechanical properties [**147**].

TOPAS 5013 has a norbornene content ca. 77%, which corresponds to the higher range of percentage compared to other grades. T_g is a thermal property which can be related to molecular weight via the Fox-Flory equation, given in Equation 6.2 (re-arranged to solve for number averaged molecular weight) [**153**].

$$\boldsymbol{M_n = \frac{K}{T_g^{\infty} - T_g}} \qquad \text{Equation 6-2}$$

T_g^{∞} is the glass transition temperature of the melt were to have infinite molecular weight and K is a constant specific to the free volume of a polymer part. The free volume is the space created by the presence of a polymer chain end. A reduction in molecular weight causes a decrease in T_g because the shorter molecular chains are able to move more easily than long ones, and consequently do with less required kinetic energy (temperature) compared to longer chains [**154**]. Thus, a lowering of the T_g value is indicative of reduced molecular weight. Although infinite T_g and K were not determined for COC, a decrease in T_g was taken to be the result of a decrease in molecular weight as a general trend.

A reduction of T_g during molding was expected due to the inherent degradation which occurs during the injection molding process. The degradation and reduced

molecular weight of the part has significant implications in subsequent mechanical properties of the part. As far as the author is aware, there is no public literature available regarding the effect of the injection molding process on the thermal properties of COC.

For thermal testing, 3 samples were loaded into each pan per trial, in which the sample masses were between 5 and 6 g. The additional ejector tab was removed from the sample so that only the tensile bar was loaded into the pan. The test was run in accordance with ASTM standard E1356-08. DSC tests were conducted under N_2 atmosphere in which the system was equilibrated at 80 ^{o}C (at least 50 ^{o}C below suspected glass transition) for 3 minutes, heated at a rate of 10 ^{o}C per minute until reaching 180 ^{o}C, and cooled at 10 ^{o}C per minute to 80 ^{o}C. 2 runs (6 samples total) were conducted per condition and 3 trials were run. The 2 runs were averaged for each condition. 3 separate trials were run to increase statistical significance. Heating and cooling was conducted under a nitrogen atmosphere. For analysis, the midpoint temperature was taken as the value of T_g for all runs. A two-tailed paired t-test was used to assess significance in which $p < 0.01$ was assumed to be significant.

6.1.3 Results

It was determined that although a discrepancy existed between the designed cavity and actual cavity, the cross-sectional gauge region area was relatively close to the intended value. As expected from the inherent effects of mechanical micromilling, nanoscale roughness was left on the cavity surface from the machining operation (Figure 6-4D).

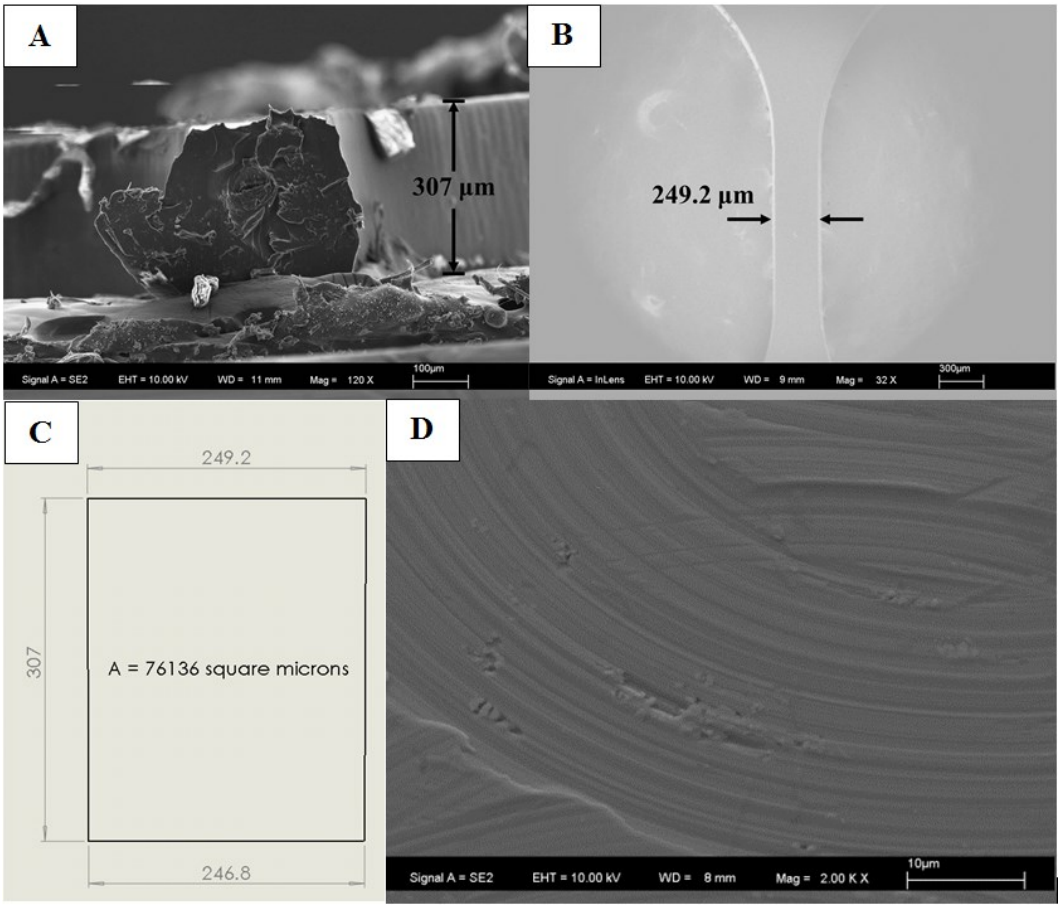

Figure 6-4: Micrograph of Micro-tensile Bar thickness (A) and width (B). (C) is a schematic of the gage cross-sectional area (units are in µm). (D) shows nanoscale roughness of the tooling cavity surface.

6.1.3.1Mechanical Analysis

Stress-strain curves were successfully generated for all conditions, in which a representative plot is shown in Figure 6-5. In comparing a micro tensile bar stress-strain curve to a typical curve for a macroscale specimen molded with the same material, a few discrepancies are apparent. The microscale specimen shows a greater ultimate tensile stress, greater elongation, and shallower slope (i.e., lower elastic modulus).

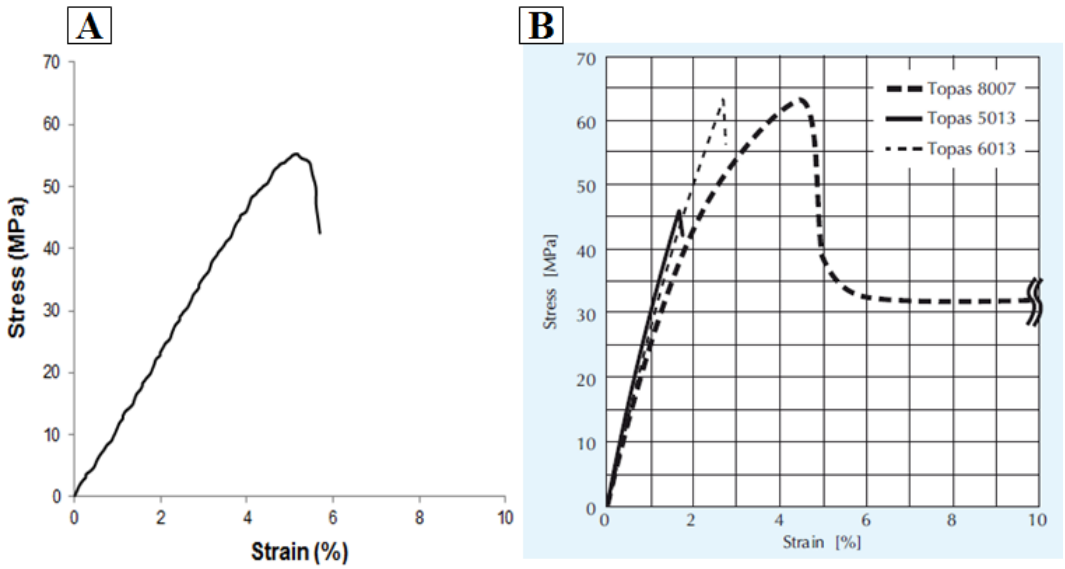

Figure 6-5: Representative stress-strain curve of micro tensile study for TOPAS 5013 (A) and stress-strain curve from TOPAS brochure showing different grades of COC (B) . ISO 527, which is similar standard to ASTM D638, was used.

Processing parameters were shown to only slightly affect elastic modulus, with no apparent trend based on injection velocity and mold temperature. However, elastic modulus was dramatically lower (1200 – 1350 MPa) compared to that of macroscale molded COC (measured to be 3091 ± 32 MPa). The overall reduction in elastic modulus could be due to the degradation associated with excessive shear, as the polymer melt is forced through a relatively small micro-cavity region. The only notable differences between samples based on processing changes are between the two lower mold temperatures at the lowest velocity and between parts molded at low and high velocity at a mold temperature of 82.2 ^{o}C. In both cases, there is not a high level of significance.

Previous results have found that decreasing the tensile specimen size increases yield strength and tensile modulus, as shown in Figure 6-7. The cross-sectional area of the micro tensile bar used for the given study is 0.0761 mm^2 and the range of elastic moduli was 1200 to 1330 MPa, which is slightly below the value obtained in the previous

study [**74**]. However, the results obtained in Figure 6-7 were done so using a strain rate of 0.167/min (over four times the rate of that of the current study) which can result in higher values due to the well-known strain-rate dependence of mechanical properties.

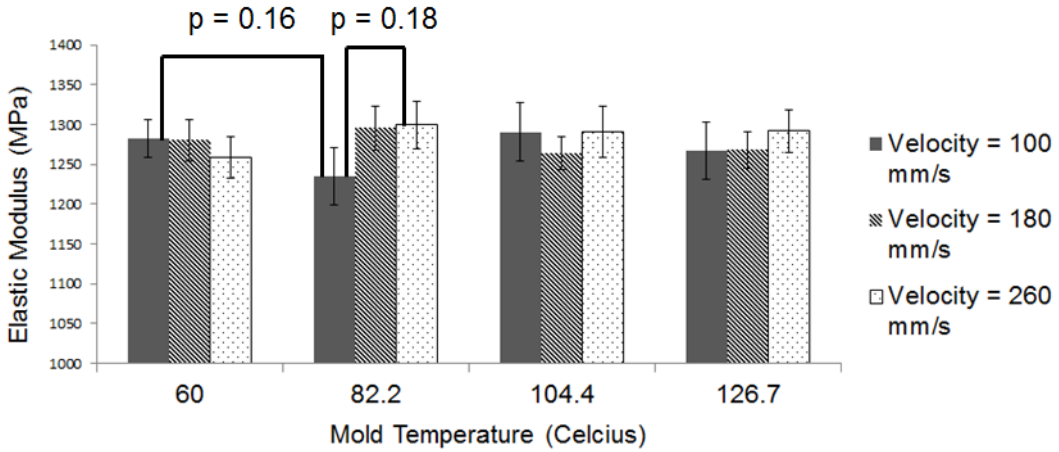

Figure 6-6: Elastic Modulus of COC as a function of processing parameters. Values are average ± standard error.

It is also important to note that the tensile testing assembly can dramatically affect results. Due to the use of equipment not specifically designed for gripping micro tensile specimens, the custom grips grasped the shoulders of the tensile bars through the use of cavities machined into the grips, as shown in Figure 6-8. The effective gage region at the moment the part begins to engage in tensile deformation is equal to the distance between grips, which is shown to be 2.212 mm. Consequently, the entire region between the grips, inclusive of the transition region between gage and shoulder, was tested.

When testing a molded part for mechanical properties, it is important to know the speed of force the part will be exposed to in actual operation. The given research seeks to explore the effects of microscale molding on polymer microfeatures, so that their use for mechanical control of the bio-interface will be better understood. Forces and stress values

of focal adhesion applied forces have been measured. However, there are no values available of the speed with which such forces are applied.

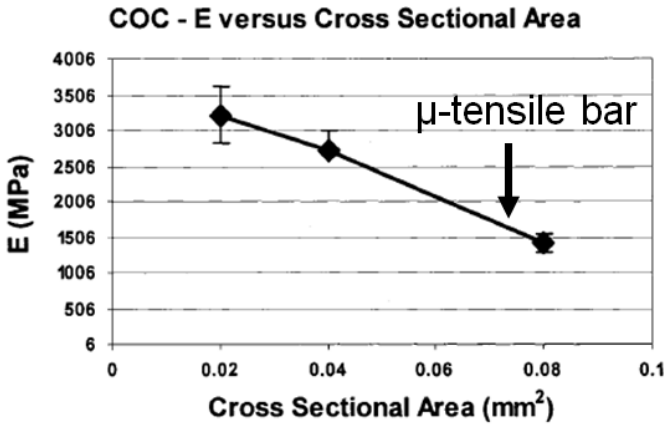

Figure 6-7: Reduction in elastic modulus as a function of increasing cross-sectional area [74].

Consequently, understanding mechanical properties for a range of strain rate may be beneficial in cultivating a comprehensive understanding of the potential manner in which the polymer substrate could respond to such forces.

Over the wide range of processing parameters used (injection velocity: 100 – 260 mm/s, T_{mold}: 60 – 126.7 ^{o}C), the elastic modulus was relatively unaffected. The consistency across conditions may prove useful during micromolding, as extreme molding conditions often need to be used to achieve acceptable levels of replication. To reach the desired replication without sacrificing mechanical properties would be ideal.

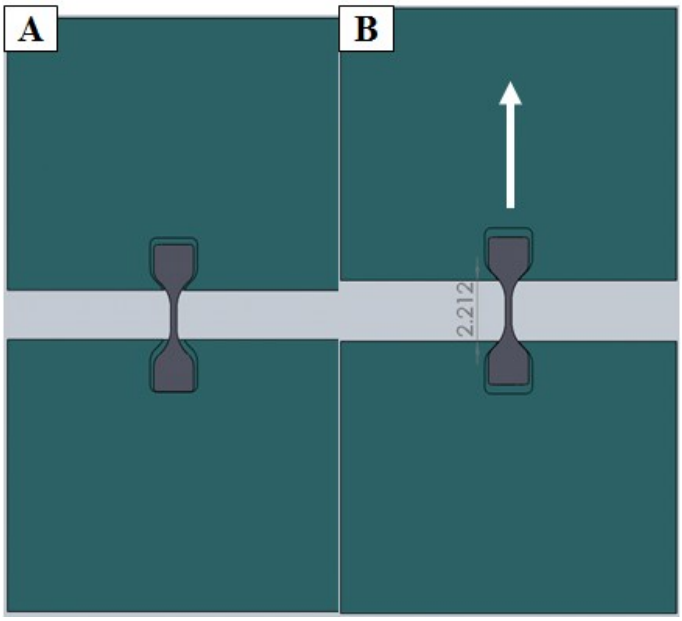

Figure 6-8: Schematic of tensile testing set-up showing manner in which manually placed specimen (A) is fixed during stretching (B). Units are in mm.

6.1.3.2 *Thermal Analysis*

Glass transition temperature was determined for all molding conditions and unmolded controls (pellets). A characteristic curve is shown in Figure 6-9. An endothermic dip is visible at the transition zone, in which energy is being supplied to the sample to initiate the phase change. The transition is fairly small, which could be an indication of the sample mass being relatively low. The glass transition is the initiation of movement of amorphous or "glassy" polymer chains. The onset of the glass transition temperature is often given as a value for ejection temperature for injection molding.

There was a very apparent dependence of processing parameters on glass transition temperature. It was interesting to note that T_g values were within error of the control T_g for 2/3 of the conditions. A certain level of degradation occurs during molding, as the polymer is melted, sheared, and pressurized into a final cavity. For a few

conditions, namely the highest injection rate for the middle mold temperature ranges, the glass transition temperature appears to be higher than that of the unprocessed polymer. Such results may be caused by phenomena other than molecular weight variation. Potentially, the enhanced shear caused by the polymer melt passing through the small cross-sectional gage region of the cavity may have aligned the molecules to a greater degree, thereby creating a higher level of orientation. The enhanced molecular order may have then requiring additional kinetic energy to mobilize the molecules, resulting in higher values of T_g.

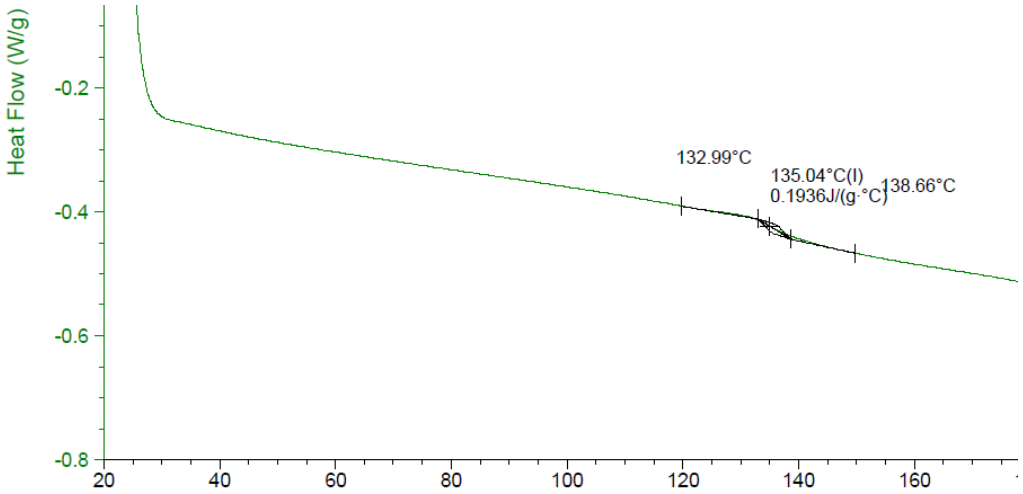

Figure 6-9: Characteristic DSC graph with measurement of glass transition temperature.

No consistent trend was observed for changes in mold temperature and changes in injection velocity. A few values were statistically significant, as shown in Figure 6-10. However, the differences were unexpected and are somewhat difficult to explain. It was anticipated that lower mold temperatures and higher injection velocities would reduce glass transition temperature due both in part to increased shear. Excessively high shear rates can result in polymer degradation leading to a reduction in molecular weight.

Potentially enhanced molecular orientation was responsible for a higher order structure more resistant to polymer chain mobilization (i.e., higher T_g).

In general T_g values were low for the highest mold temperature compared to others. The higher mold temperature was expected to allow for molecular relaxation and a reduction in shear rate, thereby promoting a higher value of T_g. The decrease may be due to the extended period of time during molding that the hotter surface walls permitted the melt to be sheared prior to freezing. The hot mold walls can delay solidification while molding is still in the holding phase, thereby allowing for additional applied force to the molecules and potentially additional shear can result.

In relating thermal results to mechanical results, it appears that the reduction or enhancement of thermal properties does not significantly alter mechanical properties of the molded parts for the range tested. Simulation was not performed as the unchanging elastic modulus with processing parameters made further investigation unnecessary. The lack of correlation between tensile and thermal properties indicates that the polymer used appears to be relatively insensitive to variations in processing conditions in terms of mechanical properties. Although the mechanical properties are relatively unaffected by processing changes, DSC results indicate the change in macromolecular structure, which can alter the molecular orientation and conformation at the substrate surface. In terms of interaction between polymer substrate and biological cell, the microstructure variation could have an impact on cell function.

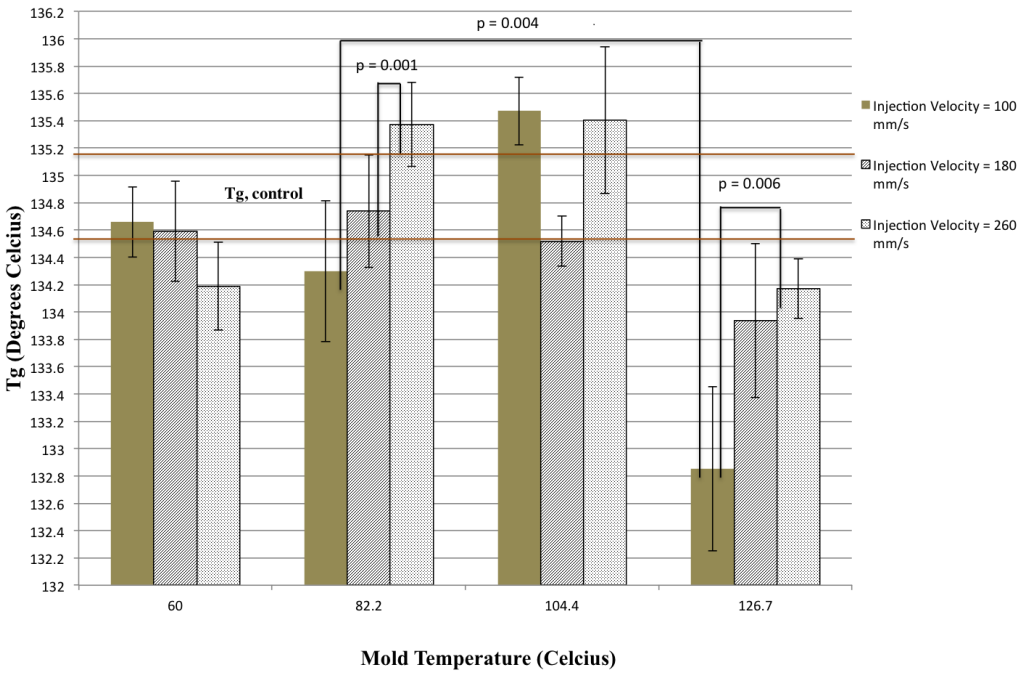

Figure 6-10: Glass transition temperature as a function of injection velocity and mold temperature. Bars represent standard error.

6.1.4 Conclusion

A micro-tensile bar mold insert was successfully designed, manufactured, and used to mold COC tensile bars at different processing conditions. Mechanical and thermal properties were examined as a function of molding parameters. Elastic modulus was dramatically reduced compared to macroscale results, but did not show sensitivity to processing conditions.

Thermal analysis revealed a range of T_g values, indicating processing dependent molecular weight. The alteration in molecule chain length was not large enough to induce dramatic mechanical differences, though could affect other properties, such as optical and long-term mechanical behavior. Moreover, the modified macromolecular surface structure may present a process-dependent chemical environment if biological cells were to interface with the surface. Considering cells are sensitive to chemical structure in

addition to topography and substrate stiffness, such microscale changes during processing must be controlled for optimum cellular response.

6.2 Microscale Tensile Specimen Trial 2 – Thermoplastic Polyurethane

The effects of processing on thermal and mechanical properties of semi-crystalline polymers are more complicated than amorphous polymers due to the multi-phase morphology of the material. It is claimed that the degree of crystallinity is the single most important characteristic of a polymer that determines its mechanical properties and the macromolecular structure is responsible for the initial reaction of a material to stress [**155**,**156**]. Therefore, concurrently analyzing the mechanical and morphological properties of a polymer will give a deeper understanding of the relationship between the two.

In the case of TPU, the percentage of hard and soft segments has an effect on the levels of crystallinity. Processing conditions can alter the type of crystalline structures formed, thereby creating a processing-dependent network of polymer chains which will react a particular way when exposed to forces. Variations in microfluidic flow for parts molded with different injection velocities and mold temperatures were expected to induce differences in both mechanical and thermal properties.

6.2.1 Micro Tensile Bar Cavity Design

An enhanced micro tensile specimen design was engineered to avoid the use of the extra tab used in the COC micro tensile bar analysis. The additional tab was used due to the pre-designed ejector pin sizes being larger than the size of the shoulder regions of

the micro tensile specimen. Smaller ejector pins were used such that the ejector pins could fit into the shoulders of the tensile bar. A schematic of the new mold design is shown in Figure 6-11. The ejector pin size was reduced from 0.065'' in diameter to 0.046875'' (3/64'') in diameter. Another important change made to the insert was the choice of tooling material. 1018 steel was used instead of 6061 aluminum to avoid premature damage of the mold, which was incurred multiple times in the previous study. A CAD model of the insert is shown in Figure 6-11. A 2^{o} angle was applied to the vertical surfaces of the cavity to facilitate demolding. The overall geometry was kept consistent with that of the previous trial (with COC).

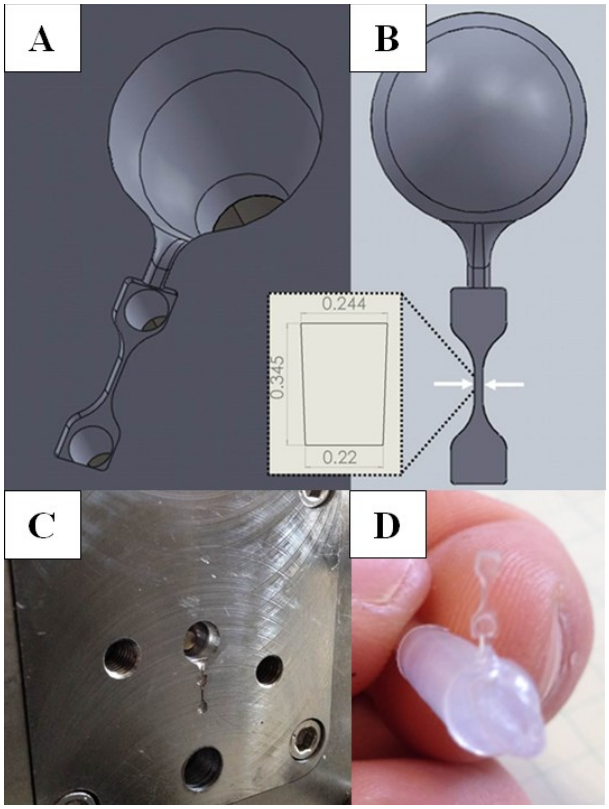

Figure 6-11: CAD model of micro tensile specimen cavity for trial 2 (A) CAD molded part (B) with designed cross-section (inset; dimensions are given in mm), actual steel insert fixed to moving mold half (C), and actual molded TPU part.

6.2.2 Experimental

Molded parts were characterized using the similar techniques to Section 6.1, but adapted to better understand the effects of processing on polymer crystallinity. Dramatic property changes were expected due to microscale effects. Moreover, additional polymer characterization was conducted to assess the cause of significant variability in results comparing one batch to another. Analyses were run in triplicate for molding, tensile testing, and DSC.

6.2.2.1 Molding

The material was dried at 100 ^{o}C for 3.5 h. Mold temperature and injection velocity were varied for the given study, while other settings were kept constant (Table 6-3). Three different temperatures and three different velocities were used (Table 6-4). Thermoplastic polyurethane (TPU) is more shear sensitive compared to the other polymers used, and it has previously been reported that the polymer has virtually no processing window [**157**]. In fact, the recommended maximum shear rate of Texin 985 (TPU) is 20,000 s^{-1}, compared to 40,000 s^{-1} for the other polymers used throughout the given research (PS, COC). Mold temperatures were chosen to be at the high range of recommended values and above. Molding pressure and velocity profiles were recorded directly off of the molding machine control screen via digital photograph.

Table 6-3: Constant (top) and varied (bottom) parameters used for TPU micro tensile testing study.

Process Parameter	Value
$t_{inj} + t_{hold}$ (s)	5
t_{cool} (s)	15
Holding Pressure (MPa)	70
Barrel Temperatures (°C)	212.8/210/207.2/ 204.4/198.9
V/P Switchover (mm)	2

Table 6-4: Varied parameters for TPU micro tensile bar molding.

Condition	Mold Temperature (°C)	Injection Velocity (mm/s)
1	37.8	50
2	37.8	100
3	37.8	130
4	48.9	50
5	48.9	100
6	48.9	130
7	54.4.	50
8	54.4.	100
9	54.4.	130

6.2.2.2 Mechanical Characterization of TPU

As was the case with the first study, tensile testing was performed to assess the effect of processing conditions on elastic modulus, a property that controls the response of a pillar to bending loads used for the cell sensing model previously described in Section 3.4. Thermoplastic polyurethane is a block copolymer with a multi-phase semi-crystalline morphology. The deformation mechanics of semi-crystalline materials is a fairly complicated activity, as failure of the molecules involves intralamellar slipping of crystalline blocks and disentanglement of amorphous regions [**158**]. The level of

crystallinity of a molded polymer part is dictated by initial synthesis and molding conditions involved with fabricating the part.

Tensile testing was performed to observe processing effects on microfeature mechanical properties. Tensile testing protocol was identical to that of the COC micro tensile testing experiments, except six samples were tested per condition. The crosshead speed was slightly different due to the different gage length of the part. A speed of 0.00167 mm/s, which corresponds to a strain rate of 0.0454/min, was used. The first two trials were performed using resin obtained years prior, while the third trial utilized resin received within the past year. The results were compared and significance was identified via a two-tailed paired student's t-test, in which $p < 0.05$ was considered significant.

6.2.2.4 TPU Thermal Characterization

Every mechanical study on mechanical properties should be coupled with a detailed investigation of morphology [**156**]. Moreover, the effect of micro-injection molding process on morphology has received little research attention thus far [**159**]. Given the relatively complex microstructure of thermoplastic polyurethane (TPU), its mechanical utilization as a microscale molded part will be better understood and characterized through the thermal analysis of micromolded TPU parts. Differential scanning calorimetry (DSC) provides two main pieces of information regarding a semi-crystalline polymer part useful to understanding mechanical properties: melting behavior and residual crystallinity from processing [**120**].

Due to the semi-crystalline nature of TPU, properties associated with the phase transition of crystalline regions were measured through the use of DSC in accordance

with ASTM standard D3418-12 to obtain properties associated with melt temperature, such as onset temperature, melt peak temperature, and heat of fusion, which is directly related to crystallinity. DSC tests were conducted under N_2 atmosphere with heating and cooling rates of 10 ^{o}C. The system was equilibrated at 40 ^{o}C for 3 minutes, heated to 250 ^{o}C, and then cooled to 40 ^{o}C.

Three samples were used per run, and two runs were conducted per condition, for a total of six tested samples. The two runs were compared to assure consistent parts for each condition. Each set of three samples were approximately 7 mg. Tensile test specimens were cut into two to fit into DSC pans. Each pan was crimped shut prior to loading into the calorimeter tray. The study was conducted twice with the older resin batch and a third time with a newer batch.

6.2.2.5. Spectroscopic Characterization – FTIR

The dramatic variations in thermal and mechanical properties based on polymer lot led to further analysis of the raw material. The relative chemical compositions of both TPU lots were analyzed through Fourier-Transform Infrared Spectroscopy – Attenuated Total Reflectance (FTIR-ATR). Representative pellets were tested for both lots. 16 scans were run and averaged for each run, and the two curves were compared to note relative variation in chemical bonds present.

6.2.2.6 Melt Viscosity Characterization

To further understanding the differences between the two polymer lots, a melt viscosity test was run using the procedure outlined in ASTM D4440. Viscosity was

measured as a function of frequency, strain amplitude, temperature and time. A Rheometrics ARES Dynamic Mechanical Analysis (DMA) System was employed to observe and compare the two TPU resin lots.

Two parallel plates were used, in which gap of 1.25 mm was maintained between the plates. An initial strain vs. viscosity test was run to determine the strain at which polymer viscosity began to decrease, and the given strain was used for the frequency sweep tests. Tests were run isothermally at 200, 205, 210, 215, and 220 ^{o}C, allowing a 5 minute soak time in between temperatures. The polymers were tested at frequencies between 0.1 and 10. Viscosity, storage, and loss moduli were collected.

6.2.3 Results

The cross-section of the gage region was slightly undersized from the designed size, as shown in Figure 6-12B. The difference is attributed partly to shrinkage of the polymer and partly to the tool diameter being slightly smaller than expected potentially due to tool wear.

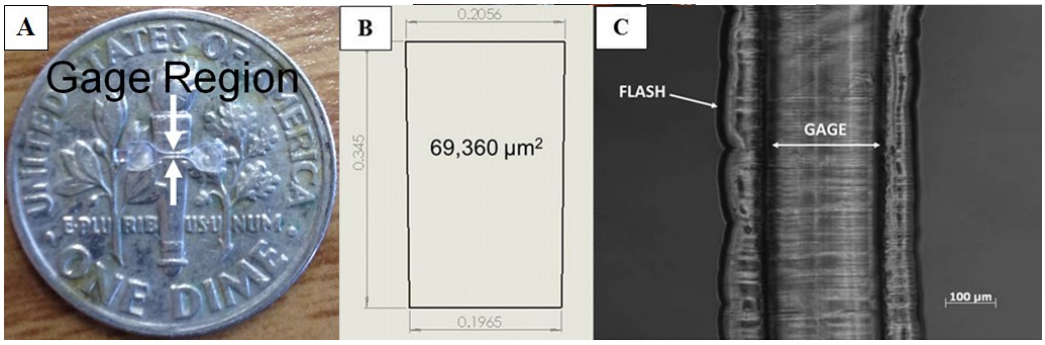

Figure 6-12: TPU micro tensile bar on dime as a size reference (A), actual cross-section of gage region (B), and optical micrograph of gage region (C).

The pressure profiles (Figure 6-13) all exhibited a spike slightly beyond the V/P switchover. It appears that more pressure built up for higher velocities, resulting in a less visible spike near the end of fill. In all cases, the plunger retracted slightly when transitioning from the filling to holding phase due to the large change between injection pressure and set holding pressure.

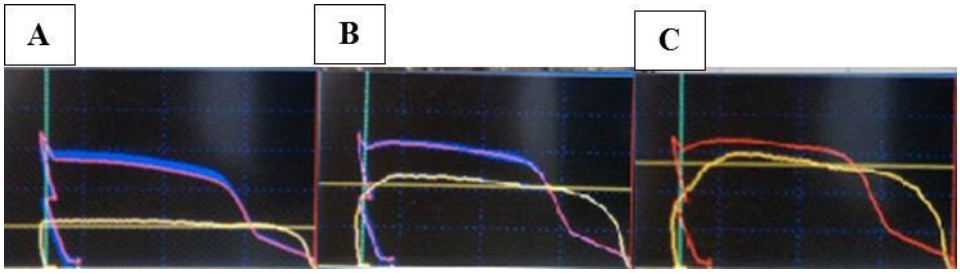

Figure 6-13: Injection pressure and velocity as a function of plunger position at mold temperature of 38 ^{o}C and injection velocities of 50 mm/s (A), 100 mm/s (B), and 130 mm/s (C). Red curves indicate pressure, yellow curves indicate velocity, and the vertical line indicates the V/P switchover location.

6.2.3.1 Mechanical Analysis

The use of different batches of TPU resulted in dramatically different mechanical properties. Although both materials were dried at the same temperature and for the same amount of time, there were significant discrepancies in elastic modulus, in which values of the newer resin batch were approximately half that of the aged resin batch. The first two trials were compared to the third to illustrate the effects of aging on mechanical and thermal properties. The third trial was assessed in detail as a function of processing conditions.

The aged resin lot had an average elastic modulus of 35.3 ± 0.8 MPa, while the newer lot had an average modulus of 16.4 ± 0.4 MPa. The difference is assumed to be the result of a modified crystalline morphology. With regards to the new lot, processing

settings had a dramatic effect on elastic moduli, and several trends were seen. Values ranged from 14.2 – 18.0 MPa, which is slightly higher compared to macroscale testing (E = 12.5 MPa). Figure 6-14 shows that higher mold temperatures and injection velocities led to higher values. Higher mold temperatures could serve to reduce shearing within the gate region and prevent extensive material degradation that may occur during processing of lower mold temperature samples. The same explanation can be used for the cause of increasing modulus with decreasing injection velocity. Lower velocity should create a reduced shear rate profile, thereby limiting molecular chain scission during the molding process.

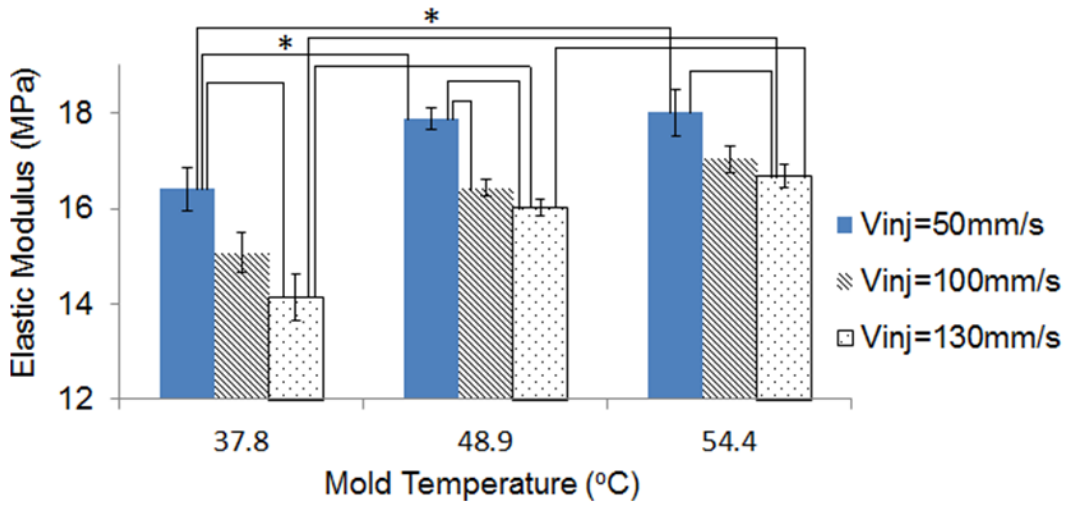

Figure 6-14: Elastic modulus of TPU micro tensile bar specimens as a function of mold temperature and injection velocity used during processing. Brackets with * are $p < 0.05$ and brackets without are $p < 0.01$.

A higher mold temperature should decrease the thickness of the frozen layer, reducing shear as a result. Thus, with control of microscale mechanical properties, the elastic modulus could be selectively chosen based on processing conditions. However, the morphological effects of processing should concomitantly be considered to better understand the overall properties of the polymer part.

6.2.3.2 Thermal Analysis

A comparison between resin pellets from both lots was made to assess the effects of extended storage time on thermal properties. The difference from one lot to the other was dramatically different, in which multiple curves present in the aged resin did not exist for the newer lot (Figure 6-15). The new peaks are associated with some form of crystalline structure that either developed over the course of the aging period, or were the result of differences in synthesis. The relative sizes of the exothermic peaks of the aged samples also indicate a general increase in crystallinity. This is further validated by the presence of a distinct endothermic peak during heating that is barely existent for the newer lot.

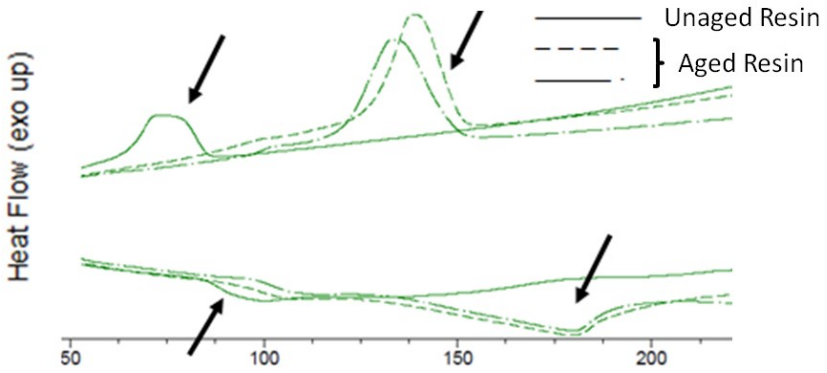

Figure 6-15: DSC curves of resin lots highlighting key differences (shown by arrows).

The endothermic peaks generated by the molded samples were dramatically different from that of the unprocessed pellets. The effects of molding processing conditions on morphology of TPU has previously been explored using DIN ISO 527 type 5 A specimens, in which increasing processing temperature reduced the elastic modulus and decreased average crystallite size [**160**]. Figure 6-16 illustrates the removal of an

endothermic dip and shift of an exothermic peak with processing. The cause of the initial pellet dip around 85 ^{o}C is not clear. The peak shift to a lower temperature could be an indication of modified crystalline morphology to a less ordered crystalline structure due to processing.

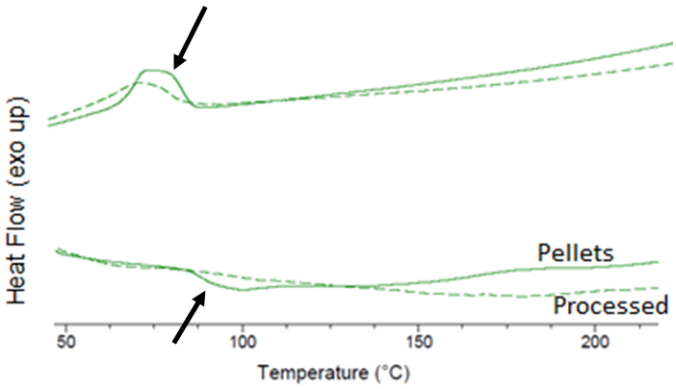

Figure 6-16: Comparison of unprocessed sample (resin pellet) to mold micro tensile bar of TPU. Arrows indicate key modifications of processing.

The objective of the given research was not to compare resin lots, but to compare processing effects on final morphological structure and relate results to mechanical properties, similar to what Stribeck et al achieved at the macroscale [**160**].

For processed samples, the endothermic peaks corresponding to melt enthalpy were fairly insignificant. This phenomenon is due to the quasi-crystalline nature of the TPU hard domains which provide a relatively weak signal [**161**]. Melt peaks, which can be indicative of crystallite size [**160**] , were found to have no consistent trend (Table **6-5**). The change in mechanical properties of TPU with no significant change in melt temperature with varying mold processing temperatures has previously been observed [**122**].

Table 6-5: Melting peak temperature for different molding conditions (units in ^{o}C).

Injection Velocity (mm/s)	Mold Temperature (°C)		
	100	**120**	**130**
50	158.32	162.6	157.47
100	163.3	159.42	159.47
130	159.31	161.15	162.35

Figure **6-17** shows a few distinct changes between the sample with highest and lowest moduli. The endothermic dip associated with the heat of fusion appears to be slightly more developed for the low modulus curve compared to the other curve, which could be the result of an increase level of crystallinity. In addition, the exothermic recrystallization peak of the low modulus curve is shifted to a lower temperature and appears smaller. The shift could be due to the presence of soft segment crystallization, a phenomenon that has been linked to exceptional tensile properties [**161**].

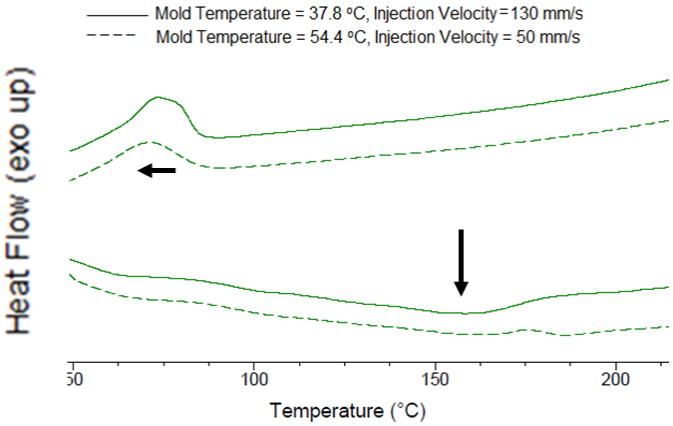

Figure 6-17: DSC curve of sample with highest elastic modulus (dashed line) and lowest elastic modulus (solid line). Arrows point out differences between curves.

Although it is unclear as to what morphological alterations are occurring, it does appear that there is a discrepancy in crystalline structure, which undoubtedly has an effect on polymer material properties.

6.2.3.3 FTIR / DMA Analysis

FTIR absorbance spectra revealed key variations in types and prevalence of chemical bonds. The differences are thought to be either the effects of aging, changes in synthesis methods, or a combination of both.

Some of the primary bond locations on the spectra are shown in Table 6-6. Changes in intensity of such bonds can indicate the relative amount of certain molecular constituents and give a more comprehensive understanding of molecular composition and morphology, especially when combined with other characterization techniques.

Table 6-6: Typical polyurethane peak positioning data [125].

PEU band assignment	Position (cm^{-1})
Free C=O	1730
H-bonded C=O	1704
NH bend	1596
Amide II	1530
CN stretch	1223
C-O-C stretch	1108
C-O-C stretch	1082

Figure 6-18 shows a portion of the FTIR spectrum, indicating a few noticeable curve differences. There appears to be a difference in ether bond stretching, as the two curves are dramatically different at both 1108 cm^{-1} and 1082 cm^{-1}. The aged resin batch has a more prominent peak at 1082 cm^{-1}, while the new batch has a stronger peak at 1108 cm^{-1}. There is a distinct small peak present at approximately 1565 cm^{-1} that barely exists in the old resin batch, which corresponds to bending of an amide II bond, which is

associated with conformational changes [**162**]. Differences in spectral results for the amide I and amide II regions can be attributed to time-dependent phase separation of urethane hard segments upon room temperature aging [**163**]. The new batch appears to have a stronger peak present at 1730 cm^{-1}, which corresponds to a higher amount of C=O bonds. To observe the manner in which chemical bond variations affected polymer viscoelasticity, melt viscosity provided a comparison between the two lots isothermally.

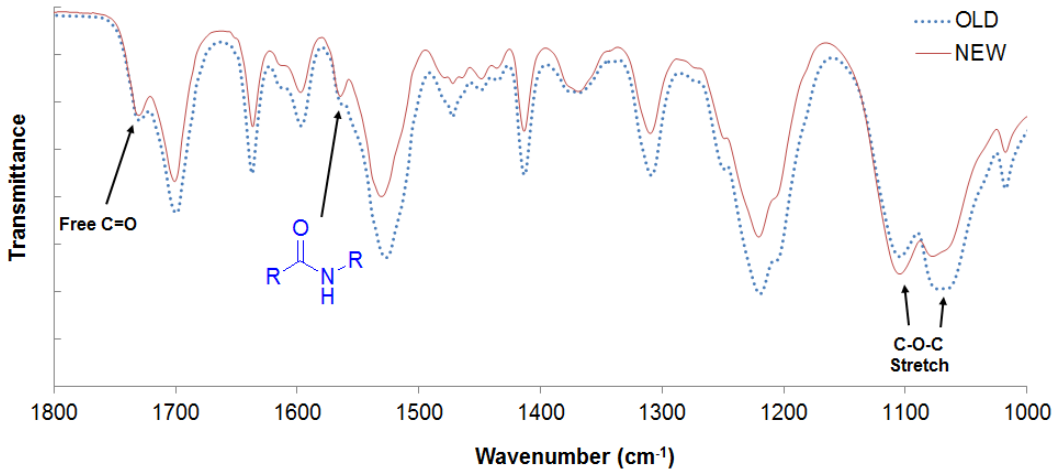

Figure 6-18: FTIR spectrum of old and new TPU, illustrating curve differences.

Melt viscosity results showed significant viscosity and modulus differences between the two resin batches. The aged batch appears to have a lower viscosity for all frequency values and at both temperatures (Figure 6-19). It appears that the viscosity of the aged batch is more sensitive to changes in melt temperature, especially at a frequency of 1. In Figure 6-20, the storage modulus of the new batch stays significantly lower than the old batch for all frequencies. The lower values are constant with those obtained from micro tensile testing results.

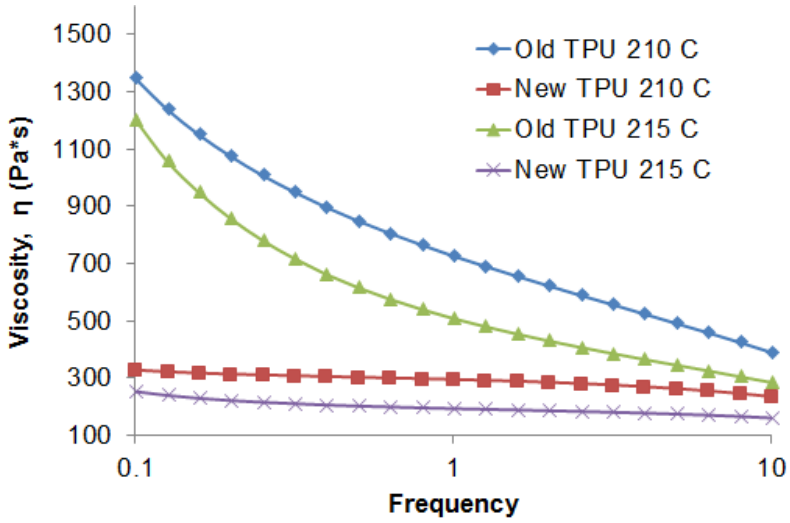

Figure 6-19: Viscosity as a function of testing frequency. Aged batch has consistently higher viscosity. Viscosity is more consistent at higher melt temperatures.

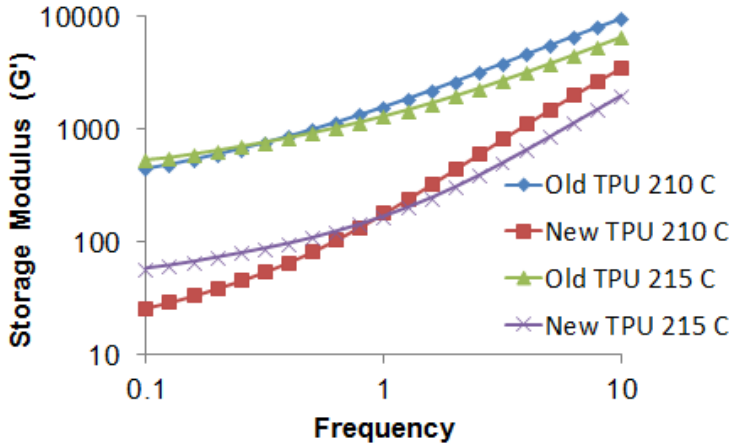

Figure 6-20: Storage modulus as a function of testing frequency. Newer batch has lower modulus, and both polymers are less sensitive to frequency at higher melt temperatures.

6.2.3.4Simulation

The molding process was simulated in Autodesk Moldflow, in which experimental molding parameters were input into the software. It was expected that higher injection velocities would result in higher shear rates present in the molded part. Shear rate should increase with increasing flow rate, assuming the channel throw which

the polymer flows maintains the same geometry. However, the converse was true, as shown in Figure 6-21. Maximum shear rate inside the gage region actually increased with decreasing injection velocity.

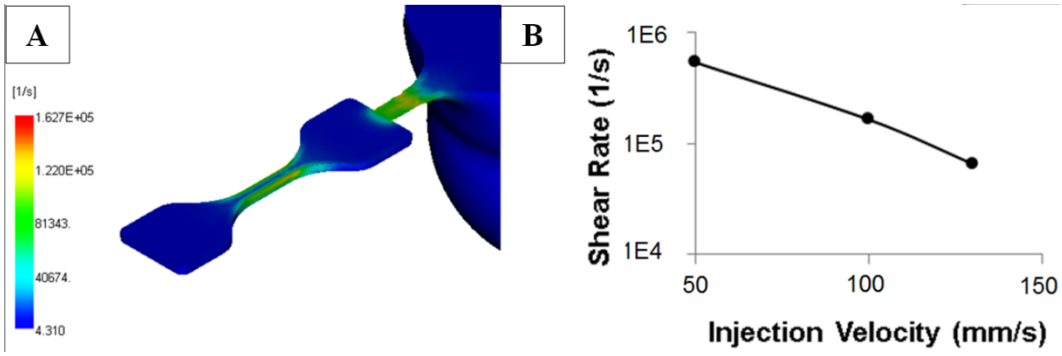

Figure 6-21: Representative shear rate distribution during filling of micro tensile bar (A), and maximum shear rate as a function of injection velocity for TPU molded with mold temperature of 37.8 ^{o}C (B).

A possible explanation of the unexpected results is that the lower velocity caused the polymer to shear less up to the location of the gage region (i.e., as it passed from sprue to runner to gate), giving it a higher viscosity, which would create a higher shear rate while travelling through the channel. Figure 6-22 shows the temperature distribution inside the gage region. Directly at the walls the temperature is equal to the set mold temperature, while there is a slight increase in temperature near the wall due to shear stress imposed on the molecules, imparting additional kinetic energy. To develop an understanding of why shear rate may be lower and higher injection velocities, the temperature and shear rate distribution were analyzed.

The shear rate distributions across the gage region in Figure 6-23 show a reduction in shear rate with an increase in mold temperature and increase in injection

velocity. A somewhat peculiar result present in the shear rate profiles, as the shear rate reduction caused by the increase in mold temperature in the low velocity case is more significant than the reduction for the middle velocity (i.e., the profiles switch their order comparing low to high mold temperatures).

Figure 6-24 shows the temperature distribution with the temperature measurement range shown across the gage region. Higher shear rates result in higher temperatures close to (but not at) the mold walls and a higher injection velocity appears to reduce the variation of temperature across the thickness of the channel (Figure 6-25). The change in mold temperature doesn't appear to significantly affect the melt temperature.

Shear rate and temperature both have an effect on the viscosity of the polymer as it travels through the cavity. In the case of microfluidic flow, the typical viscosity profile becomes more condensed, as the middle of the channel is brought closer to the high shear region near the wall. Thus, profiles like the ones seen in Figure 6-26 can occur

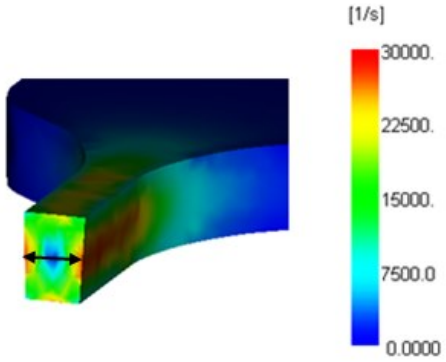

Figure 6-22: Shear rate distribution with measured shear rate location in gage region (double headed arrow).

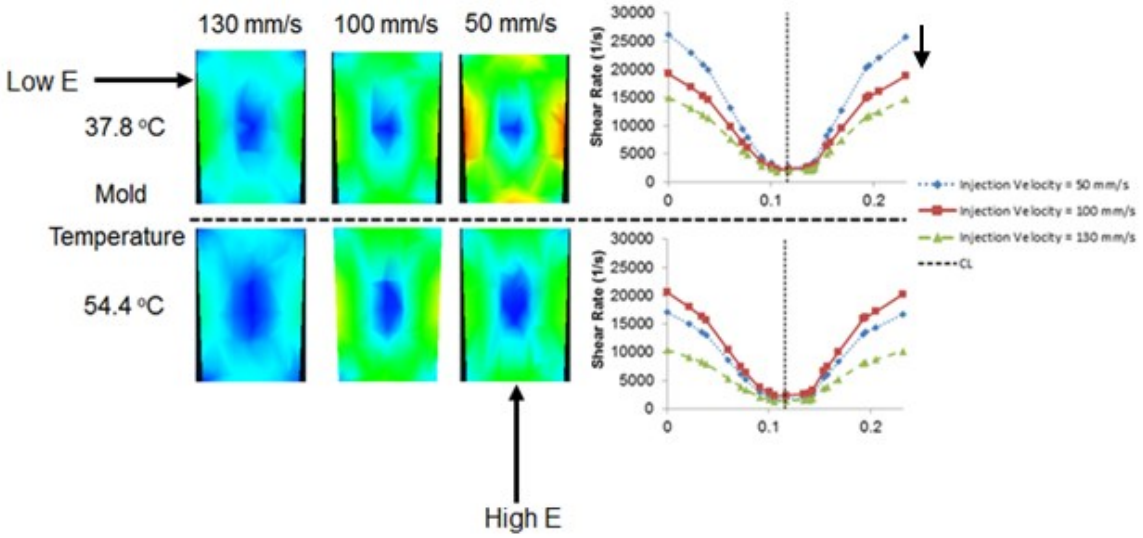

Figure 6-23: Shear rate distribution for gage cross-section for high and low mold temperatures at different injection velocities. Arrow on right indicates the increased reduction of shear rate for the 50 mm/s injection velocity condition at the higher mold temperature.

It appears that in transitioning from the low to high mold temperature, the middle velocity experiences a decrease in viscosity. The reduction could be the result of increased shear rate the middle velocity also was subjected too with an increase in mold temperature.

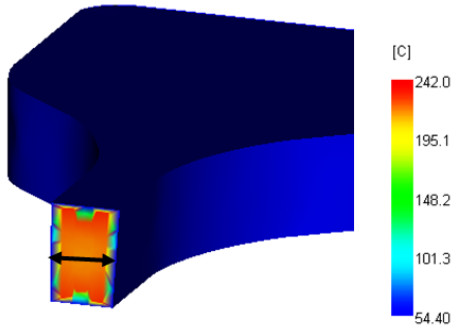

Figure 6-24: Temperature distribution with measured temperature location in gage region (double headed arrow).

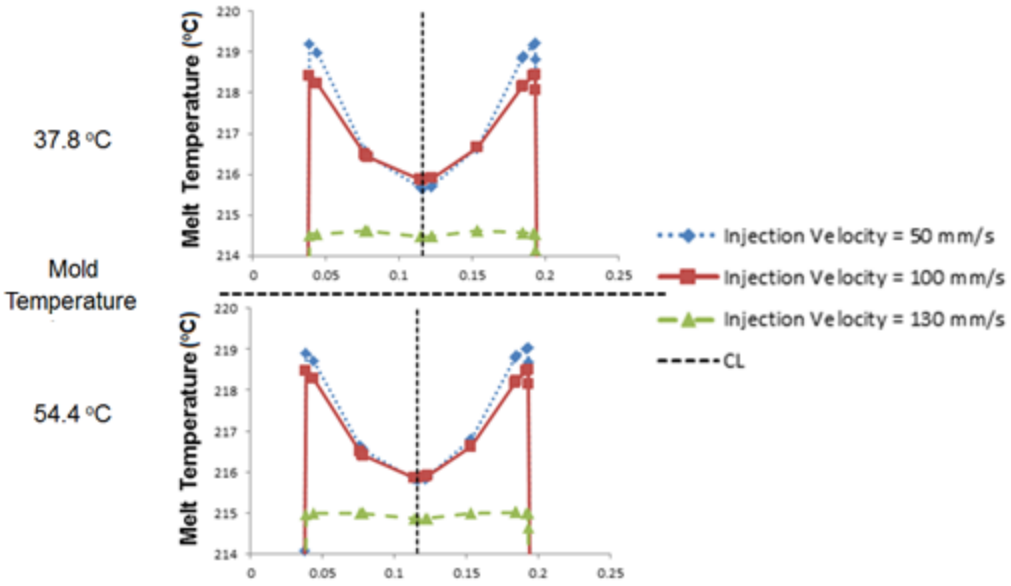

Figure 6-25: Temperature distribution across gage region for high and low mold temperatures for different injection velocities.

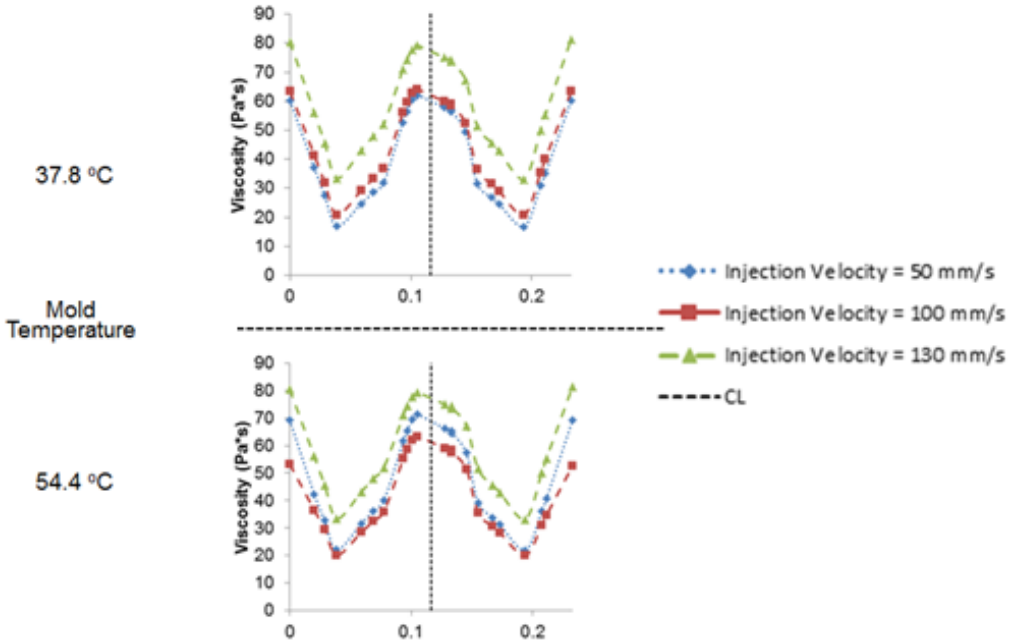

Figure 6-26: Viscosity distribution across channel for high and low mold temperatures and different velocities.

Given the results of simulation, it appears that the highest modulus was attained through processing conditions allowing for the highest melt temperature, moderate to

high shear rate, and moderate viscosity compared to other conditions. Possibly, the higher shear rate contributed positively to molecular chain orientation, providing the part a greater amount of tensile resistance as a result. The results presented here are based on the assumption that no microscale flow effects are occurring, such as wall slip, surface tension modification, and elasticity effects [**43**].

7 Conclusions and Future Recommendations

Moving forward to the next steps of the project, there are many aspects that can be improved upon and explored, furthering the potential for the use of micro and nanostructured surfaces to direct stem cell behavior. The following suggestions are conceived from a combination of difficulties encountered during the given research, robust collaborative discussion with multi-disciplinary research colleagues, and ideas realized from review of various scientific literature.

7.1 Part Demolding

As previously mentioned, equally important to adequate feature filling is successful demolding of the features from their respective cavities. Feature geometry, material shrinkage, and the method of ejection all contribute to the process of part removal from the cavity.

The most immediate concern to be addressed is the modification of the ejector system. The slightest amount of deflection of the part can cause a dramatic deflection at the microscale, imparting deleterious torque and risking feature fracture during ejection. To counteract any unnecessary part bending, a stripper plate can be employed, in which a

portion of the cavity would serve as the ejector system. The special "stripper plate," shown in Figure 7-1, will be fixed to ejector pins, and the ejector plate system will function identically to its previous conformation.

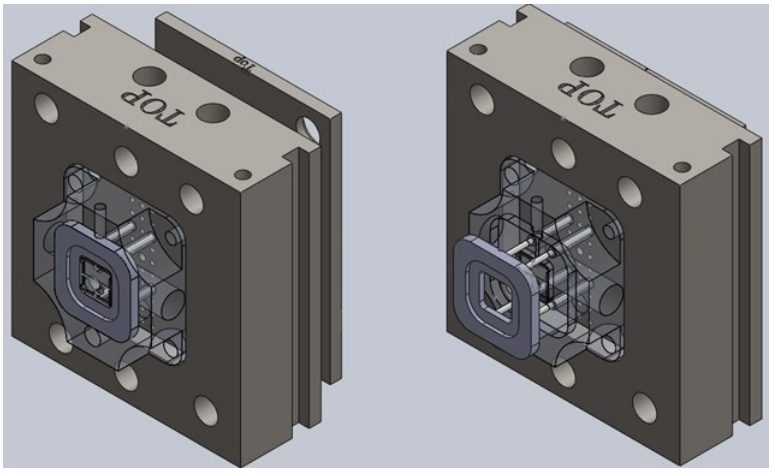

Figure 7-1: CAD representation of stripper plate assembly illustrating the movement of the stripper plate outward from the aluminum insert. Aluminum inserts is made transparent to display ejector pins.

The investigation of mold coatings should also be conducted to address demolding replication and consistency concerns. Coatings were not extensively covered in the given work, as the main focus was the development of the microcavity geometry. However, the synergistic combination of an optimized geometry and applied coating would be ideal for enhancing results. Moreover, to enhance replication further, the identification of a coating that could simultaneously retard heat transfer during filling and facilitate part release during demolding (i.e., low thermal conductivity and low surface energy) would be highly beneficial to the project. For the anti-stiction material used, the coating must be applied conformally to preserve the intended dimensions of the molded part, and maintain its integrity over the course of many molding cycles. In the case of using an

induction coupled plasma (ICP) system, the chamber should be kept at a low pressure to promote conformal deposition, and the pressure and temperature should be optimized to achieve the desired coating thickness [**164**].

7.2 Micro/Nanoscale Design

The next steps regarding design of the micro/nanofeatured bio-interface should include areas not explored during the given research. Firstly, within the microscale domain, higher aspect ratio pillars with slight tapers should be further investigated. The high level of microfeature consistency recently attained needs to be proven in a high aspect ratio regime. The passivation compensation technique introduced in this paper is a very useful tool to use for further realizing capabilities of tapered tooling. The roughness could potentially be further reduced through either strategic conformal surface coatings or through additional etching recipe modification.

Once high aspect ratio microscale features are successfully replicated, the nanoscale must be explored to obtain a more comprehensive understanding of nanotopography on hMSC response. A manufacturing technique capable of nanoscale feature patterning is necessary for the tooling inlays. UV lithography has been continuously developing sophisticated methods to reduce feature sizes, with dimensions reaching values < 193 nm (water immersion lithography [**165**]. A concurrent understanding of the size-dependent effects of processing and the impartation of processing-dependent mechanical properties needs to occur to manufacture a well-tuned interface. To complement large-area nanoscale manufacturing, characterization

techniques capable of assessing replication across the entire surface should be implemented to assure proximity effects do not compromise feature uniformity.

Moreover, gradient topography surfaces should be explored at both the micro and nanoscale to test the effects of variant stiffness and feature height on hMSC behavior. Cells are equipped with a sensitively to stiffness gradients through a phenomenon known as "durotaxis," in which they preferentially move towards the more rigid regions. It is thought that durotaxis may be the impetus that is responsible for cellular migration to regions in need of wound repair [**166**]. Thus, gradient surfaces could mimic *in vivo* regions of variant stiffness, thereby inducing specific hMSC behavior in response.

7.3 Micro/Nano Feature Characterization

A critical component of feature design will be the mechanical characterization of micro/nano features. Prior to quantification of The isolation of features for subsequent mechanical analysis was unable to be achieved due to the excessive thickness of the substrate base and the difficulty in isolating a select plane of microfeatures for characterization. Additional methods to test microfeatures need to be developed and implemented to more comprehensively measure the properties of the pillars.

If isolation is unable to be accomplished, other less conventional techniques could be implemented. For example, the immunofluorescent labeling of the fibronectin-coated tips of micropillars used by Chen et al. could be implemented in combination with an imposed fluidic flow across the microfeatured surface at a particular flow rate corresponding to a specific force [**166**]. The deflection of the features could then be measured and microscale Young's modulus could be obtained through the relation

between pillar dimensions, applied bending force, and subsequent deflection. The same fluorescent labeling could also be used in conjunction with optical tweezers, in which an optical laser would apply a specific bending force (due to the light-scattering forces experienced by the exposed microfeature), and the resultant deflection could be observed through the change in pillar tip position. Optical tweezers are capable of applying nano Newton forces to microscale components [**167**].

Another potential method could be the use of a microscopy probe which applies a force laterally to the surface of the microfeatured substrate. In a process called "lateral force microscopy (LFM)," the cantilever would move across the surface and deflect features at the tip, measuring deflection in response to applied forces.

7.4 Micro/Nano Feature Bending Mechanics Considerations

The bending response of a micro-injection molded polymer beam requires a deep understanding of the effects of processing, feature geometry, and micro/nanoscale material properties. Using bulk mechanical properties procured from macroscale mechanical characterization and the use of generalized bending mechanics can result in incorrect assumptions of the mechanical response of micro/nanopillars to cellular traction forces.

The first consideration involves the use of compliant polymers. During bending, the compliance of the macroscale polymer base can contribute to the overall deflection of the pillar. Figure 7-2 shows the different factors that figure in to cumulative pillar deflection.

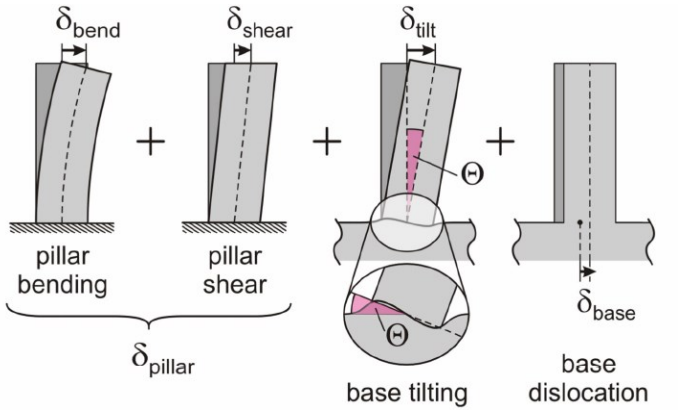

Figure 7-2: Schematic of different contributions to pillar deflection [167**].**

In addition, microscale morphology present within such features must be further assessed, as it serves to dictate mechanical response. Previous work has revealed the initiation of crystallinity inside of microfeatures due to high shear rates aligning macromolecular chains during filling [**159**].

The enhanced crystallinity (semi-crystalline polymers) or general increase in molecular order (amorphous polymers) has the potential to increase mechanical resistance of the microfeature to applied forces. If attempting to reduce apparent stiffness, the processing-induced molecular alignment may work in a counter-productive manner. A potential method to solve such a dilemma is a process known as "annealing," in which polymer molecular order is reduced by slowly heating the part to a temperature beyond its glass transition point. Annealing is routinely used in industry as a method to relieve internal stresses created from the frozen-in molecular order associated with the injection molding process. The annealing semi-crystalline polymers may cause an alteration of crystalline structure and may promote microphase separation in the case of block copolymers [**169**]. Consequently, the effects of annealing on properties should be comprehensively assessed and conditions should be optimized (i.e., rate of temperature

increase, time at maximum temperature, cooling rate, etc.) to be tuned to the appropriate stiffness for target mimicked biological tissue modulus.

7.5 Commercialization Considerations

Although the given technology may be relatively far from an industrially adopted solution, it is important to mention (and eventually address) the concerns that need to be overcome for the polymer substrate to be a viable product.

In terms of a final part to be integrated into the cell culture environment, the substrate needs to take a geometrical form that is easy to handle and use, while still being manufacturable with a high level of precision. Micro-injection molding machines have a relatively limited volume capacity (15 cm^3 for the largest model [**38**]). Thus, to incorporate highly consistent micro/nanotopography into the existing industry standard cell culture well plates, micro-injection molding cannot directly be used to make such a part.

A few options exist to address the issue. A separate insert that could be placed in cell culture wells could be used, similar to what has been done for the given research. To further enhance the insert, the shape could be modified to occupy the entire well to ensure all cells are exposed to the micro/nano topography present. To incorporate the features into the existing part, traditional macroscale molding could potentially be used, with highly localized mold temperature control near the topographic regions. Although shot size control would comparatively be reduced, the effects may be insignificant compared

to precise temperature control at the melt-mold interface. Use of a hot runner system (melt delivery domain maintained about T_{melt} of the polymer; current method used to make cell culture plates) will serve to create relatively low viscosity and hopefully promote filling.

In terms of micro/nano featured tooling, the inlay material should be further explored to identify the optimal tooling for high-rate long production time manufacturing. Significant focus has been on the use of metal tooling for improved durability over silicon. However, although silicon is more brittle, the metals used for electrodeposition are relatively malleable and display reduced mechanical properties at higher processing temperatures and pressures. One potential solution is bulk metallic glass, which can be machined or formed with sub-micron precision [**16**].

The overall steps forward should be to attempt molding higher aspect ratio features with slight tapers such that reduced apparent stiffness is achieved while simultaneously allowing for feature consistency and stability during demolding and handling. Further development of the cell sensing model will be development based on future quantitative cellular results in the form of proliferation and differentiation.

7.6 Conclusion

Tremendous potential lies in the ability to control stem cell fate through the use of substrates capable of being manufactured in a high rate highly reliable manner. The research presented here demonstrates the enhanced the ability to manufacture substrates with consistent topography. In the process, a more in depth knowledge of tooling and

processing effects on part quality and properties has been cultivated. It is clear that topography is capable of dramatically altering the behavior of hMSCs in an in vitro environment, and further refinement of substrate design, manufacturing, and characterization will serve to optimize a biointerface with the capability to direct stem cells for remedial cellular engineering purposes.

References

[1] P. M. Gilbert, H. M. Blau M. P. Lutolf, "Designing materials to direct stem-cell fate," *Nature*, vol. 462, pp. 433-441, 2009.

[2] S.U. Kim and J. Vellis, "Stem Cell-Based Cell Therapy in Neurological Diseases: A Review," *Journal of Neuroscience Research*, vol. 87, pp. 2183-2200, 2009.

[3] V.F.M. Segers and R.T. Lee, "Stem-cell therapy for cardiac disease," *Nature*, vol. 451, pp. 937-942, 2008.

[4] R.J. McMurray, "Nanoscale surfaces for the long-term maintenance of mesenchymal stem cell phenotype and multipotency," *Nature Materials*, vol. 10, pp. 637-644, 2011.

[5] G.Q. Daley, "The Promise and Perils of Stem Cell Therapeutics," *Cell Stem Cell*, vol. 10, pp. 740-749, 2012.

[6] Schwarz EJ, Prockop DJ, Black IB Woodbury D, "Adult rat and human bone marrow stromal cell differentiate into neurons," *Journal of Neuroscience Research*, vol. 61, pp. 364-370, 2000.

[7] M. Kassem, *Annals of the New York Academy of Sciences*, vol. 1067, pp. 436-442, 2006.

[8] A.J. Engler, "Matrix strains induced by cells: Computing how far cells can feel," *Cellular and Molecular Bioengineering*, vol. 2, no. 1, pp. 39-48, 2009.

[9] B. Lewin, *Cells*, B. Lewin, Ed. Sudbury, MA: Jones and Bartlett, 2007.

[10] D.E. Ingber, "Tensegrity 1. Cell structure and hierarchical systems biology," *Journal of Cell Science*, vol. 116, no. 7, pp. 1157-1173, 2003.

[11] A.J. Engler, "Matrix Elasticity Directs Stem Cell Lineage Specification," *Cell*, vol. 126, pp. 677-689, 2006.

[12] Y.S. Pek, "The effect of matrix stiffness on mesenchymal stem cell differentiation in a 3D thixotropic gel," *Biomaterials*, vol. 31, pp. 385-391, 2010.

[13] D.E. Discher, "Tissue Cells Feel and Respond to the Stiffness of Their Substrate,"

Materials and Biology Review, vol. 310, pp. 1139-1143, 2005.

[14] Y. Sasai, "Surface modification of polystyrene dishes using plasma techniques to enhance cell adhesion and proliferation," in *19th International Symposium on Plasma Chemistry*, Bochum, 2009.

[15] H.N. Kim, "Patterning Methods for Polymers in Cell and Tissue Engineering," *Annals of Biomedical Engineering*, vol. 40, no. 6, pp. 1339-1355, 2012.

[16] N. Zhang, "Replication of micro/nano-scale features by micro injection molding with a bulk metallic glass mold insert," *Journal of Micromechanics and Microengineering*, vol. 22, p. 065019, 2012.

[17] Y.-K. Shen, "Analysis for microstructure of microlens arrays on micro-injection molding by numerical simulation," *International Communications in Heat and Mass Transfer*, vol. 35, pp. 723-727, 2008.

[18] W. Lee, "Nanostructuring of a Polymeric Substrate with Well-Defined Nanometer-Scale Topography and Tailored Surface Wettability," *Langmuir*, vol. 20, pp. 7665-7669, 2004.

[19] H.J. Ensikat, "Superhydrophobicity in perfection: the outstanding properties of the lotus leaf," *Beilstein Journal of Nanotechnology*, vol. 2, pp. 152-161, 2011.

[20] H. Zhang, "Progress on gecko-inspired micro/nano-adhesion arrays," *Bionic Engineering*, vol. 55, pp. 1843-1850, 2010.

[21] M. Madou, *Fundamentals of Microfabrication: The Science of Miniaturization*, 2nd ed.: CRC Press, 2002.

[22] Z. Cui, *Micro-Nanofabrication: Technologies and Applications*. Beijing: Higher Education Press, 2005.

[23] Aachboun S. and Ranson P., "Deep anisotropic etching of silicon," *Journal of Vacuum Science and Technology A*, vol. 17, pp. 2270-2273, 1999.

[24] R. L. Bayt, K. S. Breuer A. A. Ayon, "Deep reactive ion etching: a promising technology for micro- and nanosatellites," *Smart Materials and Structures*, vol. 10, pp. 1135-1144, 2001.

[25] M.A. Douglas, "Trench etch process for a single-wafer RIE dry etch reactor," 4,784,720, November 15, 1988.

[26] S.H. Yoon, "Evaluation of novel tooling for nanoscale injection molding," in *SPIE International Symposia, Smart Structures & Materials / NDE*, San Diego, 2005, pp. 107-116.

[27] T. Copponnex, P. Mele J. Giboz, "Microinjection molding of thermoplastics polymers: a review," *Journal of Micromechanics and Microengineering*, vol. 17, pp. R96-R109, 2007.

[28] M. Heckele, W.K. Schomberg M. Worgull, "Large-scale hot embossing," *Microsystems Technologies*, vol. 12, pp. 110-115, 2005.

[29] V. Srivastava, H.K. Taylor, M.R. Hale, D.E. Hardt, L. Anand D.L. Henann, "Metallic glasses: viable tool materials for the production of surface microstructures in amorphous polymers by micro-hot-embossing," *Journal of Micromechanics and Microengineering*, vol. 19, p. 115030, 2009.

[30] K. K. Gleason, D. J. Edell, E. F. Gleason S.J. Limb, "Flexible fluorocarbon wire coatings by pulsed plasma enhanced chemical vapor deposition," *Journal of Vacuum Science and Technology*, vol. 15, pp. 1814-1818, 1997.

[31] A. Angelov, "A Feasibility Study for sub-100 nm Polymer Injection Molding," in

ANTEC, Cincinnati, 2007, pp. 2987-2991.

[32] L.P. Yeo, "Design of Experiment for Optimization of Plasma-Polymerized Octafluorocyclobutane Coating on Very High Aspect Ratio Silicon Molds," *Langmuir*, vol. 22, no. 24, pp. 10196-10203, 2006.

[33] S.-H. Yoon, "Effect of Processing Parameters, Antistiction Coatings, and Polymer Type when Injection Molding Microfeatures," *Polymer Engineering and Science*, vol. 50, no. 2, pp. 411-419, 2010.

[34] N. B. Larsen M. Matschuk, "Injection molding of high aspect ratio sub-100 nm nanostructures," *Journal of Micromechanics and Microengineering*, vol. 23, p. 025003, 2013.

[35] S. Kang, *Micro/Nano Replication*. Hoboken: Wiley, 2012.

[36] B. Sha, "Investigation of micro-injection moulding: Factors affecting the replication quality," *Journal of Materials Processing Technology*, vol. 183, pp. 284-296, 2007.

[37] A.C. Liou, "Injection molding of polymer micro- and sub-micron structures with high-aspect ratios," *International Journal of Advanced Manufacturing Technology*, vol. 28, pp. 1097-1103, 2006.

[38] C. Yang, "Microinjection molding of microsystem components: new aspects in improving performance," *Journal of Microengineering and Mechanics*, vol. 23, p. 093001, 2013.

[39] C. Yang, "Replication characterization of microribs fabricated by combining ultraprecision machining and microinjection molding," *Polymer Engineering and Science*, vol. 50, pp. 2021-2030, 2010.

[40] H.-Y. Lin, "Experimental and analytical study on filling of nano structures in micro injection molding," *International Communications in Heat and Mass Transfer*, vol. 37, pp. 1477-1486, 2010.

[41] S. Khalilian, "The Application of Commerical Injection Molding Software to Micro-Component Design and Process Development," in *ICOMM*, Victoria, BC, 2013, pp. 50-56.

[42] C. Yang, "Replication Characterization in Injection Molding of Microfeatures With High Aspect Ratio: Influence of Layout and Shape Factor," *Polymer Engineering and Science*, vol. 51, no. 5, pp. 959-968, 2011.

[43] A. Gava, "On the performance of a viscoelastic constitutive model for micro injection moulding simulations," *eXPRESS Polymer Letters*, vol. 6, no. 5, pp. 417-426, 2012.

[44] P. He, "Influence of key factors on the wall slip phenomenon in micro flow," *Advanced Materials Research*, vol. 472-475, pp. 2415-2421, 2012.

[45] D. Yao, "Simulation of the filling process in micro channels for polymeric materials," *Journal of Micromechanics and Microengineering*, vol. 12, pp. 604-610, 2002.

[46] W. Michaeli G. Potsch, *Injection Molding: An Introduction*, 2nd ed.: Hanser, 2008.

[47] PMC, "Mold Temperature Control Effectiveness: Electric Heat vs. Pressurized Water," PMC, Cincinnati,.

[48] M. Naitove, "PMC Proves it's not too late to Pioneer in Medical Molding," Plastics Technology, 2010.

[49] C. Gornik, "Injection Moulding of Parts with Microstructured Surfaces for Medical Applications," in *Macromolecular Symposium*, Weinheim, 2004, pp. 365-374.

[50] J. Bae, H. Kim, S. Kang Y. Kim, "Modeling of passive heating for eplication of

submicron patterns in optical disk substrates.," *Journal of Physics D: Applied Physics*, vol. 37, pp. 1319-1326, 2004.

[51] J. Han, J. Lim, M. Choi, Y. Han, J. Hong, S. Kang N. Lee, "Injection Molding of Nanopillars for Perpendicular Patterned Magnetic Media with Metallic Nanostamp," *Japanese Journal of Applied Physics*, vol. 47, no. 3, pp. 1803-1805, 2008.

[52] J.I. Goldstein, *Scanning Electron Microscopy and X-Ray Microanalysis*.: Kluwer Academic / Plenum Publishers, 2003.

[53] E. Puukilainen, "Superhydrophobic Polyolefin Surfaces: Controlled Micro- and Nanostructures," *Langmuir*, vol. 23, pp. 7263-7268, 2007.

[54] K.S. Sorensen, "On-Chip Liquid Control Using Striped Surface Topography Fabricated by Polymer Injection Molding," in *16th International Conference on Miniaturized Systems for Chemistry and Life Sciences*, Okinawa, 2012.

[55] Y. Yuan et al, *Surface Science Techniques*, G. Bracco, Ed.: Springer, 2013.

[56] Z. Yoshimitsu, "Effects of Surface Structure on the Hydrophobicity and Sliding Behavior of Water Droplets," *Langmuir*, vol. 18, pp. 5818-5822, 2002.

[57] R. Ayala, "Engineering the cell-material interface for controlling stem cell adhesion, migration, and differentiation," *Biomaterials*, vol. 32, pp. 3700-3711, 2011.

[58] (2013) ramé-hart contact andle goniometers and teniometers. [Online]. http://www.ramehart.com/contactangle.htm

[59] C.N.C. Lam, "Study of the advancing and receding contact angles: liquid sorption as a cause of contact angle hysteresis," *Advances in Colloid and Interface Science*, vol. 96, pp. 169-191, 2002.

[60] C. Kumar, *Biomimetic and Bioinspired Nanomaterials*.: Wiley-VCH, 2010.

[61] K.-Y. Yeh, "Contact Angle Hysteresis on Regular Pillar-like Hydrophobic Surfaces," *Langmuir*, vol. 24, pp. 245-251, 2008.

[62] L. Bacakova et al, "Modulation of cell adhesion, proliferation and differentiation on materials designed for body implants," *Biotechnology Advances*, vol. 29, pp. 739-767, 2011.

[63] "Studies on the biocompatibility of materials: Fibroblast reorganization of substratum-bound fibronectin on surfaces varying in wettability," *Journal of Biomedical Materials Research*, vol. 30, pp. 385-391, 1996.

[64] M.J. Dalby, "The control of human mesenchymal cell differentiation using nanoscale symmetry and disorder," *Nature Materials*, vol. 6, pp. 997-1003, 2007.

[65] K.J. Cha, "Injection molded Nano Petri dishes: A new platform for studying cell," in *ICOMM*, Victoria, BC, 2013, pp. 305-308.

[66] C.H. et al Ahn, "Disposable Smart Lab on a Chip for Point-of-Care Clinical Diagnostics," in *IEEE*, vol. 92, 2004, pp. 154-173.

[67] Y. Gao, "Influence of Hot Embossed Process Parameters on Biodegradable Polymer Microstructure for Drug Delivery," in *IEEE*, Kaohsiung, Tiawan, 2011, pp. 1246-1249.

[68] G. Schwartz, "Flexible polymer transistors with high pressure sensitivity for application in electronic skin and health monitoring," *Nature Communications*, vol. 4, 2012.

[69] C. Mohrdieck, "ATheoretical Description of Elastic Pillar Substrates in Biophysical Experiments," *ChemPhysChem*, vol. 6, pp. 1492-1498, 2005.

[70] X. Zheng, "An optical Moir technique for cell traction force mapping," *Journal of Micromechanics and Microengineering*, vol. 18, p. 125006, 2008.

[71] K.A. Kilian, "Geometric cues for directing the differentiation of mesenchymal stem cells," *PNAS*, vol. 107, no. 11, pp. 4872-4877, 2010.

[72] M.J. Dalby, "Investigating filopodia sensing using arrays of defined nano-pits down to 35 nm diameter in size," *The International Journal of Biochemistry & Cell Biology*, vol. 36, pp. 2005–2015, 2004.

[73] J. Fu, "Mechanical regulation of cell function with geometrically modulated elastomeric substrates," *Nature Methods*, vol. 7, no. 9, pp. 733-736, 2010.

[74] A.M. Tom, "An Investigation of Micro-scale Fabrication Using the Injection Molding Process," Lehigh University, Bethlehem, PA, 2007.

[75] AK Angelov, "Numerical and Experimental Studies in Development of Polymer Injection Micro Molding," Lehigh University, Bethlehem, PA, 2007.

[76] A.K. Angelov J.P. Coulter, "The Development and Characterization of Polymer Microinjection Molded Gratings," *Polymer Engineering and Science*, vol. 48, no. 11, pp. 2169-2177, 2008.

[77] IH Jaafar, "An Investigation of Mechanically Tunable and Nanostructured Polymer Scaffolds for Directing Human Mesenchymal Stem Cell Development," Lehigh University, Bethlehem, PA, 2011.

[78] A. C. Eringen, "A Lubrication Theory for Fluids with Microstructure," *International Journal of Engineering Science*, vol. 33, no. 15, pp. 2297-2308, 1995.

[79] E.E. Rosenbaum, "Wall Slip in the Capillar Flow of Molten Polymers Subject to Viscous Heating," *AIChE Journal*, vol. 43, no. 3, p. 598, 1997.

[80] J.I. Craig O.A. Bauchau, "Euler-Bernoulli beam theory," Solid Mechanics and Its Applications, 2009.

[81] A.J. Bohl F. M. Sasoglu, "Parallel force measurement with a polymeric microbeam array using an optical microscope and micromanipulator," *Computer Methods and Programs in Biomedicine*, vol. 93, pp. 1-8, 2009.

[82] P. Du, "Extension of the beam theory for polymer bio-transducers with low aspect ratio and viscoelastic characteristics," *Journal of Micromechanics and Microengineering*, vol. 20, p. 095016, 2010.

[83] Y. Xiang, "Analysis of soft cantilevers as force transducers," *Applied Physics Letters*, vol. 90, p. 133901, 2007.

[84] J. R. Hutchinson, "Shear Coefficients for Timoshenko Beam Theory," *Journal of Applied Mechanics*, vol. 68, pp. 87-92, 2001.

[85] D.A. Hanson, D.D. Schlaepfer S.K. Mitra, "Molecular Architecture of focal contacts," *Nature Reviews Molecular Cell Biology*, vol. 6, pp. 56-58, 2005.

[86] S. S. Hur, "Live Cells Exert 3-Dimensional Traction Forces on Their Substrata," *Cellular and Molecular Bioengineering*, vol. 2, no. 3, pp. 425-436, 2009.

[87] M. Kato, "Using Model Substrates To Study the Dependence of Focal Adhesion Formation on the Affinity of Integrin-Ligand Complexes," *Biochemistry* , vol. 43, pp. 2699-2707, 2004.

[88] T. Zhao, "How Focal Adhesion Size Depends on Integrin Affinity," *Langmuir*, vol. 25, pp. 1540-1546, 2009.

[89] E.K.F. Yim, "Nanotopography-induced changes in focal adhesions, cytoskeletal organization, and mechanical properties of human mesenchymal stem cells," *Biomaterials*, vol. 31, no. 6, p. 1299, 2010.

[90] CY Hui, "Constraints on Microcontact Printing Imposed by Stamp Deformation," *Langmuir*, vol. 18, pp. 1394-1407, 2002.

[91] Y Zhang, "Replica Molding of High-Aspect-Ratio Polymeric Nanopillar Arrays with High Fidelity," *Langmuir*, vol. 22, pp. 8595-8601, 2006.

[92] P Roca-Cusachs, "Stability of Microfabricated High Aspect Ratio Structures in Poly(dimethylsiloxane)," *Langmuir*, vol. 21, pp. 5542-5548, 2005.

[93] R Spolenak, "Adhesion design maps for bio-inspired attachment systems," *Acta Biomateriala*, vol. 1, pp. 5-13.

[94] C.M.F. Barry, "Tooling for Injection Molded Micro and Nanoscale Features," Nano Summit, 2010.

[95] (2013) Hubbard-Hall. [Online]. http://www.hubbardhall.com/chemical-apps-semiconductor-photoresists.htm

[96] "825 Positive Photoresist: Positive Working Photoresist Systems for the Semiconductor Industry," Arch Chemicals,.

[97] S. Aachboun, "Deep anisotropic etching of Silicon," *Journal of Vacuum Science and Technology A*, vol. 17, no. 4, pp. 2270-2273, 1999.

[98] I.W. Rangelow, "Critical tasks in high aspect ratio silicon dry etching for microelectromechanical systems," *Journal of Vacuum Science and Technology A*, vol. 21, no. 4, pp. 1550-1562, 2002.

[99] S. Tanzi, "Fabrication of combined-scale nano- and microfluidic polymer systems using a multilevel dry etching, electroplating and molding process," *Journal of Micromechanics and Microengineering*, vol. 22, p. 115008, 2012.

[100] C.B. Labelle, "Investigation of flourocarbon plasma deposition from c-C4F8 for use as passivation during deep silicon etching," *Journal of Vacuum Science and Technology*, vol. 22, no. 6, p. 2500, 2004.

[101] L.A. Wolderling, "Periodic Arrays of deep nanopores made in silicon with reactive ion etching and dep UV lithography," *Nanotechnology*, vol. 19, p. 145304, 2008.

[102] Heckele M. and Schomberg W. K., "Review on micro molding of thermoplastic polymers," *Journal of Micromechanics and Microengineering*, vol. 14, pp. R1-R14, 2004.

[103] Lee M.-W., Lee S.G., Lee E.H., Park S.-G. Jo S.-B., "Characterization of a modified Bosch-type process for silicon mold fabrication," *Journal of Vacuum Science and Technology*, vol. 23, no. 4, pp. 905-910, 2005.

[104] K.G. Lee, T.J. Lee, B.G. Choi, J.Y. Park, C.Y. Jung, C.-S. Lee, S.J. Lee B.I. Kim, "A continuous tilting of micromolds for fabricating polymer microstructures in microinjection," *Lab on a Chip*, vol. 10, p. 1039, 2013.

[105] "Revisiting micro hot-embossing with moulds in non-conventional materials," *Microsystem Technologies*, vol. 13, pp. 475-481, 2007.

[106] N. Roxhed, "A method for tapered deep reactive ion etching using a modified Bosch process," *Journal of Micromechanics and Microengineering*, vol. 17, pp. 1087-1092, 2007.

[107] S. Colpo, F. Giacomozzi, S. Ronchin, A. Q. A. Qureshi, B. Margesin D. Vasilache, "Variable isotropy Deep RIE process for through wafer via holes manufacturing," in *SPIE*, 2011.

[108] K. D. Munck, N. Pham, O. Luhn, A. Aarts, P. D. Moor, K. Baert, C. Van Hoof D. S.

Tezcan, "Development of Vertical and Tapered Via Etch for 3D Through Wafer Interconnect Technology," in *Electronics Packaging Technology Conference*, 2006.

[109] Colli A., Fasoli A., Luo J. K. Flewitt A. J., Ferrari A. C., and Milne W. I. Fu Y. Q, "Deep reactive ion etching as a tool for nanostructure fabrication," *Journal of Vacuum Science Technology B*, vol. 27, pp. 1520-1526, 2009.

[110] Zijlstra T., van der Drift E. Blauw M. A., "Balancing the etching and passivation in time-multiplexed deep dry etching of silicon," *Journal of Vacuum and Science Technology B*, vol. 19, pp. 2930-2934, 2001.

[111] Maluf N., *An Introduction to Microelectromechanical Systems Engineering*. Boston: Artech House, 2000.

[112] V.M. Donnelly, G.R. Bogart, R.L. Opila, A. Kornblit C.B. Labelle, "Investigation of fluorocarbon plasma deposition from c-C4F8 for use as passivation during deep silicon etching," *Journal of Vacuum Science and Technology A*, vol. 22, pp. 2500-2507, 2004.

[113] A. Chandekar, "Fabrication of stamps for microcontact printing by injection molding," *Microelectronic Engineering*, vol. 85, pp. 187-194, 2008.

[114] "Product Information: Styron 666D," Americas Styrenics, 2011.

[115] "Autodesk Moldflow Material Database,".

[116] "Product Information: EC6600," Americas Styrenics, 2011.

[117] T.A. Osswald, *International Plastics Handbook*.: Hanser, 2006.

[118] N.K. Inkson, "Predicting low density polyethylene melt rheology in elongational and shear flows with ‘‘pom-pom’’ constitutive equations," *Journal of Rheology*, vol. 43, no. 4, pp. 873-896, 1999.

[119] S. Yamasaki, "Effects of aggregation structure on rheological properties of thermoplastic polyurethanes," *Polymer*, vol. 48, pp. 4793-4803, 2007.

[120] A. Rochman A. Frick, "Characterization of TPU-elastomers by thermal analysis (DSC)," *Polymer Testing*, vol. 23, pp. 413-417, 2004.

[121] A. Frick, "Characterization of TPU-elastomers by thermal analysis (DSC)," *Polymer Testing*, vol. 23, pp. 413-417, 2004.

[122] G. Bandur, G. Rusu G.R.E. Maries, "Influence of Processing Temperature on Some Mechanical-Physical Properties of Thermoplastic Polyurethane Desmopan KA 8377 Used for Injection Moulding of Performance Sport Products," *Chemical Bulletin of Politehnica*, vol. 53, no. 67, 2008.

[123] P.K. Annamalai, S.J. Eichhorn, R. Rusli, S.J. Rowan, E.J. Foster, C. Weder J. Mendez, "Bioinspired Mechanically Adaptive Polymer Nanocomposites with Water-Activated Shape-Memory Effect," *Macromolecules*, vol. 44, no. 17, pp. 6827-6835, 2011.

[124] C. Weder, "Self-Assessing Photoluminescent Polyurethanes," *Macromolecules*, vol. 39, pp. 9581-9589, 2006.

[125] T. G. Vargo, "A Surface Spectroscopic and Wettability of a Segmented Block Copolymer Poly(etherurethane)," *Applied Spectroscopy*, vol. 45, no. 3, p. 448, 1991.

[126] MK Shin, "Size-dependent elastic modulus of single electroactive polymer nanofibers," *Applied Physics Letters*, vol. 89, p. 231929, 2006.

[127] (2013) Styrolution Global. [Online]. http://www.styrolution.net/wa/steu~fr_FR/portal/show/common/content/products/styrenics/polystyrol/mechanical_properties_polystyrene

[128] I. Dris, "Material and process parameters and their effects on the degree of groove

replication in DVD disks," in *Proc. SPIE*, 2002, p. 4342.

[129] N. Gadegaard, "Injection Moulding Difficult Nanopatterns with Hybrid Polymer Inlays," *Macromolecular Materials and Engineering*, vol. 297, pp. 1075-1080, 2012.

[130] S. Klapakjian, *Manufacturing Processes for Engineering Materials*, 3rd ed.: Addison-Wesley, 1997.

[131] X. Lu, "Low-Density Polyethylene Superhydrophobic Surface by Control of Its Crystallization Behavior," *Macromolecular Rapid Communications*, vol. 25, pp. 1606-1610, 2004.

[132] C. Y. Yue R. K. Jena, "Cyclic olefin copolymer based microfluidic devices for biochip applications: Ultraviolet surface grafting using 2-methacryloyloxyethyl phosphorylcholine," *Biomicrofluidics*, vol. 6, p. 012822, 2012.

[133] S.B. Tor, J.-H. Chun, N.H. Loh, D.E. Hardt Y.W. Loke, "Micro Injection-Molding of Cyclic Olefin Copolymer Using Metallic Glass Insert," *Manufacturing Systems and Technology*, 2007.

[134] W.K. Schomburg M. Heckele, "Review on micro molding of thermoplastic polymers ," *Journal of Micromechanics and Microengineering*, vol. 14, pp. R1-R14, 2004.

[135] L. Gao, "Contact Angle Hysteresis Explained," *Langmuir*, vol. 22, pp. 6234-6237, 2006.

[136] M.L. Carman et al, "Engineered antifouling microtopographies – correlating wettability with cell attachment," *Biofouling*, pp. 1-11, 2006.

[137] L. Feng, "Petal Effect: A Superhydrophobic State with High Adhesive Force," *Langmuir*, vol. 24, pp. 4114-4119, 2008.

[138] W.S. Leong, "Thickness sensing of hMSCs on collagen gel directs stem cell fate," *Biochemical and Biophysical Research Communications*, vol. 401, pp. 287-292, 2010.

[139] C. Carlson, J. Bozzelli, M. Groleau S. Mertes, "What Position On The Viscosity Curve Is The Most Repeatable With Respect To End Of Fill Cavity Psi," in *Annual Technical Conference*, 2001.

[140] A.C. Liou and R.H. Chen, "Injection molding of polymer micro- and sub-micron structures with high-aspect ratios," *International Journal of Advanced Manufacturing Technology*, vol. 28, pp. 1097-1103, 2006.

[141] H.L. Zhang, "Mold surface roughness effects on cavity filling of polymer melt in micro injection molding," *International Journal of Advanced Manufacturing Technologies*, vol. 37, pp. 1105-1112, 2008.

[142] G Lucchetta, "Effects of the cavity surface finishing on the polymer filling flow in micro injection moulding," in *13th International Conference on Metrology and Properties of Engineering Surfaces*, 2011.

[143] Y. Guo, "Study of the demolding process—implications for thermal stress, adhesion and friction control," *Journal of Micromechanics and Microengineering*, vol. 17, pp. 9-19, 2007.

[144] J.Y. Lim, "Osteoblast Adhesion on Poly(L-lactic Acid)/Polystyrene Demixed Thin Film Blends: Effect of Nanotopography, Surface Chemistry, and Wettability," *American Chemical Society*, vol. 6, no. 6, p. 3319, 2005.

[145] E. Thomas, "Impact of wastewater fouling on contact angle," *Biofouling* , vol. 25, no. 5,

pp. 445-454, 2009.

[146] L. Xie, "Effect of micro tensile sample's cross section shape on the strength of weld line in micro injection molding process," *Microsystem Technologies*, vol. 15, pp. 1031-1037, 2009.

[147] S. Meister, "Influence of manufacturing conditions on measurement of mechanical material properties on thermoplastic micro tensile bars," *Polymer Testing*, vol. 32, pp. 432-437, 2013.

[148] E. Haberstroh, "Determination of Mechanical Properties Suitable for Microsystems," *Journal of Polymer Engineering*, pp. 111-118, 2001.

[149] D. Drummer S. Meister, "Influence of manufacturing conditions on measurement of mechanical material properties on thermoplastic micro tensile bars," *Polymer Testing*, vol. 32, pp. 432-437, 2013.

[150] D.S. Gianola, "Micro- And Nanoscale Tensile Testing Of Materials," *The Member Journal of Minerals, Metals, and Materials Society*, pp. 24-35, 2009.

[151] J. Jeong S. Shanmugham, "Polymer Nanowire Elastic Moduli Measured with Digital Pulsed Force Mode AFM," *Langmuir*, vol. 21, pp. 10214-10218, 2005.

[152] R.R. Lamonte, "Cyclic Olefin Copolymers," *Advanced Materials and Processes*, 2001.

[153] H.E. Assender, G.A.D. Briggs V.N. Bliznyuk, "Surface Glass Transition Temperature of Amorphous Polymers. A New Insight with SFM," *Macromolecules*, vol. 35, pp. 6613-6622, 2002.

[154] J. Mark, *Physical Properties of Polymers*, 3rd ed.: Cambridge University Press, 2004.

[155] Y. Kong, "The measurement of the crystallinity of polymers by DSC," *Polymer*, vol. 43, no. 14, pp. 3873-3878, 2002.

[156] A. Frick, "Study of the Inlfuence of Melt Prosessing on Segmented Polyurethanes Morphology," *Macromolecular Symposium*, vol. 294, pp. 102-108, 2010.

[157] J.L. Mead, C.M.F. Barry, D.J. Carter M.W. Alabran, "Effects of Tooling and Injection Molding Conditions on Nanoscale Replication of Thermoplastic Elastomers," in *Annual Technical Conference*, 2007, pp. 1990-1994.

[158] J. Rieger Y. Men, "Role of Entangled Amorphous Network in Tensile Deformation of Semicrystalline Polymers," *Physical Review Letters*, vol. 91, no. 9, p. 095502, 2003.

[159] C. Yang, "Flow-induced morphology evolution of uniformly miniaturized high-density polyethylene parts prepared by micro-injection molding," *The International Journal of Advanced Manufacturing Technology*, vol. 68, no. 5-8, p. 1745, 2013.

[160] N. Stribeck, "Structure and Mechanical Properties of an Injection-Molded Thermoplastic Polyurethane as a Function of Melt Temperature," *Macromolecular Chemistry and Physics*, pp. 1-14, 2011.

[161] M.F. Sonnenschein, "Enhancing polyurethane properties via soft segment crystallization," *Polymer*, vol. 46, pp. 10158-10166, 2005.

[162] S.-Y. Lin, "Thermal micro ATR/FT-IR spectroscopic system for quantitative study of the molecular structure of poly(N-isopropylacrylamide_ in water," *Polymer*, vol. 40, pp.

2619-2624, 1999.

[163] I. Yilgor, "FTIR investigation of the influence of diisocyanate symmetry on the morphology development in model segmented polyurethanes," *Polymer*, vol. 47, pp. 4105-4114, 2006.

[164] S.-B. Jo, "Fabrication and surface treatment of silicon mold for polymer microarray," *Surface & Coatings Technology*, vol. 188-189, pp. 452-458, 2004.

[165] D.P. Sanders, "Advances in Patterning Materials for 193 nm Immersion Lithography," *Chemical Reviews*, vol. 110, pp. 321-360, 2010.

[166] M.T. Breckenridge et al, "Substrates with Engineered Step Changes in Rigidity Induce Traction Force Polarity and Durotaxis," *Cellular and Molecular Bioengineering*, 2013.

[167] J.L. Tan, "Cells lying on a bed of microneedles: An approach to isolate mechanical force," *PNAS*, 2003.

Vita

John Rodgers was born on December 17th in Bethlehem, PA to Scott and Sara Rodgers. He received a B.S. in Bioengineering in 2008 and an M.S. in Mechanical Engineering in 2010, both from Lehigh University. Following the completion of his advanced degree, John decided to temporarily pursue a career as a cruise ship entertainer, singing with his acapella group around the ship to thousands of guests. He returned in January of 2011 to begin his doctorate in Mechanical Engineering at Lehigh.

During his academic career, John has written numerous conference papers, and was published in Plastics Engineering Magazine and the Journal of Micro and Nanomanufacturing. John has received the Excellence in Polymer Science Award and has been awarded multiple Society of Plsatics Engineers travel awards. He has presented his research during university lectures, at high schools, and at professional conferences over the course of his research. He was also a teaching assistant for Lehigh's Mechanical Engineering manufacturing course. John is very appreciative of his time at Lehigh and the knowledge he has gained during the experience.